MECHANICS-BASED ESTIMATION OF INTRAOPERATIVE SOFT TISSUE DEFORMATION FOR ENHANCING NAVIGATION DURING IMAGE-GUIDED LIVER INTERVENTION

By

Jon S. Heiselman

Dissertation

Submitted to the Faculty of the

Graduate School of Vanderbilt University

in partial fulfillment of the requirements

for the degree of

DOCTOR OF PHILOSOPHY

in

BIOMEDICAL ENGINEERING

August 31, 2020

Nashville, Tennessee

Approved:

Michael I. Miga, Ph.D.

Brett C. Byram, Ph.D.

Benoit M. Dawant, Ph.D.

William A. Grissom, Ph.D.

Sunil K. Geevarghese, M.D.

ACKNOWLEDGMENTS

I owe special thanks to the many people who have made this journey possible. Foremost, I would like to thank my advisor and mentor Dr. Michael Miga, who has not only provided the resources necessary to complete this thesis, but over the years has widened my perspectives on personal values, effective leadership, and career skills, and has encouraged me to continuously exceed my own expectations. He has taught me what it means to lead with compassion, enthusiasm, and integrity that have cultivated an irreplaceable environment for learning and mastery within the lab, across Vanderbilt, and beyond our own institution among collaborators. I would also like to thank the members of my thesis committee, Dr. Brett Byram, Dr. Benoit Dawant, Dr. Will Grissom, and Dr. Sunil Geevarghese, who have given helpful comments and suggestions throughout the development of this work. I am especially appreciative to Dr. Geevarghese, who provided for me the opportunity to engage with his clinical practice to better learn how engineering may integrate with surgery in the present and into the future. In addition, I am grateful to our clinical collaborators Dr. Bill Jarnagin and Dr. Peter Kingham at Memorial Sloan Kettering Cancer Center, and Dr. Amber Simpson who is now at Queen's University. Lastly, I would like to recognize the funding sources that have made these efforts possible: the National Institutes of Health grants R01CA162447, T32EB021937, and R01EB027498.

I must also thank my wonderful labmates, past and present, for their continued support over the years: Rebekah Griesenauer, for your inspiration and candor; Jarrod Collins, for the ideas we have shared and conversations I have learned from; Saramati Narasimhan, for always keeping a positive outlook; Ma Luo, for your kindness, intelligence, diligence, and camaraderie—it has been a wholehearted pleasure taking this journey with you since the first day stepping into lab; and Winona Richey, for becoming a long-lasting friend whose ferocity can overcome any challenge. I could not have made it this far without you. I am also grateful to Dr. Logan Clements and Dr. Jared Weis, who provided reliable insight in

the early phases of the work. Most of all, I give the greatest thanks to my parents, siblings, and personal friends who have regularly motivated me to stay ambitious. I owe particular thanks to Erin, whose stable love and patience have kept me on track and have helped guide doubt towards determination.

TABLE OF CONTENTS

LIST OF TABLES

LIST OF FIGURES

LIST OF ABBREVIATIONS

2D Two-Dimensional

3D Three-Dimensional

CBCT Cone Beam CT

CT Computed Tomography

HCC Hepatocellular Carcinoma

ICP Iterative Closest Point

iCT Intraoperative CT

IGLS Image-Guided Liver Surgery

iUS Intraoperative Ultrasound

LLR Laparoscopic Liver Resection

mCRC Metastatic Colorectal Cancer

MHD Modified Hausdorff Distance

MR Magnetic Resonance

OLR Open Liver Resection

PDE Partial Differential Equation

RMS Root Mean Square

TRE Target Registration Error

wICP Weighted Iterative Closest Point

CHAPTER I

Introduction

I.1 Specific Aims

Surgical and interventional procedures such as resection, ablation, and biopsy depend on knowledge of the intraoperative positions of lesions and other relevant structures. In the context of liver therapy, maximizing effectiveness of treatment and minimizing risk of complication requires accurate localization of clinical targets such as lesions and complicating anatomy such as the hepatic vasculature and bile ducts. For primary and secondary liver cancers, liver resection remains the preferred treatment and offers the best curative outcomes outside of transplantation [26–28]. Recent trends have suggested that laparoscopic liver resection (LLR) offers significant advantages for the patient, including faster recovery and fewer complications as compared to open liver resection (OLR), with no detriment to mortality or oncological control [29, 30]. However, LLR places additional demands on the surgeon that may exacerbate an already steep learning curve [31–33]. In both approaches, technologies capable of improving intraoperative localization are likely to lead to improved interventional capability.

Whereas guidance with intraoperative computed tomography (CT) or magnetic resonance (MR) imaging would provide the most accurate structural information, intraoperative tomographic imaging with CT or MR is costly, requires highly specialized operating suites, and greatly disrupts surgical workflow. More commonly, intraoperative ultrasound (iUS) is used to identify the extent of disease burden, including the number and positions of lesions and their relations to the vascular and biliary hepatic anatomy [34, 35]. While iUS may assist with detection of nodules in multifocal presentations of disease, iUS cannot be considered a comprehensive intraoperative guidance solution; in metastatic colorectal cancer patients, malignant tumors may appear isoechoic to the surrounding liver tissue in up to

43% of patients [36]. Furthermore, chemotherapeutic treatment may shrink tumors beyond the detectability limit of iUS before the time of intervention. These sonographically occult tumors may remain pathologically active in more than 80% of patients who had complete response on CT and ultrasound imaging [37], and therefore require further treatment based on their known positions in preoperative diagnostic image sequences.

Although image guidance techniques referencing high-quality preoperative images of the patient would therefore seem ideal, changes to the organ between preoperative imaging and intraoperative procedural time points represents a major challenge to localizing preoperatively identified targets to quantitative accuracy in the intraoperative physical space of the patient in the operating room. In particular, soft tissue deformation caused by procedural access to and manipulation of the organ can cause substantial guidance errors. The overarching goal of this dissertation is to improve the fidelity of image-guided delivery of treatments for liver disease by establishing a model-based approach to compensate preoperatively imaged anatomy for intraoperative deformations by using intraoperative data sources amenable to the surgical workflow. The primary hypothesis is that a mechanics-based approach for modeling soft tissue deformation can lead to superior localization accuracy and quantifiable certainty in the fidelity of image-guided interventions. Towards this end, this dissertation undertakes the following specific aims:

Aim 1: Characterize intraoperative liver deformation and establish a model-based approach to reconstruct and compensate for soft tissue deformation. The first aim of this dissertation is to characterize the severity of intraoperative deformation sources by measuring the magnitude of liver deformation between organ shape derived from preoperative diagnostic imaging and laparoscopic and open intraoperative approaches. This characterization utilizes clinical data from 25 human patients. With this knowledge, a preliminary mechanics-based model was developed to reconstruct deformation throughout the full volume of the preoperative anatomy using sparse intraoperative deformations observed on the organ surface. To validate, organ phantom environments were constructed to

emulate clinical sources of soft tissue deformation and enable realistic algorithmic evaluation of registration accuracy between preoperative and intraoperative organ conformations. Furthermore, intraoperative surface data requirements were identified with respect to registration accuracy.

Aim 2: Improve the accuracy of deformable liver registration by incorporating sparse iUS data with a model-based deformation correction framework. The second aim of this dissertation is to incorporate subsurface information from tracked iUS to extend guidance fidelity beyond the limits possible with intraoperative organ surface data alone. The mechanics-based deformation model from Aim 1 was extended and formalized into the novel linearized iterative boundary reconstruction method, and constraints from iUS data were incorporated and evaluated within clinically attainable limitations. A simulation platform was created to allow for extensive validation of registration accuracy across broad ranges of data sparsity and model resolution. The approach was applied to three clinical cases of image-guided liver surgery.

Aim 3: Create a model for predicting distributions of deformable registration error from intraoperative patterns of data coverage. The third and final aim of this dissertation is to establish a novel approach to describe how the uncertainty of deformable registration is affected by the configuration of data provided. A lower bound for registration uncertainty was derived based on the dissipation of elastic energy from data constraints. A model was created to predict the spatial distribution of registration error at every location in the organ from uncertainty measured through patient-specific patterns of intraoperative data. This approach represents a first of its kind framework for predictively modeling the error of deformable registration, with direct applications in guiding the locality of data collection to reliably ensure high accuracy, and in providing a real-time intraoperative assessment of registration confidence to inform operative risk when using image guidance to navigate and

localize. The predictive error model was evaluated using an extended series of data derived from the simulation platform developed in Aim 2.

I.2 Impact

The proposed aims establish a highly accurate and workflow-amenable method for correcting soft tissue deformation during image-guided open and laparoscopic liver procedures. Theoretical frameworks were developed for efficiently performing deformable registration in addition to predicting deformable registration accuracy purely from the provided coverage of intraoperative data. The implications of this new predictive capability are especially significant. Up to now, the reliability of deformable registration methods has not been proven and no mechanisms have yet been proposed that may lead to an understanding of the emergence and propagation of errors in deformable registration systems. The new ability described herein to quantifiably predict registration accuracy from the intrinsic spatial effects of data constraints describes a mechanism through which errors can be understood and controlled to improve the accuracy and fidelity of image guidance. This advance may be a necessary step for further development and adoption of image-guided procedures, through providing a quantitative descriptor of trustworthiness against which intraoperative risk can be assessed. Ultimately, the novel capabilities introduced in this dissertation are designed to enable and ensure consistently accurate image-guided localization of interventional targets in the presence of soft tissue deformation, to improve the precision and safety of therapeutic delivery.

I.3 Dissertation Structure

In Chapter II, this dissertation begins with a background overview of the clinical significance and state of the art of image guidance and registration methods for open and laparoscopic liver procedures. Then, Chapter III provides a comprehensive overview of methods used throughout the aims of the dissertation. The next chapters describe the development of the specific aims of the dissertation. Chapter IV details characterization of deformation

in laparoscopic and open liver approaches, and an algorithm for reconstructing deformation from sparse surface data. Chapter V describes the linearized iterative boundary reconstruction method for deformable registration of image-to-physical patient anatomy and the impact of subsurface iUS feature constraints on registration accuracy. Chapter VI defines and develops an uncertainty metric for deformable elastic registrations and predictively relates this uncertainty to registration error. Finally, Chapter VII summarizes the contributions of this dissertation and concludes by outlining future directions for continued investigation. The appendices of this dissertation outline details towards reproducing liver deformations in phantom environments (Appendix A), updates to a registration challenge presented to the image guidance community (Appendix B), a separate study on the effects of feature constraints from iUS image content (Appendix C), and additional characterization studies performed during the development of this dissertation (Appendix D).

CHAPTER II

Background

The first section of this chapter begins with an overview of the clinical significance of liver disease from the perspective of incidence, treatment options, and criteria for surgical resection. This section then concludes with a discussion on the need for guidance technologies to address limitations with treatment capability, surgical capability, and the effect on these clinical barriers. The next section of this chapter provides an overview of the nature and utility of image guidance platforms on the delivery of treatment, with emphasis on the important components of these systems. Finally, the third section describes the causes of intraoperative liver deformation that compromise the accuracy of modern image guidance systems, and the current state of the art for registration methods and their validation when correcting for these effects.

II.1 Clinical Significance

The occurrence and treatment of hepatic tumors presents a major challenge in modern health care. In the United States, approximately 42,800 new cases of primary liver cancer and 30,200 resulting deaths are projected to occur in 2020 [38]. Worldwide, these numbers exceed 782,000 new cases and 745,500 deaths per year [39]. In addition to primary liver cancers such as hepatocellular carcinoma (HCC), the liver is a preferential secondary target for metastatic neoplasms of gastrointestinal cancers. The majority of hepatic tumors arise from metastatic colorectal cancer (mCRC); of the 148,000 new cases of colorectal cancer expected to occur in the United States in 2020 [38], up to 78% of these patients eventually develop metastatic liver disease [40, 41]. Additionally, the liver is the main target of secondary metastases from primary cancers of the pancreas, esophagus, and stomach. Within three years of initial diagnosis, 85% of pancreatic cancers (57,600 projected new cases in 2020), 52% of esophageal cancers (18,400 projected new cases in 2020), and 39% of stom-

ach cancers (27,600 projected new cases in 2020) develop metastases in the liver [38, 42]. Other primary cancers with predilection for liver metastasis include the breast (30%), kidney (19%), and lung (16%), however treatment options in these cases become complicated due to the liver rarely being the sole site targeted by metastatic spreading from these primary organs [42]. Overall, the total combined burden of primary and secondary cancer in the liver is over 360,000 patients per year in the United States alone (greater than 1 in 1000).

II.1.1 Treatment Options

Typically, surgical resection is the preferred treatment for primary and secondary hepatic malignancies, offering the best long-term survival outside of transplantation [43]. While resective therapy is associated with 5-year survival of 23–63% for HCC [44] and 16–74% for mCRC [45] depending on patient selection, only 20% of patients are immediately eligible for resection due to complicating factors such as tumor multifocality, involvement with vasculature, and insufficient volume of the future liver remnant [43, 46, 47]. While chemotherapeutic and embolization techniques can potentially bridge to surgical resection by down-staging tumors and increasing liver volume, a host of other thermal, electrical, and chemical locoregional ablative therapies have entered the treatment paradigm to supplement otherwise inoperable or very early stage disease [48]. In current clinical practice, radiofrequency ablation is the most common ablative therapy indicated for non-resectable liver disease, for which 5-year survival can reach up to 55% for HCC [49] and 53% for mCRC [50] in carefully selected patients. While ablation of small lesions may be performed percutaneously, advances in therapeutic techniques have led to use of ablative modalities during surgery. Local recurrence rates are significantly lower when radiofrequency ablation is performed in open surgical approach rather than percutaneously [51], and combined resective plus ablative therapies have expanded candidacy for resection as a treatment option for patients with numerous, multifocal, or bilobar tumors [52–54].

II.1.2 Resection Criteria

Resectability of the liver is largely governed by the volume of liver remaining after resection and the positions of lesions relative to the surrounding hepatic vessels. The vascular anatomy of the liver is highly unique, being one of only two portal blood systems in the human body. The portal vein from the gastrointestinal tract and the hepatic artery from the aortic branch represent separate blood supplies to the liver, which mix inside the sinusoids of the liver parenchyma and eventually collect and drain through the hepatic vein to the inferior vena cava. These aspects, in addition to biliary drainage of the liver, must be maintained after resection. The structure of the hepatic vessels gives rise to the anatomical division of the Couinaud segments of the liver, which divide the liver into eight functional regions that each contain a branch of the hepatic artery, portal vein, bile duct, and hepatic vein. Due to the ability of the liver to regenerate, resection can be highly aggressive. In patients with otherwise healthy liver, up to 80% of the total liver volume can be safely resected, although hepatic injury caused by chemotherapy, steatosis, or cirrhosis may reduce the safely resectable volume to 60–70% or less [55]. These considerations give rise to four main criteria that determine surgical resectability: (1) complete resection of disease with negative margins, (2) at least two adjacent segments spared, (3) vascular inflow and outflow and biliary drainage preserved for all remaining segments, and (4) sufficient volume of liver remaining after resection suitable to the health or dysfunction of the liver [56]. Due to the anatomically-driven nature of liver resection, surgical resection planes are established by the intraoperative positions of lesions with respect to surrounding vessels to establish adequate margins, maximize remaining volume, preserve circulation in the liver remnant, and minimize risk of serious complications such as bile leak and vascular hemorrhage [31, 57]. In non-anatomical wedge resections where more parenchyma is preserved, even greater care must be taken when determining which vessels to transect or spare in the context of patient-specific interactions between tumor and vasculature.

II.1.3 Disappearing Liver Metastases

In patients with unresectable liver metastases, neoadjuvant chemotherapeutic regimens are put in place to slow progression or downstage disease with the goal of converting patients to surgical candidates. For these patients undergoing systemic chemotherapy, up to 36% of liver metastases experience complete radiological response, where lesions become undetectable or vanish using standard imaging techniques [58]. While this response may seem favorable, it has been shown that over 80% of these cases with complete radiographic response leave behind microscopic disease that leads to local recurrence [37]. Due to accumulated liver toxicity and the inability of chemotherapeutic regimens to produce lasting curative outcomes after remission, clinical recommendations advise resection of all responding or disappearing lesions when possible [59, 60]. However, resection of these disappearing or partially responding lesions can be highly challenging because the lesion may neither be palpable nor visible with iUS at the time of surgery [37], and therefore the surgeon must rely on alternative visualization and guidance techniques [61].

II.1.4 The Laparoscopic Surgical Approach

Although open surgery remains the most prevalent approach for liver resection, the number of laparoscopic resections has increased exponentially in the past two decades [62, 63]. Whereas open approaches utilize a large incision to access and expose the abdominal cavity to the surgical team, the laparoscopic approach aims to reduce invasiveness and trauma by performing surgery through small ports created by trocars placed in the abdominal wall. Typically, the abdominal cavity is tightly packed with organs and peritoneal fluid. In order to produce adequate surgical working space, pneumoperitoneum is created in the abdominal cavity by insufflation with carbon dioxide or another inert gas to intraabdominal pressures of 10–15 mmHg [64]. After insufflation, the interior of the abdominal cavity is monitored using a video feed acquired from a laparoscope. In comparison to the open approach where a large laparotomy affords wide access to internal organs, the closed nature

of laparoscopy restricts the ability to observe and manipulate objects inside the abdominal cavity. However, retrospective meta-analyses and a recent randomized controlled trial comparing laparoscopic and open liver resection have shown that LLR is attributed with numerous benefits to the patient including significantly less blood loss, shorter postoperative hospital stay, lower consumption of pain medication, and lower overall morbidity, while maintaining equivalent surgical outcomes to OLR [29,30,63]. Laparoscopic delivery of therapy is becoming increasingly prevalent, with the number of LLR cases now representing up to 5–30% of all liver resections at most centers and up to 50-80% at expert institutions [65]. However, a high level of additional technical training is required by practicing surgeons as evidenced by a learning curve of 45–60 LLR cases before complication rates and outcome measures stabilize [33].

The additional difficulty of LLR over OLR can be attributed to lack of information regarding subsurface anatomy, restricted view of the intra-abdominal space, and loss of dexterity and hand-eye coordination. During laparoscopy, the locations of structures beneath the surface of the liver are difficult to identify since the conventional means of manual palpation is eliminated as normally performed in open procedures. While hand-assisted laparoscopy can regain some capability, the insertion of a hand port obscures the visual field and diminishes benefits gained by reduced invasiveness [66]. As a result, hand-assisted laparoscopy is used in less than 17% of LLR cases [62, 67]. To compound, narrow fields of view in conventional laparoscopic camera systems conceal information and potentially endanger surrounding tissues when navigating and manipulating instruments [68]. Finally, laparoscopic manipulation of instruments is highly challenging. Tool motions inside the abdomen are mirrored relative to the actions of the surgeon due to a mechanical fulcrum at the site of every access port. Laparoscopic video displayed on operating room monitors further decouples hand-eye coordination and tool manipulation, requiring significant mental adaptation from the surgeon. These visualization and manipulation constraints lead to reduced control over managing intraoperative complications, which often require im-

mediate conversion to open approach [69]. Approximately 8–10% of all LLR procedures require intraoperative conversion to open surgery, and more than 40% of these converted cases are attributable to unintentional damage to blood and biliary vessels or concern over oncological margins during resection [66, 70]. These challenges also harm the ability to maneuver and interpret the position of laparoscopic iUS images, which could otherwise be highly valuable for interrogating known or disappearing lesions, detecting new lesions, and identifying vascular anatomy hidden beneath the surface of the liver [34, 71, 72]. Only 43% of laparoscopic surgeons reported regular use of laparoscopic iUS in their practices due to difficult experiences with manipulation, lesion sensitivity, transducer size and field of view, image quality, and interpretation of the surrounding anatomical context [73, 74]. To return intuitive tool actuation to the surgeon, early strides towards robotic laparoscopic liver surgery are being made; robotic laparoscopic approaches may improve surgical dexterity [75] and have been shown to be safe and cost-effective for liver resection [76]. However, LLR still requires alternative solutions that reclaim and improve upon visualization of hidden anatomy to more accurately deliver treatment in this highly constrained environment.

II.1.5 Barriers in Clinical Practice

Intraoperative localization of anatomy is an essential cornerstone to nearly every course of liver cancer intervention. From the onset of disease, biopsy of liver lesions remains a clinical necessity, and can be done either percutaneously or during exploratory laparoscopy when diagnosis cannot by made through imaging [77]. However, false negative rates caused by inaccuracies when targeting small lesions are approximately 10% [78, 79]. With effective targeting already relevant to minimizing the chance of track seeding, targeted biopsy samples may become increasingly important for precision medicine initiatives should personalized pharmacotherapy and monitoring begin to utilize tumor-specific molecular bio-

markers and genomic information for determining the most effective chemotherapeutic agents.

To achieve long term disease-free survival, all malignant hepatic lesions must be treated by either resection or ablation. In open liver interventions, the standard of care is to use manual palpation and freehand iUS to identify and remove all sites of disease within the organ [80]. Yet, up to 43% of patients have liver tumors that may not be visible in iUS without exogenous contrast due to similarities in acoustic impedance or disappearance caused by chemotherapeutic treatment [36]. In addition to these limitations, laparoscopic constraints outright remove the ability to palpate and impair the adoption of iUS. These barriers prevent direct intraoperative visualization of disease, and require alternative solutions capable of guiding intervention to target.

Intraoperative localization and targeting becomes particularly important for locoregional therapies, especially when treating non-resectable disease with complex anatomical involvement or alongside resection in combination therapies [81–84]. Laparoscopic approaches to ablation have been suggested to offer substantial advantages by providing better visualization and access in comparison to percutaneous ablation and faster recovery and reoperation compared to open ablation [85–87]. However, between 6–13% of laparoscopic microwave and radiofrequency ablations are found to incompletely treat the tumor [88–90], suggesting that current targeting of the ablation zone may not be sufficiently accurate.

II.2 Image Guidance Platforms for Intraoperative Navigation

Image guidance aims to overcome these clinical barriers by providing an accurate reference for the patient anatomy during intervention, the goal being to improve the ability to localize and target designated structures and navigate around areas of complicative concern. High-resolution diagnostic CT and MR imaging modalities are generally considered to provide superior quality of information for image guidance than their intraoperative imaging counterparts, which are difficult to integrate with surgical workflow. Ideally, an alignment

between feature-rich anatomical structures in preoperative data and the physical intraoperative environment would establish a basis for surgical navigation. Image-to-physical registration establishes such a mapping between preoperatively designated structures in diagnostic images and the intraoperative anatomical configuration of the patient. Consensus recommendations for LLR have suggested that intraoperative guidance using preoperative images could be a useful tool for visualizing subsurface anatomy, determining and navigating resection planes, and assisting the realization of preoperative plans to facilitate more complex laparoscopic procedures, reduce risk of complications, and potentially extend patient candidacy for laparoscopic resection. [65, 91]. In OLR, this style of image guidance has successfully been used to localize disappearing metastases not initially identified with iUS, prospectively demonstrating that these technologies can significantly improve surgical technique through more effective removal of liver disease compared to the standard of care [92, 93].

To date, only two image guidance systems have been approved by the United States Food and Drug Administration for open liver procedures: Pathfinder Explorer (formerly owned by Analogic Corporation, Peabody, MA, USA) and CAS-One Liver (CAScination, Bern, Switzerland) [94]. These two systems are shown in Figure II.1. Both systems consist of separate displays for the surgeon and an assistant, and a tracking system for measuring intraoperative tool positions. Each platform requires three key components for image-guided surgical navigation: (1) an anatomical model from preoperative planning, (2) intraoperative tool tracking, and (3) registration. The following sections will describe each aspect.

II.2.1 Preoperative Planning

Preoperative CT or MR imaging is standard of care for staging liver disease and is performed for every patient. In the preoperative planning phase, the liver parenchyma, major vessel branches, and lesions can be segmented from these images as displayed in Figure

Figure II.1: Image guidance systems approved by the United States Food and Drug Administration for liver surgery. (a) Pathfinder Explorer, (b) CAS-One Liver.

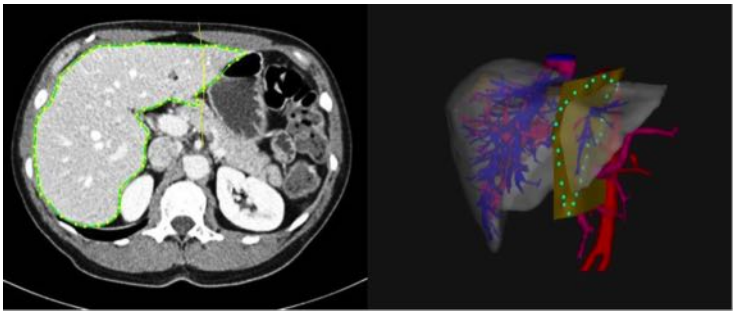

Figure II.2: Example of a preoperative plan from Scout Liver software. Left: Preoperative CT image with segmented boundary of the liver in green. Right: Visualization of segmented liver showing the hepatic (red) and portal (blue) vasculature branches. The planned resection plane (yellow) divides the tumor (brown) from the healthy liver remnant. Images reproduced from [21].

II.2. From these organ models, surgical plans for resection planes or ablation trajectories can be determined for optimizing future liver remnant volume, division of vasculature, coverage of ablation zones, and other aspects of treatment delivery [21]. Recently, it has been shown that the preoperative application of these visualization technologies is associated with significant improvements compared to control group on intraoperative blood loss, operation time, postoperative complications, postoperative liver function, and short-term tumor recurrence [95]. While Figure II.2 shows the Pathfinder planning workflow, Scout Liver, the approach used by CAScination utilizes a similar liver planning tool designed by MeVis [96]. Both image guidance systems aim to relate intraoperative positions of surgical tools to these types of anatomic representations of surgical plans.

II.2.2 Intraoperative Tracking and Data Collection: Surface Measurement

Image guidance systems function by tracking the position and orientation of surgical tools with reference to a sensing device. These sensing devices most often consist of optical trackers that use two cameras and an infrared light emitter to triangulate the three-dimensional positions of sterile reflective fiducials rigidly affixed to tools, and consequently their tool tips, with localization accuracy below 1 mm [97]. Other tracking methods have also been proposed, including electromagnetic tracking [98] and tracking within video co-

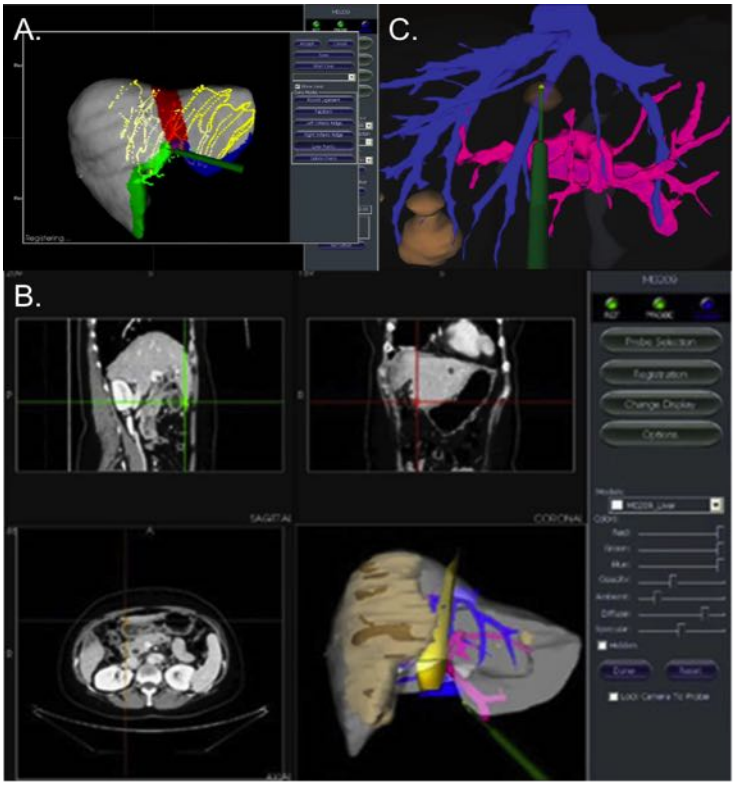

Figure II.3: Example of intraoperative guidance using the Pathfinder Explorer surgical navigation system. (a) A characterization of the organ surface consists of acquiring a set of points across the visible extent of the anterior surface and on salient features of the liver, which include the falciform and inferior ridges shown in red, green, and blue. (b) After registration, the intraoperative display shows the corresponding location of a tracked tool on the preoperative image and surgical plan. (c) An ablation probe (green) is guided to the tumor (brown) in the context of the 3D subsurface anatomy using the navigation system. Images reproduced from [22–24].

ordinates [99]. With registration, or alignment between intraoperative physical tools and the preoperative model, real-time intraoperative tracking allows simultaneous visualization, interrogation, localization, and targeting within virtualized patient anatomy defined during preoperative planning. Figure II.3 shows an example of tracked guidance using the Pathfinder display.

To achieve image-to-physical registration, information that characterizes the intraoperative organ anatomy must be collected and digitized using tracking systems. These intraoperative organ digitizations can be collected by several instrumentation techniques, of which

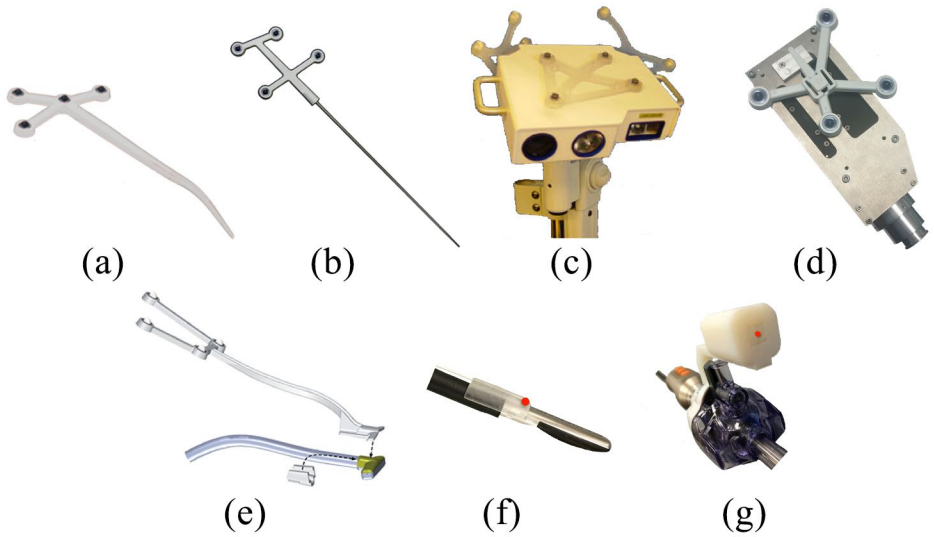

Figure II.4: Example of tracked tools for intraoperative organ measurement. (a) Optically tracked stylus for open liver surgery. The tip is curved to improve access to the superior aspect of the liver in surgical presentation. (b) Optically tracked stylus for laparoscopic liver surgery. The stylus tip is elongated for compatibility with trocar cannulae. (c) Optically tracked laser range scanner. (d) Optically tracked conoscopic holography sensor. (e) Optically tracked ultrasound transducer (image reproduced from [24]). (f) Electromagnetically tracked laparoscopic ultrasound transducer (image reproduced from [25]). (g) Electromagnetically tracked stereo laparoscope (image reproduced from [25]). Positions of electromagnetic tracking coils marked by red dot.

several are illustrated in Figure II.4. Often, data collection and registration is performed using planned apneic periods and gating to control for respiratory motion across time [100].

Organ surface data can be obtained by tracing an optically tracked stylus over the surface of the liver [101]. However, physical contact with the organ is required and error can arise from deformation response of the tissue. Non-contact methods such as tracked conoscopic holography [102, 103], tracked laser range scanning [104] and tracked laser triangulation [105] are capable of acquiring similar surface characterizations with reduced surface noise. In a comparison study on a porcine liver, a tracked stylus produced surface error of 4.4 ± 1.2 mm, tracked laser range scanning 3.3 ± 0.8 mm, and tracked conoscopic holography 1.7 ± 0.8 mm [106]. In a separate study, tracked laser triangulation yielded a surface error of 1.3 ± 0.8 mm [105]. Practical experience has indicated that these non-

contact digitization methods tend to achieve smaller regions of organ surface data coverage due to line of sight constraints and limited control over the freehand laser beams at high angles of incidence on the periphery of the liver (see Appendix A). In additional unpublished work, a silicone liver phantom was mounted inside a mock abdominal cavity and the organ surface was laparoscopically characterized using an optically tracked conoscope and stylus. Compared to the stylus, the conoscopic holography sensor provided significantly smaller extent of organ surface coverage by $7.8 \pm 5.5\%$ of the total surface area ($p < 10^{-6}$, paired t-test).

During laparoscopy, stereo camera reconstruction techniques have also been explored for obtaining non-contact organ surface digitizations [107, 108]. However, short baseline distance between stereo laparoscope cameras and intraoperative factors such as blood accumulation, specular reflection, and surgical smoke from electrocautery can severely deteriorate the quality of these methods in clinical applications [109, 110]. Contact-based surface characterizations obtained by an optically tracked stylus remain the current standard, and methods to resample and regularize error sources from this choice of instrumentation have been developed [111]. However, future works beyond the aims of this dissertation are needed to evaluate which digitization methods are optimal for acquiring intraoperative data necessary for registration during open and laparoscopic procedures, considering that a tradeoff often exists between accuracy and burden to surgical workflow. Due to workflow constraints, almost all intraoperative organ digitizations are incomplete, meaning that image-to-physical registration must usually be performed using sparse data, posing a significant algorithmic challenge.

II.2.3 Intraoperative Tracking and Data Collection: Ultrasound

Tracked intraoperative ultrasound represents another technique for accessing intraoperative information about the organ. In tracked iUS, an optical or electromagnetic tracking device is attached to the ultrasound transducer to quantitatively relate the coordinate frame

of the iUS image to the spatial coordinates of the patient. While optical tracking has intrinsically better accuracy than electromagnetic tracking, in the case of laparoscopic tracked iUS, electromagnetic tracking has been shown to be slightly more accurate due to the ability to place tracking objects closer to the transducer and reduce lever-arm magnification of tracking error [112]. Due to line of sight constraints, optical trackers must be rigidly affixed to laparoscopic devices outside the abdomen and therefore leave an offset of up to 30 cm between tracking fiducials and device tip. However, electromagnetic tracking coils can be directly attached near the tool tip as shown in Figure II.4f and passed through the trocar. Xiao *et al.* found that electromagnetic tracking was 2–3 times more accurate than optical tracking for laparoscopic configurations that required optically tracked fiducials to be placed 15–25 cm away from a transducer or laparoscope tip [112]. However, electromagnetic tracking introduces additional equipment and wired connections to tracking coils during operation and therefore optical tracking may still be considered favorable.

Most applications of tracked iUS in open and laparoscopic approaches have been aimed at coregistration of iUS with CT or MR for the purpose of improving localization of subsurface features with reference to preoperative image volumes [113]. While clinical adoption of laparoscopic iUS has been incomplete, image-to-physical guidance could help provide anatomical context when navigating laparoscopic transducers and subsequently improve usability [24, 114–116]. Figure II.5 illustrates an example of coregistration between tracked iUS and an anatomical model from preoperative planning, as well as an example of anatomical features visible in iUS images. Although there is great potential for positions of features from tracked iUS images to be quantitatively used as direct data sources for registration, obtaining subsurface organ data from tracked iUS is more challenging than organ surface digitization techniques, and algorithms that intend to utilize iUS in this way must also aim to minimize workflow burden. Aspects such as reconstruction of three-dimensional (3D) volumes from tracked two-dimensional (2D) iUS and feature segmentation can add additional time, and intraoperative deformation caused by contact between

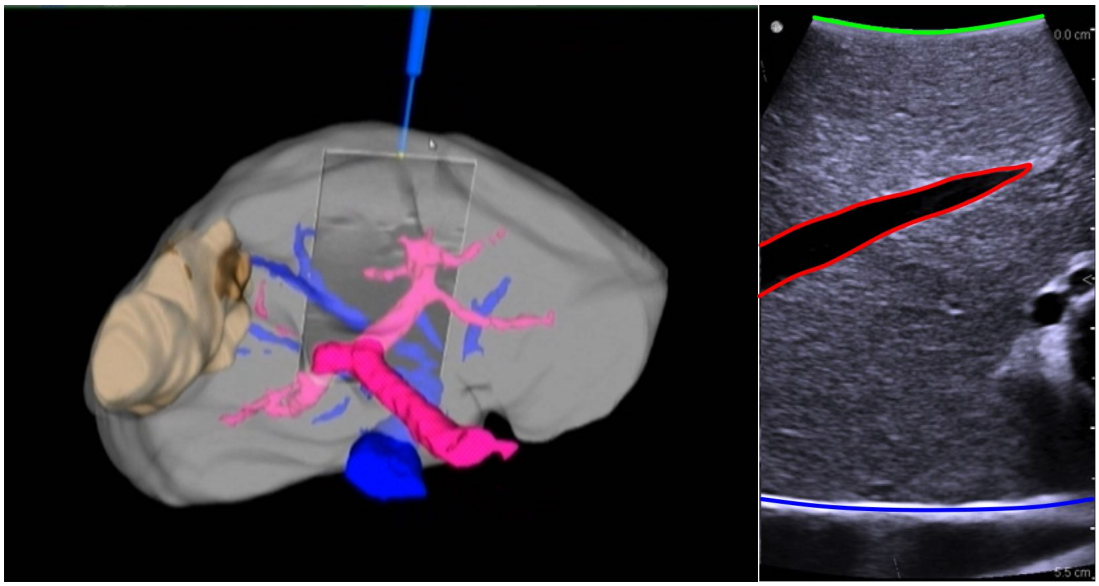

(a) (b)

Figure II.5: Tracked intraoperative ultrasound for image-guided procedures. (a) Coregistration between tracked iUS and liver anatomy from preoperative planning. (b) Features consistently visible in tracked iUS include the posterior surface, hepatic vessels, and anterior surface as marked by the blue, red, and green lines, respectively.

the ultrasound transducer and soft tissue can compromise the spatial validity of subsurface ultrasound data. While strategies to compensate for deformation caused by tracked ultrasound probe contact exist [117, 118], these approaches add complexity in an environment where minimizing the intraoperative footprint of data collection is a major consideration.

II.2.4 Rigid Registration

Both the Pathfinder Explorer and CAS-One Liver image guidance systems utilize rigid registration methods to align intraoperative physical space with preoperative image space. Two common approaches are used for rigid registration. In its current realization, the CAS-One system uses point-based registration, where 4–6 fiducial points are intraoperatively identified on the organ surface and their corresponding positions are manually located in the preoperative CT image [96]. Point-based registration determines a closed form solution to the spatial rotation and translation of coordinate spaces that minimizes the distance be-

tween corresponding fiducials in image and physical space [119]. However, the overall accuracy of point-based registration is sensitive to fiducial localization error, defined as the distance between a measured fiducial point and its ground truth coordinate position. Due to liver anatomy lacking clear anatomical surface landmarks, these fiducials may become difficult to accurately locate in some hepatic procedures. Conversely, the Explorer system uses a surface-based registration method, which avoids the need for manual fiducial designation and instead minimizes the residual error between the preoperative organ model and sparse digitizations of the intraoperative liver surface. The iterative closest point (ICP) algorithm repeatedly performs point-based registrations between nearest neighbors in two misaligned surfaces, with closest point correspondences being updated each iteration until a tolerance criterion is met [120]. However, the closest point operator does not perfectly determine correspondence and the ICP method is highly dependent on the initial orientation of surfaces. To improve the robustness of ICP, Clements *et al.* introduced the salient feature weighted ICP registration algorithm that is used in the Explorer system and throughout this dissertation [121]. This method takes advantage of preoperatively and intraoperatively designated anatomical labels to weight the closest point correspondence on each iteration so that salient anatomical features preferentially align. Salient feature patches on the liver are preoperatively selected on the left and right inferior ridges of the liver and along the falciform ligament. Intraoperative surface points are collected in these salient patch regions and on the larger anterior surface. The weighted ICP algorithm by Clements *et al.* produces a rigid transformation that minimizes the distance between the preoperative organ surface and the feature-weighted intraoperative data points. Although fast and effective, rigid registration cannot account for intraoperative soft tissue deformation or other shape changes of the organ. These nonrigid effects can severely limit the accuracy of rigid image-to-physical alignments.

II.3 Intraoperative Soft Tissue Deformation

The liver can experience significant soft tissue deformation between the preoperative and intraoperative presentations of the organ. Under normal circumstances, the liver is held in the abdomen by several main ligaments. The falciform and the round ligaments attach the anterior of the liver to the ventral wall, while the left and right triangular ligaments anchor the superior surface of the liver to the diaphragm. The posterior surface of the liver is also attached to the stomach and duodenum by the ligaments of the lesser omentum. During surgery, these ligaments are dissected to increase the mobility of the liver. This mobilization changes the distribution of forces on the liver and often manifests as an outward spreading motion of the organ. In OLR, laparotomy pads are packed beneath the surface of the liver to control hemostasis and improve organ presentation, which can give rise to further deformation. Human studies quantifying the amount of liver deformation in OLR have established that intraoperative surface displacements can be expected to exceed 20 mm relative to the preoperative organ shape [122, 123]. In LLR, while mobilization is not as aggressive and some ligaments may be left intact, other considerations can also cause deformation relative to the original preoperative organ shape. One consideration is the change in patient orientation between preoperative imaging performed in the supine position and the intraoperative tilt of the operating table. Intraoperatively, patients can experience up to a 30º incline in the reverse Trendelberg position and up to a 15º semilateral adjustment [124]. These changes alter the direction of gravity relative to how the liver is supported in the abdominal cavity during imaging, and have been observed to be a source of navigation inaccuracy in laparoscopic image guidance [125]. However, the main contributors to laparoscopic soft tissue deformation are the events that surround the process of abdominal insufflation.

Upon insufflation, the abdominal cavity expands to accommodate internal gas pressure. This expansion of the abdominal cavity has been shown to cause distension and displacement of the ventral wall and diaphragm [126, 127] to which the liver is directly attached

by the falciform ligament and the left and right triangular ligaments, respectively. Insufflation therefore pulls these ligaments into tension as the abdominal cavity expands, placing mechanical force on the liver. Furthermore, insufflation can displace the bowel and other structures on top of which the liver rests. To further complicate intraoperative deformation, surgeons may elect to dissect any number of hepatic ligaments to mobilize the liver and improve organ retraction, leaving a complicated profile of external forces on the liver that varies from case to case. Several animal studies have been carried out to quantify the effects of insufflation on liver deformation. Zijlmans *et al.* found that insufflation pressures of 12 mmHg in pigs produced tumor displacements of 28.0 ± 1.9 mm in the craniocaudal direction, 18.3 ± 1.8 mm in the anteroposterior direction, and 2.3 ± 0.5 mm in the lateral direction [128]. These directions of shift are expected based on craniocaudal diaphragmatic motion and anteroposterior ventral wall motion. Estimations of porcine liver deformation during laparoscopy have also been performed by Vijayan *et al.* [129] and Johnsen *et al.* [130], where shifts exceeding 35 mm and deformations exceeding 11 mm were found. However, no clinical analyses of liver deformation during laparoscopy have otherwise been performed in humans until the work presented in Chapter IV of this dissertation.

II.3.1 State of the Art: Deformation Correction for Hepatic Guidance

Several approaches for correcting deformation have been developed for image-to-physical registration using intraoperative surface data of the liver. Masutani *et al.* proposed an early method that used free-form deformation modes to match the preoperative shape of the liver to a partial patch of the liver surface [131]. Cash *et al.* developed a linear elastic biomechanical model constrained by closest point boundary conditions to correct for unaccounted deformation after rigid registration [132]. Dumpuri *et al.* improved this method by applying a surface Laplacian equation to extrapolate closest point distances from sparse intraoperative data onto the model as displacement boundary conditions [133]. Allan *et al.* presented a nonrigid registration method to stereo-reconstructed laparoscopic surfaces

using coherent point drift [3,134]. Suwelack *et al.* employed a model that mixed elastic mechanical response with boundary conditions formulated as electrostatic attractive forces to match the shapes of preoperative and intraoperative models of the liver [1]. More recently, Plantefève *et al.* established a laparoscopic nonrigid registration pipeline that produced a dynamic elastic registration from tracked texture landmarks [4]. Other variants reported by Reichard *et al.* projected spring force boundary conditions from a stereo reconstructed depth map onto an elastic biomechanical model [6]. However, many of these approaches either lack mechanics-based constraints that allow deformation to be modeled accurately beyond the immediate neighborhood of intraoperative data [3, 131, 134], or many methods treat deformation through direct application of digitized intraoperative surfaces as boundary conditions [1, 4, 6, 132, 133], which may not adequately align regions with poor data coverage and can have unfavorable responses to untreated sources of noise during intraoperative clinical data collection. Uncharacterized clinical noise also represents a major concern for the translation of deep learning approaches that have recently been trained for deformable image-to-physical liver registration such as presented by Pfeiffer *et al.* [135].

As opposed to using surface data to directly apply boundary conditions on a biomechanical model, a more robust approach is to utilize energy minimization or reconstruct a solution from a constrained set of possible deformations that are expected to occur on the basis of the anatomical support of the organ. Rucker *et al.* first addressed this consideration in the context of open liver surgery by proposing an inverse method that solves for an initially unknown bivariate polynomial parameterization of displacement boundary conditions across the posterior surface of the liver using strain energy regularization [2]. With this proposed framework, the deformable registration problem could be recast as an intraoperative optimization of a set of model parameters that describe the unknown distributed load applied to the support surface of the organ to reconstruct the observed intraoperative deformation from a combination of responses to anatomically parameterized boundary conditions. This method was initially validated in a liver phantom against ground truth subsurface targets [2]

and was later validated for OLR during clinical application using vascular targets localized with tracked intraoperative ultrasound [5] as well as in a blinded perception study where the deformable correction method was rated with significantly higher guidance fidelity than rigid registration [22]. This anatomy-driven, constraint-based energy approach has carried on to influence newer registration methods. Recent methods towards deformation-corrected augmented reality by Özgür *et al.* have attempted to perform projection-based registration between 3D preoperative plans and 2D monocular laparoscopic images using an iterative approach to anatomic constraint-based boundary conditions [7]. Peterlik *et al.* introduced a Lagrange multiplier method to more softly implement boundary condition constraints [8], and Modrzejewski *et al.* contributed an energy minimization approach that also handles collision constraints [10].

II.3.2 State of the Art: Hepatic Registration to Ultrasound Data

Automatic methods for registration of iUS imaging with preoperative CT or MR images have been developed using optimization of image similarity metrics such as normalized cross correlation [11, 12], linear combination of linear correlation [13], edge-intensity joint entropy [15], and local structure orientation descriptors [18]. However, many of these intensity-based registration techniques are designed for percutaneous intervention where small deformations and good initial alignments are possible. To accommodate larger deformations, Lange *et al.* introduced a thin plate spline registration method using distances to known subsurface vessel centerline landmarks as constraints when optimizing a normalized gradient field image similarity measure [14]. However, the appropriateness of inter-modality similarity measures is not clear when anatomical features with disparate intensity profiles in each modality must be accurately aligned, and furthermore their computation can be time-consuming. More recent approaches that attempt to address registrations with large deformation have started to forego image intensity information and instead relate sparse vessel contours or centerlines from ultrasound images to the geometry of preopera-

tively segmented organ models. Song *et al.* developed a locally rigid registration technique to match skeletonized vessel tree centerlines extracted from 3D freehand ultrasound with corresponding geometry from preoperative imaging [17], while Nazem *et al.* developed an ICP variant to rigidly register liver vessels and surfaces derived from 2D ultrasound images to corresponding CT orientations [16].

Nonrigid registration methods that utilize ultrasound subsurface data in large deformation scenarios are scarce. While much focus has been placed on registration of complete vessel trees in the current body of literature, the need to acquire large amounts of 3D ultrasound data in these approaches represents a clinical challenge. Evaluations of registration accuracy in these methods have also focused on assessing the error of targets located immediately near vessel bifurcations in the ultrasound field of view. It remains to be seen how registration error extrapolates to more distant targets in the liver and also to assess the comparative benefits of combining surface and subsurface data in a realistic setting for registration. Achieving high registration accuracy across the bulk of the liver likely requires biomechanical models for nonrigid deformation correction. However, integration of subsurface ultrasound data with biomechanical models is largely unexplored despite evidence that subsurface data can improve registration. Rucker *et al.* showed that adding a single known subsurface landmark into a surface-based deformation correction approach reduced the average registration error from 4.0 mm to 3.3 mm [2], and Ramalhinho *et al.* identified that compensation of rigid breathing motion was 22% better when using a combination of information from the organ surface and subsurface vessels [19]. Major advances in hepatic image guidance would likely be seen if tracked ultrasound data acquisition became more streamlined and if guidelines were determined to inform what ultrasound targets in the liver may yield the most efficient impact to registration fidelity [136].

II.3.3 State of the Art: Validation of Registration Methods

Correction of soft tissue deformation is necessary to attain clinically desirable levels of localization error for OLR and LLR, typically regarded to be less than 3-5 mm in comparison to clinically established 10-mm oncological margins [110, 137]. Table II.1 and Table II.2 present a summary of the validation steps and reported accuracies taken by the most relevant methods described in the previous two sections. References [1–4, 6–10] examine contemporary work on liver registration algorithms that do not use iUS data, while references [5, 11–20] examine how ultrasound features are clinically validated when they are used within registration. It is important to note that evaluation of registration error does not yet have an established clinical standard because intraoperative limitations of the operating room prevent acquisition of ideal human validation data. For example, intraoperative tomographic imaging with CT or MRI is not a practical validation tool outside of highly specialized centers because it requires a complete disruption of the surgical workflow. In addition, even when these powerful technologies are available, there still can be temporal disparity between intraoperative data acquisition methods used for driving registration and imaging data for validating the approach. For this reason, the field has heavily relied on simulation and phantom studies on mock organs to characterize registration accuracy. Whereas validation targets can be dispersed and clearly delineated in a phantom environment for measurement of target registration error (TRE), in the clinical environment, this is not possible. Only a handful of studies have attempted to perform quantitative clinical validation of liver registration error using feature targets beneath the surface of the organ using iUS [5, 13–15, 18]. In the majority of published work, clinical validation in humans is either not performed [1, 6, 8, 10, 16, 17], done purely qualitatively [7, 11], or with limited quantification of residual error instead of target error [2, 4].

Target registration error remains the gold standard metric for validating registration accuracy. TRE is defined as the distance between target points measured in one space and their corresponding positions from another space after registration:

$$\text{TRE} = \sqrt{(\boldsymbol{y} - \mathcal{T}(\boldsymbol{x}))^T (\boldsymbol{y} - \mathcal{T}(\boldsymbol{x}))} \tag{II.1}$$

where $\boldsymbol{y}$ is the position of a target in the first space, $\boldsymbol{x}$ is the corresponding target position in the second space, and $\mathcal{T}(\cdot)$ is a transformation between spaces. However, the magnitude of TRE can depend on the relative positioning of targets within the organ relative to data provided, and also can depend on the severity of underlying deformation. These confounding influences require additional qualification of TRE measurements when reported. Meanwhile, residual error is defined as the distance between the original and transformed points used for registration. In the context of rigid point-based registration, residual error is referred to as fiducial registration error (FRE). However, residual error is uncorrelated with TRE and therefore is not a useful metric for overall registration accuracy beyond providing a sense for algorithmic convergence [9, 138].

In clinical situations where corresponding points may not be able to be measured, TRE measurements cannot be achieved. This situation often arises when intraoperative cross-sectional imaging is not possible. As an alternative, several studies have used distance between anatomical feature contours from 2D iUS to provide an average projective distance of anatomical registration error [5, 15, 20]. This feature contour error can be defined as,

$$\text{Feature Contour Error} = \frac{1}{N_A} \sum_{\boldsymbol{y}_i \in A} \min_{\boldsymbol{x}_i \in B} d(\boldsymbol{y}_i, \mathcal{T}(\boldsymbol{x}_i)) \tag{II.2}$$

where A is a sparse feature contour from iUS, B is the complete feature from preoperative imaging, and $\min d(\cdot,\cdot)$ is the closest point distance function.

Regarding the existing body of works that measure registration error by iUS with human data [5, 13–15, 18], it is very important to note that algorithms designed for different data input are also validated to different standards depending on the instrumentation available. For example, [13–15] are designed for registration of 3D ultrasound to other 3D tomographic image volumes. While it is possible to quantify target registration errors

Organ Surface Registration								
Study	**Intraoperative Data Source for Registration**	**Registration Method**	**Model Constraints**	**Validation Data (Number of Trials)**	**Deformation Magnitude Mean ± Std (Max) [mm]**	**Residual Error Mean ± Std (Max) [mm]**	**Target Error Mean ± Std (Max) [mm]**	**Contour Error Mean ± Std (Max) [mm]**
Suwelack et al. (2014)	Intraoperative CT full surface	Linear elastic corotational finite elements	Model-data attractive force	Phantom (3)	23.9 (46.6)	—	2.3 (4.2)	—
	CT-simulated anterior surface					—	5.1	—
	CT-simulated stereo patch					—	8.7	—
Rucker et al. (2014)	Tracked stylus sparse surface plus tracked LRS patch	Linear elastic finite elements	Model-data surface error, strain energy	Phantom (5)	9.5 ± 2.2 (23)	—	3.3 ± 0.5	—
				Clinical OLR (5)	(12)	2.7 ± 0.6	—	—
Allan et al. (2015)	Stereo reconstructed surface	Coherent point drift	Model-data surface error	Phantom (16)	(2)	0.9 ± 1.2	—	—
Plantefève et al. (2016)	Stereo reconstructed landmarks	Linear elastic corotational finite elements	Model-data attractive force	Simulated (1)	10.1	—	3 (12)	—
				Clinical LLR (2)	N.R.	1.1	—	—
Clements et al. (2016)	Tracked stylus sparse surface	Linear elastic finite elements	Model-data surface error, strain energy	Clinical OLR (6)	5.6 ± 2.2 (21.1)	2.9 ± 0.7 (16.4)	—	2.7 ± 0.7 (9.9)
Reichard et al. (2017)	Stereo reconstructed surface	Linear elastic finite elements	Model-data attractive force, stereo depth map	Simulated (4)	(50)	—	(14)	—
Özgür et al. (2018)	Marked contours from 2D laparoscope image	Hyperelastic finite elements	Anatomical priors, projective contour depth	Simulated (1)	70	—	5 to 22	—
				Phantom (1)	N.R.	—	11.2 ± 5.7 (33.6)	—
				Clinical LLR (2)	—	—	—	—
Peterlik et al. (2018)	Intraoperative CT full surface	Linear elastic corotational finite elements	Lagrange multipliers, numerical damping	Simulated (4)	14.2 ± 0.25 (54.8)	—	3.7 ± 0.3 (11.1)	—
				Clinical flank-to-supine (9)	15.0 (51.4)	—	3.8 ± 0.5 (9.7)	—
Heiselman et al. (2018)	Tracked stylus sparse surface	Linear elastic finite elements	Model-data surface error, anatomical priors, strain energy	Phantom (54)	14.7 ± 5.6	0.8 ± 0.4	6.4 ± 2.5	—
				Clinical OLR (25)	5.5 to 9.3	1.1 ± 0.4	—	—
				Clinical LLR 7mmHg (25)	6.2 to 11.9	1.4 ± 0.5	—	—
				Clinical LLR 14mmHg (25)	7.7 to 12.6	1.4 ± 0.6	—	—
Modrzejewski et al. (2019)	Stereo reconstructed surface	Linear elastic finite elements	Model-data attractive force, strain energy	Porcine LLR (13)	33 ± 22 to 105 ± 60	—	20 (75)	—

Table II.1: Summary of recent deformable registration works utilizing only organ surface data. N.R. short for not reported. Studies include Suwelack *et al.* [1], Rucker *et al.* [2], Allan *et al.* [3], Plantefève *et al.* [4], Clements *et al.* [5], Reichard *et al.* [6], Özgür *et al.* [7], Peterlik *et al.* [8], Heiselman *et al.* [9], and Modrzejewski *et al.* [10].

Subsurface Feature Registration								
Study	**Intraoperative Data Source for Registration**	**Registration Method**	**Model Constraints**	**Validation Data (Number of Trials)**	**Deformation Magnitude Mean ± Std (Max) [mm]**	**Residual Error Mean ± Std (Max) [mm]**	**Target Error Mean ± Std (Max) [mm]**	**Contour Error Mean ± Std (Max) [mm]**
Blackall et al. (2005)	2D ultrasound intensities	B-spline free form deformation	Pearson cross correlation	Volunteer PC (5)	N.R.	—	5 to 10	—
Nakamoto et al. (2007)	Tracked freehand 3D ultrasound intensities	B-spline free form deformation	Normalized cross correlation	Porcine LLR (2)	(10.8, 13.3)	—	1.0 to 1.3 (2.7)	—
Wein et al. (2008)	Tracked freehand 3D ultrasound intensities	Affine	Linear combination of linear correlation	Clinical flank-to-supine (25)	(13–71)	9.5 (15.3)	8.1 (21.5)	—
Lange et al. (2009)	3D ultrasound intensities and vessel centerlines	Thin plate spline	Normalized image gradient field, centerlines	Clinical PC (3)	4.4 to 4.7	—	2.6 to 4.9	—
Lee et al. (2011)	3D ultrasound intensities, vessels, and surfaces	B-spline free form deformation	Intensity and intensity gradient joint entropy	Volunteer PC (10)	4.8 ± 2.6	—	2.4 ± 1.1	2.8 ± 1.2 (4.5)
Nazem et al. (2014)	2D ultrasound vessels and surfaces	Rigid	Unscented Kalman filter, iterative closest point	Phantom (1)	0	—	(9)	—
Song et al. (2015)	Tracked 2D ultrasound vessel centerlines	Rigid	Iterative closest point	Porcine LLR (2)	Minimal	—	3.7 to 4.5 (7.2)	—
Yang et al. (2016)	2D ultrasound vessels	Rigid	Local structure orientation descriptors	Phantom (1)	N.R.	—	1.8 ± 1.9	—
				Clinical PC (9)	N.R.	—	2.0 ± 0.8	—
Ramalhinho et al. (2017)	Tracked 2D ultrasound vessel contours and surfaces	Rigid	Iterative closest point	Porcine LLR (1)	N.R.	—	6.5 ± 3.5 (13.1)	—
Heiselman et al. (2020)	Tracked 2D ultrasound vessel contours, centerlines, and surfaces	Linear elastic finite elements	Model-data surface error, strain energy	Simulation (6291)	13.8 ± 1.9	—	3.9 ± 0.7	—
				Clinical OLR (3)	8.0 ± 3.9 (17.0)	1.0 ± 0.7 (3.8)	—	2.7 ± 2.1 (10.6)

Table II.2: Summary of rigid and deformable registration works utilizing anatomical features from iUS data. PC short for percutaneous approach. N.R. short for not reported. Studies include Blackall *et al.* [11], Nakamoto *et al.* [12], Wein *et al.* [13], Lange *et al.* [14], Lee *et al.* [15], Nazem *et al.* [16], Song *et al.* [17], Yang *et al.* [18], Ramalhinho *et al.* [19], and Heiselman *et al.* [20].

using corresponding points between preoperative imaging and densely sampled 3D intraoperative ultrasound, it is far less feasible to select corresponding points for validation from sparse 2D ultrasound planes. For example, although the clinical experiment from [18] does select landmarks from 2D US images, it must be stressed that these corresponding landmarks were selected on a resliced 2D image plane from MR following registration. Since all landmarks were selected on a projected plane, the reported error underapproximates the true measurement of TRE in 3D space. In some works such as [5] and [15], projected error of vessel contour features is reported because these accuracy metrics still represent the orientation and alignment of the US-derived feature with respect to the underlying 3D geometry that has been registered. When TRE cannot be measured, feature contour error may be considered to be a better representation of registration error than vessel centerline measures such as those reported in [14, 16, 17] because centerline approximations from 2D images discard information about the orientation of the feature, and centerline approximations can become inaccurate for curving vessels imaged obliquely or near vessel bifurcations.

In summary, clinical validation of liver registration is quite difficult to fully achieve, limiting its realization in many existing works. While it is possible to quantify TRE using corresponding points between preoperative imaging and densely sampled 3D intraoperative ultrasound, it is far less feasible to select corresponding points for validation from sparse 2D ultrasound planes. When clinical data is not accessible, organ phantoms and simulation remain accepted ways to generate validation data.

CHAPTER III

Methodology

The next chapters of this dissertation describe a series of studies that aim to improve the fidelity of intraoperative image guidance through measuring, modeling, and correcting for soft tissue deformation during registration. First, this chapter provides an overview of the theoretical and mathematical basis for these approaches. The sections of this chapter will begin with a description of a model for the behavior of soft tissue deformation through linear elastic mechanics, a discussion on material properties, and the finite element method for solving these equations of linear elasticity. These concepts in elastic mechanics will then be applied to forward and inverse problems, and registration through modal representations of linear elastic deformation. Finally, Saint-Venant's principle and its energetic statements are described, foundations of thermoelasticity are reviewed, and a workup towards a novel definition of thermodynamic and information-theoretic registration entropy is developed.

III.1 Linear Elastic Models for Deformable Registration

In many situations, soft tissue can be modeled as a linearly elastic continuum. Linear elasticity is governed by three fundamental relations:

(1) Newton's second law, conservation of force

$$\nabla \cdot \overline{\overline{\sigma}} + F = \rho \ddot{u}, \tag{III.1}$$

(2) The linear stress-strain relation

$$\overline{\overline{\sigma}} = \mathbb{C} : \overline{\overline{\varepsilon}}, \tag{III.2}$$

and (3) The infinitessimal strain-displacement relation,

$$\overline{\overline{\varepsilon}} = \frac{1}{2}(\nabla u + (\nabla u)^T), \tag{III.3}$$

where $\overline{\overline{\sigma}}$ is the Cauchy stress tensor,

$$\overline{\overline{\sigma}} = \begin{bmatrix} \sigma_{xx} & \tau_{xy} & \tau_{xz} \\ \tau_{yx} & \sigma_{yy} & \tau_{yz} \\ \tau_{zx} & \tau_{zy} & \sigma_{zz} \end{bmatrix} \tag{III.4}$$

$\overline{\overline{\varepsilon}}$ is the Cauchy strain tensor,

$$\overline{\overline{\varepsilon}} = \begin{bmatrix} \varepsilon_{xx} & \gamma_{xy} & \gamma_{xz} \\ \gamma_{yx} & \varepsilon_{yy} & \gamma_{yz} \\ \gamma_{zx} & \gamma_{zy} & \varepsilon_{zz} \end{bmatrix} \tag{III.5}$$

u is displacement, $\ddot{u}$ is acceleration, ρ is the material density, F is an externally applied or body force, $\mathbb{C}$ is a fourth-order material tensor, and $(:)$ is the second order tensor inner product. At rest, tissue can be considered to have reached static equilibrium setting $\ddot{u} = 0$.

The tensor equation III.2 can be described in Voigt notation to allow $\mathbb{C}$ to be written in matrix form C such that

$$\sigma = C\varepsilon \tag{III.6}$$

$$\sigma = \begin{bmatrix} \sigma_{xx} \\ \sigma_{yy} \\ \sigma_{zz} \\ 2\tau_{yz} \\ 2\tau_{zx} \\ 2\tau_{xy} \end{bmatrix} \tag{III.7}$$

$$\varepsilon = \begin{bmatrix} \varepsilon_{xx} \\ \varepsilon_{yy} \\ \varepsilon_{zz} \\ 2\gamma_{yz} \\ 2\gamma_{zx} \\ 2\gamma_{xy} \end{bmatrix} \tag{III.8}$$

and

$$C = \frac{E}{(1+\nu)(1-2\nu)} \begin{bmatrix} 1-\nu & \nu & \nu & 0 & 0 & 0 \\ \nu & 1-\nu & \nu & 0 & 0 & 0 \\ \nu & \nu & 1-\nu & 0 & 0 & 0 \\ 0 & 0 & 0 & \frac{(1-2\nu)}{2} & 0 & 0 \\ 0 & 0 & 0 & 0 & \frac{(1-2\nu)}{2} & 0 \\ 0 & 0 & 0 & 0 & 0 & \frac{(1-2\nu)}{2} \end{bmatrix} \tag{III.9}$$

under the condition of material isotropy where E is the Young modulus and ν the Poisson ratio. Similarly, the strain-displacement relation III.3 can be rewritten as,

$$\varepsilon = \begin{bmatrix} \frac{\partial u_x}{\partial x} \\ \frac{\partial u_y}{\partial y} \\ \frac{\partial u_z}{\partial z} \\ \frac{\partial u_y}{\partial z} + \frac{\partial u_z}{\partial y} \\ \frac{\partial u_z}{\partial x} + \frac{\partial u_x}{\partial z} \\ \frac{\partial u_x}{\partial y} + \frac{\partial u_y}{\partial x} \end{bmatrix}. \tag{III.10}$$

Substituting into III.1, these relations lead to the more compact Navier-Cauchy displacement equations for isotropic linear elasticity at static equilibrium that are used throughout this work,

$$\frac{E}{2(1+\nu)}\nabla^2 u + \frac{E}{2(1+\nu)(1-2\nu)}\nabla(\nabla\cdot u) + F = 0 \tag{III.11}$$

where $\nabla^2 u = \nabla\cdot\nabla u$. These equations can also be described using the Lamé parameters $\lambda = \frac{E\nu}{(1+\nu)(1-2\nu)}$ and shear modulus $\mu = \frac{E}{2(1+\nu)}$ to yield,

$$\mu\nabla^2 u + (\lambda+\mu)\nabla(\nabla\cdot u) + F = 0. \tag{III.12}$$

These equations represent a boundary value problem, where displacements throughout the volume of the domain can be solved if boundary conditions for the values of displacement and force are known on the edge of the domain.

Finally, the strain energy U of any deformation state is the inner product between stress and strain integrated across the volume of the domain,

$$U = \frac{1}{2}\int \overline{\overline{\sigma}} : \overline{\overline{\varepsilon}}\, dV = \frac{1}{2}\int \sigma\cdot\varepsilon\, dV. \tag{III.13}$$

III.2 Material Properties

The equations for linear elasticity are parameterized by Young's modulus and Poisson's ratio. Clinically, these parameters are typically unknown and highly variable between patients due to the genesis of fibrosis and cirrhosis that stiffen the liver during the progression of liver disease as scar tissue is deposited within the organ. In particular, the Young's modulus of the liver can change drastically depending on the state of fibrosis, from 0.6–4000 kPa [139]. Regarding Poisson's ratio, soft tissue is generally considered nearly incompressible with values ranging between 0.45 and 0.49 [140]. Empirically, prior work has found that the value $\nu = 0.45$ is appropriate for modeling the behavior of soft tissue [4,8,132,141].

Despite these limitations, it should be noted that if III.11 is purely displacement-driven setting external forces to zero, and Young's modulus is treated as homogeneous throughout the domain, then the modulus completely factors out of this constitutive equation. Therefore under this special scenario the exact value of the modulus does not affect displacement solutions, and only serves to scale the strain energy associated with the displacement field. This property is used to our benefit in later chapters to make registration methods more robust to patient variation. In the case of heterogeneous moduli, it can be seen that only the relative ratios of moduli become important to the displacement solution. Heterogeneity does occur in the liver, for example liver tumors can be many times stiffer than the surrounding parenchyma. Although the difference in stiffness depends on the biology of the tumor and the state of liver fibrosis, methods such as MR and ultrasound elastography could make a heterogeneous model with known parameters feasible within a reasonable workflow. However, preliminary investigations on the influence of heterogeneous material properties on registration error have not shown significant differences in accuracy in comparison to homogeneous models [142, 143]. While these results do not rule out the possibility that incorporating liver heterogeneity might improve model accuracy, it may be a small effect compared to other sources of error from nonlinearity or measurement.

While most biological tissues have nonlinear stress-strain responses, the extent to which the linear elastic assumption may affect registration accuracy is difficult to assess. While it is possible that deformations may be large enough that the small strain assumption of linear elasticity is violated, the stress-strain curve for liver tissue is approximately linear up to and beyond 5% elongation and compression [144, 145]. While regionally isolated deformations certainly could occur in the nonlinear range, these loads are not usually distributed over the entire liver, meaning that most of the liver responds in the linear portion of the stress-strain curve. Even in highly deforming areas, a linear model would still provide partial compensation compared to a more embellished nonlinear constitutive model with more extensive runtime requirements. Depending on the application, linear elastic models may

be sufficient if inaccuracies incurred by foregoing nonlinear material effects are smaller than other sources of noise such as instrument digitization errors that can be as large as several millimeters.

In general, liver tissue also has viscoelastic properties [145]. However, in many cases the tissue has relaxed to a state of static equilibrium at the time of organ measurement. An assumption of static equilibrium can be suitable for image-guided surgery because registrations are performed intermittently on a stationary organ at discrete phases of the procedure. If a registration were actively updating in real time in response to continuous data streams, then strain rate dependent viscoelastic effects may need to be accounted for. Nevertheless, based on current research and industry-realized systems of image guided liver surgery, the context of intraoperative workflow around usage of the guidance system is compatible with the former assumption.

III.3 The Finite Element Method

In this work, the finite element method is used to solve the equations of linear elasticity. This method requires subdivision of the domain into smaller geometric regions known as finite elements and enforces the partial differential equation (PDE) through a variational weak formulation. An approximate solution is obtained from the weak form of the PDE by requiring an integrated weighted residual error to vanish across the domain. In this work, a segmentation of the liver is provided to a custom mesh generator [146] to create a mesh of tetrahedral elements with edge lengths of approximately 4 mm. These tetrahedral meshes consist of a set of vertices (or "nodes") and a list of vertex connections that define each element. Given a set of boundary conditions applied to the mesh domain, deformations can be simulated using this approach.

Consider a domain of material $\mathcal{M}$ over which the Navier-Cauchy equation III.12 is to be enforced. Then the structure of the displacement function across each element can be approximated by a set of weights applied to basis functions that describe the shape of each

finite element. In this work, linear Lagrange basis functions are used such that displacement can be interpolated at any point inside a tetrahedral element by,

$$\widetilde{u}(x) = \sum_{j=1}^{N} \widetilde{u}_j \phi_j(x) \tag{III.14}$$

where $\widetilde{u}(x)$ is the approximated displacement, N is the number of element vertices, $\widetilde{u}_j$ is a weight representing the displacement at each vertex, and $\phi_j(x)$ is the linear Lagrange basis function that gives rise to the natural coordinates of the element under the constraints $\sum_{j=1}^{N} \phi_j(x) = 1$ and $0 \leq \phi_j(x) \leq 1$. Conveniently, the derivatives $\nabla\widetilde{u}$ can be expressed by

$$\nabla\widetilde{u}(x) = \sum_{j=1}^{N} \widetilde{u}_j \nabla\phi_j(x). \tag{III.15}$$

For a linear shape function, $\nabla\phi_j(x) = \nabla\phi_j$ is constant throughout the element. However, higher order elements such as quadratic tetrahedra can be used to permit more variation. These forms can be substituted into the Navier-Cauchy equation to enforce the differential equation across each element $\mathcal{E} \in \mathcal{M}$.

The weak form of the differential equation is obtained by the Galerkin method of weighted residuals, which allows for solutions of the element vertex displacements $\widetilde{u}_j$ by forcing the weighted integral of a residual function towards zero across the problem domain. In the case of linear elasticity at static equilibrium, the residual function $R(x)$ is equation III.12 with all terms moved to the left side,

$$R = \mu\nabla^2 u + (\lambda + \mu)\nabla(\nabla \cdot u) + F, \tag{III.16}$$

which must equal zero to satisfy the exact solution to the PDE. The Galerkin method applies a weight function to $R(x)$ that matches the basis from III.14. In other words, the Galerkin weighted residual method specifies that the functional form of the approximated solution matches the form of an error function Ψ defined over the weighted residuals of the PDE caused by any differences between approximated and exact solutions,

$$\Psi(x) = \sum_{i=1}^{N} R(x)\phi_i(x). \tag{III.17}$$

This error is forced to vanish across the domain by requiring that

$$\int_{\mathcal{M}} \Psi(x)\, dV = 0. \tag{III.18}$$

Equations III.16–III.18 lead to the following weak form of III.12,

$$\mu \int_{\mathcal{M}} \phi_i \nabla\cdot\nabla u\, dV + (\lambda+\mu)\int_{\mathcal{M}} \phi_i \nabla(\nabla\cdot u)\, dV + \int_{\mathcal{M}} F\phi_i\, dV = 0. \tag{III.19}$$

with implicit summation across all basis functions ϕ_i. This equation can be converted to first order using the product rule and Stokes' divergence theorem,

$$\int_{\mathcal{M}} \phi_i \nabla\cdot\nabla u\, dV + \int_{\mathcal{M}} \nabla\phi_i\cdot\nabla u\, dV = \int_{\mathcal{M}} \nabla\cdot(\phi_i\nabla u)\, dV = \oint_{\partial\mathcal{M}} \phi_i \nabla u\cdot\hat{n}\, dA \tag{III.20}$$

$$\int_{\mathcal{M}} \phi_i \nabla(\nabla\cdot u)\, dV + \int_{\mathcal{M}} (\nabla\cdot u)\nabla\phi_i\, dV = \int_{\mathcal{M}} \nabla(\nabla\cdot(u\phi_i))\, dV = \oint_{\partial\mathcal{M}} \phi_i(\nabla\cdot u)\hat{n}\, dA \tag{III.21}$$

where $\hat{n}$ is the unit normal of the domain boundary, to produce,

$$\begin{aligned}\mu \int_{\mathcal{M}} \nabla\phi_i\cdot\nabla u\, dV + (\lambda+\mu)\int_{\mathcal{M}} (\nabla\cdot u)\nabla\phi_i\, dV &= \int_{\mathcal{M}} F\phi_i\, dV \\ &+ \mu\oint_{\partial\mathcal{M}} \phi_i\nabla u\cdot\hat{n}\, dA + (\lambda+\mu)\oint_{\partial\mathcal{M}} \phi_i(\nabla\cdot u)\hat{n}\, dA.\end{aligned} \tag{III.22}$$

Substituting the linear forms III.14 and III.15 for the approximate displacement and displacement gradient,

$$\begin{aligned}\sum_j \widetilde{u}_j\left(\mu\int_{\mathcal{M}} \nabla\phi_i\cdot\nabla\phi_j\, dV\right) + \sum_j \widetilde{u}_j\left((\lambda+\mu)\int_{\mathcal{M}} (\nabla\cdot\phi_j)\nabla\phi_i\, dV\right) &= \int_{\mathcal{M}} F\phi_i\, dV \\ &+ \mu\oint_{\partial\mathcal{M}} \phi_i\nabla u\cdot\hat{n}\, dA + (\lambda+\mu)\oint_{\partial\mathcal{M}} \phi_i(\nabla\cdot u)\hat{n}\, dA.\end{aligned} \tag{III.23}$$

Equation III.23 can be rewritten as the linear system of equations

$$A_{ij}\widetilde{u} = b_i, \tag{III.24}$$

where A_{ij} is a $3M \times 3M$ matrix and b_i is a $3M \times 1$ vector, where M is the number of vertices in the mesh. A_{ij} and b_i can be assembled from element submatrices $A_{ij}^{\mathcal{E}}$ and subvectors $b_i^{\mathcal{E}}$ corresponding to element integrations over III.23. Boundary conditions are applied by setting displacement, force, and flux terms associated with particular vertices or elements directly in the system of equations defined by III.24. Finally, the approximate solution to displacement at each node of the mesh can be solved from

$$\widetilde{u} = {A_{ij}}^{-1} b_i, \tag{III.25}$$

after which strain and stress can be recovered through III.10 and III.6, respectively.

III.4 Forward and Inverse Modeling

The conventional usage of a finite element model is the forward application, in which the mesh and boundary conditions are provided as known inputs, and given material properties as model parameters, then a predicted deformation response can be computed. Solving III.25 amounts to a forward solution. However, many engineering applications cannot be adequately addressed by forward models such as these. The registration problem is one such example, in which the initial mesh geometry is known and material properties can be estimated, however the boundary conditions that give rise to the underlying deformation between preoperative and intraoperative organ conformations are in reality unknown. To address, inverse modeling approaches (see Figure III.1) become necessary. Whereas boundary constraints must be applied directly in a forward model, the registration problem instead can be solved in a more theoretically founded way via a reconstructive inverse model that estimates the underlying configuration of boundary conditions that must have

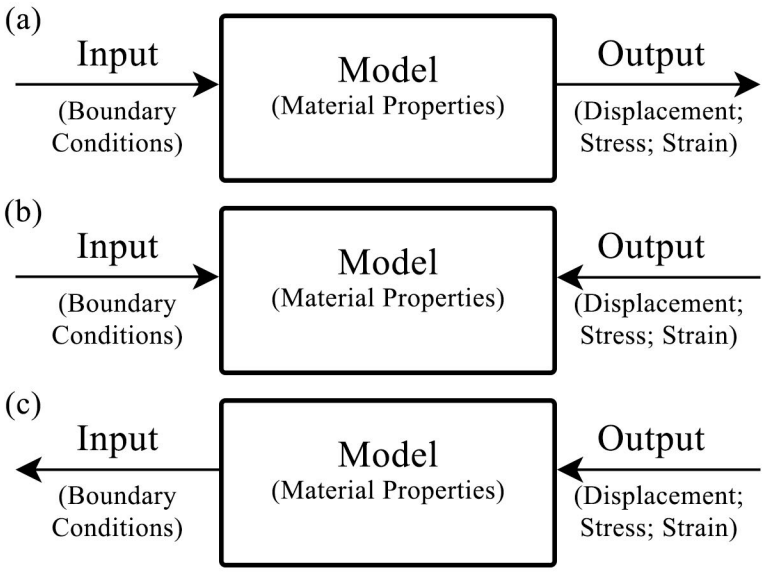

Figure III.1: Forward and inverse modeling approaches. (a) In the forward model, inputs and model parameters are known, and the objective is to determine a predicted output response from these quantities. (b) In the parametric inverse model, a known input is provided and the output is measured, with the objective of recovering or fitting the model parameters. (c) In the reconstructive inverse model, partial output responses to an unknown input are measured; given known model parameters, the inputs that must have led to the observed response are determined.

been applied to the organ mesh in order to produce an observed state of deformation. Appendix B provides an example of the potential loss in accuracy when forward as opposed to inverse models are used during registration to predict deformation deeper in the organ.

Inverse methods are often implemented with optimization frameworks around a forward model. For example, the registration problem could be implemented as determining a spatial transformation $\mathcal{T}(x) = x + \widetilde{u}(x)$ where $\widetilde{u}(x) = \widetilde{u}(x, BC)$ depends on a set of boundary conditions BC, such as:

$$\arg\min_{BC} L\left(x + \widetilde{u}(x, BC), S(x+u)\right), \tag{III.26}$$

where $\widetilde{u}(x, BC)$ is a predicted forward model displacement solution from III.25 as a function of the applied boundary condition set, $S(x+u)$ is an observed sampling of the true displacement field, and $L(x, y)$ is a loss function that describes the error between pre-

dicted and observed positions. Since independent boundary conditions can be defined at every vertex or boundary element of the mesh, the degrees of freedom can be large and considerably underdetermined by the sampled data. In order to perform this optimization more effectively, it is beneficial to construct a mathematical basis for the set of feasible deformations to reduce the parameter space of the optimization.

III.5 Modal Representation of Deformation

Any linear function must satisfy two properties: (1) additivity $f(a+b) = f(a) + f(b)$, and (2) homogeneity $f(ca) = cf(a)$ for all a, b and constant c. These properties give rise to the principle of superposition, which states that any response f can be written as a weighted sum of a linearly independent basis f_i such that $f = \sum_i w_i f_i$ and the property $\sum_i w_i f_i \neq 0$, $\forall w_i \neq 0$ is satisfied, where f_i is an admissible *mode* of the response f. This relation can be represented as,

$$f = \begin{bmatrix} f_1 & f_2 & f_3 & \dots & f_n \end{bmatrix} \begin{bmatrix} w_1 \\ w_2 \\ w_3 \\ \dots \\ w_n \end{bmatrix} = J_f w, \tag{III.27}$$

where $J_f = \frac{\partial f}{\partial w}$ is the Jacobian of f with respect to w.

The finite element equations of linear elasticity are completely linearized, which arises from the linearity of III.6 and III.10, in addition to the use of Lagrange basis functions in III.14–III.15 and assembly of A_{ij} and b_i from III.23–III.24. Consequently, the principle of superposition holds for any combination of linearly independent boundary condition inputs. This principle states that a parameterization of the displacement, strain, and stress solutions throughout the domain therefore can be expressed as,

$$\begin{aligned} \widetilde{u} &= J_u \alpha \\ \widetilde{\varepsilon} &= J_\varepsilon \alpha \\ \widetilde{\sigma} &= J_\sigma \alpha \end{aligned} \tag{III.28}$$

where α is a set of mode weights and J_u, J_ε, and J_σ represent the displacement, strain, and stress responses to linearly independent sets of boundary condition modes applied to III.24. The set of deformations spanned by these modes is the convex set of any linear combination of boundary conditions encoded within the response matrices, for which any linear combination parameterized by α must also satisfy the governing PDE III.12. This process allows any number of deformations to be simulated without requiring repeated inversion of A_{ij} by instead combining solutions of precomputable modal responses. By constraining the number of boundary condition modes or their applied sites to preempted anatomical regions, a smaller feasible set can be established to allow for rapid estimation of deformation from the state vector α without losing important modes of variation. This approach is the basis for the registration methods introduced in Chapter IV and Chapter V. In this case, the registration problem simplifies to a significantly lower-dimensional optimization compared to III.26,

$$\arg\min_{\alpha} L\left(x + J_u \alpha, S(x+u)\right), \tag{III.29}$$

where the cardinality $|\alpha|$ rarely needs to exceed 150, compared to $|BC| > 10^5$ for a full-resolution reconstruction on a typical liver mesh.

III.6 The Saint-Venant Principle

The Saint-Venant principle is a phenomenon that describes how the difference between two statically equivalent loads that are distributed differently on the same region of a material domain will become sufficiently small at arbitrarily large distances from the site of the load.

Namely, the difference in far-field effects between two locally different representations of the same statically equivalent load, for example a point load or a uniform load with the same sum of forces over a region of the boundary, will eventually vanish with distance away from the boundary. While this effect was first described qualitatively by Saint-Venant in 1855, quantitative theory did not arrive until just under a century later when Von Mises published a derivation in the absence of tangential loads [147], which was soon extended by Sternberg to the simultaneous application of multiple forces at different points on the boundary [148]. Both approaches described the dilatational strain at any point interior to a cylindrical or infinite half-plane domain as a function of axial loads placed on the boundary. However, a proof for the *relative* relationship between the difference in applied loads and the resulting difference in effects at a distant point was not established until theory published by Toupin in 1965, which was also shown to be valid for arbitrarily shaped domains [149]. In modeling deformation for the purpose of registration of soft tissues, the work encompassed by this dissertation leverages the Saint-Venant principle to permit local redistribution of modal descriptions of deformation while maintaining identical far-field effects. Furthermore, the relationships derived by Toupin are also used to address concepts in registration uncertainty.

More formally, Toupin's description of the Saint-Venant principle is governed by a decay relationship for the strain energy associated with the difference between two loading configurations at the boundary, as both effects propagate through the domain. Toupin proved the relationship,

$$\frac{U(r)}{U(0)} \leq \exp\left(-\int_0^r \frac{1}{s_c(s)} ds\right) \tag{III.30}$$

where $U(0)$ is the total strain energy in domain $\mathcal{M}$ caused by the difference between two loads, $U(r)$ is the strain energy contained in the subdomain of $\mathcal{M}$ greater than distance r from the boundary load, and $s_c(s)$ is a characteristic length equal to

$$s_c(s) = \sqrt{\frac{\mu^*}{\rho\,\omega_0{}^2(s)}} \tag{III.31}$$

where ρ is material density, $\omega_0(s)$ is the lowest fundamental frequency of free vibration within the section of $\mathcal{M}$ between the boundary load and distance s, and $\mu^* = \mu_M{}^2/\mu_m$ is an effective elastic modulus where $\mu_M = 2\mu + 3\lambda$ is the maximum elastic modulus and $\mu_m = 2\mu$ is the minimum elastic modulus associated with the eigenvalues of the material tensor C from III.9 [150]. Toupin then proved validity of the Saint-Venant principle by relating the exponential decay of $U(r)$ with the magnitude of strain at position r, which must eventually become sufficiently small at arbitrarily large r.

In this work, ω_0 and hence s_c are taken to be constant to provide a simplified form of Toupin's result,

$$\frac{U(r)}{U(0)} \leq \exp(-kr) \tag{III.32}$$

which describes the proportion of energy from the boundary that has dissipated before reaching distance r, with decay rate $k = \sqrt{\rho\,\omega_0{}^2/\mu^*}$. The characteristic frequency ω_0 is approximable by the Rayleigh quotient, which can be computed from equating the potential energy of an admissible deformation with the kinetic energy of its undamped oscillation. An *admissible* deformation is defined to be one that satisfies the field equations of linear elasticity. For a deformation $\langle u, \overline{\overline{\varepsilon}}, \overline{\overline{\sigma}} \rangle$, the potential energy can be expressed as,

$$U = \frac{1}{2}\int \overline{\overline{\sigma}} : \overline{\overline{\varepsilon}}\; dV = \frac{\mu^*}{2}\int \overline{\overline{\varepsilon}} : \overline{\overline{\varepsilon}}\; dV. \tag{III.33}$$

Furthermore, the kinetic energy of free vibration is,

$$K = \frac{1}{2}\int \rho(\omega u)\cdot(\omega u)\; dV = \frac{\rho\,\omega^2}{2}\int u \cdot u\; dV. \tag{III.34}$$

Equating these two quantities, the Rayleigh quotient is obtained to give the lowest natural frequency of free vibration,

$$\omega_0{}^2 \approx \omega^2 = \frac{\mu^*}{\rho} \frac{\int \overline{\overline{\varepsilon}} : \overline{\overline{\varepsilon}}\, dV}{\int u \cdot u\, dV}. \tag{III.35}$$

III.7 Principles of Thermoelasticity

Classical concepts in thermoelasticity attempt to describe the effect of thermal stresses and thermal strains caused by exertion of work, heat transfer, and environmental changes in temperature. These directions towards which classical theories have matured most may be less applicable during registration, where deformations are expected to take place under constant temperature and heat flow is not a major consideration. However, as will be shown in this section, thermoelastic concepts can provide a framework for understanding the entropy of deformation, which can be translated by Boltzmann's equation into a measure for the uncertainty of a particular deformation state. In this section, a derivation has been furnished under isothermal conditions to describe how thermodynamic entropy is related to elastic strain to incentivize how registration uncertainty can be measured by the number of deformations available to a single equilibrium state.

By the first law of thermodynamics, the internal energy of any system is the sum of its stored energy. At static equilibrium, the internal energy is equal to the strain energy state variable $U = \frac{1}{2} V \sigma \cdot \varepsilon$. The thermodynamic equations of state specify that

$$\begin{aligned} H &= U + PV \\ G &= H - TS \end{aligned} \tag{III.36}$$

where the enthalpy H is the internal energy adjusted by the amount of expansion work required to make room for the system in pressurized space, the free energy G is the maximum amount of useful non-expansion work that can be extracted from the system, P is the pressure of the system, V is the volume of the system, T is the absolute temperature of the

system, and S is the entropy of the system. These equations of state can be combined and their differentials expressed as

$$\partial G = \partial U + P\partial V + V\partial P - T\partial S - S\partial T. \tag{III.37}$$

Under isothermal and isobaric conditions, $\partial T = \partial P = 0$. Additionally, for an equilibrium state satisfying $\nabla \cdot \overline{\overline{\sigma}} = 0$ and the remaining linear elastic conditions, free energy is constant and requires that $\partial G = 0$. These conditions lead to

$$T\partial S = \partial U + P\partial V. \tag{III.38}$$

The differential volume can be expressed in terms of the determinant of the deformation gradient F, where

$$F = I + \nabla u = \begin{bmatrix} 1+\frac{\partial u_x}{\partial x} & \frac{\partial u_x}{\partial y} & \frac{\partial u_x}{\partial z} \\ \frac{\partial u_y}{\partial x} & 1+\frac{\partial u_y}{\partial y} & \frac{\partial u_y}{\partial z} \\ \frac{\partial u_z}{\partial x} & \frac{\partial u_z}{\partial y} & 1+\frac{\partial u_z}{\partial z} \end{bmatrix} \tag{III.39}$$

and $\partial V = V\det(F) \approx V(\partial\varepsilon_{xx} + \partial\varepsilon_{yy} + \partial\varepsilon_{zz})$ to first order strain terms, with $\partial V/V$ being the volumetric strain.

Lastly, the differential of the strain energy is $\partial U = \frac{V}{2}\sigma \cdot \partial\varepsilon + \frac{V}{2}\varepsilon \cdot \partial\sigma + \frac{1}{2}\sigma \cdot \varepsilon\partial V = V\sigma \cdot \partial\varepsilon + \frac{1}{2}\sigma \cdot \varepsilon\partial V$. Combining these results,

$$\partial S = \frac{V}{T}\left(\sigma \cdot \partial\varepsilon + \left(P + \tfrac{1}{2}\sigma \cdot \varepsilon\right)\left(\partial\varepsilon_{xx} + \partial\varepsilon_{yy} + \partial\varepsilon_{zz}\right)\right) \tag{III.40}$$

This result of entropic elasticity characterized by the temperature independence of $\partial S/\partial\varepsilon$ has been previously described [151] and signifies that in an isothermal domain, any change in the entropy of the system is matched by a proportional change in admissible strain that gives rise to apparent metastability of the strain field under equilibrium conditions. In the opposing direction, admissible changes in the strain field also cause a

proportional change in entropy that must be configurational in nature. *The relationship of III.40 suggests that within an observed equilibrium state, strain and entropy can be freely exchanged under isothermal and isobaric conditions. Entropy can be borrowed from one region of the system to introduce change in the strain of the system about another region, to produce an observed state within the minimum energy and maximum entropy principles.* This situation can be intuited using an example of an elastic band in one dimension fixed at both ends. Compared to the resting state of the band that would be predicted based on length measurement, other unknown effects applied to the system can cause internal redistribution of entropy and strain, for example the existence of some traction applied to the center of the band that causes relative stretch and change in configurational entropy on one side, and relative compression and change in configurational entropy on the other, leading to a new strain configuration that still satisfies the equilibrium field equations and the length boundary conditions of the system so long as the traction is sustained.

This potential reconfiguration of entropy and strain can be interpreted through Landauer's principle, which introduces the concept of physicality of information by postulating that the knowledge of whether an unknown effect has been applied to the system is associated with its own configurational or information entropy ∂S_L equal to the change in system entropy when the effect is either added or removed. Therefore, unobservable information from unknown sources can be associated with changes in entropy that may virtually shift the internal state of the system, in this case the configuration of strain, from an initial prediction based on incomplete information. Boltzmann's formula states that

$$S = k_B \ln(\Omega), \tag{III.41}$$

where Ω is the number of state configurations and k_B is the Boltzmann constant. Therefore the information entropy logarithmically affects the number of strain states that are admissible to an observed equilibrium. To apply these concepts, if the uncertainty of a registration is related to the number of admissible strain states Ω_i that can potentially confound

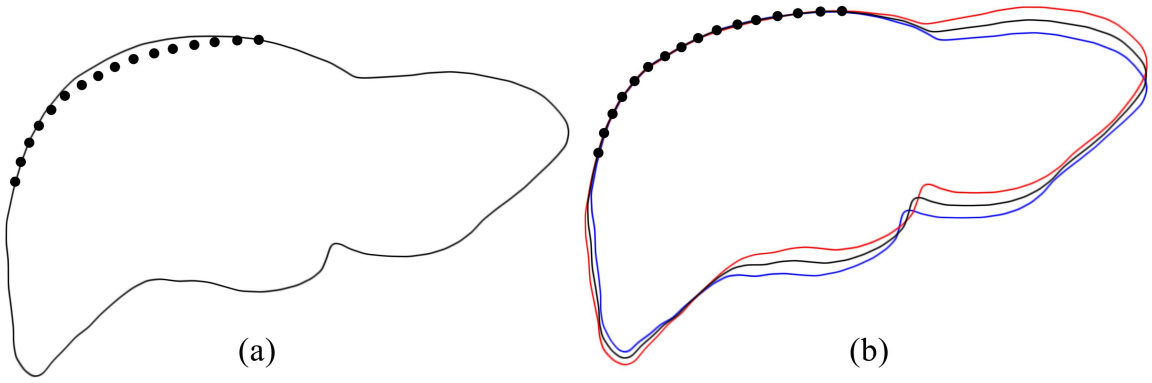

Figure III.2: Uncertainty in deformable elastic registration. (a) Rigid registration between intraoperatively measured data (black points) and preoperative organ model (black contour); the distances between the points and the contour are constraints that are minimized during registration. (b) Elastic registration of preoperative organ model to intraoperative data points; uncertainty is caused by the existence of many solutions (such as the red, black, and blue contours) that each satisfy the constitutive equations of elasticity and simultaneously minimize the residual distances between model and data, and can manifest due to unobservable information affecting the equilibrium solution.

determination of the actual state from unknown effects present under the observed equilibrium conditions, then the registration uncertainty can be considered to be some function of the information entropy $S_i = k_B \ln(\Omega_i)$.

III.8 Registration Uncertainty

In general, registration is ill-posed in the sense that many possible solutions can exist given the information provided to the problem. In the context of deformable registration, multiple admissible displacement fields may exist that match the observed data provided to the registration. An example of this possibility is illustrated in Figure III.2. Accordingly, to measure the uncertainty of the registration, a method must be established to either count the number of possible states that satisfy the constitutive and data constraints, or measure the information entropy of the system around the equilibrium condition that satisfies these constraints.

Consider a system initially in state Q to be perturbed at point source i on the boundary of the domain, and define state R to be the perturbed state. By the canonical ensemble in

statistical mechanics, the likelihood ratio of observing particles of the system in each state is described by the Boltzmann factor,

$$\frac{p_R}{p_Q} = \exp\left(\frac{U_Q - U_R}{nk_BT}\right) = \exp\left(-\frac{U_i}{nk_BT}\right), \tag{III.42}$$

where p_k is the probability of observing state k, $U_i = U_R - U_Q$ is the energy of perturbation from source i, and $n = \frac{\rho V}{M} N_A$ is the number of particles in the domain for average molar mass M and Avogadro's constant N_A. The total Gibbs entropy of state k is defined,

$$S_k = -n\,k_B\,p_k \ln(p_k). \tag{III.43}$$

If the problem is scaled so that the initial probability p_Q = 1 and subsequently $S_Q = 0$ to represent complete certainty of the initial state, the entropy S_R reduces to,

$$S_R = \frac{U_i}{T} \exp\left(-\frac{U_i}{nk_BT}\right). \tag{III.44}$$

The Taylor expansion of S_R around $U_i = 0$ is

$$S_R = nk_B \sum_{j=1}^{\infty} \frac{(-1)^{j-1}}{(j-1)!} \left(\frac{U_i}{nk_BT}\right)^j \approx \frac{U_i}{T} \tag{III.45}$$

to first order. Since $S = k_B \ln(\Omega)$, S_R measures the increase in the number of internally possible strain states Ω_R relative to a certain and singular initial state ($\Omega_Q = 1$), caused by injection of energy into the system. During registration, the most probable strain state is predicted based on the information provided, whereas the strain state that actually occurs is a state selected from Ω_R given additional missing information.

If the Toupin decay relation III.32 is substituted such that $U_i = U(r) \leq U(0)\exp(-kr)$, then the entropy of any boundary effect on the deformation around r can be bounded by a positional measure $S_R(r)$. By III.32, the amount of strain energy $U(r)$ in the domain beyond radius r from point source i diminishes as the interface r expands from r_1 to r_2. Likewise,

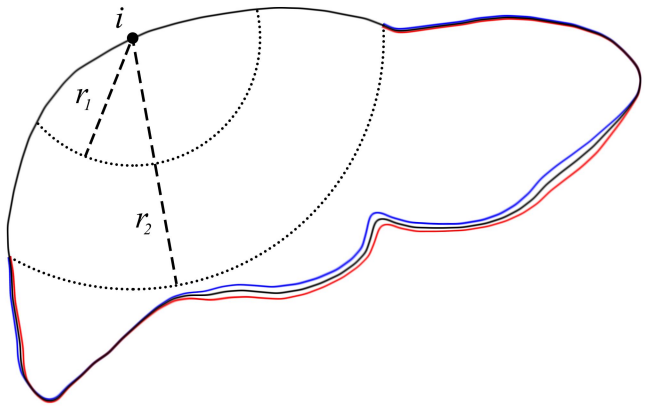

Figure III.3: Positional entropy around a point source i at radius r. The configurational entropy $S(r)$ is related to the number of admissible deformations that exist in the subregion beyond r. Red, black, and blue contours signify some admissible deformation states beyond radius r_2.

the amount of configurational entropy $S_R(r)$ in the subregion beyond r also diminishes as the radius of the interface expands, where the configurational entropy $S_R(r)$ encodes the total number of admissible deformation configurations beyond r, illustrated in Figure III.3. The registration uncertainty up to position r is $S_R(0) - S_R(r)$ and is therefore proportional to $-S_R(r)$ relative to the magnitude of the overall excitation. These quantities will be described and applied in more detail when registration uncertainty is investigated in Chapter VI, where the uncertainty derived from the information-theoretic quantity Shannon information is $-\ln(U)$ and shares similar small-energy behavior with the thermodynamically derived $-S_R$ while not requiring temperature or molar count to compute.

CHAPTER IV

Characterization and Correction of Intraoperative Liver Deformation

IV.1 Summary and Contributions

Soft tissue deformation can be a major source of error for image-guided interventions. Deformations associated with laparoscopic liver surgery can be substantially different from those associated with open approaches due to intraoperative practices such as abdominal insufflation and varying degrees of mobilization from the supporting ligaments of the liver. This chapter aims to improve the potential for image guidance techniques in laparoscopic and open approaches to liver surgery by performing a novel characterization of intraoperative liver deformation from clinically-acquired human data, and by establishing a novel strategy for correcting intraoperative soft tissue deformations for nonrigid deformable registration of preoperative patient anatomy and surgical plans to the intraoperative organ configuration of the patient using surface measurements.

In this chapter, a novel characterization of organ deformation was performed to compare the relative change in organ shape between the preoperative and intraoperative conformations of the liver. As noted in Section II.3, while human studies have shown that intraoperative deformations can exceed 20 mm during OLR, no studies have yet characterized the magnitude of laparoscopic liver deformation in the clinical setting. In this work, data from 25 human patients undergoing planned laparoscopic-to-open conversion under image guidance at Memorial Sloan Kettering Cancer Center were analyzed. The study consisted of a pairwise, paired analysis of the relative magnitudes of deformation between the shapes of the liver reconstructed from (a) preoperative imaging, (b) laparoscopic approach at standard insufflation pressure and (c) reduced insufflation pressure, and (d) during open surgery to directly compare laparoscopic and open deformations of the liver in a diverse set of pa-

tients. This study represents the first published report measuring laparoscopic deformations in the human clinical setting.

A novel deformation correction strategy was also proposed in this chapter, leveraging a set of control points placed across anatomical regions of mechanical support provided to the liver with the goal of decomposing and reconstructing an anatomically constrained configuration of mechanical loads applied to the organ given sparse measurements of the organ surface. This correction method was retrospectively applied to the clinical series of 25 laparoscopic-to-open conversions performed under image guidance, in addition to a phantom framework designed to enable quantitative validation of registration accuracy for applications in image-guided LLR. This phantom-building process is necessary because intraoperative validation target data cannot be measured directly from the patient without adding critically disruptive intraoperative imaging steps to the surgical workflow. The physical simulation environment emulates laparoscopic deformations of the liver through a mock organ phantom, and the details of the development of this system are provided in Appendix A. The accuracy of the proposed deformable registration method was compared to existing surface-based rigid registration [121] and a previously published deformable registration method [2]. Further analysis of the proposed registration method was also performed to characterize limits on accuracy with respect to the amount of surface data provided to the registration.

The combined progress made through this chapter represents fundamental advancement towards defining the need for deformable registration methods during LLR and OLR while providing potential approaches to correct for deformation during registration and evaluate resulting accuracy. These contributions have continued to motivate additional works such as the evolution of the registration methodology presented in Chapter V, the need for and design of phantom datasets such as the sparse data challenge described in Appendix B, and the pursuit of untangling the relationship between data distribution and registration accuracy that becomes fully realized in Chapter VI.

Characterization and Correction of Soft Tissue Deformation in Laparoscopic Image-Guided Liver Surgery

The work presented in this chapter appears in and is reprinted with permission from,

[9]: J. S. Heiselman, L. W. Clements, J. A. Collins, J. A. Weis, A. L. Simpson, S. K. Geevarghese, T. P. Kingham, W. R. Jarnagin, and M. I. Miga, "Characterization and correction of soft tissue deformation in laparoscopic image-guided liver surgery," *Journal of Medical Imaging*, vol. 5, no. 2, pp. 021203, 2018. (© 2018 SPIE)

This work was selected for additional feature, which has been incorporated into this chapter with permission from,

[152]: J. S. Heiselman, J. A. Collins, L. W. Clements, J. A. Weis, A. L. Simpson, S. K. Geevarghese, T. P. Kingham, W. R. Jarnagin, and M. I. Miga, "Technical note: Nonrigid registration for laparoscopic liver surgery using sparse intraoperative data," in *Proceedings of SPIE Medical Imaging*, vol. 10576, pp. 1–12, 2018. (© 2018 SPIE)

IV.2 Abstract

Laparoscopic liver surgery is challenging to perform due to a compromised ability of the surgeon to localize subsurface anatomy in the constrained environment. While image guidance has the potential to address this barrier, intraoperative factors, such as insufflation and variable degrees of organ mobilization from supporting ligaments, may generate substantial deformation. The severity of laparoscopic deformation in humans has not been characterized, and current laparoscopic correction methods do not account for the mechanics of how intraoperative deformation is applied to the liver. We first measure the degree of laparoscopic deformation at two insufflation pressures over the course of laparoscopic-to-open conversion in 25 patients. With this clinical data alongside a mock laparoscopic phantom

setup, we report a biomechanical correction approach that leverages anatomically load-bearing support surfaces from ligament attachments to iteratively reconstruct and account for intraoperative deformations. Laparoscopic deformations were significantly larger than deformations associated with open surgery, and our correction approach yielded subsurface target error of 6.7 ± 1.3 mm and surface error of 0.8 ± 0.4 mm using only sparse surface data with realistic surgical extent. Laparoscopic surface data extents were examined and found to impact registration accuracy. Finally, we demonstrate viability of the correction method with clinical data.

IV.3 Introduction

In liver interventions such as resection and ablation, reliable localization of subsurface structures is required to guide resection planes and accurately deliver treatment. While manual palpation is conventional for identifying these structures during open procedures, this technique is not typically available during laparoscopy. As a result, laparoscopic interventions are often restricted by the ability of the surgeon to approximate the intraoperative positions of lesions and vessels from unregistered preoperative image volumes or experiential knowledge. In comparison with the traditional open approach, laparoscopic liver resections are associated with significant patient benefits, such as reduced blood loss, shorter duration of hospital stay, and fewer postoperative complications with no detriment to overall mortality or oncological adequacy [29, 30]. However, the learning curve for laparoscopic liver resection is considerable, and it is estimated that 10% of all major laparoscopic liver resections require intraoperative conversion to an open approach [66]. Principally, uncontrollable bleeding and unintentional damage to surrounding structures are the causes of conversion in 38% of all converted cases, and an additional 5% of converted cases are attributed to concern over oncological margins [70].

Currently, the laparoscopic approach for hepatic resection critically depends on the skill and experience of the surgeon. Liver resection requires determination of which vessels to

spare or interrupt in the context of patient-specific vasculature and tumor positions [35,91]. However, the ability to localize subsurface vessels and tumors using traditional palpation techniques is impaired during laparoscopy. These errors may be an important factor contributing to the high rate of laparoscopic-to-open conversion and contribute to the frequently reported steep learning curve of laparoscopic liver resection [33, 153, 154]. Recent consensus recommendations have suggested that intraoperative guidance using preoperative images could be a useful tool for visualizing subsurface anatomy, determining the resection plane, and navigating laparoscopic resection [65]. With its potential to assist with these challenging tasks, image guidance could facilitate more complex laparoscopic procedures, reduce the risk of complications, and potentially extend patient candidacy for laparoscopic resection.

To date, conventional image-guided approaches for laparoscopic liver surgery have been limited. Approaches that have been investigated typically utilize rigid registrations, which cannot account for intraoperative soft tissue deformation [17,23,101,105,110,155]. One major source of deformation in laparoscopic procedures is the process of insufflation where the abdominal cavity is pressurized with carbon dioxide. Insufflation has been shown to cause distension and displacement of the ventral wall and diaphragm [126, 127], which are normally joined to the liver by the falciform and the left and right triangular ligaments, respectively (Figure IV.1a). During insufflation, these ligaments are pulled into tension as the abdominal cavity expands, conducting forces from abdominal motions and resulting in deformation of the liver. Intraoperative deformation is further complicated by mobilization of the liver from its supporting ligaments, which may be done to varying degrees of completion depending on the degree of organ mobilization required. While porcine models of abdominal insufflation demonstrate that vessel centerlines can shift up to 35 mm and experience nonrigid deformations of more than 11 mm [129,130], no clinical analysis of human liver deformation during laparoscopy has been performed. The first aim of this work is to

quantify the amount of deformation attributed to the laparoscopic approach from a series of 25 clinical laparoscopic-to-open conversions.

Several approaches for correcting deformation have been developed for image-to-physical registration using partial liver surfaces. Masutani and Kimura [131] proposed an early method that used free-form deformation modes to match the preoperative shape of the liver to a patch of intraoperative surface data. Cash *et al.* [132] developed a linear elastic biomechanical model constrained by closest point boundary conditions to register the preoperative liver to intraoperative surface data. Dumpuri *et al.* [133] improved this method by applying a surface Laplacian equation to extrapolate closest point distances from sparse intraoperative data onto the model. In recent years, nonrigid registration methods have been developed for the laparoscopic environment. Allan et al. [3] developed a nonrigid registration method to stereo-reconstructed laparoscopic surfaces using coherent point drift [134]. Suwelack *et al.* [1] employed a model that mixed elastic mechanical response with electrostatic attractive forces to matc*et al.* h the shapes of preoperative and intraoperative models of the liver. A more recent publication by Plantefève *et al.* [4] established a laparoscopic nonrigid registration pipeline that produced a dynamic elastic registration from tracked texture landmarks. Another variant reported by Reichard et al. [6] projected spring force boundary conditions from a stereo-reconstructed depth map onto a biomechanical model. However, these approaches either fail to use mechanics-based models [3, 131, 134] or treat deformation correction through direct application of digitized intraoperative surfaces as boundary conditions [1, 4, 6, 132, 133]. While the former methods do not accurately model deformation beyond the immediate neighborhood of intraoperative data, the latter methods may not adequately align regions with poor data localization and can have unfavorable responses to untreated sources of intraoperative surface noise. Additionally, stereo vision surface reconstructions and feature tracking can become unpredictable in the presence of specular highlights and laparoscope illumination, blood covering intraoperative surfaces, occlusion by laparoscopic tools, and surgical smoke from electrocautery [109]. A more

robust approach is to reconstruct a solution from a constrained set of possible deformations that are expected to occur on the basis of anatomical support of the organ, as opposed to using surface data to directly apply boundary conditions to the model. Rucker *et al.* [2] addressed this by proposing an inverse method that optimized an initially unknown polynomial family of displacement boundary conditions applied to an anatomical support surface that serves as the mechanical foundation for intraoperative liver deformation. This method has been shown to be effective at correcting intraoperative deformation in open clinical practice [5].

In this work, we adopt the anatomically constrained comprehensive surface reconstruction strategy explored by Rucker *et al.* but report a realization of biomechanical boundary conditions for the purpose of laparoscopic nonrigid registration, with two key contributions. First, as opposed to open surgery where only one support surface exists, the laparoscopic configuration of the liver is mechanically supported by four distinct regions: the falciform, the left and right triangular ligament attachments, and the organ posterior where the liver makes contact with the bowel. We reformulate boundary conditions using a control point strategy that allows any number of independent support surfaces to be considered. Our correction method is based on establishing a set of deformations that are expected to result from intraoperative loads applied to the laparoscopic support surfaces where forces are conducted to the organ. Second, our reformulation makes no underlying assumption about the functional form of displacement boundary conditions and consequently the resulting displacement solution over the support surfaces. This reconceptualization of support surface interactions is intended to improve the fidelity of the model-reconstructed deformation. The second aim of this work is to evaluate our proposed correction framework in a series of phantom and clinical experiments.

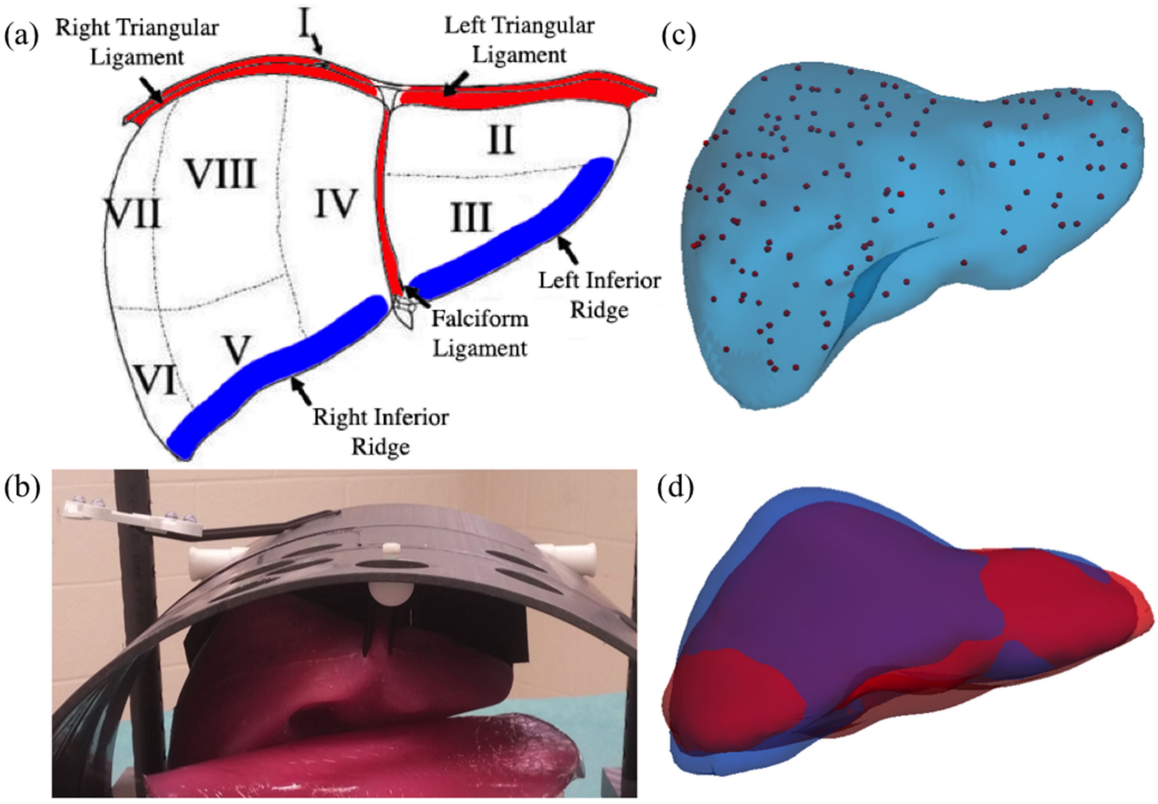

Figure IV.1: (a) Anatomy of the liver, adapted from Kingham *et al.* [23]. The falciform and left and right triangular ligament attachments shown in red are put in tension during insufflation due to expansion of the abdominal cavity. Two salient anatomical features of the liver are shown in blue. (b) The liver phantom is suspended in an insufflated mock abdomen without mobilization from its ligaments. (c) Positions of the 147 subsurface targets distributed throughout the volume of the phantom. (d) Segmented preoperative and intraoperative phantom volumes are shown in blue and red, respectively. The difference between surfaces demonstrates the deformation reproduced in the laparoscopic phantom simulator.

IV.4 Methods

Our dual aims of measuring and correcting laparoscopic deformation consist of four parts: (1) characterization of the intraoperative liver surface during clinical cases of laparoscopic-to-open conversion, (2) reproduction of realistic laparoscopic deformations in a controllable phantom, (3) evaluation of intraoperative deformation in clinical and phantom data, and (4) deformation correction using intraoperative sparse surface data in retrospective clinical and phantom datasets.

IV.4.1 Clinical Data Collection

The clinical data used throughout this work originate from a previous study by Kingham *et al.* [23]. A total of 32 patients were enrolled in a protocol approved by the institutional review board at Memorial Sloan-Kettering Cancer Center wherein a laparoscopic staging procedure was performed prior to an open resection under image guidance. From segmented preoperative CT or MRI images, three-dimensional (3D) model surfaces of the liver were generated using surgical planning software (Scout™ Liver, Analogic Corporation, Peabody, Massachusetts). Tetrahedral meshes were created from these liver surfaces using customized software for mesh generation [146]. With the intention of eventual conversion to open laparotomy, intraoperative laparoscopic exploration was performed to gauge the severity and resectability of disease. During this exploratory step, the falciform ligament was dissected to expose the anterior surface of the liver. Sparse representations of the anterior surface and anatomical features of the liver were then collected with an optically tracked laparoscopic stylus through a minimally invasive surgical guidance system (Explorer™ MIL, Analogic Corporation, Peabody, Massachusetts) [101]. Liver surface and feature data were collected at a standard insufflation pressure of 14 mmHg then at a reduced insufflation pressure of 7 mmHg. Following conversion to open, these digitizations were repeated. All collections were performed during apneic phases induced at end-expiration to minimize the impact of respiratory motion [100]. These digitizations

provide an anatomically labeled sparse 3D point cloud of the shape of the intraoperative organ surface. Whereas the study by Kingham *et al.* aimed to directly compare the accuracy of image-to-physical rigid registrations between laparoscopic and open surgical approaches, in this work, the laparoscopic and open surface collections are used to quantify the magnitudes of liver deformation among preoperative, laparoscopic, and open organ configurations (Section IV.5.1), as well as to demonstrate clinical feasibility of our correction approach (Section IV.5.2). To enable paired statistical comparisons across intraoperative conditions, this study uses 25 of the previously reported 32 patients that possessed intraoperative data under all three intraoperative scenarios of both laparoscopic insufflation pressures and open approach.

IV.4.2 Phantom Data Collection

Intraoperative surgical constraints make obtaining a sufficient amount of clinical data for subsurface validation of registration algorithms particularly challenging. Therefore, a tissue-mimicking phantom and abdominal frame were created to reproduce laparoscopic deformations [156] (Appendix A). In brief, a mock abdomen was constructed at insufflated dimensions, and nine laparoscopic access ports were placed in clinically relevant positions. Mock detachable falciform and triangular ligaments were used to suspend a liver phantom inside the abdomen, with partial support provided by a simulated bowel structure on the organ posterior. Figure IV.1a and Figure IV.1b show the anatomical attachments to the liver and the deformation experienced by the phantom in the laparoscopic simulator. Through suspending the phantom in the enlarged abdominal cavity and removing ligament attachments, intraoperative deformations associated with a fixed insufflation level and adjustable organ mobilization can be reproduced. With the phantom, three states of intraoperative deformation were considered: no mobilization, left mobilization, and right mobilization. The falciform and the left or right triangular ligaments were removed for left or right mo-

bilization, respectively. No ligament attachments were removed for the no-mobilization condition.

The phantom was constructed from 50% Ecoflex® 00-10 platinum-cure silicone mixed with 30% Silicone Thinner® and 20% Slacker® Tactile Mutator (Smooth-On Inc., Pennsylvania). A total of 147 radiopaque target beads were placed throughout the volume by carefully pouring the silicone around a network of threads to which the beads were weakly adhered by a thin layer of petroleum jelly. The threads were withdrawn from the cured silicone, leaving the target beads distributed as shown in Figure IV.1c. The segmented positions of these beads in pre- and post-deformation CT images allow validation of target error after registration. The phantom was molded after a physical liver 3-D printed from a preoperative patient CT. A pre-deformation, preoperative image of the phantom was taken before demolding. In the same manner as the clinical cases, the pre-deformation CT was segmented and a preoperative organ model was generated. Intraoperative deformation was applied by suspending the phantom from its ligament attachments in the abdominal frame. Left and right mobilizations were performed as previously described to produce three configurations of intraoperative deformation in total. A post-deformation CT image was acquired for each scenario, and sparse digitizations of the anterior surface and salient features were collected through the nine access ports in the abdominal enclosure using a tracked laparoscopic stylus and tracked conoscope (ConoPoint-10, Optimet Inc., Jerusalem, Israel) [103, 106]. Segmented pre- and post-deformation CT liver phantom volumes are shown in Figure IV.1d.

IV.4.3 Evaluation of Intraoperative Deformation

Our clinical intraoperative data for each patient at three phases of laparoscopic-to-open conversion enable tracking of organ surface deformation for each individual liver throughout the operation. The sparse surface data collected during the laparoscopic and open approaches are representative of organ shape at each of the three intraoperative conditions:

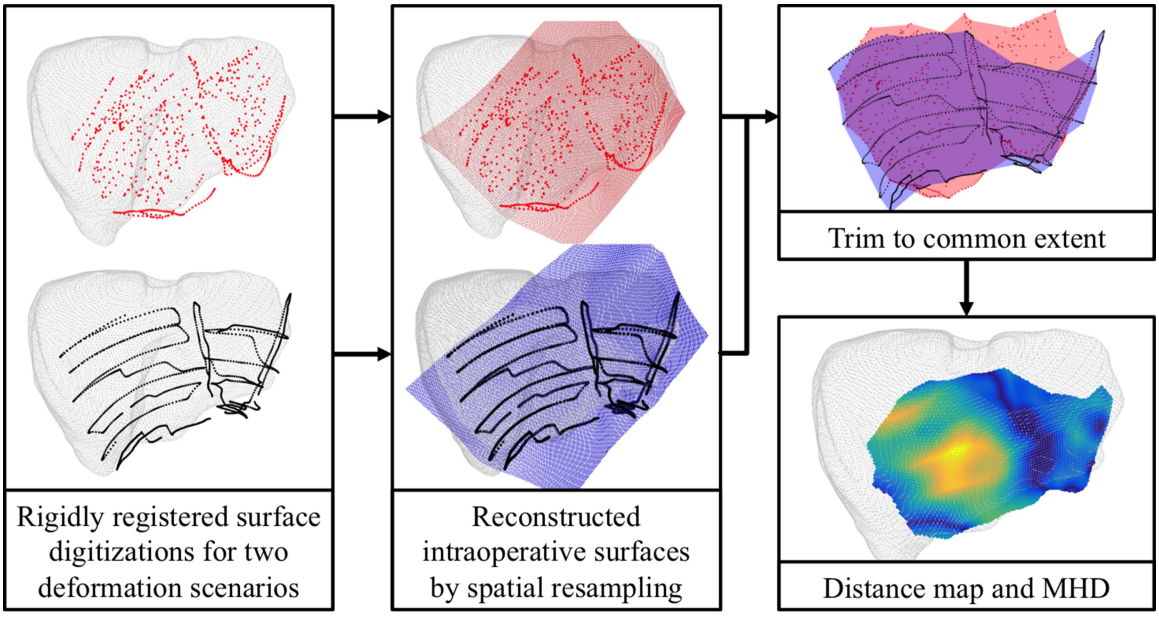

Figure IV.2: Overview of intraoperative organ shape comparison. Sparse point clouds of the intraoperative organ shape under two distinct operative conditions are coregistered to the preoperative liver surface and resampled into full reconstructed surfaces. Distance measures of shape dissimilarity are computed for only the resampled points that are enclosed by the extents of both data sources (purple region).

laparoscopic high insufflation pressure (Lap14mmHg), laparoscopic low insufflation pressure (Lap7mmHg), and open approach (Open). Our objective is to quantify the magnitude of deformation existing among pairs of organ conformations, done by coregistering and reconstructing full surfaces from sparse data as summarized in Figure IV.2.

IV.4.3.1 Rigid Registration

To compare the deformation between two sparse surfaces, registration to a common reference frame is needed. For each patient, all intraoperative point clouds were rigidly registered to the surface of the preoperative liver using a salient feature-weighted iterative closest point algorithm [121]. This registration method takes advantage of preoperatively and intraoperatively designated anatomical labels to bias closest point correspondence such that salient anatomical features preferentially align. This registration method is preferred since it produces consistent coregistrations even in the presence of significant deformation.

The salient features used in this study include the falciform ligament and the left and right inferior ridges. The algorithm produces a rigid transformation that minimizes the feature-weighted distance between the preoperative surface and the intraoperative data points. We should also note that following rigid registration to the preoperative liver, we employ a spatial resampling strategy to reconstruct more complete surfaces of the deformed intra-operative organ shapes from sparse sets of points. This approach was reported in previous work with a detailed analysis of how it improves fidelity of both rigid and non-rigid registration [111].

IV.4.3.2 Surface Resampling

In brief, the resampling approach assumes that the elevation of the organ surface in $\mathbb{R}^3$ can be represented by a continuous function $z = f(x,y)$. The sparse data were rotated onto their major principal axes $\hat{x}$ and $\hat{y}$ such that the smallest principal direction aligned with $\hat{z}$. The complete surface was reconstructed on a triangulated rectilinear grid with $h = 1$ mm spacing using a regularized interpolation method to fit scattered data [157]. The method solves for the elevation $\hat{z}_g$ at every grid point in relation to the elevation of each data point $\hat{z}_d$, subject to barycentric interpolation:

$$\sum_{j=1}^{3} \lambda_i \hat{\mathbf{z}}_{g,i} = A\hat{\mathbf{z}}_g = \hat{\mathbf{z}}_d, \tag{IV.1}$$

where i corresponds to the vertices of the triangle that encloses the data point and λ_i is the barycentric coordinate. Since this linear system is underdetermined, a regularizer is used to enforce smoothness through a second order finite difference approximation to the Laplacian at every grid point:

$$\nabla^2 \hat{z}_g^{i,j} \approx \frac{\hat{z}_g^{i+1,j} + \hat{z}_g^{i-1,j} + \hat{z}_g^{i,j+1} + \hat{z}_g^{i,j-1} - 4\hat{z}_g^{i,j}}{h^2} = B\hat{\mathbf{z}}_g = 0, \tag{IV.2}$$

The regularizer is scaled to the matrix norm of A and is further controlled by a stiffness parameter k such that the elevation of the resampled grid can be determined by solving the sum of Equations IV.1 and IV.2:

$$\left(A + k\frac{||A||}{||B||}B\right)\hat{\boldsymbol{z}}_g = \hat{\boldsymbol{z}}_d, \tag{IV.3}$$

Each reconstructed surface is then trimmed to the spatial extent of its raw intraoperative data. The boundary is established by constructing an alpha shape around the rotated point coordinates belonging to the first two principal axes. The alpha shape as introduced by Edelsbrunner and Mücke [158, 159] is a subset of the Delaunay triangulation controlled by a parameter a, where boundary simplices are eroded until a disk of radius $\sqrt{a}$ can be constructed on the exterior of each edge and the disk contains no other vertices. Hence, while the Delaunay triangulation is convex, alpha shapes are capable of fitting concave boundaries. The built-in MATLAB implementation of alpha shape was used to reject resampled grid points that extended beyond the data boundary. For the purpose of comparing two intraoperative surfaces, the reconstructed surfaces were trimmed to the union of both alpha shapes. In the present study we employed values of $k = 10$ and $a = 22$.

IV.4.3.3 Shape Comparison Metric

The modified Hausdorff distance (MHD) metric [160] is chosen to characterize the difference between organ surfaces as a quantification of surface deformation. MHD is an appropriate metric for its ability to measure average shape distortion. Briefly reviewed here, for two sets of points X and Y, MHD is defined as the maximum of the average closest point distance from every point in X to any point in Y and the dual average closest point distance from Y to X:

$$\overline{d}_{CP}(X,Y) = \frac{1}{|X|}\sum_{\boldsymbol{x}\in X}\min_{\boldsymbol{y}\in Y}\left(||\boldsymbol{x}-\boldsymbol{y}||\right), \tag{IV.4}$$

$$\text{MHD} = \max\left(\overline{d}_{CP}(X,Y), \overline{d}_{CP}(Y,X)\right). \tag{IV.5}$$

While the MHD metric can underpredict in situations with large discrepancies between surface curvatures [161], these circumstances would require either misregistration or unrealistic deformation and are not expected to occur.

IV.4.4 Deformation Correction Strategy

The overarching strategy to correct for soft tissue deformations is shown in Figure IV.3 with the goal of producing an accurate volumetric alignment between the preoperative organ data and the intraoperative organ presentation. Anatomical support surfaces that bear intraoperative load are identified on the preoperative image-derived biomechanical model and control point selections are designated on these surfaces. A set of predicted deformations are precomputed from displacement perturbations of each control point, creating an effective Jacobian that measures the change in deformation across the mesh with respect to control point motion. Intraoperatively, the shape of the preoperative liver is fit to sparse intraoperative surface data by iteratively solving for a linear combination of model-predicted deformations using the Levenberg–Marquardt nonlinear optimization method. Finally, a model relaxation is performed to locally improve the registration near the support surfaces. These steps are described in more detail in the following sections.

IV.4.4.1 Finite Element Model

A finite element model was employed to simulate deformation on a preoperatively constructed tetrahedral mesh. The model is governed by the standard Navier–Cauchy constitutive equations for linear elasticity in three dimensions

$$\frac{E}{2(1+\nu)(1-2\nu)}\nabla(\nabla\cdot\boldsymbol{u}) + \frac{E}{2(1+\nu)}\nabla^2\boldsymbol{u} + \boldsymbol{F} = 0, \tag{IV.6}$$

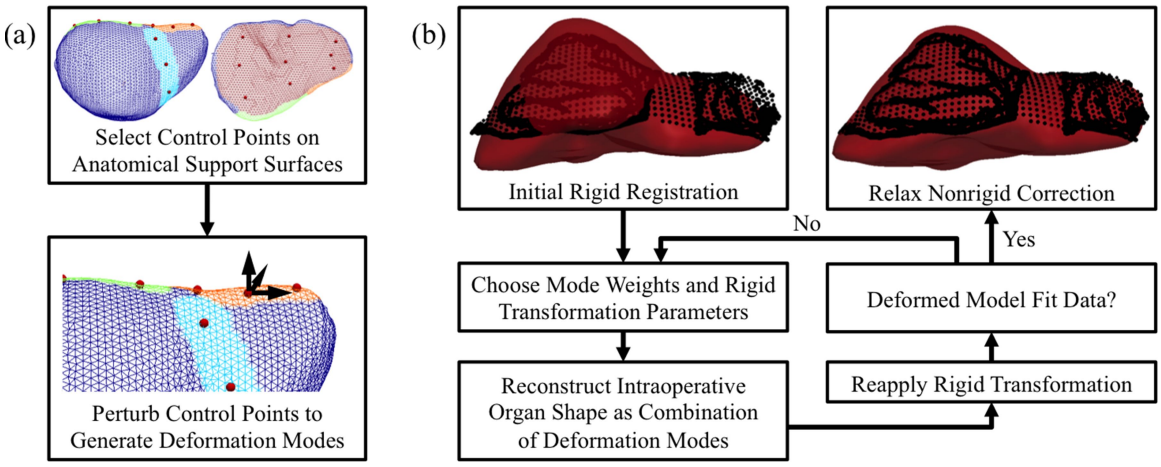

Figure IV.3: Overview of deformation correction algorithm. (a) Model solutions are computed for perturbations of a choice of control points. (b) Nonrigid correction is performed by iteratively updating a set of parameters that are used to reconstruct the intraoperative organ shape from precomputed modes of expected deformation.

where $\boldsymbol{u}$ is the displacement for each node in the mesh, $\boldsymbol{F}$ is the applied force distribution, E is Young's modulus, and ν is Poisson's ratio. This system of partial differential equations is solved via the Galerkin weighted residual method using linear Lagrange basis functions and the assumption of isotropic material properties consistent with Rucker *et al.* [2]. This approach enables the model displacements to be solved from the linear system of equations

$$K\boldsymbol{u} = \boldsymbol{f} \tag{IV.7}$$

where K is the global stiffness matrix. However, in a major departure from the approach used by Rucker *et al.,* where a family of *a priori* polynomial displacement solutions were prescribed to a single support surface, in our proposed approach we instead apply independent control point perturbations as displacement boundary conditions on four separate anatomical support surfaces.

IV.4.4.2 Control Point Selection

The falciform ligament, the left and right triangular ligaments, and the posterior surface are modeled as support surfaces where intraoperative forces influence the liver. Boundary faces associated with these four supports are designated on the mesh of the preoperative liver. Control points are chosen on the support surfaces by parameterizing a curve $\boldsymbol{p}(s)$ to each ligament support and a surface $\boldsymbol{q}(s,t)$ to the posterior support such that

$$\boldsymbol{p}(s) = \begin{cases} x(s) = \sum_{i=0}^{P} a_i s^i \\ y(s) = \sum_{i=0}^{P} b_i s^i \\ z(s) = \sum_{i=0}^{P} c_i s^i \end{cases} \tag{IV.8}$$

$$\boldsymbol{q}(s,t) = \begin{cases} x(s) = \sum_{i=0}^{P} \sum_{j=0}^{i} a_{i,j} s^{i-j} t^j \\ y(s) = \sum_{i=0}^{P} \sum_{j=0}^{i} b_{i,j} s^{i-j} t^j \\ z(s) = \sum_{i=0}^{P} \sum_{j=0}^{i} c_{i,j} s^{i-j} t^j \end{cases} \tag{IV.9}$$

where $P = 5$ is the order of fit and $a \in \boldsymbol{A}_s$, $b \in \boldsymbol{B}_s$, and $c \in \boldsymbol{C}_s$ are the linear weights for the polynomial subspace of each support surface parameterization. For each point $\boldsymbol{x}_j$ in the support surface x_s, the parameter s_j is determined by normalizing the distance from $\boldsymbol{x}_j$ to the point $\boldsymbol{x}^* \in x_s$ that is most distant from the centroid of the support

$$s_j = \frac{||\boldsymbol{x}_j - \boldsymbol{x}^*||}{\max\left(||\boldsymbol{x}_j - \boldsymbol{x}^*||\right)}. \tag{IV.10}$$

The parameter t_j is established by normalizing the distance from $\boldsymbol{x}_j$ to $\boldsymbol{p}(s_j)$ by a curve parameterized to either the upper boundary nodes of the support surface $\boldsymbol{p}^+(s)$ or the lower boundary nodes $\boldsymbol{p}^-(s)$, depending on the position of $\boldsymbol{x}_j$ relative to $\boldsymbol{p}(s)$ such that $t_j \in [-1,1]$

$$t_j = \frac{||\boldsymbol{x}_j - \boldsymbol{p}(s_j)||}{\max\left(\boldsymbol{p}^{\pm}(s_j) - \boldsymbol{p}(s_j)||\right)}. \tag{IV.11}$$

The vectors of weights $\boldsymbol{A}_s$, $\boldsymbol{B}_s$, and $\boldsymbol{C}_s$ are solved using ordinary least squares such that the support surface parameterizations best fit the positions of the n_s vertices on the mesh that belong to each support surface.

$$X(s) = \begin{bmatrix} 1 & s_1 & {s_1}^2 & \dots & {s_1}^P \\ 1 & s_2 & {s_2}^2 & \dots & {s_2}^P \\ \vdots & \vdots & \vdots & \ddots & \vdots \\ 1 & s_{n_s} & {s_{n_s}}^2 & \dots & {s_{n_s}}^P \end{bmatrix}, \tag{IV.12}$$

$$X(s,t) = \begin{bmatrix} 1 & s_1 & t_1 & \dots & s_1{t_1}^{P-1} & {t_1}^P \\ 1 & s_2 & t_2 & \dots & s_2{t_2}^{P-1} & {t_2}^P \\ \vdots & \vdots & \vdots & \ddots & \vdots & \vdots \\ 1 & s_{n_s} & t_{n_s} & \dots & s_{n_s}{t_{n_s}}^{P-1} & {t_{n_s}}^P \end{bmatrix}, \tag{IV.13}$$

$$[\boldsymbol{A}_s \ \boldsymbol{B}_s \ \boldsymbol{C}_s] = (X^T X)^{-1} X^T x_s. \tag{IV.14}$$

An M number of control points are evenly spaced across each dimension of the parameterized supports by finding the closest vertices on the mesh to $\boldsymbol{p}(s)$ or $\boldsymbol{q}(s,t)$ at interior grid points created by dividing s and t into $M+1$ intervals. A parameter sweep across the placement of 1 to 5 control points on each ligament attachment site and 3 to 48 control points on the posterior support surface showed that no significant difference existed over target registration error (TRE) in the phantom among these choices of control points ($p > 0.9$, one-way analysis of variance; maximum change of 0.5 mm). A choice of $M = 3$ control points on the laparoscopic support surfaces of the liver, as shown in Figure IV.3a, was selected.

IV.4.4.3 Generation of Deformation Modes from Displacement Boundary Conditions

Forward model solutions to 1 mm displacement perturbations in the x-, y-, or z-directions of each control point are simulated keeping all other control points stationary and all other nodes stress free. These solutions produce a set of intraoperative deformation modes that estimate linear gradients to point load perturbations of the support surface. The resulting displacement, stress, and strain solutions establish the rows of the $3n \times k$ Jacobian matrix J_u and the $6n \times k$ Jacobian matrices J_σ, and J_ε, respectively, where n is the number of nodes in the mesh and k is triple the number of control points, equal to the total number of perturbations made. These Jacobian matrices can be precomputed and used to quickly estimate intraoperative deformations. A parameter vector $\boldsymbol{\alpha}$ of length k is determined such that a linear combination of the deformation modes estimates the intraoperative node displacements, stresses, and strains

$$\boldsymbol{u} = J_u \boldsymbol{\alpha}, \tag{IV.15}$$

$$\boldsymbol{\sigma} = J_\sigma \boldsymbol{\alpha}, \tag{IV.16}$$

$$\boldsymbol{\varepsilon} = J_\varepsilon \boldsymbol{\alpha}. \tag{IV.17}$$

The average strain energy density $\overline{U}$ associated with a particular deformation configuration is calculated as

$$\overline{U} = \frac{1}{2}\boldsymbol{\sigma} \cdot \boldsymbol{\varepsilon} = \frac{1}{2}\boldsymbol{\alpha} {J_\sigma}^T J_\varepsilon \boldsymbol{\alpha}. \tag{IV.18}$$

This approach can be employed because the use of a linear model gives rise to the principle of superposition. Namely, because the model is a linear system, the response to any

possible change over the anatomical support surfaces is identical to the sum of responses to less complex inputs that span the total change. While we recognize that our point load perturbations do not span all possible distributed loads that may be applied to the support surfaces in truth, this assumption is needed to reduce the complexity of the inverse problem to make optimization of $\boldsymbol{\alpha}$ tractable under intraoperative time constraints. Furthermore, our approximation of the intraoperative distributed load as a statically equivalent combination of point loads is justified by Saint Venant's principle, which states that the difference between the responses to two statically equivalent loads vanishes exponentially with the distance from the load [162]. Hence, the model reconstruction is accurate in the far field, although it may experience local artifacts in the near-field on the support surfaces. A treatment to resolve this situation is described in Section IV.4.4.5.

IV.4.4.4 Reconstruction of Intraoperative Deformation

Our nonrigid registration is performed through an intraoperative optimization to find the set of model perturbations that best fit the resampled surface data. An alignment of the preoperative model to sparse intraoperative data is initialized with a salient feature-weighted rigid registration method as described in Section IV.4.3.1. After rigid registration, the salient feature and anterior surface digitizations are resampled using the surface reconstruction method described described in Section IV.4.3.2, adapted from Collins *et al.* [111]. This resampling method standardizes the density and topology of the sparse surfaces to diminish the influences of trajectory, dwell, and surface noise from intraoperative data collection. An augmented vector of model parameters $\boldsymbol{\alpha}'$ is considered, where

$$\boldsymbol{\alpha}' = [\boldsymbol{\alpha}^T,\ t_x,\ t_y,\ t_z,\ \theta_x,\ \theta_y,\ \theta_z]^T \tag{IV.19}$$

includes the rigid body translation and rotation parameters t_x, t_y, t_z, θ_x, θ_y, and θ_z in addition to the vector of linear coefficients $\boldsymbol{\alpha}$ that apply to the preoperatively determined responses to control point deformations. The corrected node positions $\boldsymbol{x}_c$ are taken to be

$$\boldsymbol{x}_c = T(\boldsymbol{x}_0 + J_u \boldsymbol{\alpha}), \tag{IV.20}$$

where $\boldsymbol{x}_0$ are the node positions of the original preoperative mesh and T is the rigid body transformation defined by the optimized translation and rotation parameters.

In a similar manner to the approach proposed by Rucker *et al.,* we employ an implementation of the Levenberg–Marquardt method [163] to find an $\boldsymbol{\alpha}'$ that minimizes a nonlinear objective function Ω based on model-data surface error regularized by strain energy

$$\Omega = \frac{1}{N} \sum_{i=1}^{N} w_i ||\boldsymbol{x}_{d,i} - \boldsymbol{x}_{c,i}||^2 + \kappa \overline{U}^2, \tag{IV.21}$$

where N is the number of resampled data points, w_i is an additional weighting factor for salient feature points, $\boldsymbol{x}_{d,i}$ is an indexed point in the resampled intraoperative surface data, and $\boldsymbol{x}_{c,i}$ is the closest point on the model surface to $\boldsymbol{x}_{d,i}$, rapidly queried using a k-d tree. We use a strain energy regularization constant of $\kappa = 10^{-8}$ in agreement with the characterization done by Rucker *et al.* The Levenberg–Marquardt update step to the parameter vector is performed iteratively, where

$$\boldsymbol{\alpha}'_{k+1} = \boldsymbol{\alpha}'_k + \left(J^T J + \lambda \operatorname{diag}(J^T J)\right)^{-1} J^T \boldsymbol{r}, \tag{IV.22}$$

until an absolute tolerance of $|\Omega_{k+1} - \Omega_k| < 10^{-12}$ is reached. The vector of residuals for our objective function is

$$\boldsymbol{r} = \left(\sqrt{w_1/N}\, ||\boldsymbol{x}_{d,1} - \boldsymbol{x}_{c,1}||, \ldots, \sqrt{w_N/N}\, ||\boldsymbol{x}_{d,N} - \boldsymbol{x}_{c,N}||, \sqrt{\kappa}\, \overline{U} \right)^T. \tag{IV.23}$$

The augmented Jacobian of residuals $J = \partial \boldsymbol{r} / \partial \boldsymbol{\alpha}'$ is computed using a forward finite difference approximation, and the damping parameter $\lambda > 0$ is updated using a trust region prediction ratio framework. We should note that Equation IV.19 represents a simultane-

ous iterative optimization of both rigid and nonrigid components of the registration. With this approach, some effects associated with rigid body rotation that can compromise linear models are diminished. Conventionally, these effects are usually compensated by a corotational finite element formulation [164], which accounts for local rotational effects at the element level. In the algorithm above, instead, the bulk rotation is determined per iteration. The advantage to this approach is that precomputation of a set of model solutions is still enabled.

IV.4.4.5 Model Relaxation

As previously discussed, due to the use of control point perturbations, model-reconstructed deformations may encounter local inaccuracies around the immediate vicinities of the applied perturbations. These artifacts may appear within the support surface regions that are represented by the control points in place of more complete distributed loads, although their influence rapidly vanishes with distance. To diminish their effect in the near-field, we have developed a model relaxation step that consists of a forward model solution to Equation IV.7 with boundary conditions consisting of a partial solution to the optimized model correction computed in Section IV.4.4.4. The solved displacements at surface nodes that do not belong to a support surface are applied directly as Dirichlet boundary conditions while the remaining surface nodes near the control points are left unconstrained. This step serves to relax the solutions over the support surfaces to the most stable model-predicted distributed loads that produce the far-field response best matching the intraoperative data. As a result, the displacement solutions over the support surfaces are not required to be of any specific functional form, such as the truncated bivariate polynomial used by Rucker *et al.*

	Preop	Lap14mmHg	Lap7mmHg	Open
Preop	0	10.1 ± 5.9	9.0 ± 7.0	6.4 ± 4.6
Lap14mmHg	—	0	6.4 ± 2.6	6.6 ± 3.3
Lap7mmHg	—	—	0	6.3 ± 2.5
Open	—	—	—	0

Table IV.1: MHD (mean $\pm$ std) in mm between preoperative, laparoscopic, and open operative conditions. The shape changes associated with each sequential step in the laparoscopic-to-open conversion appear along the first diagonal. The cumulative shape change relative to the preoperative organ is shown in the top row.

IV.5 Experimental Evaluation

IV.5.1 Evaluation of Intraoperative Deformation

For each patient, MHD was computed between pairs of organ surface data taken from presentations at 14-mmHg insufflation (Lap14mmHg), 7-mmHg insufflation (Lap7mmHg), open (Open) surgical configurations, and the rigidly registered anterior liver surface as segmented from the preoperative CT scan (Preop). Table IV.1 shows the organ surface MHD between preoperative, laparoscopic, and open surgical phases. A series of one-sample t-tests determined that all distributions of MHD were found to significantly differ from zero (all $p < 10^{-5}$; Bonferroni's multiple comparison $\alpha = 0.008$), indicating that substantial shape change occurred between each pair of interrogated operative surfaces. This shows that significant deformation occurs between (a) preoperative and intraoperative phases, (b) laparoscopic and open surgical approaches, and (c) standard and reduced levels of insufflation pressure. This last statement is especially important because it strongly suggests that insufflation has a significant impact on laparoscopic deformation of the liver.

In examining the relative magnitudes of deformation between each operative transition using paired t-tests, we find that the MHD in the initial transition from the preoperative to laparoscopic organ configuration is significantly larger than subsequent intraoperative changes where insufflation pressure is lowered ($p = 0.0012$) or where the surgical approach is converted to open ($p = 0.0011$). Meanwhile, the differences in MHD associated with lowering insufflation pressure and converting to open are similar ($p = 0.76$). This sug-

gests that the largest proportion of intraoperative deformation is associated with the initial preoperative-to-intraoperative transition, coinciding with the timing of when preoperative surgical plans would be needed to determine resection planes.

We also find that in comparison with the preoperative liver shape, the magnitude of laparoscopic deformation significantly exceeds the magnitude of open deformation ($p = 0.0019$). This finding suggests that laparoscopic deformations have the potential to compromise surgical guidance to a potentially greater degree than the deformations associated with open surgery. Figure IV.4 shows three representative distributions of closest point distance error between preoperative, laparoscopic, and open organ shapes. Compared with the preoperative organ, laparoscopic deformation tends to produce more flattening of the right lobe than does open.

Our efforts to use the laparoscopic phantom setup described in Section IV.4.2 for validation are contingent on accurately replicating intraoperative deformation of the liver. Laparoscopic-to-open conversion was also simulated in the phantom for comparison of our applied deformation with clinically observed 95% confidence intervals. Open phantom deformation was imposed by removing all supporting ligaments and packing material beneath the left and right lobes to simulate typical intraoperative placement of laparotomy pads. We note that the confidence intervals of laparoscopic deformation are comparable to the porcine insufflation landmark error ranging between 5.8 and 11.5 mm reported by Johnsen *et al.* [130] and the open surgery surface error ranging between 5 and 20 mm reported by Clements *et al.* [122]. As shown in Table IV.2, our phantom performs similarly to clinical behavior as demonstrated by magnitudes of laparoscopic and open deformation within the clinical confidence intervals. Our mock abdomen setup is designed to emulate a constant insufflation pressure that causes distension of the abdominal cavity and subsequent tension on the ligament attachments. Therefore, it is reasonable that the laparoscopic magnitude of deformation in our phantom is more consistent with 7-mmHg than 14-mmHg insufflation pressure. We do recognize that additional effects, such as the presence of am-

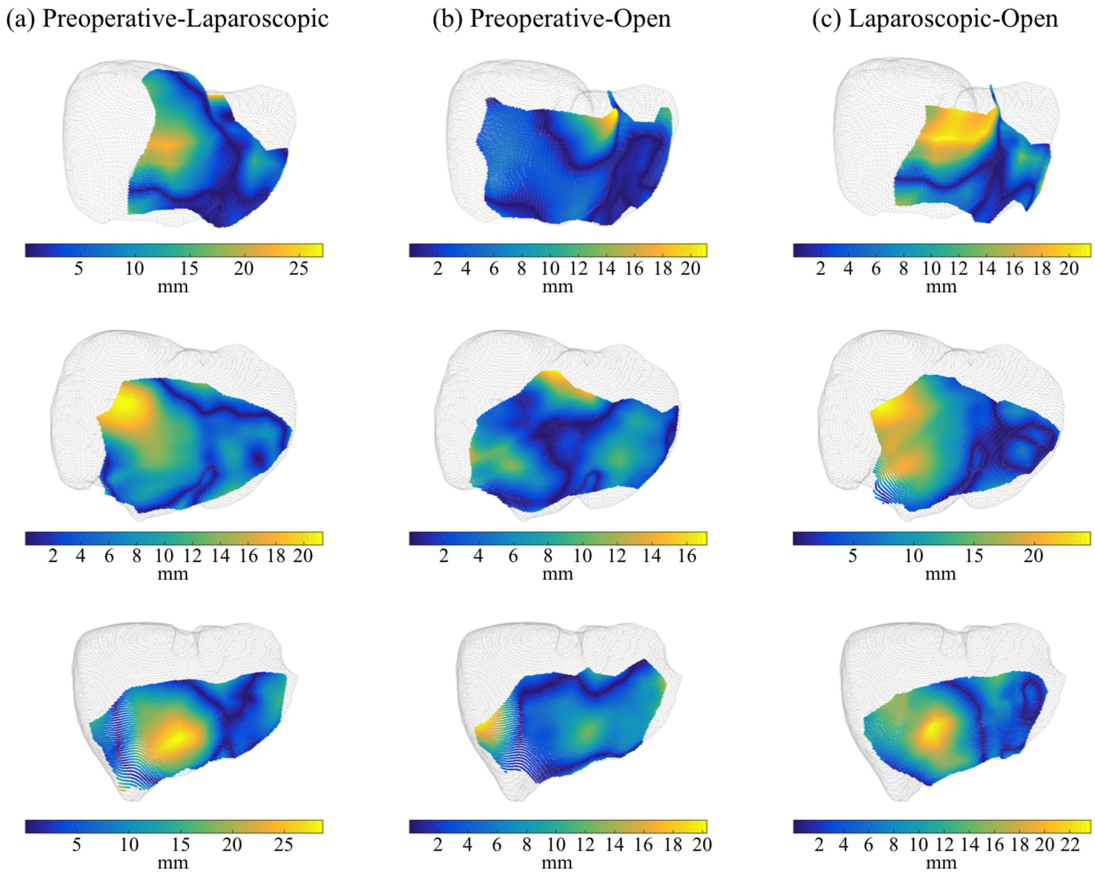

Figure IV.4: Reconstructed closest point distance error from three representative cases among the $n = 25$ between (a) preoperative and laparoscopic surfaces, (b) preoperative and open surfaces, and (c) laparoscopic and open surfaces.

	Clinical CI	Phantom
Lap14mmHg	[7.7, 12.6]	6.9
Lap7mmHg	[6.2, 11.9]	
Open	[5.5, 9.3]	8.6

Table IV.2: Confidence intervals [LB, UB] in mm for preoperative-to-intraoperative MHD shape changes from the clinical series of laparoscopic-to-open conversion. MHD for respective changes in our phantom validation setup is also presented to provide a sense for the fidelity with which intraoperative deformation is reproduced.

bient insufflation pressure on the organ, may contribute additional deformation beyond the capabilities of our phantom setup. However, this is expected to be of secondary importance because the total force applied to the exposed surface area of the liver is much smaller than the total force applied to the entire abdominal cavity, subsequently transmitted to the liver via ligament attachments.

IV.5.2 Evaluation of Deformation Correction

We evaluate our nonrigid registration algorithm in a series of experiments that use the phantom and clinical data acquired in Sections IV.4.1 and IV.4.2. These experiments include: (1) phantom comparison of the proposed nonrigid registration method with the method reported by Rucker *et al.,* (2) comparison of local surface correction in clinical and phantom datasets, and (3) the effect of surface data extent on subsurface registration accuracy.

IV.5.2.1 Comparison of Registration Methods

The three mobilization scenarios of the phantom were registered using intraoperative surface data collected through a port at the umbilicus by three methods: (a) the salient feature-weighted rigid registration by Clements *et al.* [121], which is used to initialize both (b) the nonrigid registration method by Rucker *et al.* [2], and (c) our proposed nonrigid control point registration for laparoscopic deformation of the liver. Average TRE over these cases was used to assess overall registration performance for the three methods. Since TRE samples from a spatially varying distribution of the underlying error, the proximity

Phantom Deformation	Rigid Registration: Clements *et al.*	Nonrigid Registration: Rucker *et al.*	Nonrigid Registration: Control Point Supports
Left Mobilization	13.2 ± 2.6	7.1 ± 3.5	5.9 ± 4.3
Right Mobilization	16.2 ± 6.7	8.0 ± 5.5	7.0 ± 4.6
No Mobilization	14.7 ± 6.5	8.5 ± 3.9	6.2 ± 4.1

Table IV.3: TRE (mean $\pm$ std) in mm for simulated mobilization conditions of the phantom after rigid and nonrigid registration.

of targets to known data and the uniformity of their density can affect the observed TRE. Furthermore, TRE may also depend on the amount of applied deformation. We attempt to minimize target selection bias by considering a large number of target positions dispersed evenly throughout the volume of the phantom (Figure IV.1c) and provide a reference for our reported TRE by characterizing the amount of deformation experienced by the phantom (Table IV.2).

TRE for the rigid and nonrigid registration methods is shown in Table IV.3 and qualitative registration results are shown in Figure IV.5. Across the three mobilizations of the phantom, rigid registration on average produced TRE of 14.7 ± 1.2 mm. The nonrigid correction method by Rucker *et al.* reduced average TRE to 7.9 ± 0.6 mm, representing a 46.3% improvement. On the other hand, the laparoscopic nonrigid registration method proposed in this work reduced TRE to 6.4 ± 0.5 mm, representing a 56.5% correction over rigid registration. Our proposed correction method performed 19.4% better on average ($p = 0.044$, two-sample t-test) than the method by Rucker *et al.* for deformations produced in the laparoscopic phantom setup. This improvement speaks toward the contributions of modeling the intraoperative load applied to ligaments, which are not accounted by Rucker *et al.,* and reformulating the application of boundary conditions to make no incorrigible assumptions about the spatial profile of displacement on the support surfaces.

Figure IV.6a demonstrates the shift in the observed distribution of target error between rigid and the proposed nonrigid registration methods for a representative case. Figure IV.6b shows the distribution of target error after nonrigid registration within the phantom. It can be seen that target error tends to increase with distance away from intraoperative data.

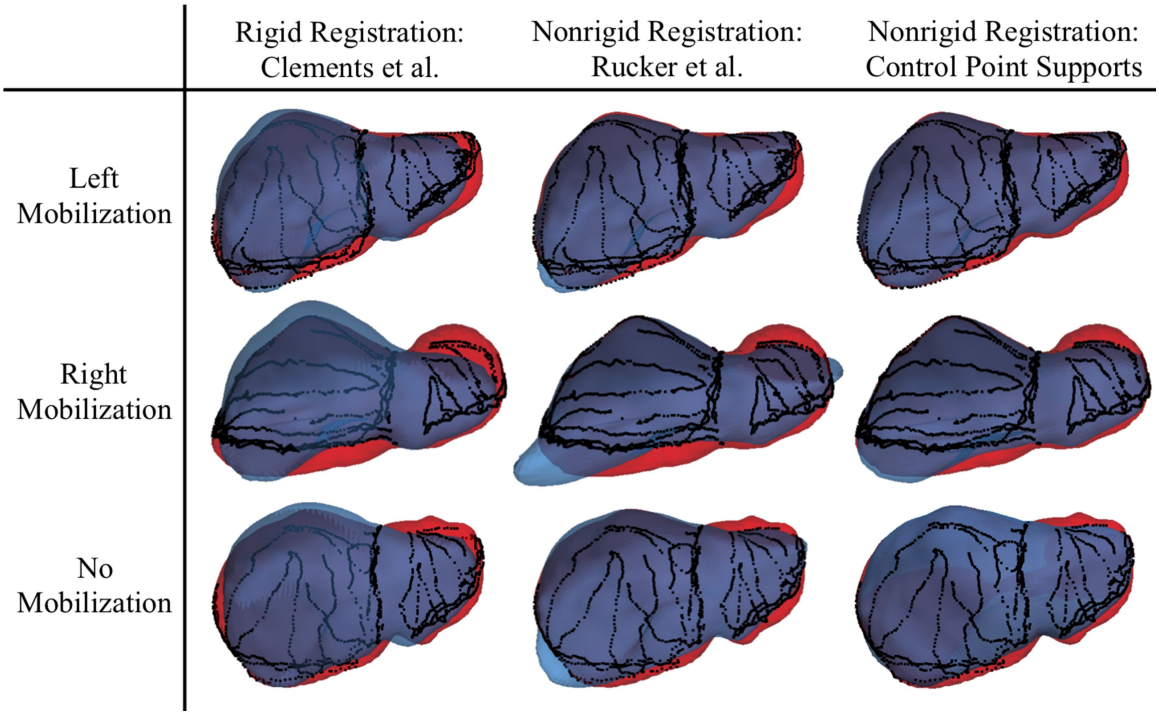

Figure IV.5: Registered preoperative liver (blue) in comparison with the ground-truth intraoperative organ shape (red) for each organ deformation and registration technique. The sparse intraoperative data used to perform the registrations are overlaid in black. Attaining perfect alignment is challenging due to incomplete coverage of the intraoperative surface data.

Furthermore, the spatial dependence of error in these results demonstrates the need for thorough sampling when evaluating target error.

IV.5.2.2 Comparison of Surface Correction

We explore clinical feasibility of our deformation correction approach through evaluating and comparing surface error in the phantom and in a retrospective analysis of the laparoscopic-to-open conversion series. Although surface error as a metric leaves much to be desired due to uncertainty in surface correspondence and insensitivity to subsurface registration accuracy, appropriately measuring target error in clinical data is burdensome due to intraoperative imaging requirements. To reduce the impact of surface digitization noise and irregular spatial weighting of points, we use a reconstructed intraoperative surface from sparse data to ensure that the surface correction measure evenly weights error across the entire area of surface coverage.

Figure IV.7 shows the surface registration error for rigid registration in comparison with our laparoscopic deformation correction method. We consistently obtain low surface errors below 2 mm in all intraoperative organ configurations. Compared with rigid, the nonrigid correction algorithm reduced surface error from 9.3 ± 5.4 mm to 1.4 ± 0.6 mm for standard insufflation pressure (Lap14mmHg), from 7.0 ± 4.6 mm to 1.4 ± 0.5 mm for reduced insufflation pressure (Lap7mmHg), and from 5.2 ± 2.0 mm to 1.1 ± 0.4 mm for open registration. Surface error for laparoscopic registrations of the phantom decreased from 5.5 ± 2.2 mm to 0.8 ± 0.4 mm after nonrigid correction. These reductions correspond to surface corrections of $84.8\% \pm 6.1\%$ for Lap14mmHg, $80.1\% \pm 7.0\%$ for Lap7mmHg, $78.7\% \pm 8.4\%$ for open organ configuration, and $85.4\% \pm 7.3\%$ for the phantom. While future subsurface validation work using intraoperative imaging is needed, these results show promise of our algorithm toward laparoscopic deformation correction in prospective clinical use.

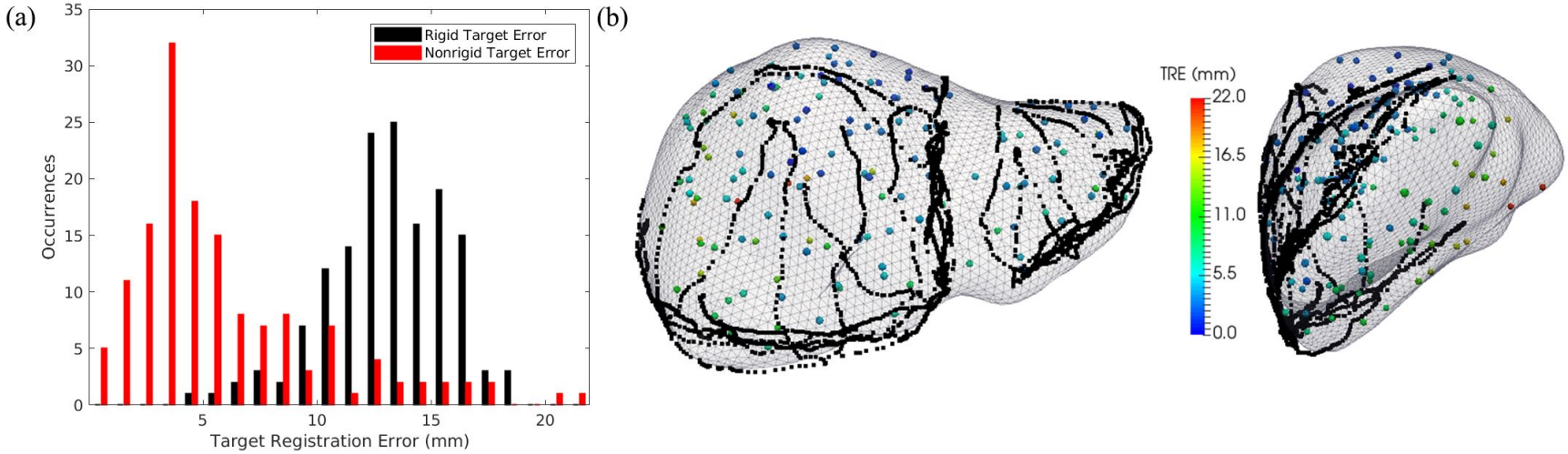

Figure IV.6: Target error for Left Mobilization. (a) Histogram of target registration error for rigid and nonrigid registrations. (b) Distribution of target errors after nonrigid registration throughout the phantom. Intraoperatively digitized organ surface data is shown in black.

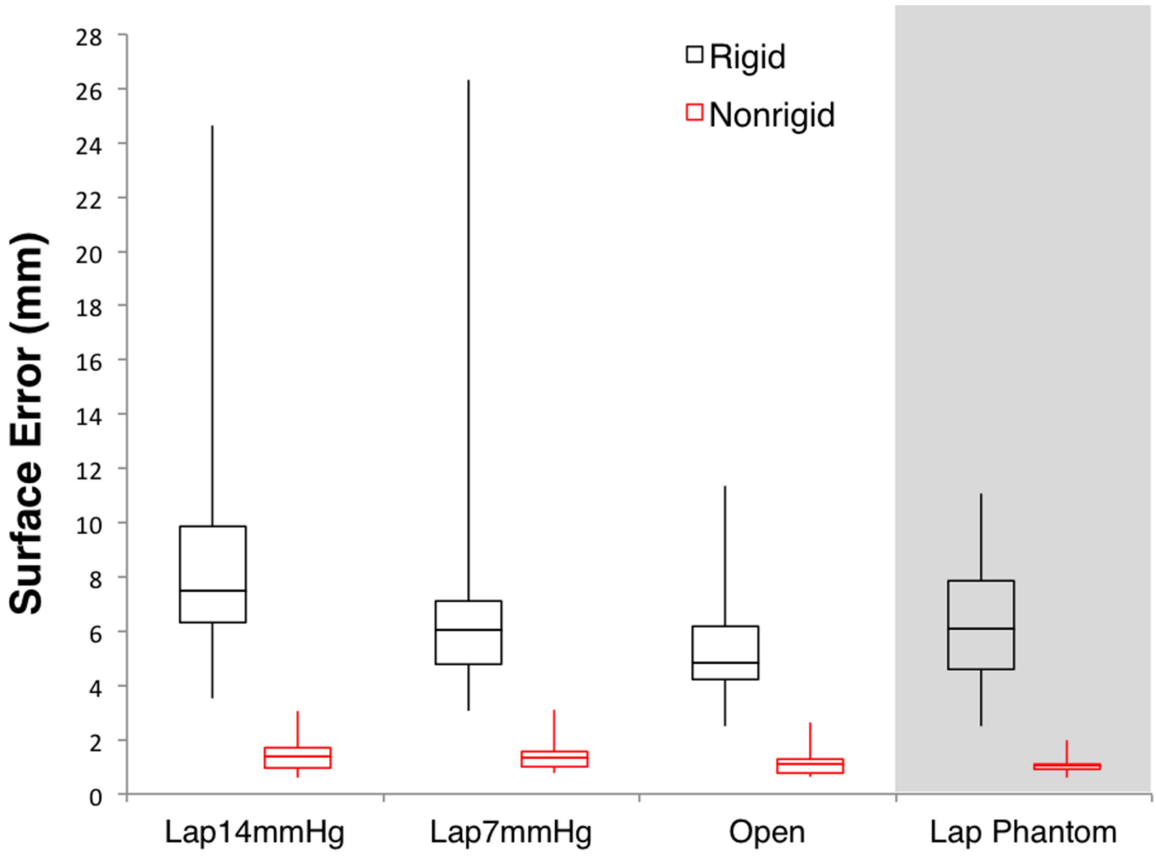

Figure IV.7: Surface correction quartiles are shown for rigid and nonrigid registrations to each series of laparoscopic and open organ configurations. The gray panel displays the distribution of surface correction among all intraoperative phantom mobilizations and surface data extents.

IV.5.2.3 Impact of Surface Data Extent

As shown in Figure IV.8a, the amount of organ surface coverage from intraoperative sparse digitizations can be highly variable. For each intraoperative surface collection, we quantify the extent of organ surface coverage as the percentage of boundary nodes on the liver model contained within an alpha shape constructed around the sparse data. To identify potential sources of variable surface extent, we collected intraoperative surface data through the nine laparoscopic ports placed in the mock abdomen and computed their extents on the phantom as presented in Figure IV.8b. These results indicate that certain ports, especially those placed in the medial right upper quadrant, can produce better extent than more lateral or inferior ports. Across standard and lowered insufflation pressures, the average surface extent from clinical data was $22.0\% \pm 8.2\%$ ($N = 50$). In the phantom, two separate digitization strategies and three different organ mobilizations across nine ports produced an average extent of $20.7\% \pm 8.8\%$ ($N = 54$). Interestingly, the extents of surface data obtained in the open approach were not significantly different, $22.4 \pm 5.4\%$ ($N = 25$). Overall, registration accuracy in the phantom as a function of extent is shown in Figure IV.9. We observe that as surface extent increases, the capability of our proposed deformation correction algorithm improves. At extents greater than 22%, the overall average TRE across all cases was 6.7 ± 1.3 mm, and all individual nonrigid registrations produced average TRE under 10 mm. Plantefève *et al.* [4] also observed similar behavior where nonrigid registration accuracy is superior at extents greater than 20% of the total liver surface. We further show that the extents of typical clinical data acquisitions tend to lie on the cusp of this threshold. It is possible that more deliberate choices in port positioning for data collection may offer straightforward improvements to laparoscopic nonrigid registrations.

IV.6 Discussion

Our registration method is distinct from other mechanics-based correction algorithms that apply boundary conditions derived directly from the positions of intraoperative surface

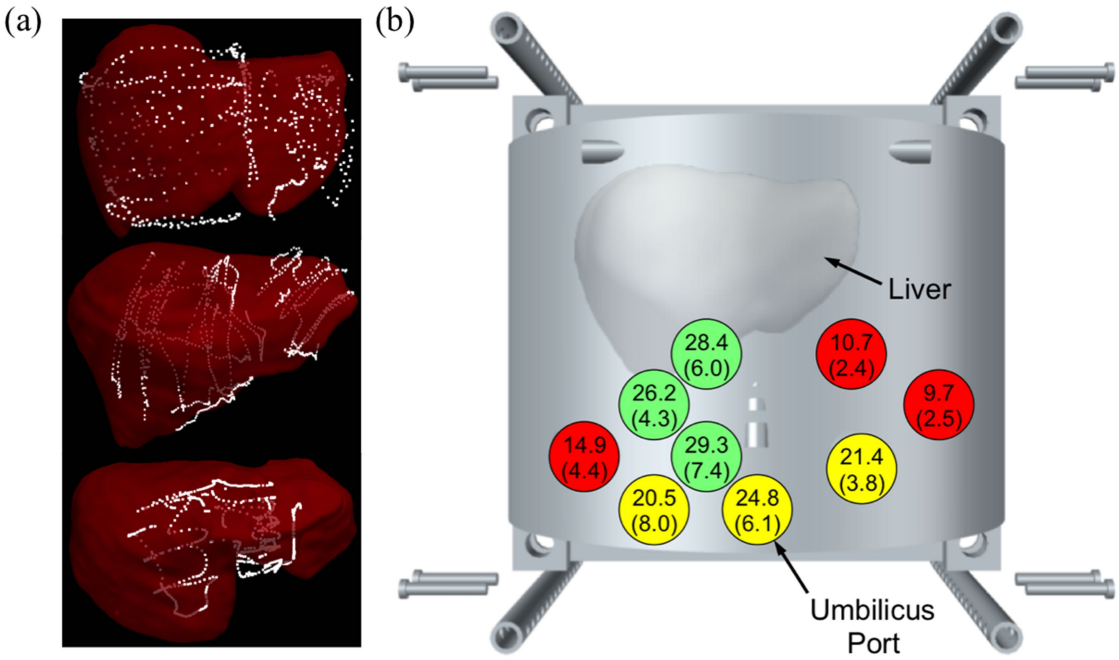

Figure IV.8: (a) Variation in available surface data extents from clinical data: 31% (top), 20% (center), and 11% (bottom). (b) Average surface data extents through each of the nine ports of the phantom, standard deviation in parentheses. Lateral ports colored in red provide average extents of less than 15% of the organ surface. Periumbilical ports in yellow offer moderate extents between 20% and 25%, and ports placed in the medial right upper quadrant yield the best available surface extents, which exceed 25% on average.

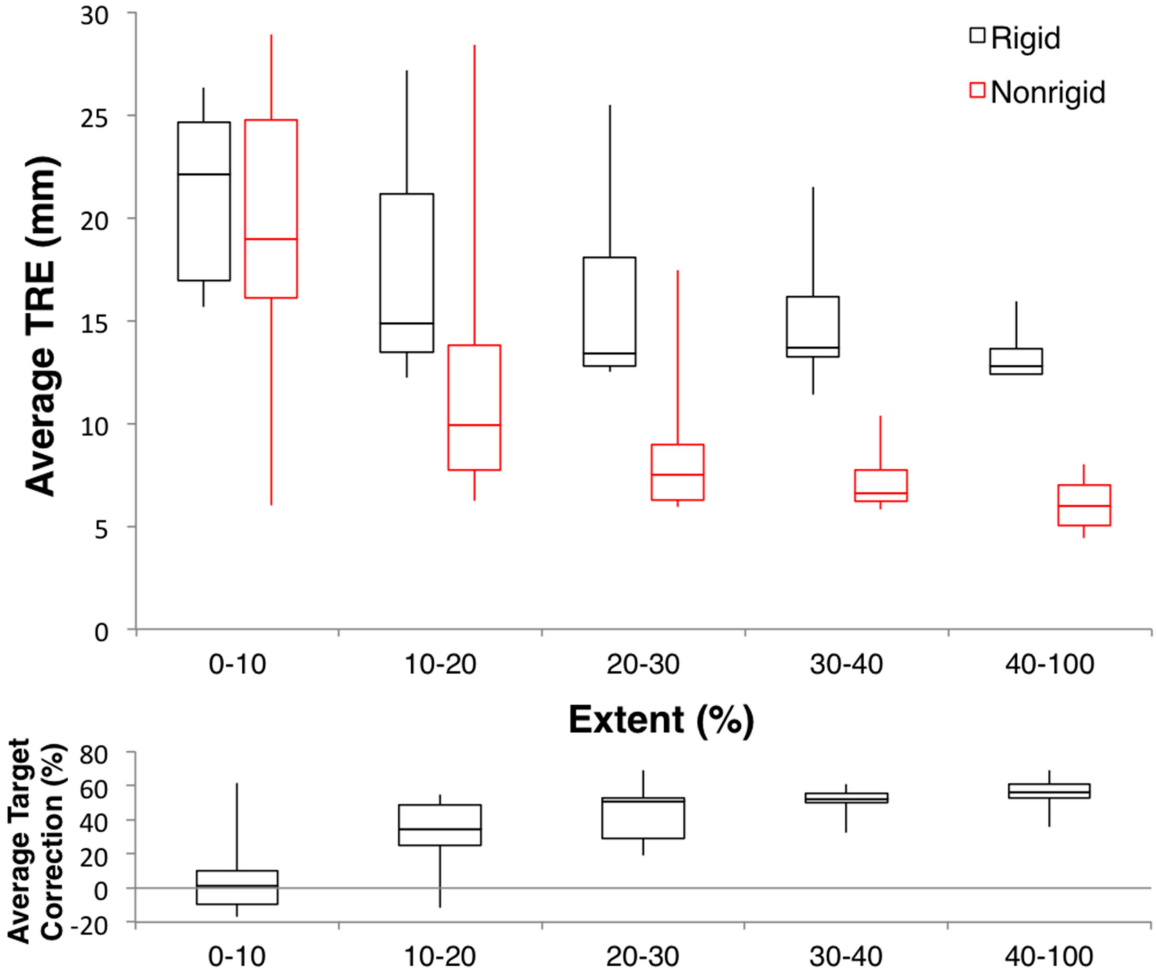

Figure IV.9: Distributions of (a) TRE and (b) target correction with respect to the extent of intraoperative surface data. The box and whiskers represent the median, upper and lower quartiles, maximum, and minimum of TRE. Our nonrigid correction contributes little improvement over rigid registration at extents smaller than 10%. However, at extents greater than 22%, the nonrigid correction algorithm offers a substantial improvement in TRE.

points. Instead, the proposed approach leverages anatomical constraints in such a way that permits only deformations that can be produced by realistic intraoperative changes to the organ. This process is done by (1) identifying support surface regions associated with intraoperative changes to mechanical load, (2) constructing a set of model perturbations based on point load displacements on the support surfaces, (3) registering and reconstructing a configuration of point load displacements from the observed intraoperative surface, and (4) relaxing the model solution. Beyond the current application to laparoscopic liver deformation, this algorithm is generalizable to other deformable soft tissues. A key advantage to the approach is that steps (1) and (2) can be completed preoperatively. Therefore, the intraoperative computational burden only consists of determining an initial rigid registration between the model and intraoperative data, optimizing the control point perturbations, and performing the relaxation step. Without extensive code optimization, the entire intraoperative registration can be performed within 140 to 320 s on a single thread using a 4.0-GHz Intel Core i7 CPU for a liver model of 30,000 nodes and ~3000 intraoperative data points. However, significant acceleration of the optimization can be expected from parallelizing the closest point correspondence in the objective function or from reducing the tolerance.

In our experience, the choice of a linear model is not a principal source of error for deformation correction in the liver due to the existence of other practical limitations. Noise in data collection, irregular point density, and variable patterns of intraoperative surface digitizations introduce inconsistencies that affect registration outcomes. Scarcity of definitive hepatic features that could offer correspondence between intraoperative digitizations and the model surface is an additional barrier to achieving accurate registration. Furthermore, incomplete surface data extents that leave regions of the model unconstrained also limit overall registration accuracy. While we attempt to alleviate some of these challenges in this work through employing data resampling and salient feature weighting in the objective function of Equation IV.21, these solutions do not fully resolve these issues and generally leave the problem ill-posed. However, the use of a linear model is unlikely to

be ideal, and efficient nonlinear treatments [164, 165] could be explored in future work to further improve registration accuracy. Another important aspect would be the incorporation of heterogeneities, such as the major vascular branches within the liver. It is likely that vessel-to-tissue interaction would alter the volumetric behavior of our model.

In our registrations, we find that the distance between an individual target and the closest surface data point used to perform the registration is moderately correlated with the individual TRE (Pearson's $r = 0.58$; 99% CI: 0.56 to 0.60). We expect that regions more distant from intraoperative surface data are prone to less accurate registration due to lack of model specificity. Ideally, errors below 5 mm across the volume of the liver would be desirable for guidance of hepatic resections. While surface error can be locally corrected past this threshold as shown by Figure IV.6, comprehensive analysis of TRE across the full volume of the liver indicates that targets farther from anterior surface data tend to perform more poorly in areas that are inadequately constrained due to a paucity of intraoperative data. Further, with the magnitude of laparoscopic deformations exceeding those of open, it is likely more challenging to achieve TRE below 5 mm across the volume of the liver under laparoscopic operative conditions. Currently, the clinical data extent is sufficient to achieve corrections with less than 10 mm of error, which may be considered adequate though not ideal. It is reasonable to expect that increasing surface extent or incorporating subsurface data into the registration workflow could improve registration by increasing the reach of intraoperative data constraints. Future work will involve the development of methods to expand intraoperative data extent through improvements to noncontact methods of laparoscopic surface acquisition and the integration of tracked intraoperative ultrasound for the purpose of validating registration error *in vivo* and as a potential source of subsurface constraints for further improving laparoscopic deformation correction methods.

IV.7 Conclusions

In this paper, we present an analysis of the extent of liver deformation among preoperative, laparoscopic, and open presentations as well as a technique for correcting deformation during image-guided laparoscopic liver surgery. Our analysis of deformation revealed that the most severe shape differences exist between preoperative and intraoperative presentations under routine insufflation conditions, which may compromise the planning stages of laparoscopic surgery. To compensate for this soft tissue deformation, we propose a correction algorithm that leverages anatomically load-bearing support surfaces of the liver to enforce model constraints and demonstrates superior deformation correction than previous realizations. Finally, we perform extensive studies to understand the influence of data coverage extent in both the phantom and clinical settings. We propose that image-guided laparoscopic liver surgery is achievable in practice with current techniques and careful consideration of the particular challenges introduced by the laparoscopic approach.

Acknowledgements

This work has been supported by the National Institutes of Health (NIH) under Grant No. R01-CA162477 and the NIH-National Institute of Biomedical Imaging and Bioengineering training Grant No. T32-EB021937. We also would like to recognize the Vanderbilt University Medical Center Radiology Support Core for their assistance with imaging in our phantom study.

CHAPTER V

Subsurface Registration via Linearized Iterative Boundary Reconstruction

V.1 Summary and Contributions

In Chapter IV, an analysis of deformable registration performance was characterized across varying extents of surface data provided to the registration method. In this chapter, tracked intraoperative ultrasound is incorporated with a novel deformable registration approach to obtain subsurface data for improving the accuracy of registration beyond the capability possible with only surface measurements. This work is the first to incorporate iUS data with model-based deformable registration of the liver. An extensive characterization of registration performance was performed with respect to the amount of iUS data provided, and clinical validation on three patients was performed to demonstrate how clinical tracked iUS data can be applied to improve the accuracy of registration while operating within clinical workflow constraints.

In addition to characterizing tracked ultrasound as a new data source for model-based liver registration, a novel registration technique is introduced. This chapter introduces the linearized iterative boundary reconstruction method, a general algorithm for deformable soft tissue registration. This approach solves for an unknown load distribution that would have been applied to an organ between preoperative and intraoperative configurations based on sparse surface and subsurface information provided. This method includes a number of technical features such as a reconstructive framework based on the Saint-Venant principle, representations of subsurface error constraints, closed form gradient computations, and linearization that allows rapid solutions to the registration problem. Beyond the validation presented in this chapter, improvements to registration accuracy using these methods are further characterized in a public dataset released by our research group to provide the reg-

istration community with a common benchmarking and validation platform. These details are provided in Appendix B.

This chapter further presents a simulation framework that combines known displacement fields with novel liver geometries and clinical patterns of data collection to generate vast combinations of registration scenarios for more extensive validation of registration algorithms against known ground truths. This simulation framework has allowed this work to leverage the largest dataset for testing deformable registration methods reported to date, in which accuracy of registrations can be evaluated across a comprehensive range of possible inputs. This chapter utilizes this simulation framework to evaluate data requirements for achieving accuracy benchmarks for deformable registration using the linearized iterative boundary reconstruction method. An extension of this work is included in Appendix C, where simulated data from this framework are used again to identify the relative importance of individual types of subsurface feature constraints contained within tracked iUS image planes. Overall, the combined developments in this chapter represent significant advances towards new approaches to surpass current clinical, methodological, and validative barriers to achieving highly accurate image-to-physical registrations.

Intraoperative Correction of Liver Deformation Using Sparse Surface and Vascular Features via Linearized Iterative Boundary Reconstruction

The work presented in this chapter appears in and is reprinted with permission from,

[20]: J. S. Heiselman, W. R. Jarnagin, and M. I. Miga, "Intraoperative Correction of Liver Deformation Using Sparse Surface and Vascular Features via Linearized Iterative Boundary Reconstruction," *IEEE Transactions on Medical Imaging*, vol. 39, no. 6, pp. 2223–2234, 2020. (© 2020 IEEE)

V.2 Abstract

During image guided liver surgery, soft tissue deformation can cause considerable error when attempting to achieve accurate localization of the surgical anatomy through image-to-physical registration. In this paper, a linearized iterative boundary reconstruction technique is proposed to account for these deformations. The approach leverages a superposed formulation of boundary conditions to rapidly and accurately estimate the deformation applied to a preoperative model of the organ given sparse intraoperative data of surface and subsurface features. With this method, tracked intraoperative ultrasound (iUS) is investigated as a potential data source for augmenting registration accuracy beyond the capacity of conventional organ surface registration. In an expansive simulated dataset, features including vessel contours, vessel centerlines, and the posterior liver surface are extracted from iUS planes. Registration accuracy is compared across increasing data density to establish how iUS can be best employed to improve target registration error (TRE). From a baseline average TRE of 11.4 ± 2.2 mm using sparse surface data only, incorporating additional sparse features from three iUS planes improved average TRE to 6.4 ± 1.0 mm. Furthermore, increasing the sparse coverage to 16 tracked iUS planes improved average TRE to 3.9 ± 0.7 mm, exceeding the accuracy of registration based on complete surface data available with

more cumbersome intraoperative CT without contrast. Additionally, the approach was applied to three clinical cases where on average error improved 67% over rigid registration and 56% over deformable surface registration when incorporating additional features from one independent tracked iUS plane.

V.3 Introduction

In nearly every treatment option for hepatic cancer, therapeutic risk and efficacy balance on the ability to accurately localize the intraoperative positions of anatomical structures and interventional targets. Surgical resection of the liver, which remains the best curative option for hepatic malignancies aside from transplantation, must be carefully planned with respect to the positions of tumors and vessels hidden beneath the surface of the organ. This planning stage is essential for ensuring adequate margins, maximizing volume and blood perfusion in the liver remnant, and minimizing risk of hemorrhage and biliary injury. However, in open and laparoscopic liver surgery alike, intraoperative deformation of the liver is unavoidable due to procedural aspects such as hemostatic perihepatic packing in open approaches, abdominal insufflation in laparoscopic approaches, retraction, and mobilization from stabilizing ligaments. These deformations can compromise intraoperative translation of surgical plans that are based on the preoperatively imaged anatomy. Significant deformations of the liver have been shown to exist between preoperative and intraoperative presentations during both open and laparoscopic surgery. In a previous study, the average magnitude of these preoperative-to-intraoperative deformations across the anterior surface of the liver were found to exceed 10 mm during laparoscopy and 7 mm during open surgery, with maximum values greater than 20 mm [9].

Various methods have been developed to compensate for intraoperative deformation of the liver in the context of image guidance, where information derived from the preoperative anatomy is updated to match the intraoperative conformation of the organ through registration techniques. Beyond rigid registration, biomechanical models based on linear

elasticity have proven to be well suited for deformable registration due to a favorable compromise between registration accuracy, computational time complexity, and intraoperative time constraints. While elastic registration methods based on organ surface data collected in the operating room are becoming more common [1, 2, 4, 6, 7, 9, 10, 22], the type and algorithmic treatment of intraoperative data sources in the registration process is becoming equally important with regard to alignment fidelity [111]. In particular, the accuracy of surface-based methods has been found to depend crucially on the amount of intraoperative data made available for registration; previous work has suggested that registration accuracy can improve if wider coverage of the liver surface can be measured [1, 4, 9]. However, limited field of view in the surgical environment can directly conflict with the goal of acquiring broad surface coverage. Whereas intraoperative volumetric imaging such as cone beam CT has been proposed to offer more complete intraoperative data for the registration task [8, 116], these approaches are costly, require specialized facilities, present a major disruption to existing surgical workflow, and are unlikely to reach the capability of updating in real time at the speed of intraoperative organ interactions.

Tracked intraoperative ultrasound offers the real-time ability to identify features at depth inside the liver and represents a powerful contribution in the image guidance toolkit. Already, intraoperative ultrasound (iUS) is commonly used during liver resection to stage disease, identify lesions invisible on CT, and determine relationships to the vascular and biliary anatomy [34]. However, due to a confluence of factors that can make lesions sonographically occult, iUS is not yet suitable as a comprehensive guidance solution and needs to be complemented by information from preoperative imaging assessments [92]. Although interpreting and localizing freehand iUS can be challenging, tracked iUS adds quantitative spatial understanding to the physical positions of features that are visible in the ultrasonic modality even if the lesion is unapparent. These features can reliably include contours of the portal and hepatic veins and the posterior surface of the liver if imaged at sufficient depth. This capability makes it possible to use subsurface features from tracked iUS as ad-

ditional constraints to improve registration accuracy beyond the capacity offered by surface data alone.

Several groups have developed methods to register iUS data with preoperative CT or MR images. Early spline methods matched 3D iUS volumes with image intensities based on similarity metrics such as normalized cross correlation [11, 12], linear combination of linear correlation [13], edge-intensity joint entropy [15], and local structure orientation descriptors [18]. However, many of these registration techniques were designed for percutaneous procedures where small deformations and good initial alignments were possible. To accommodate larger deformations, Lange *et al.* parameterized vessel features between CT and 3D iUS volumes as centerline representations to assist optimization of a thin plate spline deformation model based on a normalized gradient field image similarity measure [14]. However, registration by inter-modality similarity metrics can be slow and may not exactly match differential tissue responses to distinct imaging physics. Additionally, spline models of deformation may not produce registrations as accurate as their biomechanical counterparts [166]. More recent iUS registration methods have elected to forego image intensity information and instead relate preoperatively segmented geometric features such as vessel contours and centerlines to tracked iUS in sparse configurations where rapid intraoperative segmentation of ultrasound features becomes possible. Among these, only rigid registration techniques using vessel centerlines [17], a combination of centerlines and surface data [16], and centerline bifurcation landmarks [136] have been developed. While iUS features have been used for intraoperative validation of surface registration methods [5], deformable liver registration based on biomechanical models have yet to incorporate iUS as an intraoperative data source.

Accurate alignment of the organ surface does not guarantee a successful registration. The internal displacement field between the modeled anatomy and the true deformed state must also be accurate throughout the volume. Mechanics-based models, unlike interpolative spline methods, ensure that these fields develop realistically according to constitutive

laws of physics and their applied boundary conditions. However, mechanics-based methods are not without potential shortcomings. For example, some approaches treat intra-operative data sources as boundary forces [1, 4, 6, 10] or boundary displacements [132, 133] directly on the organ. When employed this way, these configurations of boundary conditions impart organ deformation at the sites of data collection as opposed to the regions where actual mechanical loads are applied. With the underlying sources of deformation largely ignored, these methods may not develop accurate displacement fields beyond the immediate region of data collection. These limitations have given rise to methods that commit particular attention to anatomical constraints [7], data-constrained energy minimization [8], and inverse modeling approaches that reconstruct the unknown distributed loads applied to the organ [2, 9]. In practice, due to the many forms of physical and temporal intraoperative constraints, it is also imperative that these registration methods are simultaneously fast and robust.

In this paper, a generalized algorithm is presented for reconstructing and correcting intraoperative deformation of the liver for improving registration accuracy during hepatic image guidance. While this approach adopts an inverse biomechanical model similar to [9] and [2], a new deformation framework is presented based on the Saint-Venant principle, which states that a local region of mechanical loading can be replaced with a statically equivalent load wherein the difference between loading responses exponentially vanishes with distance towards the far field. Using this principle to decompose elastic perturbations facilitates improved fidelity and robustness, and permits more controlled and realistic deformations of the liver. Other advances include subsurface error constraints that allow registration of internal hepatic features, closed form gradient computations over numerical approximations, and formalized linearization of the boundary reconstruction problem to yield a method that rapidly approximates intraoperative deformations with high accuracy given sparse intraoperative data. Equally important to presenting this novel approach, this paper demonstrates how clinical tracked iUS data can be applied to achieve a high

performance registration algorithm. In accordance with these contributions, a rigorous experimental framework has been produced that involves a combination of physical and simulation data in a controlled environment of 6,291 simulated registration scenarios. These data represent multiple liver geometries, multiple deformations, and varying amounts of sparse surface and subsurface feature data from iUS. To study the approach, registration accuracy is characterized across a wide range of sparse subsurface data configurations. Finally, a proof-of-concept experiment is illustrated with three clinical cases to demonstrate viability.

V.4 Proposed Algorithm

V.4.1 Overview of the Registration Task

Given a preoperative model of the hepatic anatomy, the registration task is to determine a displacement field that produces an optimal alignment of the preoperative model to the deformed conformation of the intraoperative physical liver. This preoperative model is comprised of triangulated meshes for the hepatic parenchyma, portal vein, and hepatic vein generated from custom surgical planning software [21]. Centerline representations of the preoperative portal and hepatic veins are created with the open source Vascular Modeling Toolkit [167], and a tetrahedral finite element mesh of the liver parenchyma is produced with a custom mesh generation software [146]. Tetrahedral meshes are discretized to 4 mm edge length and consist of approximately 25,000 vertices for a typical liver.

In a liver navigation system [100], sparse intraoperative data of the organ surface is collected using an optically tracked stylus and sparse subsurface data from tracked iUS imaging. The tracked iUS setup consists of an Aloka T-probe transducer (Hitachi Aloka Medical Ltd., Wallingford, Connecticut) attached to an optically tracked rigid body calibrated using the N-wire phantom method [168]. Experiences with this tracked iUS system have already been reported in [5] and [24]. New to this work, intraoperative positions of the portal and hepatic vein contours and the posterior surface of the liver are segmented from

iUS image planes when visible, using lines drawn on a graphical display and rasterized into points via the Bresenham line algorithm [169]. Vessel centerline points are approximated as in-plane centroids of the segmented vessel contours. To minimize intraoperative workflow burden, it is important to note that only a handful of iUS planes are used. With rigid registration as the current FDA-approved standard for image guidance during liver procedures, a salient feature weighted iterative closest point rigid alignment [121] is established between the intraoperative organ surface data and the preoperative model for initialization.

From this initial rigid alignment, the proposed algorithm aims to reconstruct an initially unknown set of boundary conditions representing the intraoperative deformations experienced by the organ by using sparse surface and subsurface measurements. The overall registration approach is depicted in Figure V.1 and is described in more detail in the following sections.

V.4.2 The Boundary Reconstruction Problem

An isotropic linearly elastic finite element model is employed to simulate deformation of the liver. At static equilibrium, linear elasticity is governed by the Navier-Cauchy equations in three dimensions:

$$\frac{E}{2(1+\nu)}\nabla^2 \boldsymbol{u} + \frac{E}{2(1+\nu)(1-2\nu)}\nabla(\nabla \cdot \boldsymbol{u}) + \boldsymbol{F} = 0, \tag{V.1}$$

where E is the Young modulus, ν is the Poisson ratio, $\boldsymbol{u}$ is displacement, and $\boldsymbol{F}$ is applied force. Following [2], the values $E = 2100$ kPa and $\nu = 0.45$ are used. With the Galerkin weighted residual method on linear Lagrange basis functions, this system of partial differential equations can be rewritten as:

$$K\boldsymbol{u} = \boldsymbol{f} \tag{V.2}$$

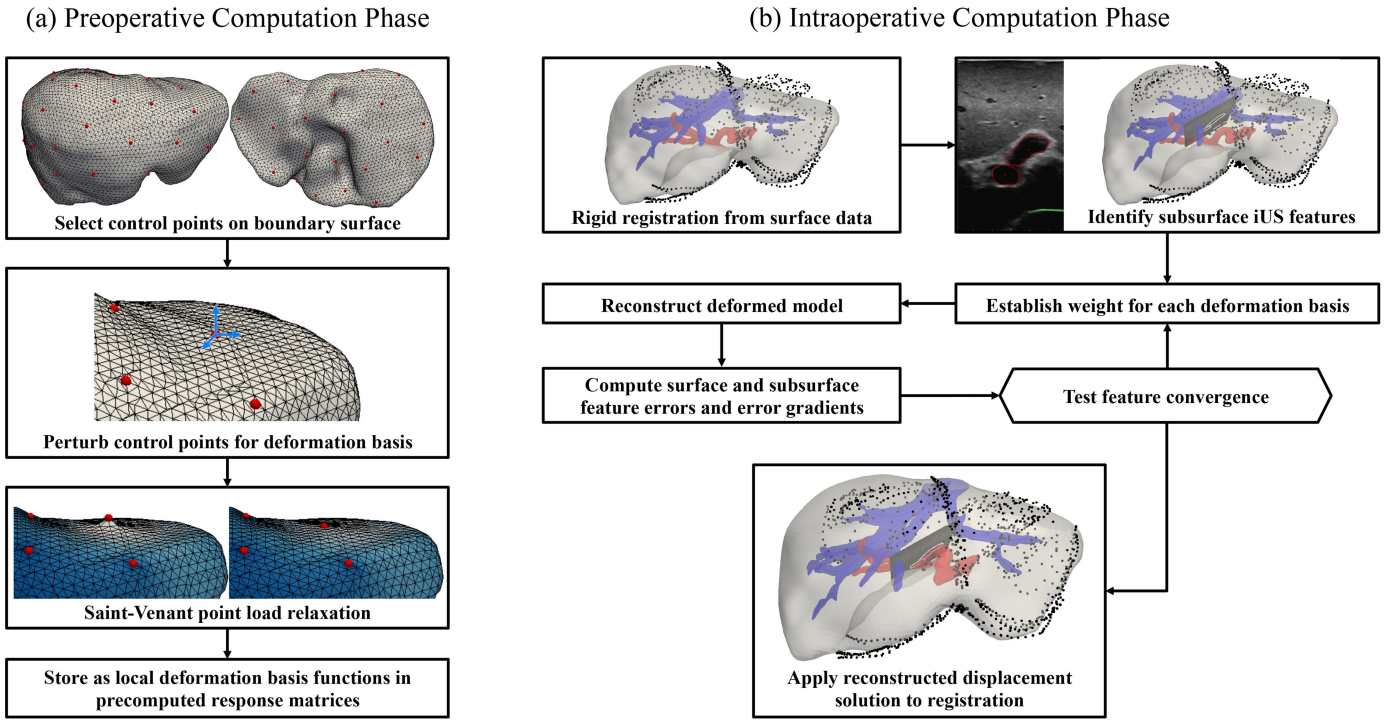

Figure V.1: Overview of the proposed algorithm for boundary condition reconstruction in a deformable registration framework for hepatic image guidance. (a) In the preoperative computation phase, a series of control points are evenly distributed across the surface of the organ. Linear elastic responses to control point perturbations in three orthogonal directions establish a basis of deformations across the mesh. Point loads are then relaxed to their Saint-Venant far field equilibria. These steps are computed in advance of the procedure. (b) Sparse data of the organ surface are collected intraoperatively and a rigid registration between image and physical patient spaces is performed. Features in tracked iUS planes are manually designated and transformed into sparse point clouds. Based on these surface and subsurface points, weights for a linear combination of the precomputed basis deformations are optimized to minimize error between intraoperative data and the deformable model. (© 2020 IEEE)

where K is the global stiffness matrix and $\boldsymbol{f}$ is a vector of known forcing conditions. In the forward boundary value problem, the displacement vectors $\boldsymbol{u}$ throughout the domain can be solved only if displacements and forces on the boundary are known. The inverse boundary reconstruction problem attempts to resolve the distributed loading conditions on the boundary that establish the displacement response $\widetilde{\boldsymbol{u}}$ that best approximates the partially observable true displacement field $\boldsymbol{u}$ without exact spatial correspondence being known.

V.4.3 Linearized Basis of Displacements

By the principle of superposition, a basis of displacements could be constructed such that $\widetilde{\boldsymbol{u}} = {J_u}^* \boldsymbol{\alpha}^*$, where the matrix ${J_u}^*$ represents displacement responses to independent unit displacements of every boundary node in each spatial direction and the vector $\boldsymbol{\alpha}^*$ represents the weight for each basis with length triple the number of boundary nodes. Solving for $\boldsymbol{\alpha}^*$ would represent the full resolution boundary reconstruction problem where every boundary node on the mesh is permitted independent degrees of freedom. However, reconstructing the full resolution problem is not feasible due to computational time constraints and limited information rendering the solution extremely underdetermined.

Dimensionality can be substantially reduced by pruning the reconstructive degrees of freedom to displacements on a subset of control points distributed across the boundary. In this way, the unknown distributed load applied to the domain is approximated as a statically equivalent linear combination of responses to locally consolidated point loads. By the Saint-Venant principle, differences between the deformation responses of the true and the approximated loading configurations quickly vanish with distance. To simulate the basis of localized boundary load responses, control points are evenly spaced on the surface of the mesh using k-means clustering, with $k = 45$. The control points are independently perturbed in each Cartesian direction to generate $3k$ total modes of deformation. Displacement responses for each mode are solved from Equation V.2 by applying a boundary condition with 5 mm displacement in the direction of the active control point perturbation and zero

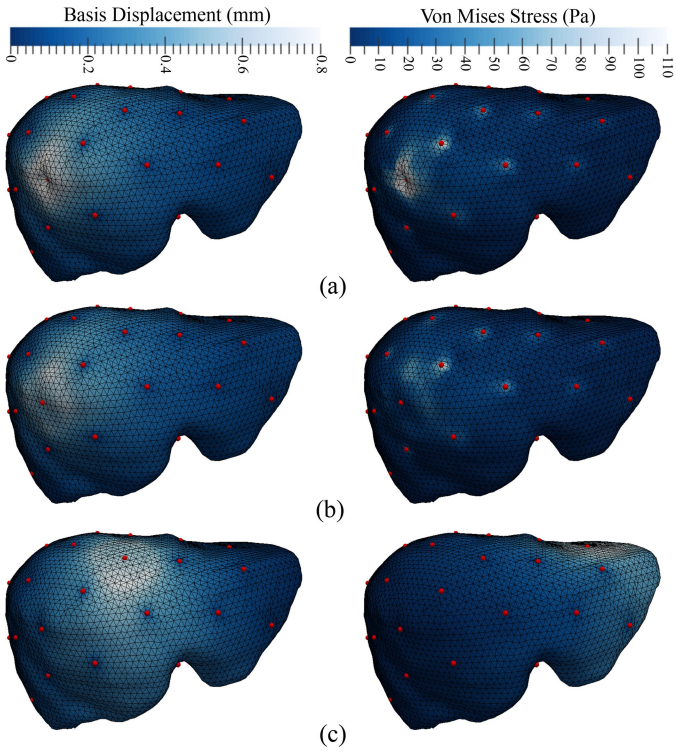

Figure V.2: Control point deformation modes. Control points shown in red are distributed across the surface of the mesh. (a) Displacement response (left) and stress response (right) to a control point perturbation of 5 mm in the +x direction. (b) Displacement response (left) and stress response (right) after Saint-Venant point load relaxation. (c) Relaxed displacement responses for other control point deformation modes on the mesh. Each mode represents a deformation basis in the local vicinity of the control point. (© 2020 IEEE)

displacement boundary conditions at all remaining control points. With each resulting displacement solution, stress and strain are computed from conventional stress-strain and strain-displacement relations for linear elasticity. Figure V.2a shows the displacement and stress responses to one such point load perturbation. However, by focusing the total boundary condition effect from a local neighborhood into a single point, local artifact arises from approximating a smoothly varying distributed load on the surface as a series of point effects. To address these irregularities, point load responses are relaxed back onto to the boundary nodes in the local neighborhood of the control point.

To accomplish relaxation, the Saint-Venant principle is invoked again to determine a statically equivalent load that is redistributed across the locally aggregated boundary re-

gion surrounding the control point. Each point load is relaxed by establishing a radius of half the distance between control points, or equivalently the Voronoi tile of the k-means cluster, and solving Equation V.2 for the self-equilibrated response of the local region when the far field displacement responses of all other boundary nodes are immobilized. The displacement and stress solutions after relaxing the applied point load are shown in Figure V.2b and additional examples of relaxed displacement mode responses for other control point perturbations are shown in Figure V.2c. Each relaxed control point response becomes a mode of variation in the reconstructive basis, representing a spatially local deformation applied to the mesh. For the purpose of reconstruction from sparse data, this approach is beneficial in comparison to more spatially distributed spectral [170] and polynomial [2] function bases that can produce extrapolative error when fitting local data.

With these relaxed responses to control point boundary perturbations, a displacement response matrix J_u is constructed where each column of length $3M$ corresponds to a relaxed displacement solution vector to one of the $3k$ rows of control point perturbations, where M is the number of nodes in the mesh. The relaxed stress and strain solutions for each perturbation response are similarly assembled into the stress response matrix J_σ and the strain response matrix J_ε. With superposition, a reconstructed deformation state that also satisfies Equation V.1 can be linearized as:

$$\widetilde{\boldsymbol{u}} = J_u \boldsymbol{\alpha} \tag{V.3}$$

$$\widetilde{\boldsymbol{\sigma}} = J_\sigma \boldsymbol{\alpha} \tag{V.4}$$

$$\widetilde{\boldsymbol{\varepsilon}} = J_\varepsilon \boldsymbol{\alpha} \tag{V.5}$$

where $\widetilde{\boldsymbol{u}}$, $\widetilde{\boldsymbol{\sigma}}$, and $\widetilde{\boldsymbol{\varepsilon}}$ are the approximated displacement, stress, and strain values for the deformation defined by the relaxed control point response matrices J_u, J_σ, and J_ε, and $\boldsymbol{\alpha}$ is the deformation state vector of length $3k$.

V.4.4 Intraoperative Reconstruction

To solve for the deformation state, Levenberg-Marquardt optimization is employed to iteratively minimize model-data error and the strain energy of the system in a scheme that also optimizes rigid transformation parameters. This optimization of rigid parameters allows a global minimization of element rotations to reduce incurred rotational inaccuracies inherent to linear elasticity. While co-rotational models are sometimes used to compensate, these formulations incorporate geometric nonlinearities that disrupt the superposition leveraged in this application. Hence, the total deformation state to reconstruct is the parameter vector $\boldsymbol{\beta}$ of length $3k+6$ defined as

$$\boldsymbol{\beta} = [\boldsymbol{\alpha},\ \boldsymbol{\tau},\ \boldsymbol{\theta}] \tag{V.6}$$

where $\boldsymbol{\tau}$ is a vector of rigid translations and $\boldsymbol{\theta}$ is a vector of rigid rotations about the x, y, and z axes. These parameters are determined by minimizing the least squares objective function

$$\Omega(\boldsymbol{\beta}) = \sum_F \frac{w_F}{N_F} \sum_{i=1}^{N_F} {f_i}^2 + w_E {f_E}^2 \tag{V.7}$$

where f_i denotes the error between the deformed model and the data point i of N_F total points within an intraoperatively collected point cloud for feature F, w_F is the weight of the feature, f_E is the average strain energy of the deformation state, and w_E is a regularizing strain energy weight that controls the deformability of the registration. This objective function distinguishes the error terms for distinct types of features that can comprise the intraoperative data. From digitization of the organ surface, features include the falciform

ligament, the left and right inferior ridges, and the general anterior liver surface. From tracked iUS, features can consist of the posterior liver surface, hepatic and portal vein contours, and hepatic and portal vein centerlines. Finally, single corresponding fiducial points can be used when they are available in controlled phantom environments that have embedded and measurable intraoperative target positions. To determine model-data error, a distance vector $\boldsymbol{p}_i$ is defined as

$$\boldsymbol{p}_i = \boldsymbol{y}_i - S_i\left(R(\boldsymbol{x}_0 - \bar{\boldsymbol{x}}_0 + J_u\boldsymbol{\alpha}) + \boldsymbol{\tau} + \bar{\boldsymbol{x}}_0\right) \tag{V.8}$$

where $\boldsymbol{y}_i$ is the intraoperative data point, $\boldsymbol{x}_0$ are the initial coordinates of the undeformed mesh, $\bar{\boldsymbol{x}}_0$ is the centroid of $\boldsymbol{x}_0$, S_i is a sampling operation encoding correspondence between model and data, and the rotation matrix R is defined as

$$R = R(\boldsymbol{\theta}) = R(\theta_x)\,R(\theta_y)\,R(\theta_z)\,. \tag{V.9}$$

The sampling operation S_i is implemented as a closest point operator that selects the nearest feature point in the deformed model to $\boldsymbol{y}_i$. The sampling operation is updated every iteration and also applies the computed deformation to subsurface vessel models and preoperatively designated fiducial positions by interpolating displacements from the deformed mesh.

For feature data points corresponding to a geometric model surface, the model-data error term becomes a sliding constraint taken to be the magnitude of the vector projection onto $S_i\hat{\boldsymbol{n}}$, the unit normal direction at the closest surface point:

$$f_{surface} = \left(S_i\hat{\boldsymbol{n}}\right)^T \boldsymbol{p}_i. \tag{V.10}$$

This sliding constraint is maintained for centerline feature data points by taking the magnitude of the vector rejection of $\boldsymbol{p}_i$ from $S_i\hat{\boldsymbol{t}}$, the unit tangent vector at the closest point on the centerline model, which can be derived to be

$$f_{centerline} = \sqrt{\boldsymbol{p}_i{}^T \boldsymbol{p}_i - (\boldsymbol{p}_i{}^T S_i \hat{\boldsymbol{t}})^2}. \tag{V.11}$$

Finally, the error term for single fiducial points is simply the Euclidean distance between the model-predicted and measured fiducial location

$$f_{fiducial} = \sqrt{\boldsymbol{p}_i{}^T \boldsymbol{p}_i}. \tag{V.12}$$

The energy penalty function is represented by the average strain energy density distributed over the mesh vertices,

$$f_E = \frac{1}{2M} \boldsymbol{\alpha}^T \left(J_\varepsilon{}^T J_\sigma \right) \boldsymbol{\alpha} \tag{V.13}$$

where M is the number of nodes in the mesh. For all registrations, the weights in Equation V.7 for the falciform and inferior ridges are chosen to be 0.3 m^{-2}, the strain energy weight 10^{-8} Pa^{-2}, and all other weights 1.0 m^{-2}.

From an initial estimate $\boldsymbol{\beta}_0 = 0$, Levenberg-Marquardt optimization iteratively solves for $\boldsymbol{\beta}$ by the step

$$\boldsymbol{\beta}_{n+1} - \boldsymbol{\beta}_n = \left(J^T W J + \lambda \,\mathrm{diag}(J^T W J) \right)^{-1} J^T W \boldsymbol{f} \tag{V.14}$$

where the minimized errors are $\boldsymbol{f} = [\boldsymbol{f}_i,\ f_E]$, the function weights are stored in the square diagonal matrix $W = \mathrm{diag}\,(w_F/N_F,\ w_E)$, the regularization parameter λ is controlled by a trust region prediction ratio, and the Jacobian of the error is $J = \partial \boldsymbol{f} / \partial \boldsymbol{\beta}$. Table V.1 shows closed form expressions for the error terms and their derivatives comprising J. The termination condition is established as $|\Omega(\boldsymbol{\beta}_{n+1}) - \Omega(\boldsymbol{\beta}_n)| < 10^{-12}$.

Regarding material properties, it is important to note that the displacement and strain solutions of the deformation model are independent from the Young modulus because only pure displacement boundary conditions and no boundary forces are applied in Equation

Function	f	$\boldsymbol{q}_i^T$	$\partial f/\partial \boldsymbol{\alpha}$	$\partial f/\partial \boldsymbol{\tau}$	$\partial f/\partial \boldsymbol{\theta}$
$f_{surface}$	$(S_i\hat{\boldsymbol{n}})^T \boldsymbol{p}_i$	$(S_i\hat{\boldsymbol{n}})^T$	$-\boldsymbol{q}_i^T S_i R J_u$	$-\boldsymbol{q}_i^T S_i$	$-\boldsymbol{q}_i^T S_i \frac{\partial R}{\partial \boldsymbol{\theta}} (\boldsymbol{x}_0 - \bar{\boldsymbol{x}}_0 + J_u \boldsymbol{\alpha})$
$f_{centerline}$	$\sqrt{\boldsymbol{p}_i^T \boldsymbol{p}_i - (\boldsymbol{p}_i^T S_i \hat{\boldsymbol{t}})^2}$	$\frac{\boldsymbol{p}_i^T - (\boldsymbol{p}_i^T S_i \hat{\boldsymbol{t}})(S_i \hat{\boldsymbol{t}})^T}{\sqrt{\boldsymbol{p}_i^T \boldsymbol{p}_i - (\boldsymbol{p}_i^T S_i \hat{\boldsymbol{t}})^2}}$	$-\boldsymbol{q}_i^T S_i R J_u$	$-\boldsymbol{q}_i^T S_i$	$-\boldsymbol{q}_i^T S_i \frac{\partial R}{\partial \boldsymbol{\theta}} (\boldsymbol{x}_0 - \bar{\boldsymbol{x}}_0 + J_u \boldsymbol{\alpha})$
$f_{fiducial}$	$\sqrt{\boldsymbol{p}_i^T \boldsymbol{p}_i}$	$\frac{\boldsymbol{p}_i^T}{\sqrt{\boldsymbol{p}_i^T \boldsymbol{p}_i}}$	$-\boldsymbol{q}_i^T S_i R J_u$	$-\boldsymbol{q}_i^T S_i$	$-\boldsymbol{q}_i^T S_i \frac{\partial R}{\partial \boldsymbol{\theta}} (\boldsymbol{x}_0 - \bar{\boldsymbol{x}}_0 + J_u \boldsymbol{\alpha})$
f_E	$\frac{1}{2M} \boldsymbol{\alpha}^T (J_\varepsilon^T J_\sigma) \boldsymbol{\alpha}$	—	$\frac{1}{M} \boldsymbol{\alpha}^T (J_\varepsilon^T J_\sigma)$	0	0

Table V.1: Closed form expressions for model-data errors and gradients. (© 2020 IEEE)

V.1. However, the strain energy is directly proportional to modulus. Consequently, any difference in stiffness between the patient liver and the model can be compensated at the time of registration by adjusting the deformability parameter w_E.

V.5 Experimentation

The proposed algorithm is evaluated in a series of experiments on nine simulated deformations from three laparoscopic mobilizations transposed onto three unique liver geometries. In each of the nine deformations, 16 potential iUS plane orientations are sampled. In this dataset, registration accuracy is examined across a wide range of access to intraoperative data coverage. Furthermore, the algorithm is applied to clinical data from three cases of image-guided open liver resection, where accuracy of the method is estimated with real sources of intraoperative error.

V.5.1 Data Simulation

The data simulation process aims to map deformation fields from three different laparoscopic mobilizations of a liver phantom to three distinct liver geometries. With this approach, registration performance can be evaluated in a diverse yet controlled environment. Three human livers and their portal and hepatic veins were segmented from preoperative contrast-enhanced CT images of deidentified patients, and meshes and vessel centerlines were generated as described in Section V.4.1. Collected with these patient data were sparse

intraoperative surface patterns digitized with an optically tracked stylus spanning 25.2% (Liver 1), 14.9% (Liver 2), and 24.9% (Liver 3) of the total liver surface.

In a phantom environment, a silicone liver with 147 embedded targets was created from a 3D printed liver built from a preoperative scan of a different patient. This phantom was imaged without deformation, then placed in a mock insufflated abdomen with ligament attachments that reproduce laparoscopic changes to the liver. The phantom was re-imaged in three conditions of laparoscopic deformation: left mobilization (L), where the left triangular and falciform ligaments were dissected; no mobilization (N), where no ligaments were dissected; and right mobilization (R), where the right triangular and falciform ligaments were dissected. These phantom data were originally reported in [9]. In this paper, the phantom data provide detailed displacement fields for each laparoscopic mobilization scenario. These fields were obtained by registering the full surface and target positions from post-deformation images to their undeformed counterparts using the algorithm described in section II at a higher resolution of $k = 90$. This process yielded phantom registrations with highly accurate surface errors of 0.4 ± 0.6 mm (L), 0.4 ± 0.5 mm (N), 0.4 ± 0.7 mm (R) and target errors of 1.9 ± 1.0 mm (L), 2.1 ± 1.0 mm (N), and 2.1 ± 1.2 mm (R) based on data from CT scans with voxel resolution of $0.6 \times 0.6 \times 3$ mm. However, these phantom displacement fields do not represent the exact deformations to be reconstructed in the simulation experiments. Instead, they represent a realistic deformation template to be distorted and applied to the previous liver geometries.

Livers 1–3 were registered to the undeformed liver phantom using an affine registration followed by the optimization method from Section V.4 only to establish inexact correspondence between anatomical regions of the disparate liver shapes. Using these alignments, displacements from phantom deformations L, N, and R were mapped onto livers 1, 2, and 3 with their associated surface data patterns to produce the nine deformed livers shown in Figure V.3. It should be noted that the nine resultant livers are not purely linear elastic deformations of their original meshes. Nonlinear distortions in the displacement fields

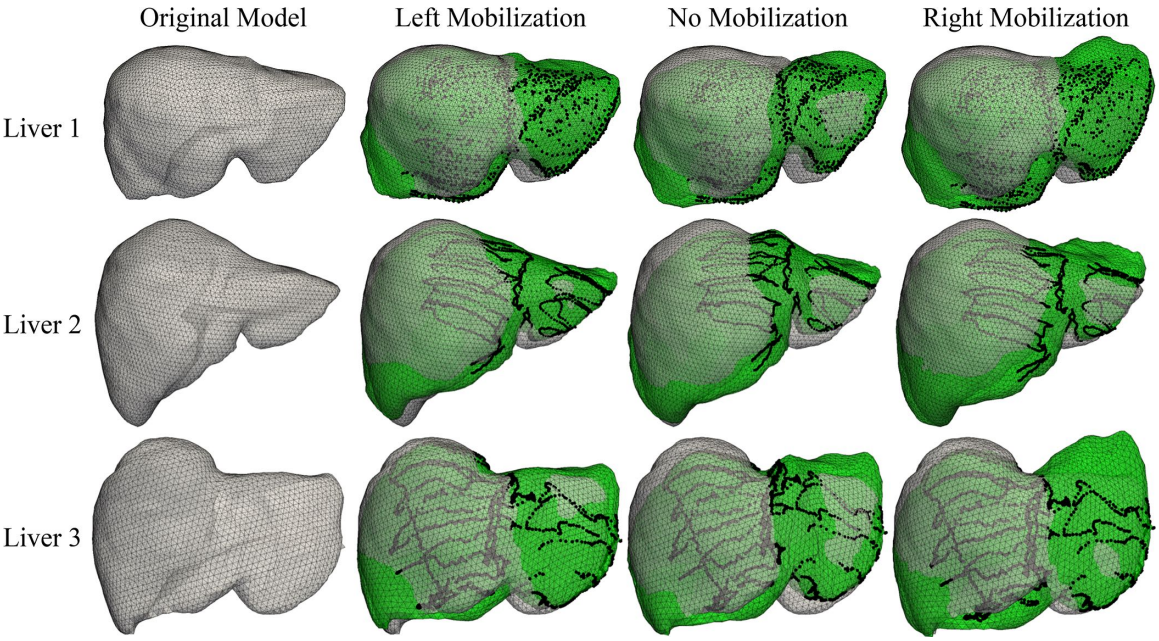

Figure V.3: Three liver geometries (white) and three applied displacement fields comprise nine simulated deformations (green). The applied deformations represent mobilization of stress-bearing ligaments on the left side, no sides, or right side of the liver in a laparoscopic phantom setup that reproduced the insufflated intra-abdominal anatomy surrounding the liver. Transposed clinical patterns of sparse surface data are shown in black. (© 2020 IEEE)

are created by the spatial mapping process between the physically deforming phantom and the novel liver geometries. In each of the nine simulated deformations, 16 iUS plane locations were sampled and geometric intersections with the deformed portal and hepatic vein models and the posterior liver surface were determined using the Möller triangle intersection algorithm [171] then rasterized into points in the iUS plane using the Bresenham algorithm [169]. Positions of the sampled iUS features are displayed in Figure V.4.

A simulated dataset is created with the nine transposed phantom deformations to examine the registration method across varying levels of intraoperative data. These levels include registration scenarios using: 1) sparse anterior surface data only, 2) subsurface data from one iUS plane in addition to the sparse surface data, 3) subsurface data from two combined iUS planes in addition to the sparse surface data, 4) data from three combined iUS planes in addition to the sparse surface data, and 5) all 16 iUS planes in addition to the sparse surface

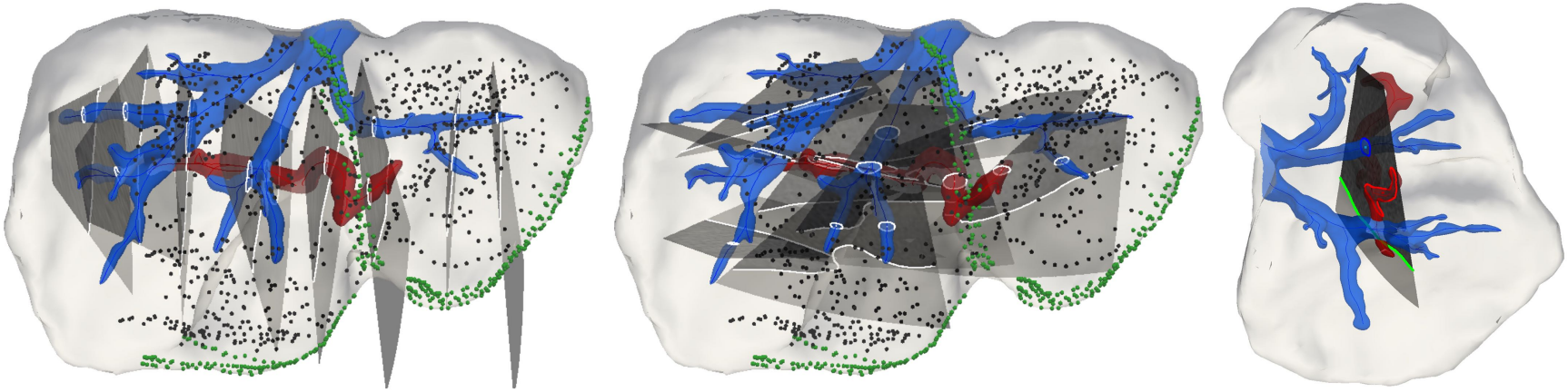

(a) (b) (c)

Figure V.4: Ultrasound plane locations sampled across the ground truth deformed Liver 1 with left mobilization (1–L). The hepatic vein is shown in blue, the portal vein in red, the anterior surface data in black, and the surface features in dark green. A total of 16 ultrasound plane locations are sampled for each simulated deformation, consisting of (a) 8 vertical planes and (b) 8 lateral planes. Subsurface features intersecting the iUS planes are shown in white. (c) A view of a single ultrasound plane orientation with hepatic vein contour (blue), portal vein contour (red), and posterior surface contour (green).

data. Furthermore, a scenario based on the deformed full anterior and posterior surfaces is included without subsurface data to compare performance against information typically available from intraoperative CT without contrast, e.g. cone beam CT (CBCT). Finally, a scenario using all ground truth deformed information, including the full liver surfaces and vessel data, is considered to evaluate optimal performance if significantly more data from intraoperative contrast-enhanced CT (iCT) were available. In total, 6,291 registration scenarios are included in the simulated dataset. For each, target registration error (TRE) is computed as the average distance of corresponding vertices between the registered and ground truth deformed meshes.

In the following sections, surface data registration is examined to identify how additional subsurface information could improve overall registration accuracy. Sparse iUS image planes are then incorporated and registration accuracy is characterized across varying levels of intraoperative access to surface and subsurface data. Finally, the iUS registration methods are applied to three cases of clinical data.

V.5.2 Limitations of Surface Registration

In Figure V.5, rigid and deformable registration results to a transposed surface data pattern are shown for one of the nine liver deformations. In this case, average TRE across the mesh was 12.4 ± 8.3 mm for rigid registration and 9.3 ± 7.3 mm for deformable registration. Qualitatively from Figure V.5c, it can be seen that registration accuracy has high spatial sensitivity, with accuracy dropping off considerably where surface data cannot be collected. This behavior has two implications. First, the spatial sampling of TRE is profoundly important, as the measured error of a single validation target can greatly vary depending on its position relative to the regions of the organ that are deforming, and how well the available data describes this deformation. Therefore, unbiased validation metrics that thoroughly sample target errors throughout the domain are needed to give a complete picture of registration accuracy. Second, the profile of data collection on the deformed organ must also be

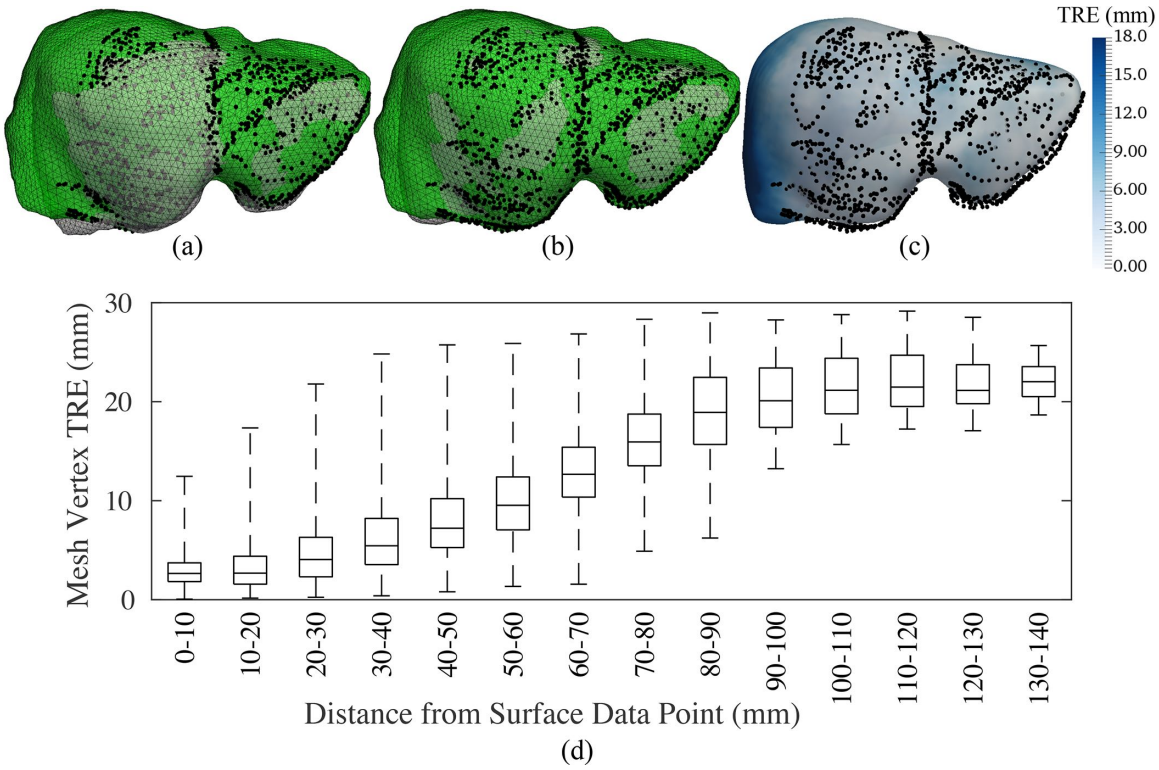

Figure V.5: An example case of registration to sparse surface data. The registered models (transparent white) are compared to the ground truth deformation (transparent green) for (a) rigid, and (b) deformable registrations to the applied clinical surface data pattern (black). In (c), the spatial distribution of TRE is shown for deformable registration to surface data. In (d), registration accuracy across the mesh is plotted against distance away from intraoperative data. Registrations are less accurate at greater distances away from data, suggesting that data coverage is a critical factor for whole organ TRE. (© 2020 IEEE)

acknowledged. As shown in Figure V.5d, the proximity of a target to its nearest intraoperative data point is a strong predictor of its registration error (Pearson $r = 0.83$). This trend suggests that distant targets may not be well constrained by intraoperative data and that intraoperatively acquired data may not completely describe the unique deformation of the organ. Ideally, data coverage should be extensive enough to enable accurate localization of anatomical structures many centimeters beneath the surface. Although surface data coverage is often inherently constrained by anatomical obstructions and limited fields of view, tracked iUS makes it possible to more effectively describe deformations in deeper regions of the liver to reduce the uncertainty of distant targets.

While TRE of surface registrations in the simulated dataset seem to be higher than those reported in [9], it should be noted that the distributions of targets are significantly different. The average distance of validation targets to the closest surface data point is 44.8 mm for the simulated data, while this metric was only 28.6 mm for the laparoscopic phantom data in [9]. Using Figure V.5d as a qualitative guide, the performance in [9] would be anticipated to be superior to the TRE reported here.

V.5.3 Data Simulation Results

To illustrate the effect of incorporating constraints from iUS data on registration accuracy, TRE is reported over a comprehensive range of access to intraoperative data. Registrations were performed on the 6,291 registration scenarios using contour, centerline, and posterior features from iUS planes in the optimization of Equation V.7. Figure V.6 shows registration results as increasing numbers of ultrasound planes are used in an example case. Results across all cases are summarized in Table V.2. In each row of Table V.2, a progressive decrease in TRE is observed as a greater amount of subsurface information is added to the deformable registration. These results are mirrored in Figure V.6, which shows probability distribution functions for target errors across the mesh vertices of all registrations in each category of intraoperative data. Clear leftward shifts and decreased weights in the tails

TARGET REGISTRATION ERRORS (MM) FOR SIMULATED LAPAROSCOPIC DEFORMATIONS

Deformation	Rigid	Surface (S)	S + 1 Plane (n = 16)	S + 2 Planes (n = 120)	S + 3 Planes (N = 560)	S + All Planes	CBCT	iCT
1–L	12.4 (±8.3)	9.3 (±7.3)	7.4 ± 1.6	6.4 ± 1.3	5.7 ± 1.0	3.5 (±2.3)	3.6 (±1.9)	2.4 (±1.7)
1–N	15.3 (±11.2)	13.5 (±10.8)	10.5 ± 2.4	8.8 ± 2.0	7.7 ± 1.6	4.7 (±3.0)	5.0 (±2.3)	3.4 (±2.0)
1–R	14.9 (±10.1)	10.8 (±8.9)	9.4 ± 2.2	8.0 ± 2.0	7.1 ± 1.6	4.2 (±2.9)	4.5 (±2.3)	3.0 (±2.0)
2–L	10.9 (±8.5)	10.4 (±8.2)	7.6 ± 1.9	6.0 ± 1.4	5.2 ± 1.0	3.1 (±2.0)	3.4 (±1.6)	2.1 (±1.4)
2–N	16.9 (±10.3)	15.8 (±11.3)	11.4 ± 2.6	9.3 ± 2.2	8.0 ± 1.6	5.2 (±3.5)	5.0 (±2.3)	3.1 (±2.0)
2–R	12.5 (±9.2)	12.3 (±8.9)	9.2 ± 2.5	7.6 ± 2.1	6.4 ± 1.6	3.7 (±2.6)	4.2 (±2.2)	2.3 (±1.8)
3–L	12.8 (±5.5)	8.5 (±6.4)	7.5 ± 1.3	6.1 ± 1.2	5.2 ± 0.9	3.1 (±2.0)	3.8 (±1.7)	2.4 (±1.5)
3–N	13.9 (±5.9)	12.0 (±6.6)	8.9 ± 1.0	7.2 ± 1.0	6.2 ± 0.8	4.4 (±2.4)	5.8 (±2.8)	3.7 (±2.2)
3–R	15.1 (±6.5)	10.3 (±7.8)	9.1 ± 2.0	7.2 ± 1.7	6.0 ± 1.4	3.6 (±2.3)	4.9 (±2.4)	3.1 (±2.0)
Average	13.8 (±1.9)	11.4 (±2.2)	9.0 ± 1.4	7.4 ± 1.2	6.4 ± 1.0	3.9 (±0.7)	4.5 (±0.8)	2.8 (±0.5)

Table V.2: Target registration errors (mean ± std) for registration using increasing intraoperative data content. Standard deviations in parentheses represent variability across mesh vertex targets within a single case (n = 1); all other standard deviations represent variability in the average mesh TRE across the constituent cases. (© 2020 IEEE)

of the distributions are seen as data content increases, and all pairwise distributions of target error significantly differ from one another (two sample K–S test, $\alpha = 0.001$). It is interesting to note that TRE is lower for registrations to all 16 iUS planes and sparse surface data than for registrations that could access the full anterior and posterior surfaces with CBCT, suggesting that reconstructive capacity could be superior with scattered iUS coverage of internal structures and sparse surface data than with thorough coverage of the surface but no subsurface information.

V.5.4 Clinical Experiments

Clinical data with tracked iUS were acquired from three patients undergoing open liver resection with informed consent and approval of the institutional review board at Memorial Sloan Kettering Cancer Center. Data were collected as described in Section V.4.1 and analyzed retrospectively. Two tracked ultrasound planes from each patient were selected on the criteria that each plane included vessel features of only the portal vein or only the hepatic vein, and each plane was separated by at least 3 cm. The distances between ultrasound plane features were 3.4 cm in the first patient (Case A), 8.3 cm in the second patient (Case B), and 6.5 cm in the third patient (Case C).

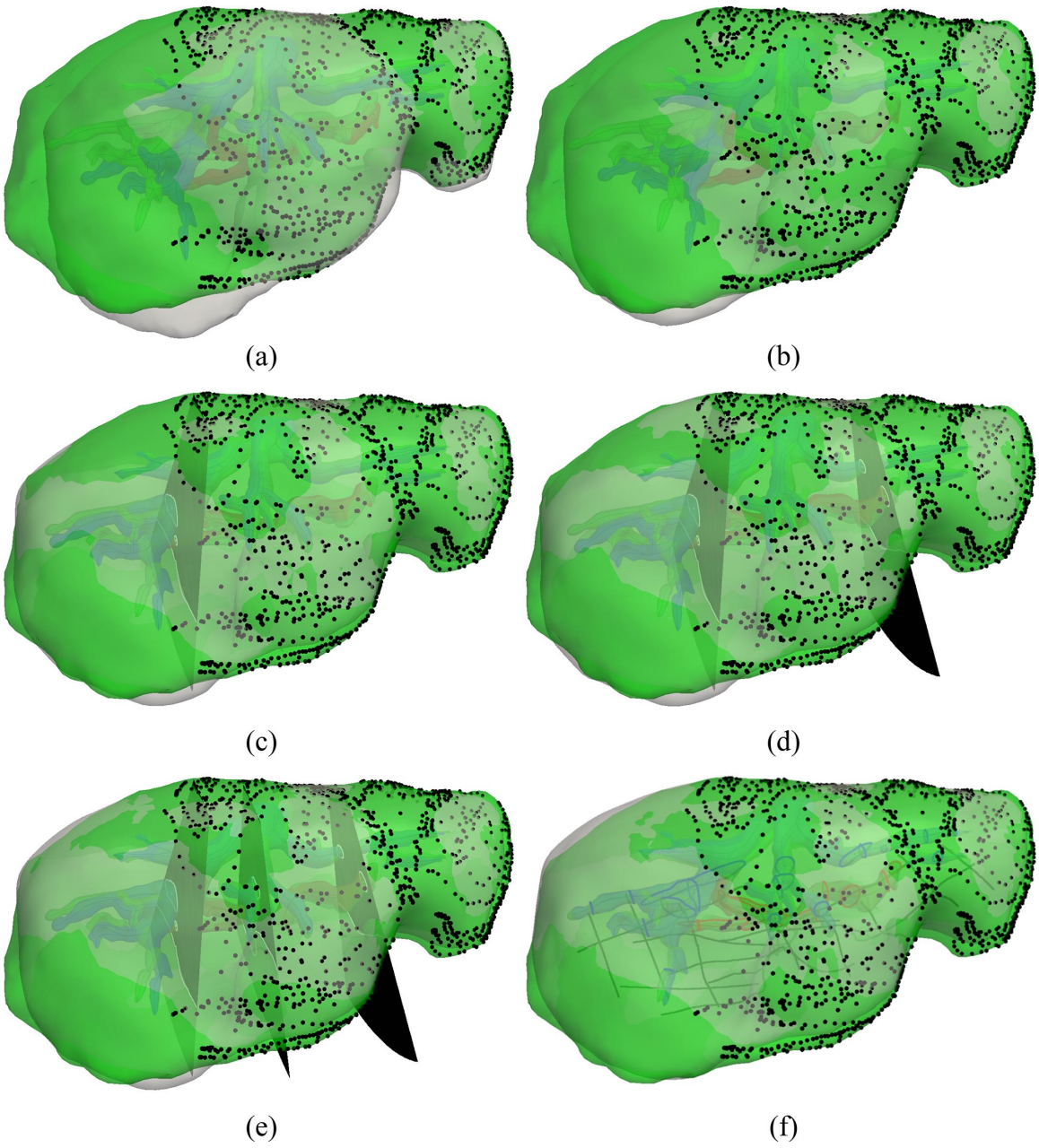

Figure V.6: Registrations to data from simulated left-mobilized deformation on Liver 1 (1–L). The ground truth deformed liver is shown in green and the registered model is shown in white. Registrations were performed to surface data with (a) rigid, (b) deformable, (c) deformable with one tracked iUS plane, (d) deformable with two tracked iUS planes, (e) deformable with three tracked iUS planes, and (f) deformable with all 16 tracked iUS planes. Average TRE across the mesh for these examples were (a) 12.4 ± 8.3 mm, (b) 9.3 ± 7.3 mm, (c) 5.9 ± 3.6 mm, (d) 5.7 ± 3.7 mm, (e) 5.2 ± 3.7 mm, and (f) 3.5 ± 2.3 mm. (© 2020 IEEE)

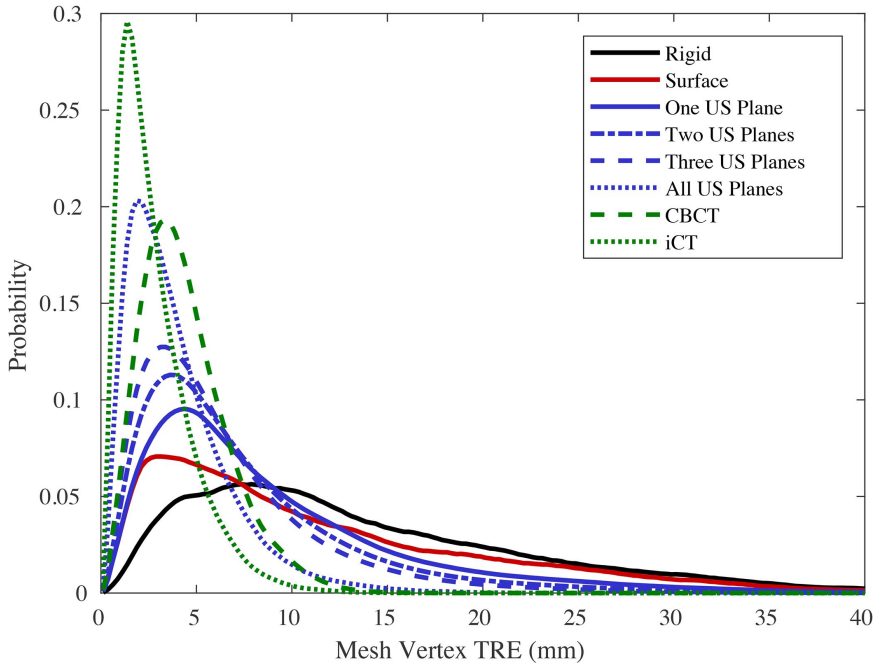

Figure V.7: Probability distributions of mesh vertex target errors resulting from all registrations to the nine simulated deformations with varying levels of intraoperative data. The clinical patterns of sparse anterior surface data are used for registrations in the black, red, and blue curves. The blue curves incorporate sparse features from increasing numbers of tracked iUS planes. The green CBCT curve uses the full anterior and posterior surfaces of the ground truth deformed mesh, and the green iCT curve uses the full surfaces in addition to the ground truth deformed vessel contours and vessel centerlines.(© 2020 IEEE)

FEATURE ERRORS (MM) FOR CLINICAL CASES

Registered Data	Case A Portal Feature Error	Case A Hepatic Feature Error	Case B Portal Feature Error	Case B Hepatic Feature Error	Case C Portal Feature Error	Case C Hepatic Feature Error
Rigid	10.8 ± 3.9 (17.0)	14.3 ± 1.8 (16.5)	4.1 ± 1.4 (7.2)	9.8 ± 1.5 (13.2)	5.4 ± 2.6 (10.0)	3.5 ± 2.0 (7.7)
Surface (S)	9.7 ± 3.6 (15.8)	12.0 ± 2.2 (15.1)	3.1 ± 1.7 (7.9)	3.2 ± 2.2 (9.9)	5.2 ± 3.5 (11.0)	3.1 ± 2.1 (8.0)
S + Portal	*1.3 ± 0.9 (3.6)*	2.9 ± 1.9 (6.2)	*0.9 ± 0.6 (2.5)*	1.3 ± 1.0 (4.2)	*1.0 ± 0.8 (2.9)*	3.0 ± 2.3 (9.1)
S + Hepatic	3.5 ± 3.1 (10.6)	*0.8 ± 0.5 (1.9)*	1.6 ± 1.3 (5.2)	*1.1 ± 0.7 (3.1)*	3.6 ± 2.5 (8.1)	*0.8 ± 0.7 (0.3)*
S + Portal + Hepatic	*1.3 ± 0.9 (3.4)*	*0.7 ± 0.4 (1.5)*	*0.8 ± 0.5 (2.2)*	*1.2 ± 0.8 (3.8)*	*1.1 ± 0.7 (2.8)*	*0.9 ± 0.7 (0.4)*

Table V.3: A summary of feature registration errors for portal and hepatic contours from tracked iUS planes in clinical cases A (left), B (center), and C (right). Rows show the feature errors for rigid registration, deformable registration based on surface data (S), and deformable registrations with additional subsurface data. Maximum values of the closest point feature distance are shown in parentheses. Values in italics mark residual error of the features used for registration. (© 2020 IEEE)

In the analysis, ultrasound plane features were used alternately as validation targets or sources of registration data. Rigid registration, deformable registration based on surface data, and deformable registration based on surface data augmented by the vessel contour, centerline, and posterior features visible in the tracked iUS plane were compared. To measure registration error, the average feature error is defined as the average distance between the iUS vessel contour points and the closest points on the registered vessel model. This metric is chosen because corresponding target points cannot be determined between the iUS image plane and the preoperative CT volume with high certainty. The feature errors from the three clinical cases are shown graphically in Figure V.8 and tabulated in Table V.3. Overall, the average feature error of the six validation targets improved 67% over rigid registration and 56% over deformable surface registration when incorporating data from the independent iUS plane. These substantial improvements were obtained under real sources of clinical noise, including tracking error, calibration error, physiological changes to the hepatic vasculature, and deformation induced by the tracked stylus and transducer. While noise sources were not specifically addressed in simulation studies, these preliminary clinical results suggest that the reconstruction method can perform remarkably well in realistic situations.

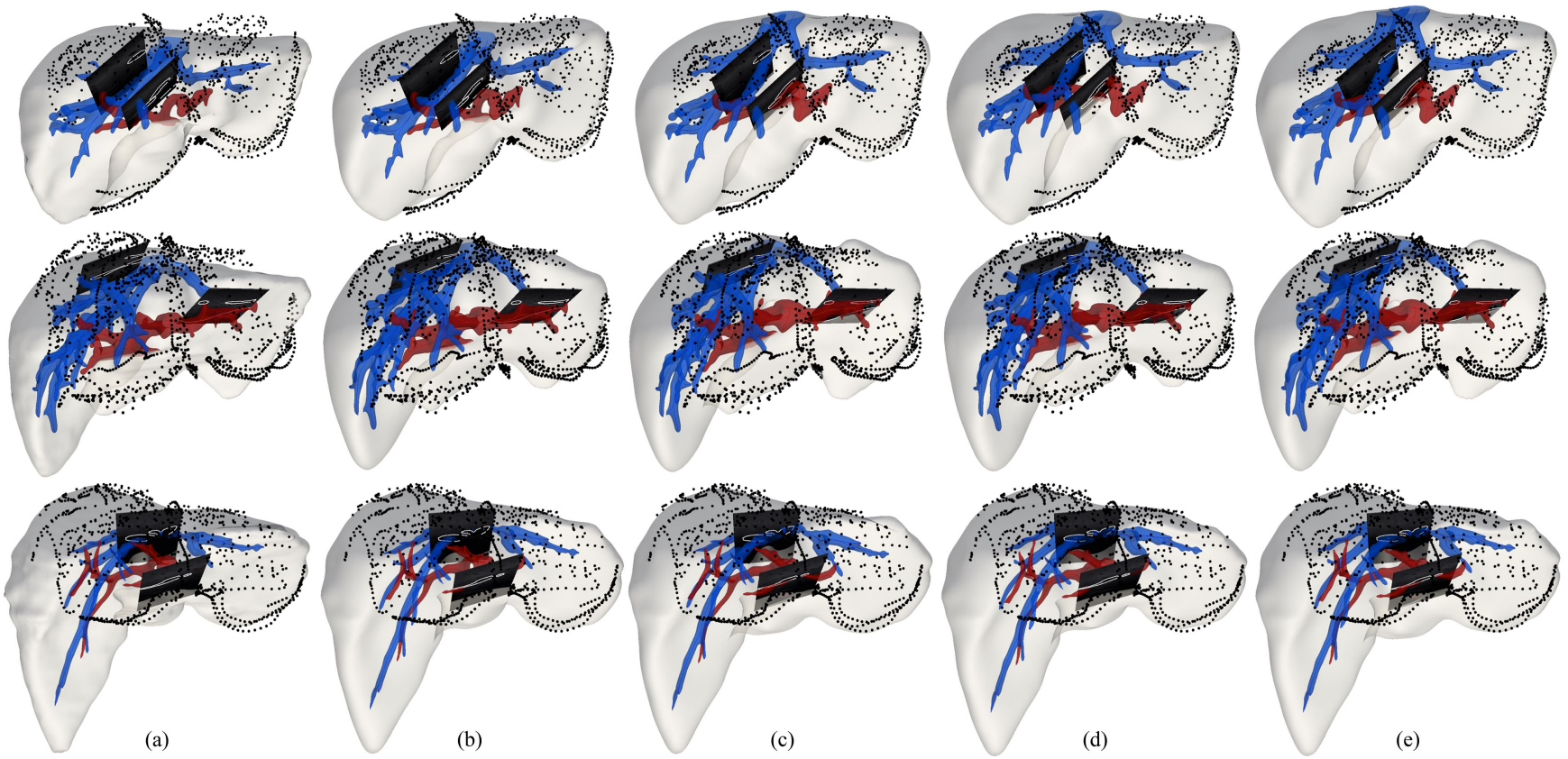

Figure V.8: Registered liver models (white surface) to surface data (black points) and features from tracked iUS (white points) for three clinical cases of image-guided open liver surgery (A – top; B – middle; C – bottom). Hepatic and portal vein vessel branches are shown in blue and red, respectively. (a) Rigid registration to surface data. (b) Deformable registration to surface data. (c) Deformable registration to surface data and the portal vein. (d) Deformable registration to surface data and the hepatic vein. (e) Deformable registration to surface data and the portal and hepatic veins.

V.6 Discussion

The results show that in challenging configurations of organ deformation and data coverage, large improvements can be made to registration accuracy by incorporating sparse features from tracked intraoperative ultrasound. Although feature errors reported for the clinical data are lower than the best TRE values from simulated data, it must be emphasized that these error metrics are not directly comparable. Because single corresponding target points cannot be exactly determined from the iUS planes, the clinical metric requires the error of iUS feature points to be projected onto the registered vessel model. This projected feature error has the effect of underestimating the true TRE. Additionally, feature errors from the clinical experiments are sampled at a single location in the liver whereas the simulated TRE metric averages the error over every vertex in the meshed domain. The simulated TRE values presented in Table V.2 account for whole organ registration error, representing a more difficult test configuration that rewards accurate predictions of deformation beyond the immediate region of data collection.

In the context of boundary value reconstruction, rich data can be derived from iUS to produce informative subsurface feature constraints that capture information about organ deformation normally inaccessible by surface digitization tools. However, in the context of clinical workflow, tracked iUS can be difficult to implement and interpret, necessitating a judicious balance between maximizing interventional benefit and minimizing intraoperative disturbance. This work shows that a variety of anatomical features visible in a small number of tracked iUS planes of the liver can significantly improve the accuracy of registration throughout the entire organ.

Regarding benchmarks for intraoperative data collection and computation time, surface points and tracked iUS planes can be collected and processed within 60 seconds. While rigid registration can be performed at frame rate, the reconstructive component of the clinical registrations completed in 37.6 ± 5.4 seconds. These registrations were performed on a single thread of a 4.0 GHz Intel Core i7 CPU. Although the total intraoperative computa-

tional burden is already low, parallelizing the model-data error and gradient computations shown in Table V.1 could further reduce the computation time. Despite manual iUS feature designation limiting continuous real-time potential, we have shown that it is possible to perform intermittent high quality registrations by estimating the deformation state vector $\boldsymbol{\beta}$. In the future, further accelerations can be made as computational efficiency continues to improve and automatic iUS vessel segmentation and surface acquisition methods become more advanced.

Another factor that affects the computational complexity is the resolution with which spatial variations in the boundary load can be reconstructed. A sufficiently large number of control points k can improve the reconstructive capacity and potentially lead to more accurate registrations. However, excessive k introduces additional degrees of freedom to the reconstructive basis that can lead to prohibitive computation cost and degrade the conditioning of the inverse problem to the point where the solution is inadequately determined by intraoperative data constraints. This relationship between TRE, the model resolution k, and the amount of data coverage is shown in Figure V.9. Though the best value of k that minimizes TRE depends on the amount of intraoperative data, the shallow minima suggest low sensitivity. The value $k = 45$ offers a good tradeoff between these considerations for the typical size of a human liver, intraoperative time constraints, and the amount of data that can be collected to resolve the reconstruction to a level of accuracy that meets clinical need.

With regard to limitations, while the simulated data show that adding the first, second, and third iUS planes to the deformable surface registration incrementally improves TRE across the mesh, the average TRE values from Table V.2 include all potential combinations of simulated iUS plane positions. The relative value of each plane was not considered in relation to the redundancy of nearby data and the profile of intraoperative deformation, causing the average TRE values to be higher than the best achievable. In registrations to the ground truth deformation 1–L, the smallest average TRE with a single iUS plane was 4.9 ±

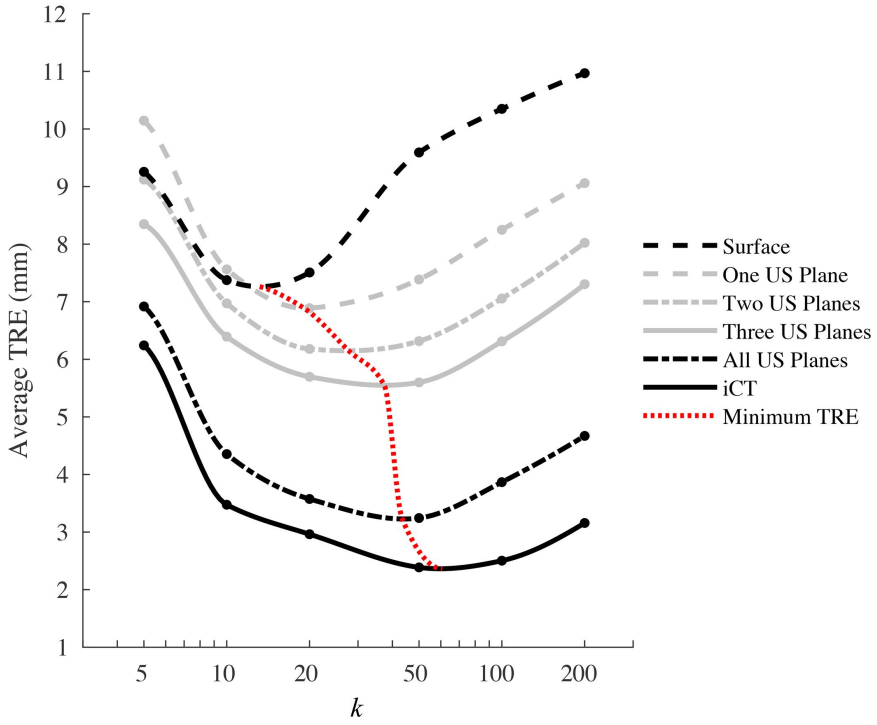

Figure V.9: Plot of average TRE values for registrations from simulated data 1–L across the number of control points k and the extent of intraoperative data available for registration. Lines were interpolated from six evaluation points with a cubic spline. The optimal value of k that minimizes TRE based on intraoperative data coverage, marked by the dotted red line, depends on a tradeoff between reconstructive model resolution and the ability to sufficiently constrain the degrees of freedom in the model. (© 2020 IEEE)

3.0 mm and the smallest average TRE with three iUS planes was 3.9 ± 2.5 mm. With 5 mm representing the clinical goal for accuracy at half the recommended oncological margin, the ability to overcome this threshold over the entire liver volume is possible with very sparse iUS coverage. While outside the scope of this paper, it may be possible to strategically plan favorable configurations of tracked iUS data collection in targeted regions to reliably decrease TRE with a predictive registration assessment framework for data sufficiency. Even so, the results from Table V.2 show that registering 16 distributed iUS planes can easily exceed the benchmark of 5 mm average TRE. As a general guide for positioning iUS planes in sparser coverage, it can be inferred from Figure V.6 that even spacing can be an effective strategy for improving registration accuracy so as to reduce the overall target-data distance shown in Figure V.5d. In the clinical experiments, while validation is less comprehensive, similarly compelling local improvements to subsurface accuracy are shown when iUS features can be used to augment surface data during registration. While these preliminary results are promising, more extensive clinical validation is eventually needed to demonstrate the ability of the algorithm to accurately reconstruct deformation responses of real tissue.

V.7 Conclusions

In this paper, a linearized iterative boundary reconstruction method for compensating intraoperative deformation of the liver using sparse surface and subsurface data is proposed. Information from tracked iUS was incorporated into the registration methodology and its impact was characterized with an expansive simulated dataset. Feasibility was also demonstrated in three clinical cases. Findings show that incorporating information from sparse intraoperative ultrasound can make significant improvements to registration accuracy for hepatic image guidance, and that strategic combinations of sparse data might have the potential to outperform seemingly more dense configurations of data.

Acknowledgements

This work was supported by the National Institutes of Health grants NCI-R01CA162477, NIBIB-T32EB021937, and NIBIB-R01EB027498.

CHAPTER VI

Uncertainty Prediction of Registration Error from Intraoperative Patterns of Data Coverage

VI.1 Summary and Contributions

Although deformable registration methods may be able to improve the accuracy of image guidance, to date, no methods have been developed to assess or estimate the uncertainty of elastic registration techniques. Intraoperative reporting of registration trustworthiness would be fundamental to a surgeon's assessment of operative risk, and deformable registration techniques are unlikely to become relied upon or integrated into the standard of care without demonstrated confidence. Moving forward, development of techniques that allow quantification of registration certainty will be essential to ensuring the safety of image-guided procedures.

In this chapter, a method is established for intraoperative prediction of registration accuracy based on intraoperative data patterns relative to a patient's organ shape. Information-theoretic uncertainty is introduced through a lower bound for the energetic dissipation of constraints described by boundary conditions. This description of registration uncertainty was found to lead to two useful metric variants that predict the accuracy of elastic registration with similar efficacy, the first a generalized metric that can be computed after any elastic registration method terminates, and the second a purely predictive metric that can be computed during data acquisition although requires additional precomputation. These metrics enable real-time intraoperative assessment of registration confidence that can be used to guide locality of data collection for maximizing registration accuracy and to provide numerical estimates and spatial maps of registration certainty for the surgeon.

These metrics were evaluated using the vast registration dataset introduced in Chapter V, with which statistical predictive models were fit. An additional data series was also

created for independent validation. This work lays the foundation for the next step in advancing registration methodologies, namely the ability to accurately predict registration outcome to build more effective strategies for managing and controlling error during the registration process.

Dispersion of Boundary Energy Predicts Elastic Registration Accuracy from Intraoperative Patterns of Data Coverage

The work presented in this chapter appears in,

J. S. Heiselman and M. I. Miga, "Dispersion of Boundary Energy Predicts Elastic Registration Accuracy from Intraoperative Patterns of Data Coverage," *IEEE Transactions on Medical Imaging*, in submission.

VI.2 Abstract

Image-guided intervention for soft tissue organs depends on the accuracy of deformable registration methods to achieve effective results. While registration techniques based on elastic theory are prevalent, no physics-constrained methods yet exist that can prospectively estimate registration uncertainty to regulate sources and mitigate consequences of localization error. This paper introduces registration uncertainty metrics based on dispersion of energy from boundary constraints to predict the proportion of target registration error (TRE) remaining after nonrigid elastic registration. These uncertainty metrics depend on the spatial distribution of intraoperative data provided to the registration method with relation to patient-specific organ geometry. Predictive linear and bivariate gamma models are fit and cross-validated using an existing dataset of 6291 simulated registration examples, plus a novel 699 simulated registrations withheld for independent validation. Average uncertainty and residual TRE are strongly correlated, with mean absolute difference in predicted TRE equivalent to 0.9 ± 0.6 mm (cross-validation) and 0.9 ± 0.5 mm (independent validation). Uncertainty maps are also generated, permitting spatially localized TRE estimates accurate to an equivalent of 3.0 ± 3.1 mm (cross-validation) and 1.6 ± 1.2 mm (independent validation). This work formalizes a lower bound for the inherent uncertainty of nonrigid elastic registration given sparse coverage of intraoperative data, and demon-

strates a relation to TRE that can be predictively leveraged to inform data collection and provide a measure of registration confidence for elastic methods.

VI.3 Introduction

Registration of medical images finds application at every stage of clinical intervention. Fundamentally, registration determines a transformation that intends to most accurately map patient anatomy between coordinate spaces given data that describe correspondence either completely, or more often incompletely. Multimodal fusion of preoperative diagnostic information, intraoperative image-guided delivery of therapy, and postoperative assessment of treatment response revolve around the ability to achieve accurate registrations of patient data observed at disparate time points and with various signal structures. The importance of registration methodologies in the treatment paradigm necessitates that errors be controlled, which can be achieved with mechanistic understanding of the emergence and propagation of error in the registration process.

The landmark paper by Fitzpatrick, West, and Maurer [172] established rigorous theory for rigid point-based registration that accurately predicts average target registration error (TRE) from the spatial configuration of target locations and the measurable fiducial points used to calculate the registration. Fitzpatrick and West [173] soon extended this work to estimate the spatial distribution of TRE surrounding these fiducials at any location of interest. These seminal works were later expanded to account for the case of anisotropic [174] and heterogeneous [175, 176] fiducial localization errors. These contributions have become profoundly important in the domain of image-guided surgery, wherein these error distributions steer the placement of fiducial markers and provide feedback on the accuracy of intraoperative guidance in rigid body scenarios suitable for point-based registration. However, these descriptions of registration error become invalid in the presence of underlying soft tissue deformation, which cannot be explained by models of fully rigid systems.

To achieve more accurate registrations in the presence of deformation, numerous registration approaches have been proposed, which are reviewed thoroughly in [177]. Of these, registration techniques based on linear elastic mechanics have become common for image guidance purposes where the data available to registration algorithms are limited [1, 2, 8, 20, 178]. These methods that rely on physics to constrain the registration problem can obtain more realistic and accurate solutions especially in scenarios of sparse data [166, 179]. Although this paper will focus on the application of image-guided liver surgery, the same principles extend to elastic registration methods for other organ systems.

Previous empirical work has shown that average TRE tends to be related to the extent of data made available for registration [1, 4, 9]. More recently, it has been shown that TRE at any location in the organ is correlated with distance between the target and the nearest data point driving the registration [20]. The objective of this paper is to establish a framework that explains how the spatial distribution of incomplete data driving a nonrigid elastic registration consequently affects the spatial distribution of TRE throughout the material domain. Similar to the foundational work by Fitzpatrick et al. [172, 173], this paper will consider both the *average* and the *spatial distribution* of error based on patient-specific organ shape and intraoperative patterns of data. Whereas rigid registration benefits from explicit mathematical expressions that explain error patterns and guide best practice, no counterpart yet exists for deformable registration methods. This paper aims to close this gap by introducing a metric for registration uncertainty based on the dispersal of energy as information from boundary conditions propagates through an elastic material. This uncertainty metric can be computed in a fraction of a second from the spatial pattern of data available for registration and is demonstrated in this paper to be highly correlated with registration fidelity. In addition, a bivariate statistical model is introduced for constructing predictive spatial distributions of registration error from this metric. Predictive accuracies of the error models are tested on an extensive existing dataset of 6,291 registrations, plus a novel dataset of 699 additional registrations created for independent validation.

The structure of this paper is organized as follows. Section VI.4 derives two metric variants for estimating spatially localized and total registration uncertainty from the spatial coverage of intraoperative data that can be instantly computed either before initiating or after completing registration. Section VI.5 describes the experimental framework used to evaluate the predictive capability of these metrics. Finally, the remaining sections discuss and conclude the work.

VI.4 A Model for Elastic Uncertainty

VI.4.1 The Elastic Registration Problem

Deformable registration in the context of image guidance aims to update a preoperative model of the organ to match an intraoperative deformation state described by sparsely measured data. Figure VI.1 illustrates some examples of data that can be obtained for liver registration. Elastic registrations usually treat the preoperative model as a continuum bounded by the domain $\mathcal{M} \in \mathbb{R}^3$ that satisfies the following three conditions:

I. The static equilibrium condition

$$\nabla \cdot \overline{\overline{\sigma}} + F = 0 \tag{VI.1}$$

II. The linear elastic condition

$$\overline{\overline{\sigma}} = \mathbb{C} : \overline{\overline{\varepsilon}} \tag{VI.2}$$

III. The linear strain-displacement relation

$$\overline{\overline{\varepsilon}} = \frac{1}{2}(\nabla u + (\nabla u)^T) \tag{VI.3}$$

where $\overline{\overline{\sigma}}$ and $\overline{\overline{\varepsilon}}$ are second-order stress and strain tensors, u is displacement, F is applied force, $\mathbb{C}$ is a fourth-order material tensor, and $(:)$ is the second-order tensor inner product. These equations are often written compactly as the Navier-Cauchy equations

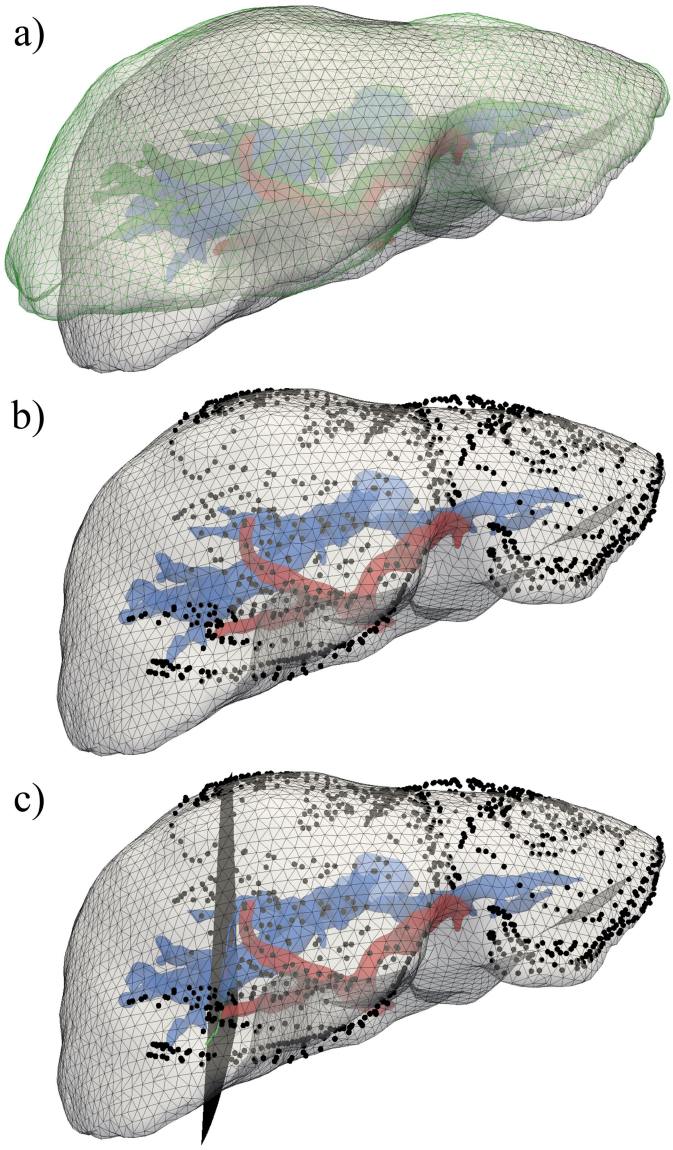

Figure VI.1: Data available for registration in hepatic image guidance. Deformable registration updates the preoperative model (parenchyma – gray; portal vein – red; hepatic vein – blue) to match intraoperative data while predicting internal displacements as accurately as possible. (a) Organ shape from intraoperative CT (green) indicates the full deformed surface of the liver. (b) In the surgical setting, points on the anterior surface of the liver (black) can be measured using tracked tools or computer vision. (c) A tracked intraoperative ultrasound plane allows localization of intrahepatic vessels and the posterior surface of the liver.

$$\mu\nabla^2 u + (\lambda+\mu)\nabla(\nabla\cdot u) + F = 0. \tag{VI.4}$$

under the condition of isotropy where λ and μ are the Lamé parameters. These equations represent the classic boundary value problem that requires knowledge about behavior on the boundary $\partial\mathcal{M}$ before a specific solution over the entire domain $\mathcal{M}$ can be solved. During registration, intraoperative data can be measured from the organ and combined with anatomical knowledge to either directly or indirectly enforce boundary conditions over the domain of the organ with the goal of accurately matching deformation between the intraoperative anatomy and an image-derived preoperative model. It should be noted that while the present description assumes linear elasticity, the same arguments may be extended to fully nonlinear representations with the addition of higher order terms on the overarching premise of strain energy decay.

VI.4.2 Transduction of Boundary Information

A crucial insight to be made is that any set of boundary conditions applied to a linear elastic domain can be decomposed into a superposition of a linearly independent basis of boundary conditions. These basis functions can be constructed point-wise so that the boundary interface $\partial\mathcal{M}$ consists of superposed independent point sources. This principle of domain decomposition is often used within the context of matrix condensation to facilitate real-time computation for *in silico* simulators that use finite element methods [180]. With this idea, consider the propagation of energy from any point source i located on $\partial\mathcal{M}$. The strain energy $U_i(r)$ stored in the domain at distance greater than r from the applied load is bounded by the Toupin-type decay [149]:

$$U_i(r) \leq U_i^0 e^{-k_i r} \tag{VI.5}$$

where $U_i{}^0 = U_i(0)$ is the total energy of perturbation and k_i is a rate constant. Whereas lossless transduction of energy from the boundary of a finite domain would be described by rigid motion such that $U_i(r) = U_i{}^0$ is necessarily zero everywhere, instead the distribution of strain energy decays exponentially with distance from the applied perturbation. Based on the Shannon information of this distribution, the uncertainty S_i of information provided by this point source measures the reduction in boundary energy that reaches any location in $\mathcal{M}$ given specified behavior from source i on $\partial\mathcal{M}$,

$$S_i(r) = -\ln\left(U_i(r)\right) \geq -k_i r - \ln\left(U_i{}^0\right). \tag{VI.6}$$

By this metric, a lower bound on the uncertainty in mechanical behavior given a known boundary condition increases linearly with distance away from that condition and logarithmically with the total energy of deformation imposed by the boundary condition. While the previous equation describes information theoretic as opposed to thermodynamic information, a thermodynamic resemblance does exist. Any mechanical excitation applied at the boundary contains directionally ordered information that randomizes, disperses, and attenuates as it propagates into the domain.

To first order approximation, the superposition of many point sources with weights α yields a strain energy state $U_\alpha(x)$ at any position $x \in \mathcal{M}$ with

$$U_\alpha(x) \leq U^0 e^{-k\delta} \tag{VI.7}$$

where $\delta = \min(||x - x_i||_2)$ is the shortest distance from x to any boundary condition located at $x_i \in \partial\mathcal{M}$, and

$$U^0 = \frac{V_\mathcal{M}}{2} \int_\mathcal{M} \left(\sum_i \alpha_i \overline{\overline{\sigma}}_i\right) : \left(\sum_i \alpha_i \overline{\overline{\varepsilon}}_i\right) d\mathcal{M} \tag{VI.8}$$

is the total energy added to the system with $V_{\mathcal{M}}$ the volume of the domain and $\overline{\overline{\sigma}}_i$ and $\overline{\overline{\varepsilon}}_i$ the basis of stress and strain tensors. The intrinsic uncertainty of the superposed state provided the configuration of boundary conditions is given by

$$S_\alpha(x) \geq k\delta - \ln\left(U^0\right). \tag{VI.9}$$

To incorporate the relationship between uncertainty and data distribution, a key observation is that any observed intraoperative data point used either directly as a boundary condition or indirectly to constrain or reconstruct one provides an uncertainty bound no stronger than an actual boundary condition that could be applied around that data point to perfectly describe the correct behavior. For a set of intraoperative data points Π, the uncertainty S_Π of the internal elastic response based on the observed data points is at least as great as the uncertainty S_α established by the correct set of superposed boundary conditions corresponding to the deformed state. The uncertainty created by the distribution of data points becomes

$$S_\Pi(x) \geq S_\alpha(x) \geq k\delta' - \ln\left(U^0\right). \tag{VI.10}$$

where the quantity $\delta' = \min\left(||x - x_\Pi||_2\right)$ now represents the distance to the closest data point $x_\Pi \in \Pi$.

Finally, the boundary information entropy H_Π is defined to be the average information over $\mathcal{M}$ given the data:

$$H_\Pi(x) = \frac{1}{V_{\mathcal{M}}}\int_{\mathcal{M}} S_\Pi(x)d\mathcal{M} = \frac{k}{V_{\mathcal{M}}}\int_{\mathcal{M}} \delta' d\mathcal{M} - \ln\left(U^0\right). \tag{VI.11}$$

Equations VI.10 and VI.11 are the main relationships introduced in this paper that measure a lower bound for the positional and average mechanical uncertainty given a spatial distribution of intraoperative data points provided for registration. In particular, the first term of these uncertainty metrics relates to the coverage of data throughout the domain of

interest while the second term relates to the amount of energy required to match a deformation state. While computations of the rate constant k and the strain energy U^0 require more description, these steps will be the focus of the following two sections. It is important to note that these quantities can be computed for a registration algorithm regardless of whether a basis for superposed boundary conditions has been explicitly defined as presented here.

VI.4.3 Rate of Information Decay

The rate of information decay k is a constant that depends on geometry and material parameters. In general, the rate constant takes the form $k = \gamma/s$, where s is a characteristic length and γ is a constant that has analytical solutions in 2D rectangular [181] and 3D cylindrical [182] coordinate systems. While s can be determined as functions of width or diameter in toy coordinate systems, in the case of arbitrary geometry [149] the characteristic length takes the form

$$s = \sqrt{\frac{\mu^*}{\rho\,{\omega_0}^2}} \tag{VI.12}$$

where $\mu^* = {\mu_M}^2/\mu_m$ for which $\mu_M = 2\mu + 3\lambda$ is the largest and $\mu_m = 2\mu$ is the smallest eigenvalue of $\mathbb{C}$ [150], ρ is the material density, and ω_0 is the lowest characteristic frequency of free vibration. Vibration theory lets this frequency be estimated from the Rayleigh quotient, which can be derived from setting the maximum potential energy of any static nonzero displacement field that satisfies Equations VI.1–VI.3 equal to the maximum kinetic energy of its undamped oscillation:

$${\omega_0}^2 = \frac{\mu^* \int_{\mathcal{M}} \overline{\overline{\varepsilon}} : \overline{\overline{\varepsilon}}\, d\mathcal{M}}{\rho \int_{\mathcal{M}} u \cdot u\, d\mathcal{M}}. \tag{VI.13}$$

If a basis of deformations is known, then the estimate can be obtained from ${\omega_0}^2 = \min\left({\omega_{0,i}}^2\right)$, where ${\omega_0}^2$ is identical to Equation VI.13 except $u = u_i$ and $\overline{\overline{\varepsilon}} = \overline{\overline{\varepsilon}}_i$.

For the purpose of describing the rate of energy decay, the characteristic length is scaled by the ratio of shear to longitudinal wave speed $1/\chi$ due to the observation that displacements applied to the boundary generate excitation that is not purely dilatational. In fact, it has been shown in the case of $\nu = 1/4$ that the amount of power radiated by a single boundary condition acting in the normal direction of a semi-infinite medium is approximately 3.7 times greater in the shear mode than the longitudinal mode of wave transmission [183]. The longitudinal wave speed $c_L = \sqrt{(\lambda + 2\mu)/\rho}$ and the shear wave speed $c_S = \sqrt{\mu/\rho}$ represent the maximum rate at which information can be propagated through the material in each mode, which gives a ratio

$$\chi = \frac{c_L}{c_S} = \sqrt{\frac{\lambda + 2\mu}{\mu}} = \sqrt{\frac{2 - 2\nu}{1 - 2\nu}} \tag{VI.14}$$

where ν is the Poisson ratio. In this way, the characteristic length s/χ now considers the dissipation of energy through the dominant shear mode and leads to the rate constant

$$k = \frac{\gamma\chi}{s} = \gamma\sqrt{\frac{(2 - 2\nu)\int_{\mathcal{M}} \overline{\overline{\varepsilon}} : \overline{\overline{\varepsilon}}\, d\mathcal{M}}{(1 - 2\nu)\int_{\mathcal{M}} u \cdot u\, d\mathcal{M}}}. \tag{VI.15}$$

or $k = \min(k_i)$ for a basis of u_i and $\overline{\overline{\varepsilon}}_i$. The rate factor γ is estimated experimentally by optimizing a root mean square (RMS) correlation coefficient described in Section VI.5.2.

VI.4.4 Energy of Deformation

The final quantity needed to compute S_Π and H_Π is the total energy of deformation U^0. Algorithmically, two variants of these uncertainty metrics are proposed depending on how k and more crucially U^0 are approximated. These variants lead to retrospective metrics S_r and H_r that utilize measurements of deformation and strain energy obtained after registration has completed, and prospective metrics S_p and H_p that use alternative estimates computed prior to initiating registration.

The retrospective metrics S_r and H_r assume a reliable estimate for the energy of deformation from the total strain energy of the registration solution,

$$U^0 = \frac{V_{\mathcal{M}}}{2} \int_{\mathcal{M}} \overline{\overline{\sigma}} : \overline{\overline{\varepsilon}} \, d\mathcal{M}. \tag{VI.16}$$

Substitution of Equations VI.15–VI.16 into Equations VI.10–VI.11 lead to generalized metrics for uncertainty S_r and entropy H_r that can be obtained after the completion of any elastic registration method from the solved displacement, stress, and strain fields, organ volume, the Poisson ratio, and the distribution of data points provided to the registration. Computation of these retrospective metrics is summarized in Algorithm 1.

Algorithm 1 Post-Registration (Retrospective) Uncertainty

RetrospectiveUncertainty[
Π – Point cloud of intraoperatively deformed organ features
M – Initial organ model rigidly registered to Π
V_M – Volume of M
$u(M,\Pi)$ – Displacement field of elastic registration from M to Π
$\varepsilon(M,\Pi)$ – Strain field of elastic registration from M to Π
$\sigma(M,\Pi)$ – Stress field of elastic registration from M to Π
ν – Poisson ratio]

1: **for** each point in M **do**
2: Compute distance $\delta(M,\Pi)$ to the nearest data point in Π
3: $ssu = \sum_{i=1}^{3} {u_i}^2$
4: $sse = \sum_{i=1}^{3} \sum_{j=1}^{3} {\varepsilon_{ij}}^2$
5: $sed = \sum_{i=1}^{3} \sum_{j=1}^{3} \sigma_{ij}\varepsilon_{ij}$ (strain energy density)
6: **end for**
7: $Id = \int \delta \, dM$
8: $Iu = \int ssu \, dM$
9: $Ie = \int sse \, dM$
10: $U = (V_M/2) \int sed \, dM$
11: $\omega = Ie/Iu$
12: $\chi = (2-2\nu)/(1-2\nu)$
13: $\gamma = 1.08$ (computed from Section VI.5.2)
14: $k = \gamma\sqrt{\chi\omega}$
15: $S_r = k\delta - \ln(U)$
16: $H_r = (k/V_M)Id - \ln(U)$
17: **return** :
S_r – Uncertainty of registration at each vertex of M
H_r – Entropy of registration over M

Whereas the generalized retrospective metrics can only be computed after registration has completed, a fully predictive metric that can be computed in real time during data collection would be invaluable for actively assisting image guided surgical applications. A fully predictive metric can be constructed if two conditions are met: if the rate constant is pre-computed from a known basis of boundary conditions or from simulating admissible displacements to estimate the Rayleigh quotient in Equation VI.13, and if the internal energy of deformation is estimated from external work. The total external work W can be approximated from model-data error after rigid registration from the Hookean relationship

$$W = \frac{1}{N_\Pi} \sum_{j=1}^{N_\Pi} \frac{1}{2} \kappa ||u_j||^2 = \frac{\kappa}{2N_\Pi} \sum_{j=1}^{N_\Pi} ||u_j||^2 \tag{VI.17}$$

where N_Π is the number of data points, κ is an effective spring constant, and $||u_j||$ is the magnitude of displacement between data point j and the corresponding position on the model, for which the closest point is the most conservative estimate. Then the energy of deformation can also be approximated as

$$\ln\left(U^0\right) = \ln\left(W\right) = \ln\left(\frac{1}{2N_\Pi} \sum_{j=1}^{N_\Pi} ||u_j||^2\right) + C \tag{VI.18}$$

where $C = \ln(\kappa)$ represents a constant shift that can be ignored for the purposes of establishing a correlation between uncertainty and registration error. Equations VI.10, VI.11, VI.15, and VI.18 then lead to fully predictive uncertainty metrics S_p and H_p that can be computed prior to registration from pre-computed examples of candidate deformations as summarized in Algorithm 2.

In the next sections, correlations of the uncertainties S_r and S_p are computed with respect to the proportion of residual target registration error defined as

$$E = TRE_d / \overline{TRE}_r \times 100\% \tag{VI.19}$$

Algorithm 2 Pre-Registration (Prospective) Uncertainty

ProspectiveUncertainty[
Π – Point cloud of intraoperatively deformed organ features
M – Initial organ model rigidly registered to Π
V_M – Volume of M
$u_1, u_2, \ldots, u_n$ – Displacement fields of candidate deformations
$\varepsilon_1, \varepsilon_2, \ldots, \varepsilon_n$ – Strain fields of candidate deformations
ν – Poisson ratio]

Ensure: Pre-compute

for $k = 1$ **to** n **do**
  for each point in M **do**
    $ssu_k = \sum_{i=1}^{3} {u_i}^2$
    $sse_k = \sum_{i=1}^{3} \sum_{j=1}^{3} {\varepsilon_{ij}}^2$
  end for
  $Iu_k = \int ssu_k \, dM$
  $Ie_k = \int sse_k \, dM$
end for
$\omega = \min(Ie/Iu)$
$\chi = (2-2\nu)/(1-2\nu)$
$\gamma = 6.62$ (computed from Section VI.5.2)
$k = \gamma\sqrt{\chi\omega}$

Ensure: Intraoperatively

for each point in M **do**
  Compute distance $\delta(M,\Pi)$ to the nearest data point in Π
end for
$Id = \int \delta \, dM$
for each point in Π **do**
  Compute distance $d(\Pi,M)$ to the nearest corresponding feature point in M
end for
$W = 1/(2N_\Pi)\sum_{i=1}^{N_\Pi} {d_i}^2$
$S_p = k\delta - \ln(W)$
$H_p = (k/V_M)Id - \ln(W)$
return :
  S_p – Uncertainty of registration at each vertex of M
  H_p – Entropy of registration over M

at each target where TRE_d is the final target registration error after deformable registration and $\overline{TRE}_r$ is the average target registration error after an initial rigid registration of the organ. Furthermore, the entropy metrics H_r and H_p are correlated against $\overline{E}$, the average proportion of residual TRE. These residual TRE values signify the relative proportion of error remaining after deformable registration. For evaluation in this paper, elastic registrations are computed using the linearized iterative boundary reconstruction method described in [20] and all variables are defined in MKS units.

VI.4.5 Spatial Distributions of Predicted TRE

Pointwise spatial estimation of residual TRE at each vertex of $\mathcal{M}$ is enabled by fitting joint bivariate gamma (bigamma) distributions relating E to S_r and E to S_p. Bivariate gamma distributions excel at describing recurring attenuation of signal due to multipath propagation or partial obstructions, and have found applications modeling fading channels in radiofrequency analysis [184] and the relationships between rainfall and runoff in hydrology [185]. The shape of the gamma distribution is highly flexible and generalizes many common distributions including the chi-square, exponential, and Rayleigh distributions. Note that if individual components of TRE are independent and normally distributed in each spatial direction as presented in [173], then the magnitude of TRE is by definition Rayleigh-distributed and the sum of squares chi-squared. These characteristics make the bigamma distribution exceptionally pertinent to the present application of describing the relationship between the dispersive propagation of boundary energy and the reduction in TRE. The bivariate gamma distribution used in this paper is a six-parameter adaptation of [186] and its formulation and parameter estimation are described in Section VI.8. Bigamma distributions $P\left(S_r, E|\hat{\theta}_r\right)$ and $P\left(S_p, E|\hat{\theta}_p\right)$ are computed by fitting distribution parameters $\hat{\theta}_r$ and $\hat{\theta}_p$ to data described in Section VI.5 using the method of Section VI.8. After these distributions are fit, the probability distribution of residual error is predicted at every spatial location from the conditional distributions $P(E|S_r)$, $P(E|S_p)$ and new val-

ues of S_r and S_p computed across $\mathcal{M}$. These pointwise probability distributions can be summarized into a spatial uncertainty map from distribution medians or confidence intervals. Algorithm 3 outlines this process for predicting residual TRE from retrospective and prospective uncertainty metrics.

Algorithm 3 Prediction of Residual TRE

PredictResidualTRE[
S – Registration uncertainty at each vertex of organ model
H – Registration entropy of organ model given data]

Ensure: Pre-compute
Set bivariate gamma parameters $\hat{\theta}_r$ and $\hat{\theta}_p$ (see Section VI.8)
Compute lookup tables $P\left(S,E|\hat{\theta}_r\right)$ and $P\left(S,E|\hat{\theta}_p\right)$ from Section VI.8
Ensure: Intraoperatively
if S, H are post-registration (retrospective) metrics **then**
    $P(S,E) = \left(S,E|\hat{\theta}_r\right)$
    $\alpha = 14.1$; $\beta = 19.0$ (see linear model Section VI.5.2)
else if S, H are pre-registration (prospective) metrics **then**
    $P(S,E) = \left(S,E|\hat{\theta}_p\right)$
    $\alpha = 5.1$; $\beta = 40.0$ (see linear model Section VI.5.2)
end if
Set p as percentile of interest (e.g. 0.5 or 0.05 and 0.95)
for each value in S **do**
    Interpolate $P(E|S)$ from joint distribution $P(S,E)$
    $F(E|S) = \int_0^x P(E|S)\,dE$ (cumulative distribution function)
    $E_p = F^{-1}(p)$ (p-quantile function)
end for
$\overline{E} = \alpha H + \beta$
return :
    E_p – p^{th} percentile of residual TRE at each vertex of organ model
    $\overline{E}$ – Average residual TRE across organ model after registration

VI.5 Experimental Simulations

VI.5.1 Data

The proposed metrics are evaluated on a dataset of 6,291 registration scenarios (dataset A, previously reported in [20]) derived from three patient-specific liver geometries (Livers 1, 2, and 3) each subjected to three unique liver deformations of mobilization from the left triangular ligament, no ligaments, or right triangular ligament (L, N and R) and mapped

from the profile of 147 target displacements in a silicone phantom after it was subjected to these deformations inside a laparoscopic simulator. For each of the nine deformed organs, a sparse pattern of anterior surface data and 16 simulated ultrasound (US) planes were generated. These data were assembled into combinatorial configurations of intraoperative data for registration, consisting of:

(i) Anterior surface data only, $n = 9$;

(ii) Anterior surface data plus one US plane, $n = 144$;

(iii) Anterior surface data plus two US planes, $n = 1{,}080$;

(iv) Anterior surface data plus three US planes, $n = 5{,}040$;

(v) Anterior surface data plus all 16 US planes, $n = 9$;

(vi) Ground truth position of the complete surface plus the complete intrahepatic vessel structure, $n = 9$.

A representative subset of examples from these data configurations is shown in Figure VI.1. TRE is measured as the Euclidean distance between the registered and ground truth positions of each vertex in the volumetric liver mesh, creating 27,218 (Liver 1), 31,044 (Liver 2), and 18,821 (Liver 3) total targets per registration instance. In total, over 161 million individual target samples are considered in this first dataset, from which model parameters are fitted and correlations between the uncertainty metrics and registration error are cross validated in a leave-one-out experimental design.

A novel dataset was also created for independent validation using the same data generative method of [20]. In this case, a displacement field was obtained from the motion of 159 target positions embedded in a silicone liver phantom imaged before and after the phantom was placed in an open surgical configuration with deformation created by perihepatic packing placed beneath the posterior surface of the liver. This displacement field

was mapped onto a novel patient-specific liver geometry consisting of 25,905 mesh vertices that are each treated as target locations. Intraoperative data were simulated combinatorially as previously described. This validation dataset (dataset B) represents 699 additional registration scenarios based on a novel liver geometry and novel deformation profile.

VI.5.2 Prediction of Average Residual Error

For each of the nine deformed organs in dataset A, Pearson correlation coefficients were computed between H_r and $\overline{E}$, and H_p and $\overline{E}$ as represented by Figure VI.3a. The RMS value of these correlation coefficients was maximized to determine the rate factor γ in Figure VI.2, from which optima were found at $\gamma_r = 1.08$ and $\gamma_p = 6.62$. These values were used for the rest of the analysis in this paper. Figure VI.3a shows strong linear relationships that suggest registration error may be minimized in each instance of organ deformation by supplying a configuration of intraoperative data that minimizes the entropy of boundary information. Furthermore, a linear regression may be used to predict the amount of elastic correction achievable from a provided pattern of intraoperative data coverage.

To assess general predictive capability across multiple deformations and organ shapes, prediction errors were cross-validated in a leave-one-out fashion. Linear regressions were fit to registrations from eight of the nine deformations in dataset A and predictions for $\overline{E}$, the average proportion of residual TRE, were made from the values of each entropy metric H_r and H_p for each registration in the left-out deformation. With respect to quantitative predictive value, if the average rigid TRE values reported in Table VI.1 were known, the RMS error in predicted average TRE after elastic registration would be 1.1 mm for the retrospective metric H_r and 1.2 mm for the prospective metric H_p across all nine leave-one-out cross-validations. These values suggest that the proposed entropy metrics predict overall registration performance quite accurately. Although the actual value of average rigid TRE is typically unknown, in practice a value could be inferred or conservatively estimated for an organ if an interpretation with spatial length scale is needed. Differences in the predicted

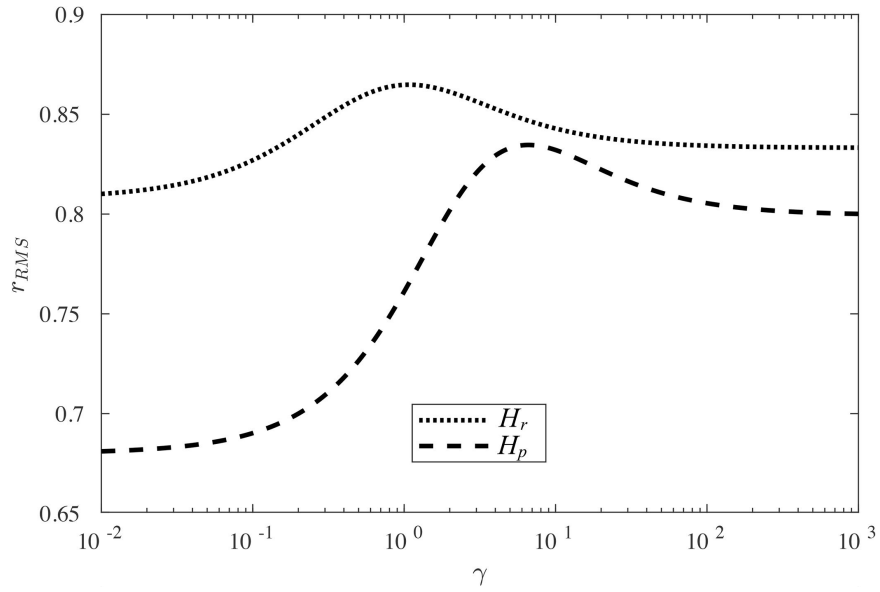

Figure VI.2: RMS Pearson correlation coefficient plotted against rate factor γ for retrospective and prospective information metrics. As γ grows large, H_Π depends only on the first distance term and as γ approaches zero, H_Π depends only on the second energy of deformation term. The existence of prominent optima suggests that both terms contribute complementary information towards predicting registration performance. At small γ, the average correlation coefficient is considerably lower for H_p than H_r because the prospective formulation approximates energy of deformation less accurately than achievable with internal strain energy. At large γ, the difference relates to rate constant computation, where the prospective metric estimates the fundamental frequency by the lowest mode response from a series of candidate deformations, whereas the post-registration internal metric computes a fundamental frequency from the actual activation of deformation modes in the system. An empirical characterization of the rate factor γ affords leniency in the approximations made for the prospective metric without sacrificing substantial predictive value.

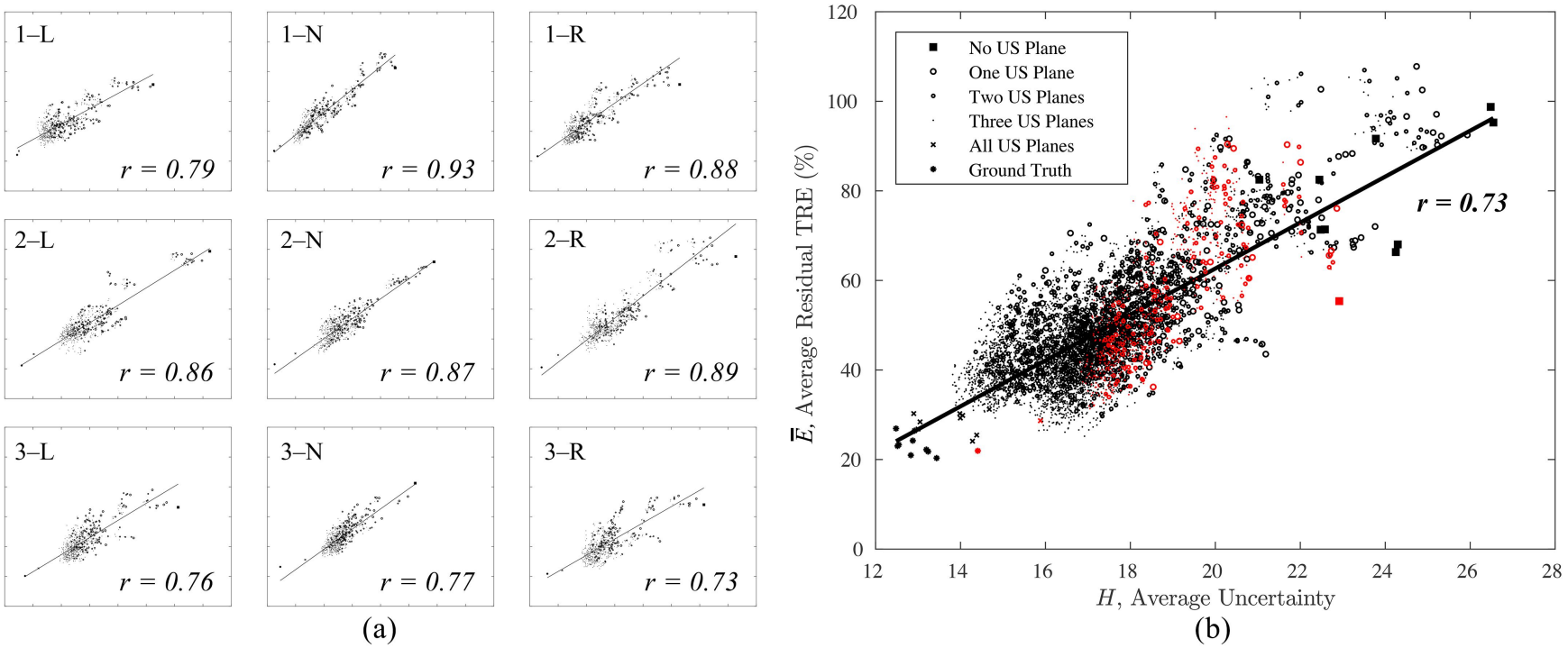

Figure VI.3: Linear regressions between average residual target registration error $\overline{E}$ and information entropy H_p with each point representing one registration to a specific configuration of intraoperative data from dataset A. (a) Correlations of $\overline{E}$ and H_p for each of the nine deformation conditions of dataset A. Axes same as (b). (b) All 6,291 registrations from dataset A and total regression line (black) plotted with the 699 registrations from the separate validation dataset (red). Legend indicates the extent of intraoperative data provided to each registration.

Deformation	Mean Rigid TRE (mm)	Error in Predicted Elastic TRE (mm), H_r	Error in Predicted Elastic TRE (mm), H_p	Error in Predicted Residual TRE (%), H_r	Error in Predicted Residual TRE (%), H_p
1–L	12.4	0.9 (0.7 ± 0.5)	0.8 (0.6 ± 0.5)	7.0 (5.9 ± 3.8)	6.3 (4.9 ± 4.0)
1–N	15.3	1.5 (1.4 ± 0.7)	2.0 (1.8 ± 0.8)	10.0 (9.0 ± 4.4)	13.1 (11.9 ± 5.5)
1–R	14.9	0.9 (0.7 ± 0.5)	1.1 (0.8 ± 0.7)	5.7 (4.5 ± 3.6)	7.3 (5.5 ± 4.8)
2–L	10.9	0.7 (0.5 ± 0.4)	0.7 (0.5 ± 0.4)	6.2 (4.9 ± 3.8)	6.4 (5.0 ± 4.1)
2–N	16.9	1.5 (1.3 ± 0.7)	1.0 (0.8 ± 0.5)	8.6 (7.7 ± 3.9)	5.6 (4.7 ± 3.2)
2–R	12.5	1.0 (0.7 ± 0.7)	1.1 (0.8 ± 0.8)	8.1 (5.8 ± 5.7)	8.8 (6.1 ± 6.4)
3–L	12.8	1.2 (1.1 ± 0.6)	1.2 (1.1 ± 0.6)	9.5 (8.5 ± 4.3)	9.6 (8.4 ± 4.7)
3–N	13.9	0.6 (0.5 ± 0.3)	0.8 (0.6 ± 0.4)	4.0 (3.4 ± 2.1)	5.4 (4.6 ± 2.9)
3–R	15.1	1.2 (1.1 ± 0.6)	1.6 (1.4 ± 0.8)	8.2 (7.2 ± 3.9)	10.9 (9.6 ± 5.3)
Total	**—**	**1.1 (0.9 ± 0.6)**	**1.2 (0.9 ± 0.8)**	**7.7 (6.3 ± 4.4)**	**8.5 (6.7 ± 5.3)**
Validation	*5.4*	*1.1 (0.9 ± 0.5)*	*0.5 (0.4 ± 0.3)*	*19.7 (17.6 ± 8.8)*	*10.2 (8.4 ± 5.9)*

Table VI.1: Prediction of average registration error from boundary information entropy. Predictive errors reported as RMSE (MAE ± STD): RMSE root mean square error; MAE mean absolute error; STD standard deviation.

and actual proportion of average residual TRE ($\overline{E}$) are shown in the last two columns of Table VI.1, with total RMS prediction error of 7.7% (H_r) and 8.5% (H_p) across the leave-one-out experiments, meaning that the metric-estimated percentage of TRE remaining after elastic registration was accurate to approximately ±8% of the underlying magnitude of rigid error.

Combining all 6291 registrations from dataset A leads to linear regressions between $\overline{E}$ and H with 95% confidence intervals and correlation coefficients

$$\overline{E} = [14.1 \pm 0.3]H_r - [19.0 \pm 1.3]; \;\; r = 0.78$$

$$\overline{E} = [5.1 \pm 0.1]H_p - [40.0 \pm 2.0]; \;\; r = 0.73$$

Prediction accuracy of $\overline{E}$ is independently evaluated with validation dataset B using these total regressions to dataset A. Figure VI.3b plots the total regression of H_p and $\overline{E}$ from dataset A compared to the values of H_p and $\overline{E}$ from all registrations in dataset B, illustrating consistent alignment of the metric regression across disparate cases. The final row of Table VI.1 provides numerical results for the accuracy of TRE prediction from retrospective and prospective entropy metrics. While the length scales of prediction errors

are in agreement between both datasets, it is expected that the percentage of residual error becomes less stable when the total energy of deformation is small, such as in the case of validation dataset B for which the average rigid TRE was only 5.4 mm. For increasingly rigid systems, $\overline{E}$ becomes more sensitive and the uncertainty bound becomes degenerate as U_0 approaches zero and ω_0 is inferred from a state approaching zero displacement and zero strain. It is intuitive that a degenerate case is reached in the limit of zero deformation because no energetic information is introduced to the system.

VI.5.3 Prediction of Pointwise Residual Error

To analyze pointwise TRE predictions, the bivariate distributions were fit and evaluated using a similar leave-one-deformation-out approach from dataset A, plus independent validation from dataset B. After registration, the 161 million target samples in dataset A provide paired observations of the uncertainty metrics S and error residuals E. These target samples are separated into nine groups respective to the underlying liver geometry and deformation profile. The joint relationships of these paired observations S and E are shown for each deformation condition in Figure VI.4a. Bigamma probability distributions $P(S,E)$ are alternately fit to all target samples from eight of the nine groups, and samples from the last group are withheld for evaluation. For evaluation, the median predicted values of $E_{0.5}$ are obtained for the withheld group using the conditional distribution $P(E|S)$. The predicted median residual $E_{0.5}$ and the actual residual E are compared in Table VI.2 for predictions based on the post-registration retrospective metric S_r and the pre-registration prospective metric S_p. If the average rigid TRE were to be known or estimated for each registration, then both the prospective and retrospective registration uncertainty metrics could predict pointwise elastic TRE from the distribution median to less than 4.5 mm RMS error across all cross-validated samples in dataset A. However, the absolute difference between the predicted and actual percentage of residual error at each target was approximately 30% RMS.

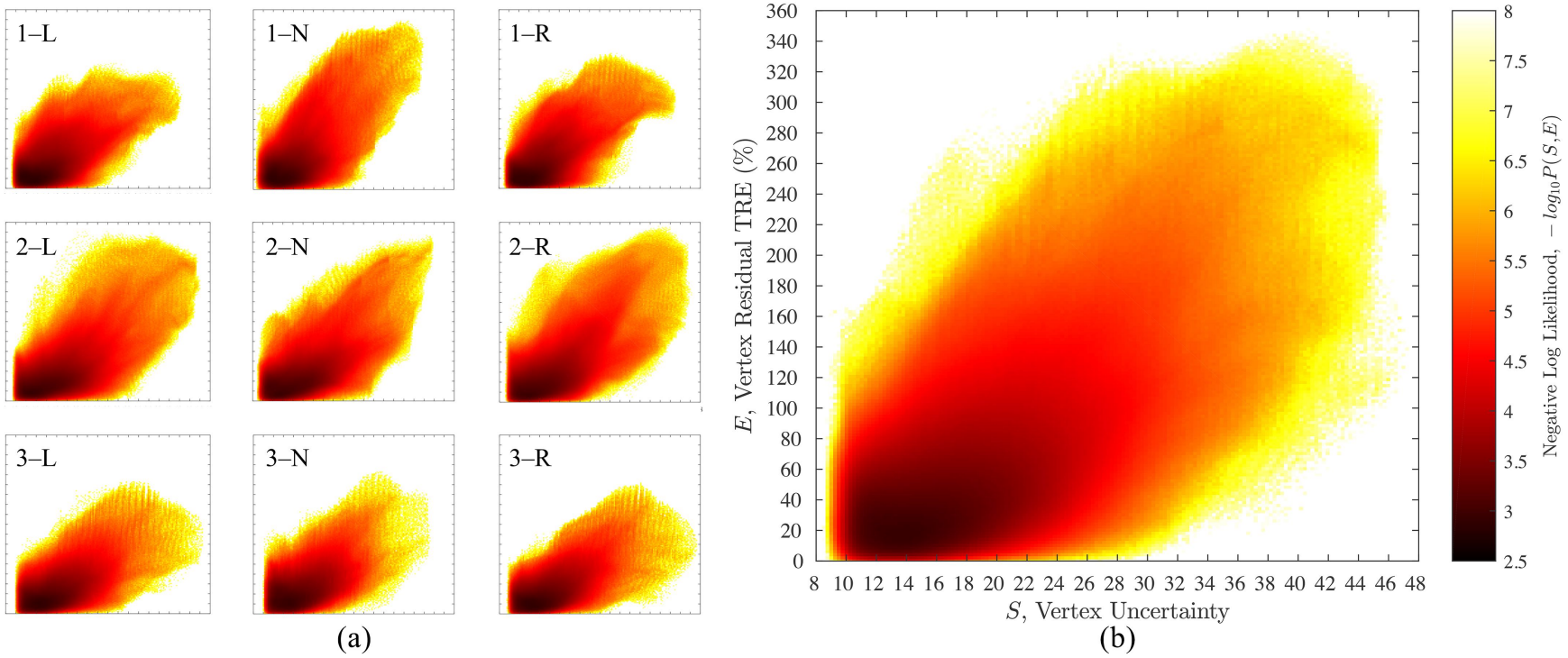

Figure VI.4: Empirical joint distributions of paired observations between residual error E and uncertainty S_p. (a) Empirical distributions drawn from all registrations of each of the nine deformation conditions of dataset A, plotted on the same axes as (b); (b) The total empirical joint distribution using all targets in dataset A.

Deformation	Mean Rigid TRE (mm)	Error in Predicted Elastic TRE (mm), S_r	Error in Predicted Elastic TRE (mm), S_p	Error in Predicted Residual TRE (%), S_r	Error in Predicted Residual TRE (%), S_p
1–L	12.4	3.4 (2.6 ± 2.3)	3.5 (2.5 ± 2.4)	27.7 (20.8 ± 18.3)	28.3 (20.5 ± 19.5)
1–N	15.3	5.7 (3.8 ± 4.3)	5.9 (3.8 ± 4.5)	37.3 (24.8 ± 27.9)	38.5 (25.1 ± 29.2)
1–R	14.9	4.5 (3.3 ± 3.1)	4.6 (3.3 ± 3.2)	30.2 (22.0 ± 20.7)	30.9 (22.1 ± 21.5)
2–L	10.9	3.4 (2.4 ± 2.4)	3.4 (2.4 ± 2.5)	30.9 (21.6 ± 22.0)	31.5 (21.7 ± 22.9)
2–N	16.9	5.4 (3.6 ± 4.0)	5.2 (3.6 ± 3.8)	32.0 (21.3 ± 23.9)	30.7 (21.0 ± 22.4)
2–R	12.5	4.5 (3.0 ± 3.3)	4.6 (3.1 ± 3.4)	35.6 (24.3 ± 26.0)	36.3 (24.6 ± 26.7)
3–L	12.8	3.2 (2.4 ± 2.0)	3.2 (2.4 ± 2.0)	24.7 (19.1 ± 15.6)	24.7 (18.9 ± 15.9)
3–N	13.9	3.5 (2.7 ± 2.3)	3.6 (2.7 ± 2.3)	25.1 (19.1 ± 16.3)	25.5 (19.4 ± 16.6)
3–R	15.1	3.6 (2.8 ± 2.3)	3.6 (2.8 ± 2.3)	24.0 (18.4 ± 15.3)	24.1 (18.8 ± 15.1)
Total	**—**	**4.3 (3.0 ± 3.1)**	**4.4 (3.0 ± 3.2)**	**30.7 (21.6 ± 21.9)**	**31.1 (21.7 ± 22.4)**
Validation	*5.4*	*2.0 (1.6 ± 1.2)*	*2.0 (1.4 ± 1.4)*	*37.0 (29.4 ± 22.5)*	*36.9 (26.3 ± 25.9)*

Table VI.2: Prediction of pointwise registration error from boundary information uncertainty. Predictive errors reported as RMSE (MAE ± STD): RMSE root mean square error; MAE mean absolute error; STD standard deviation.

All 161 million target samples from dataset A were combined into an empirical distribution (see Figure VI.4b) and bigamma distribution parameters were estimated for S_r and S_p metrics as reported and qualified in Appendix A. From these distributions, median residual TRE values were predicted from S_r and S_p computed on dataset B and were compared against the observed residual TRE. Prediction errors for these pointwise estimates from dataset B are displayed in the final row of Table VI.2 and agree in magnitude with errors obtained from the leave-one-out study on dataset A. While the results of VI.4 and Table VI.2 are informative, Figure VI.5 further illustrates predictive capability. Figure VI.4a–c demonstrate the predicted distribution of residual TRE in comparison to ground truth TRE in VI.4d–e as the amount of data provided to the registration is incremented by adding sparse features from tracked intraoperative ultrasound planes.

VI.6 Discussion

VI.6.1 Prospective Application

The contribution herein demonstrates that uncertainty in elastic registration is inherent when incomplete information is provided, and that an uncertainty metric that correlates with the proportion of TRE remaining after registration can be computed from the spatial

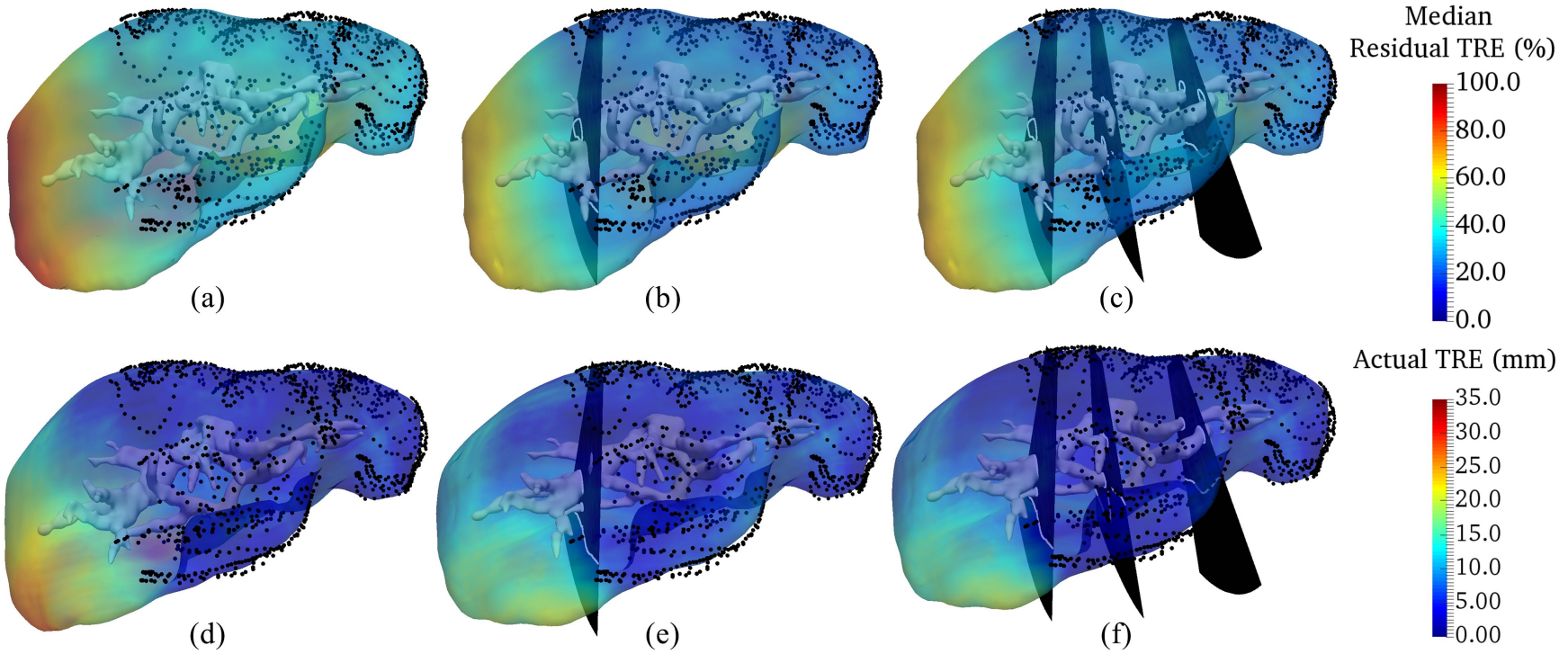

Figure VI.5: Predicted median residual TRE (top) and actual TRE (bottom) after elastic registration. (a,d) Error profiles of registration to surface data pattern (black). (b,e) Error profiles after data from one additional US plane is added to registration. (c,f) Error profiles with data from three US planes provided. The distributions of predicted residual TRE can guide additional data collection to areas of poor expected performance for improving registration fidelity.

coverage of supplied data. Registration uncertainty was found to depend on two crucial variables, firstly the distance from a target within an organ to the closest intraoperative data point that most strongly informs its motion, and secondly the total amount of deformation described by the intraoperative data. These relationships substantiate a trend for data collection that aims to maximize registration performance: data should be collected as broadly as possible, with special focus placed near interventional targets and in regions of greatest organ deformation.

However, practical constraints often make intraoperative data collection time-intensive and encumbering to personnel. These real-world limitations inspire a need for new approaches that inform and allow optimization of the data collection process. The entropy and uncertainty metrics proposed in this paper address this need in several ways. First, a monotonic decrease in total registration error over the domain is expected as entropy decreases. Subsequently, the summary number H_p can be computed and monitored in real time during data collection to potentially reveal local saturation of data coverage that ceases to improve overall registration quality. Second, the effectiveness of elastic registration at any target of interest can be estimated based on a confidence interval or average value of predicted residual error inferred from the pointwise registration uncertainty S. Third and foremost, as illustrated in Figure VI.5, a spatial map of the predicted TRE distribution can be constructed to indicate regions of poor registration performance. These maps can suggest regions requiring improvements to data coverage or they can qualify localization accuracy after registration has completed to mitigate guidance errors. Although registration to partial data fundamentally prevents exact prediction of TRE because a specific unknown underlying organ deformation must be selected from many potentially valid solutions, this paper contributes a means by which data sufficiency can be estimated through correlation to measured results.

VI.6.2 Prediction Quality

Only a small number of prior studies have aimed to experimentally validate TRE predicted by rigid registration theory. In [187], the difference between measured and estimated average TRE predicted by the method of [172] was found to be 1.3 ± 1.2 mm. In [188], pointwise measurements and estimates of TRE predicted by [176] were reported to be 3.1 ± 1.2 mm. The results reported in Table VI.1 and Table VI.2 indicate that the boundary information entropy and uncertainty metrics proposed in this work for nonrigid elastic registration are able to achieve a similar range of TRE prediction error, with average error prediction equivalent to 0.9 ± 1.6 mm and pointwise error prediction equivalent to 3.0 ± 3.1 mm if baseline rigid TRE could be anticipated or identified. However, it must be stressed that S and H are regressed to the proportion of uncorrected error after elastic registration instead of the final magnitude of TRE. This approach provides superior correlation that accounts for relative variation in initial error compared to the total capacity of correction.

VI.6.3 Limitations

The derivation presented in Section VI.4 makes a significant assumption that only the behavior of the closest information source contributes to mechanical uncertainty. While powerful results are achieved, interactions among multiple intraoperative data constraints are not considered and the derived metrics represent lower bounds for uncertainty and entropy to only first order terms. It is likely that higher-order terms could be introduced to the uncertainty model to produce a more exact bound for the dependence of elastic registration on the energetic propagation of boundary information.

Finally, while it is beneficial that the datasets used for evaluation contain large variation in data coverage for characterizing behavior across a wide range of inputs, it is possible that sensitivity of registration to marginal changes in data content may not be easily detected compared to underlying sources of registration noise such as mesh discretization, linearity assumptions, and instrumentation errors. Moreover, the parameters θ and γ optimized in

this work based on dataset A may contain latent dependency on registration method or domain parameters.

VI.7 Conclusions

This paper presents a method for estimating the spatial distribution of elastic registration uncertainty using an information-theoretic approach to characterize the dissipation of boundary energy as it propagates from data constraints towards the remaining volume of an organ. Proposed metrics for registration uncertainty can be rapidly computed for any linear elastic registration method. Regressions are fit and evaluated on over 6,000 total simulated registrations consisting of over 160 million individual targets to infer average TRE from registration uncertainty using a standard linear model and spatial covariation of variables using bivariate gamma statistics. The results illustrate that TRE remaining after elastic registration can be accurately predicted from the spatial distribution of data provided to the registration.

VI.8 Appendix: Bivariate Gamma Distribution

A six-parameter bivariate gamma distribution used in this work is extended from the five-parameter mixed effects model by G. C. Ghirtis [186] by adding one location parameter S_0 to allow translation. Suppose q, r, and s are gamma-distributed random variables. Then the uncertainty S and the proportion of residual error E are defined to be a weighted sum of the underlying random variables so that

$$S = \xi(q+r) + S_0 \tag{VI.20}$$

$$E = \eta(q+s) \tag{VI.21}$$

where ξ and η are scale parameters of the distribution. Then the joint distribution provided shape parameters a, b, and c is

$$P(S,E|\theta) = \frac{e^{-\left(\frac{S-S_0}{\xi}+\frac{E}{\eta}\right)}}{\lambda^b \mu^c \Gamma(a)\Gamma(b)\Gamma(c)} I_q \tag{VI.22}$$

where $\theta = [S_0, \xi, \eta, a, b, c]$, $\Gamma(\cdot)$ is the gamma function, and

$$I_q = \int_0^m q^{a-1}(S - S_0 - \xi q)^{b-1}(E - \eta q)^{c-1} e^q dq \tag{VI.23}$$

for $m = \min\left(\frac{S-S_0}{\xi}, \frac{E}{\eta}\right)$. The marginal distributions are also gamma-distributed according to,

$$P(S) = \frac{(S-S_0)^{a+b-1}}{\xi^{a+b}\Gamma(a+b)} e^{-\frac{S-S_0}{\xi}} \tag{VI.24}$$

$$P(E) = \frac{E^{a+c-1}}{\eta^{a+c}\Gamma(a+c)} e^{-\frac{E}{\eta}}. \tag{VI.25}$$

From a set of paired observations (S,E), parameter estimates $\hat{S}_0$, $\hat{\xi}$, $\hat{\eta}$, $\hat{a}$, $\hat{b}$, and $\hat{c}$ can be obtained by the method of moments with

$$\begin{cases} \hat{S}_0 = \min(S) \\ \hat{\xi} = var(S - \hat{S}_0)/mean(S - \hat{S}_0) \\ \hat{\eta} = var(E)/mean(E) \\ \hat{a} = \frac{mean(S-\hat{S}_0)mean(E)cov(S-\hat{S}_0,E)}{var(S-\hat{S}_0)var(E)} \\ \hat{b} = mean(S - \hat{S}_0)^2/var(S - \hat{S}_0) - \hat{a} \\ \hat{c} = mean(E)^2/var(E) - \hat{a} \end{cases} \tag{VI.26}$$

as derived in [186]. These initial parameters are further optimized using the Nelder-Mead downhill simplex method by minimizing the squared Hellinger distance defined as,

$$h^2(P,Q) = 1 - \sum_{(S,E)} \sqrt{P(S,E)Q(S,E)} \tag{VI.27}$$

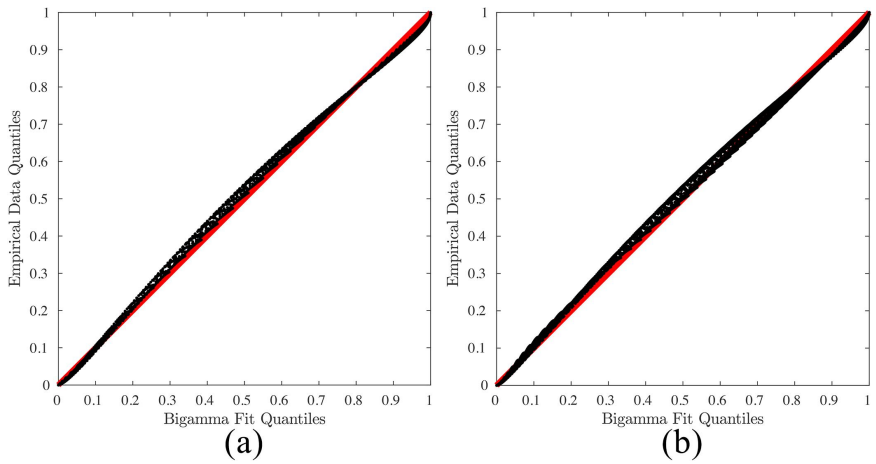

Figure VI.6: (a) Quantile-quantile plot between joint cumulative distributions of $P(S_r, E|\hat{\theta}_r)$ and $Q(S_r, E)$ from post-registration metric. (b) Quantile-quantile plot between joint cumulative distributions of $P(S_p, E|\hat{\theta}_p)$ and $Q(S_p, E)$ from pre-registration metric.

where $P(S,E)$ is given by Equation VI.22 and $Q(S,E)$ is an empirical probability distribution constructed from the set of paired observations.

The optimized parameter estimates $\hat{\theta} = \left[\hat{S}_0, \hat{\xi}, \hat{\eta}, \hat{a}, \hat{b}, \hat{c}\right]$ for S_r and S_p for all samples in dataset A are:

$$\hat{\theta}_r = [2.5268, 0.5024, 20.2834, 1.3712, 2.8348, 0.9045]$$

$$\hat{\theta}_p = [9.0537, 2.3825, 20.2154, 1.2164, 2.0696, 1.0654]$$

The quality of the distribution regressions are illustrated in Figure VI.6, which shows close agreement in quantile-quantile plots between the cumulative distributions of $P(S,E)$ and $Q(S,E)$ for S_r and S_p.

Additionally, for comparison, Appendix D provides plots for the marginal distribution fits of the bivariate gamma distribution to the empirical distribution from dataset A. Appendix D also includes plots for regression to a bivariate lognormal distribution as an alternative distribution type. From this it can be seen clearly that the bivariate gamma distribution provides a vastly superior fit.

CHAPTER VII

Summary and Future Directions

VII.1 Dissertation Summary

This dissertation presents a collection of developments towards advancing mechanics-based modeling approaches for compensating soft tissue deformation to enhance the ability to localize and treat disease during image-guided liver procedures. This dissertation makes substantial advancements to the state of the art, being the first to (1) characterize the relative magnitudes of open and laparoscopic deformations of the liver during image guidance in humans, (2) extend the accuracy of model-based deformable registration beyond conventional limitations through incorporation of subsurface features from iUS, and (3) establish a framework for predicting the accuracy and uncertainty of elastic deformable registration techniques from the configuration of constraints supplied to the registration problem. These works enable and demonstrate that high localization accuracy can be achieved in the presence of soft tissue deformation, and that quantifiable certainty can be established around the accuracy of mechanics-based deformable registration approaches. These advances are crucial to ensuring the accuracy, reliability, and safety of intraoperative image-guided procedures, and are positioned to become critical components of the next generation of image guidance systems that expand surgical, interventional, and therapeutic capabilities.

VII.2 Future Directions

Although significant improvements have been made, continued work is still required to fulfill unmet needs surrounding image-guided delivery of liver therapies. This section describes future approaches that aim to provide more accurate registrations through advanced modeling of physiological effects, and to establish a more comprehensive guidance solution for real-time visualization and navigation of deforming anatomy. Ongoing new applications for the registration methods introduced in this dissertation are also discussed.

VII.2.1 Modeling Tissue Volume and Engorgement

Although elastic deformation methods are well suited to registration and can perform quite effectively using energy minimization [10] and energy regularization [2, 20] techniques, one of the primary limitations of elastic deformation models is the inability to represent volume change without incurring large amounts of strain energy in the system. Therefore, additional modeling efforts are required to be able to more accurately represent deformation under conditions where relative change in organ volume may occur. These volume changes between preoperative and intraoperative organ states can arise from a multitude of factors, including portal vein embolization and ligation, chemotherapy, diet and hydration status, and laparoscopic insufflation pressure.

VII.2.1.1 Embolization and Ligation

Patients who do not meet eligibility criteria for resection due to insufficient liver remnant volume may undergo portal vein embolization or portal vein ligation to increase functional liver volume and bridge to potentially curative therapy through resection. In these procedures, blood flow to a branch of the portal vein is physically restricted to induce atrophy in the ipsilateral side of the liver and compensatory hypertrophy in the contralateral side [189, 190]. A meta-review of portal vein embolization showed that the average change in contralateral hypertrophic volume was +37.9% with a range of 20.5% to 69.4%, while the average change in ipsilateral atrophic volume was -12.3% with a range of -24.5% to 0.0% within one month of embolization [190]. Portal vein ligation has been shown to cause a significantly more rapid change in functional liver volume than portal vein embolization, averaging an increase of 48.8% over a median of 7.5 days [191].

VII.2.1.2 Preoperative Chemotherapy

Preoperative chemotherapy is commonly delivered to patients with metastatic disease to control progression or downstage disease to resectable limits. However, chemotherapeutic regimens can also cause volumetric change of the liver though atrophy or compensation

in response to hepatotoxicity. In cohort of 459 mCRC patients undergoing preoperative chemotherapy, volume change ranged from -40% to +19%, with median change of -2.1% [192]. Within this population, 18.5% of patients experienced atrophy of the total liver volume exceeding 10%.

VII.2.1.3 Diet and Hydration

The liver also undergoes daily cyclical changes in volume due to diet and hydration status. Throughout the day, liver volume in healthy subjects has been shown to change by an average of 17% (range 9–31%) from peak values in the morning to minimum values in the early afternoon [193]. The same study also showed that these changes in liver volume were accelerated by changes in blood sugar and diuresis [193]. These variations in liver volume have been clinically observed in patients undergoing OLR. Heizmann *et al.* performed a study comparing liver volumes of OLR patients measured with preoperative and intraoperative CT. Compared to volumes measured from preoperative imaging, the intraoperative volume of the liver was observed to differ by -13% to +24%, with average absolute change of 7% [123] due to uncontrolled variations from these effects and potential changes caused by chemotherapeutic regimens not reported in patient selection criteria.

VII.2.1.4 Laparoscopic Insufflation

Laparoscopic insufflation can also induce volume change of the liver. In a pilot experiment, contrast-enhanced CT images of a sheep liver were obtained before and after insufflation of the abdominal cavity (Figure VII.1). From these images, liver volumes were segmented and volume was found to increase by 7.0%, from 839.7 mL to 898.3 mL. The volume change induced by insufflation is likely caused by swelling in response to changes in pressure gradients across vascular inflow and outflow of the liver. Measurements made in porcine insufflation studies have indicated that pressure of the portal vein and inferior vena cava increase in a one-to-one ratio with insufflation pressure [194], while pressure of the hepatic artery remains approximately constant throughout insufflation [195]. This change in pressure

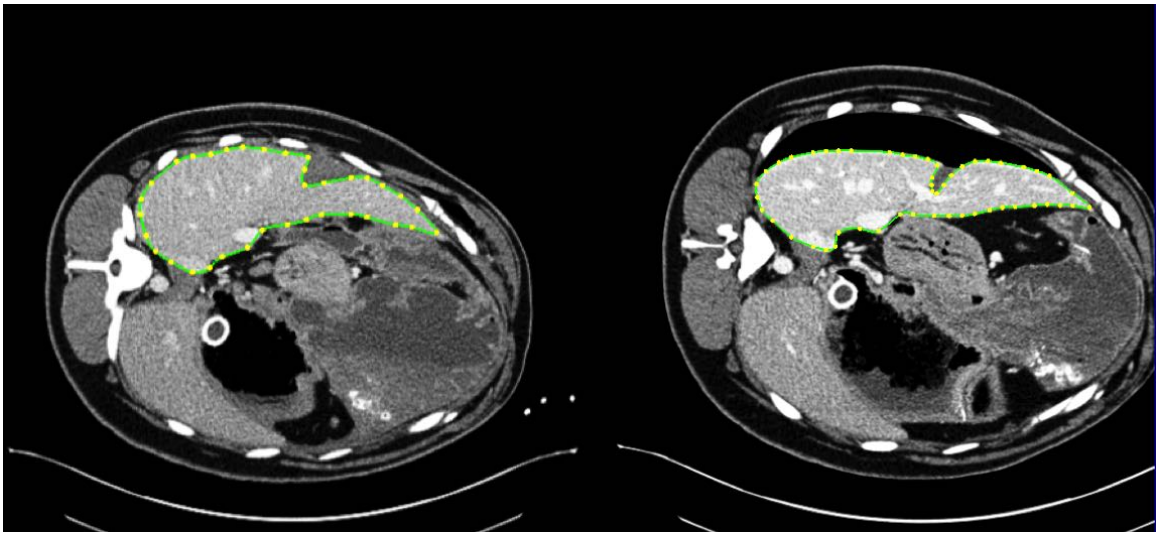

Figure VII.1: Contrast-enhanced CT image of sheep liver before insufflation (left), and after insufflation (right).

gradient across the liver may cause engorgement of the liver parenchyma through capillary fluid exchange to offset the rise in portal and venous pressures. Interestingly, the diameter of the portal vessels has been shown to decrease with insufflation pressure [196,197], which suggests that the parenchymal increase in volume exceeds volume changes associated with the diametric effects of vasoregulation.

VII.2.1.5 Limitations of Current Approach

These non-elastic sources of volume change can cause additional error when attempting to register anatomy between preoperative and intraoperatve organ states. While the volume changes reflected by embolization and ligation are the most clinically significant, it would also be desirable to account for smaller sources of volume change associated with parenchymal swelling during registration. However, preliminary investigation has shown that the current model cannot capture these effects.

In the aforementioned pilot experiment involving sheep insufflation, four biopsy clips were implanted within the liver prior to imaging for quantitative measurement of registration error. The full CT surface extracted from the intraoperative CT image was provided to

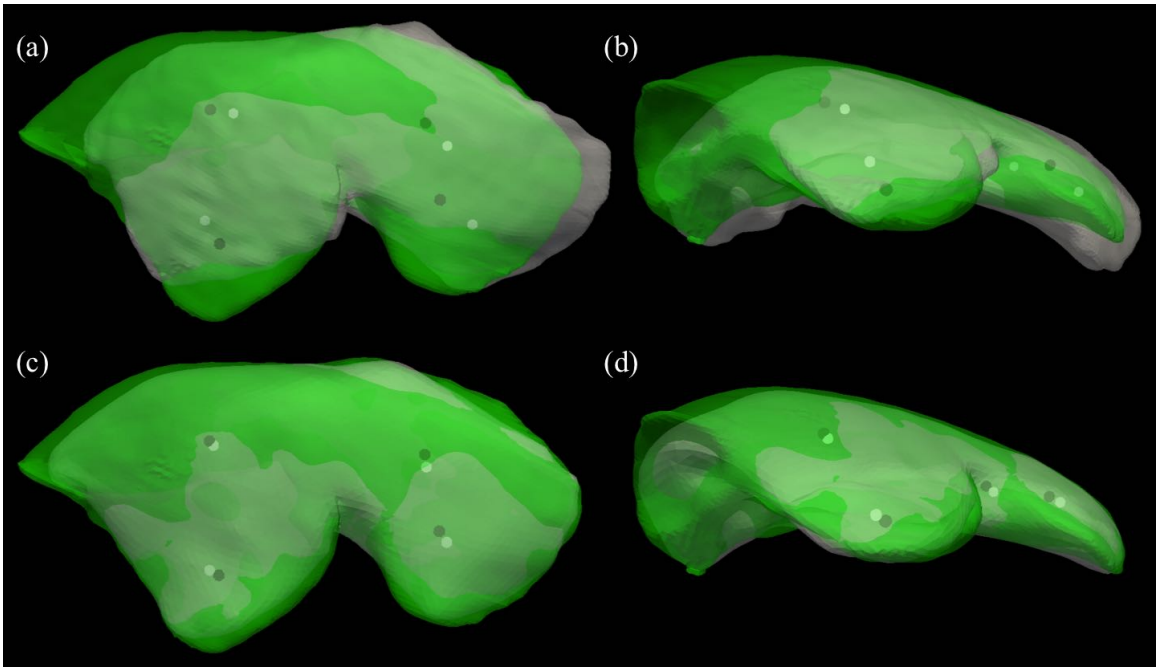

Figure VII.2: Registration of insufflated sheep liver. Intraoperative surface and biopsy clip targets shown in green and black, respectively. Registered preoperative surface and targets shown in gray and white, respectively. (a–b) Rigid registration of intraoperative and preoperative organ surfaces. (c–d) Deformable registration of intraoperative and preoperative organ surfaces.

register the preoperative volume. The initial TRE of rigid registration was 15.3 ± 3.8 mm. After applying the deformable registration method described in Chapter V, TRE decreased to 5.1 ± 1.6 mm, representing 67% correction over the accuracy of rigid registration. These registrations are shown in Figure VII.2. While this gain in accuracy is considerable, capacity for further improvement exists. It can be seen from Figure VII.2d that the deformable model is not able to account for volume change in the superior right lobe of the liver. Due to strain energy constraints, the volume of the registered preoperative liver only increased by 0.2%, leaving behind a 6.7% discrepancy in organ volume after registration. This limitation may be addressable by the incorporation of additional reconstructive modes that allow localized swelling of tissue without incurring additional strain energy penalty.

VII.2.1.6 Model Extensions

Due to the asymmetric nature of changes caused by embolization, the heterogeneity of chemotherapeutic response, and the complexity of hepatic vasculature, hepatic volume changes are unlikely to be uniformly distributed throughout the liver. Therefore, a reconstructive approach to localized models of swelling may be better suited for comprehensive solutions to clinical aspects of volume change. These volume changes can be modeled using descriptions of biphasic porous media, which consist of the conventional equations for linear elasticity coupled to a fluid phase component [198]:

$$\mu\nabla^2 u + (\lambda+\mu)\nabla(\nabla\cdot u) - a\nabla p = 0 \tag{VII.1}$$

$$a\frac{\partial}{\partial t}(\nabla\cdot u) + \frac{1}{S}\frac{\partial p}{\partial t} + k_c(p-p_c) + \nabla\cdot(-k\nabla p) = 0 \tag{VII.2}$$

where u is the displacement vector, p is the interstitial pressure of fluid within the parenchyma, μ and λ are the Lamé parameters, a is the ratio of extracted fluid volume to compressional volume change of tissue, $1/S$ is the amount of fluid that can enter the porous tissue phase without changing its volume, k_c is the capillary permeability, p_c is the capillary pressure, and k is the hydraulic conductivity.

The assumption of a fully saturated medium by $a = 1$ and $1/S = 0$ simplifies these equations to a steady state system of partial differential equations,

$$\mu\nabla^2 u + (\lambda+\mu)\nabla(\nabla\cdot u) - \nabla p = 0 \tag{VII.3}$$

$$k_c(p-p_c) + \nabla\cdot(-k\nabla p) = 0. \tag{VII.4}$$

Equation VII.4 represents continuity of fluid mass in the system, where the amount of fluid transferred across the capillary bed is determined by the elevation of the capillary

pressure compared to the interstitial pressure. If $p < p_c$, then fluid is pushed into the interstitial parenchymal volume. In the other direction, interstitial fluid will be resorbed from the liver parenchyma if $p > p_c$. The pressure gradient is then coupled to the elastic phase as a body force applied throughout the domain.

A uniform distribution of swelling can be simulated by setting k_c and p_c to small positive nonzero values. This simulation could be utilized as a mode of deformation in the reconstructive algorithm of Chapter V and excluded from the strain energy computation to allow expansion or contraction of the reconstructed liver volume depending on the sign of the mode weight.

More localized modes of swelling can also be added to the reconstruction by setting k_c to 0 and distributing pressure sources through the volume of the liver. Linearized pressure modes could be created in an analogous fashion to the control point deformation modes described in Chapter IV and Chapter V by selecting new vertices as pressure sources and alternately setting the pressure on each source to a small positive value while keeping all other source points at zero gauge pressure.

Depending on a balance between coarseness of these additional reconstructive modes and the amount of data required to resolve them, this approach could enable additional modeling of embolative, chemotherapeutic, hydration, and insufflative effects to further improve the accuracy of deformable registration using elastic methods in the presence of underlying volume changes. This addition to the model could improve intraoperative localization, navigation, and guidance during surgery and delivery of locoregional therapies, but perhaps more importantly could lead to new applications in interventional oncology that become possible through more accurate mechanics-based registrations that more effectively align longitudinal patient imaging for assessment of treatment response without introducing undesirable non-physical effects during deformable image registration [199].

VII.2.2 Real-Time Registration

Current systems that realize image-to-physical registration are designed for continual, not continuous registration updating. Chapter V demonstrates that intermittent high quality registrations are possible with a small number of iUS planes. This procedural framework has historically suited how surgeons have come to utilize existing image guidance systems based on rigid registrations, which are only capable of providing approximate accuracy and therefore cannot be fully depended upon. However, if the next generation of image guidance systems will strive to improve the standard of care by introducing fundamentally new capability to surgeons to facilitate and democratize surgical techniques that may lead to improved patient outcomes, then demonstrably accurate and reliable actively updating registrations for real-time visualization and guidance will likely become necessary.

In current clinical experiences with image-guided liver surgery, the procedure must be temporarily halted for data collection and registration. However, in reality the liver is continuously subjected to ongoing deformations during surgery. Often the data collection and registration process is achieved and controlled within planned apneic periods and respiratory gating, which requires deliberate coordination with the anesthesiologist. This shortcoming of current guidance technology majorly detracts from seamless integration of image guidance systems into operating workflows.

VII.2.2.1 Algorithms for Real-Time Registration

Existing works in the literature have proposed near real-time methods for deformable registration using rapidly updating forward simulation of coarsely discretized finite element models. However, very few have established higher fidelity reconstructive methods for intraoperative estimations of deformation. One promising direction is the use of Kalman filters to provide a discrete-time framework for approximating soft tissue deformations [200–202]. However, traditional Kalman filter approaches for finite element elasticity require inversion of the full-size mass, damping, and stiffness matrices on each

timestep [200]. The computational cost of these inversion steps becomes prohibitive for the discretization sizes of the organ required to achieve accurate deformations. Reduced order unscented Kalman filters have also been applied for intraoperative estimation of liver deformation to reduce computational complexity and avoid the need for computing explicit gradients [201, 202]. However, these unscented approaches require additional empirical sampling compared to more traditional Kalman filters and are sensitive to hyperparameter tuning if stable state prediction over time is desired.

With respect to the reconstructive biomechanical model introduced in Chapter V, the linearization of deformation modes enables a drastic reduction in computational complexity when simulating deformation through estimated state parameters, while maintaining high reconstructive accuracy. With explicit gradient forms for elastic reconstruction now defined in Chapter V, lower dimension traditional Kalman filtering approaches become straightforward to implement. For example, one possibility could look like the extended Kalman filtering approach that follows. Assuming pseudo-steady state, model positions could be predicted by displacements u_k defined by the deformation state α through the process,

$$u_k = u_{k-1} + v_{k-1}\Delta t + \frac{1}{2}a_{k-1}\Delta t^2, \tag{VII.5}$$

where $v_{k-1} = (u_{k-1} - u_{k-2})/\Delta t$ and $a_{k-1} = (u_{k-1} - 2u_{k-2} + u_{k-3})/\Delta t^2$ are $O(\Delta t)$ finite difference approximations to velocity and acceleration, respectively. This process could be expanded to a full damped mass-spring finite element system following the description in [200], but is omitted here for simplicity. With $u_k = J_u\alpha_k$, the finite difference relations simplify to a predictive process $g_{k-1}(\alpha) = g(\alpha_{k-1}, \alpha_{k-2}, \ldots, \alpha_0)$, where here

$$\alpha_{k|k-1} = g_{k-1}(\alpha) = \frac{5}{2}\alpha_{k-1} - 2\alpha_{k-2} + \frac{1}{2}\alpha_{k-3} \tag{VII.6}$$

and the instantaneous gradient is $G_k = \partial g_{k-1}/\partial \alpha_{k-1}$.

New data observations made at time step k are described by model-data errors f_k and their gradients $H_k = \partial f_k / \partial \alpha_k$ as given by Table V.1 of Chapter V. The extended Kalman filter updates the state variables on each new observation by predicting the state and its covariance by,

$$\alpha_{k|k-1} = g_{k-1}(\alpha) \tag{VII.7}$$

$$P_{k|k-1} = G_k P_{k-1} {G_k}^T + Q_k \tag{VII.8}$$

where P_k is an estimate for the covariance of α_k and Q_k is the covariance of a background process noise. The update step is described by the Kalman gain K_k,

$$K_k = P_k {H_k}^T \left(H_k P_{k|k-1} {H_k}^T + R_k \right)^{-1} \tag{VII.9}$$

$$\alpha_k = \alpha_{k|k-1} + K_k f_k \tag{VII.10}$$

$$P_k = (I - K_k H_k) P_{k|k-1} \tag{VII.11}$$

where R_k is an estimate for the covariance of measurement error. Due to the linearized parameterization of the registration problem through deformation modes α, a Kalman filter approach is likely to be an effective strategy for rapidly estimating intraoperative deformations if real-time data streams can be accessed for registration.

VII.2.2.2 Instrumentation for Real-Time Registration

Although some attention of the registration community is shifting towards real-time monitoring and updating at frame rate, intraoperative instrumentation is currently the primary bottleneck for continued development and progression of image-guided techniques. Even

during non-continuous realizations of intraoperative guidance, data collection remains a major challenge due to the convergence of many factors involving the use of nonstandard equipment and workflow constraints. Current approaches have not yet reached the level of robustness and accuracy required for intraoperative localization needs given the consequence of errors when oncological margins and critical anatomical structures are involved. However, approaches for real-time data streams in the operating room are being actively developed beyond conventional tool tracking, such as stereo surface reconstruction for OLR [203] and mosaicking of reconstructed stereo laparoscopic patches for LLR [108], which may be able to eventually provide larger amounts of time course data of intraoperative organ shape. Due to the limited amount of data that can be collected on the organ surface relative to the total amount of information needed to adequately constrain the registration, however, methods for automatic iUS image segmentation may also become important for achieving volumetrically accurate registrations. Computer vision and machine learning approaches could also assist with identifying and segmenting intraoperative features from these data streams to achieve automatic end-to-end organ measurement. With continued advances in these areas, it may become possible to eventually realize fully real-time guidance systems that close the feedback loop between patient, system, and surgeon to reach even greater potential impact of guidance technology in the intraoperative environment of surgery and intervention.

VII.2.3 Applications of Registration Methods

The registration methods developed and reported in Chapter V and Chapter VI have many potential applications outside of those already discussed in this dissertation. This section describes other ongoing applications of these techniques in current projects.

VII.2.3.1 Image-Guided Thermal Ablation

Inaccurate localization and targeting of lesions during ablative procedures may lead to incomplete treatment and local recurrence of disease. An opportunity therefore opens to

more accurately deliver treatment through image-guided systems that register the tracked intraoperative position of ablation probes to patient imaging to assist with successful tumor localization and probe placement. A recent study by Collins *et al.* [204] investigated potential improvement in the alignments of ablation antennae based on delivery under the guidance of rigid registration and under the guidance of the deformable registration method developed in this dissertation. This work demonstrated that deformable registration led to average TREs of ablation antennas between 2.5 ± 1.1 mm and 3.7 ± 1.4 mm depending on the amount of organ surface data provided, in comparison to 5.6 ± 2.3 mm and 6.0 ± 2.3 mm, respectively, for rigid registration under the same scenarios. These findings represent a large improvement over existing studies reporting the targeting accuracy of ablation antennas, which mostly range from 5–10 mm with the best method utilizing guidance by intraoperative ultrasound associated with median positioning error of 4.2 mm [205]. Collins *et al.* also found that the magnitude of error when guiding ablation antenna to target was strongly correlated to decrease in the overlap between the ablation zone and tumor volume, at a rate of 6.0% loss in tumor coverage per millimeter of registration error ($r = 0.93$) [204], suggesting that more accurate localization and targeting of ablation to tumor may impact the rate of local recurrence. However, clinical studies are eventually needed to directly support this claim.

The Chapter VI framework for estimation of registration certainty and prediction of registration error has potentially large implications for guiding ablation. This framework enables immediate predictions of registration error at each lesion within statistical confidence bounds at the time of treatment, to potentially provide greater assurance of successful delivery. Furthermore, these bounds could be combined with patient-specific treatment planning and ablation modeling to establish acceptable thresholds for intraoperative localization error based on alignment tolerances of predicted tumor coverage if ablation probes are placed under navigated guidance.

VII.2.3.2 Registration in Other Organ Systems

The linearized iterative boundary reconstruction method introduced in Chapter V is a general purpose method for reconstructing elastic deformations applied to any organ model. As such, while this dissertation focuses on deformable liver registration, the method has been applied to registration of other soft tissue organ systems as well, to date including the breast and the prostate.

A proof of concept registration was performed on preliminary data collected on a volunteer human breast. A model was built from a preoperative supine MR image, with fiducial points designated on the surface of the breast. Deformation of the breast was introduced by abduction of the arm to a 90º angle to simulate intraoperative surgical position, and the deformed positions of the designated fiducial points were recorded. Figure VII.3 shows a comparison between rigid registration and deformable registration of the preoperative anatomy to the intraoperative fiducial positions using the methods described in Chapter V. While it clearly can be seen that the deformable registration algorithm is able to effectively register the fiducials and simulate the intraoperative elevation of the shoulder in the upper lateral quadrant (upper right of image), ongoing work is being pursued in the laboratory to establish methods for measurement, validation, and potential improvement of subsurface registration accuracies using the linearized reconstruction approach. These efforts aim to enhance intraoperative surgical targeting of breast tumors to reduce re-operation rates associated with breast-conserving therapy.

The reconstructive deformable registration method was also applied to prostate registration across serial imaging of a tumor over a span of four years (Figure VII.4). These alignments aim to remove the effects of mechanical deformation so as to leave behind evidence of hyperplastic and proliferative effects to help distinguish between early stage growth of benign and malignant tumors through ongoing modeling efforts with a collaborator group.

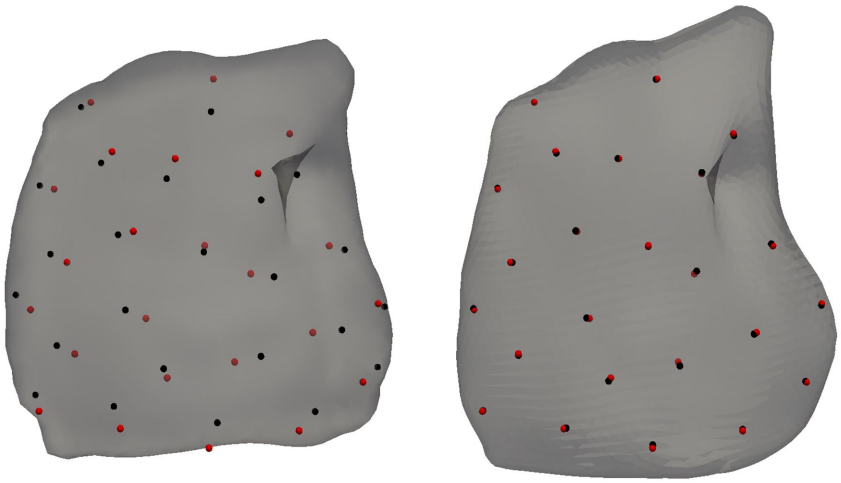

(a) (b)

Figure VII.3: Registration of a human left breast from supine MR (gray – breast surface; black – preoperative fiducial positions) to intraoperative position (red – intraoperative fiducial positions). (a) Rigid point-based registration from preoperative anatomy to intraoperative fiducials. (b) Deformable registration from preoperative anatomy to intraoperative fiducials.

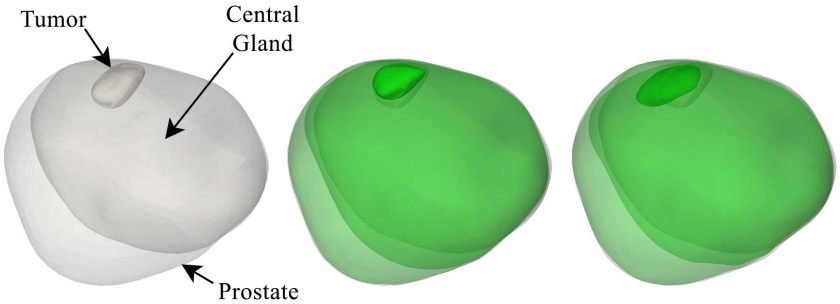

(a) (b) (c)

Figure VII.4: Registration of human prostate across a four-year time series. (a) Initial prostate geometry. (b) Registered prostate geometry after one year. (c) Registered prostate geometry after four years. Hyperplasia of the central gland and tumor are observed throughout this timespan.

VII.3 Closing Remarks

The contributions put forth in this dissertation are highly relevant to the field of deformable registration, advancing concepts in model-based registration that can lead to new algorithmic innovations as well as new clinical applications discussed in this chapter. The frameworks for mechanics-based deformable registration presented herein offer well-founded, accurate, and reliable approaches for alignment of patient-specific data to guide and improve the delivery of treatment to higher standards.

Appendix A

Emulation of the Laparoscopic Environment for Image-Guided Liver Surgery via an Abdominal Phantom System with Anatomical Ligamenture

A.1 Summary and Contributions

Due to intraoperative constraints, comprehensive target validation measurements are difficult if not impossible to obtain in the clinical setting. Therefore, creation of physical environments that reproduce the context of clinical effects are necessary for validation of algorithms intended to be applied to these situations. The work in this chapter describes the creation of a simulative environment of liver deformation in the laparoscopic setting by physically modeling insufflated dimensions of the abdomen and mobilization of ligament attachments that anchor the abdomen within. This assembly allows for reproduction of deformations that approximate intraoperative behaviors using a silicone liver phantom with a large number of embedded validation targets that can be imaged and positionally measured before and after deformations are applied. Contact and non-contact data collection and rigid registration methods are also described within this emulated laparoscopic environment to demonstrate the potential for quantitative validation of laparoscopic registration methodologies without introducing additional clinical burden.

Emulation of the Laparoscopic Environment for Image-Guided Liver Surgery via an Abdominal Phantom System with Anatomical Ligamenture

The work presented in this chapter appears in and is reprinted with permission from,

[156]: J. S. Heiselman, J. A. Collins, L. W. Clements, J. A. Weis, A. L. Simpson, S. K. Geevarghese, W. R. Jarnagin, and M. I. Miga, "Emulation of the laparoscopic environment for image-guided liver surgery via an abdominal phantom system with anatomical ligamenture," in *Proceedings of SPIE Medical Imaging*, vol. 10135, pp. 1–9, 2017. (© 2017 SPIE)

A.2 Abstract

In order to rigorously validate techniques for image-guided liver surgery (IGLS), an accurate mock representation of the intraoperative surgical scene with quantifiable localization of subsurface targets would be highly desirable. However, many attempts to reproduce the laparoscopic environment have encountered limited success due to neglect of several crucial design aspects. The laparoscopic setting is complicated by factors such as gas insufflation of the abdomen, changes in patient orientation, incomplete organ mobilization from ligaments, and limited access to organ surface data. The ability to accurately represent the influences of anatomical changes and procedural limitations is critical for appropriate evaluation of IGLS methodologies such as registration and deformation correction. However, these influences have not yet been comprehensively integrated into a platform usable for assessment of methods in laparoscopic IGLS. In this work, a mock laparoscopic liver simulator was created with realistic ligamenture to emulate the complexities of this constrained surgical environment for the realization of laparoscopic IGLS. The mock surgical system reproduces an insufflated abdominal cavity with dissectible ligaments, variable levels of incline matching intraoperative patient positioning, and port locations in accordance with

surgical protocol. True positions of targets embedded in a tissue-mimicking phantom are measured from CT images. Using this setup, image-to-physical registration accuracy was evaluated for simulations of laparoscopic right and left lobe mobilization to assess rigid registration performance under more realistic laparoscopic conditions. Preliminary results suggest that non-rigid organ deformations and the region of organ surface data collected affect the ability to attain highly accurate registrations in laparoscopic applications.

A.3 Introduction

Soft tissue deformation and inconsistent data quality can considerably contribute to registration error in image-guided liver surgery (IGLS). These factors necessitate that registration methods be quantitatively validated under realistic conditions. However, intraoperative clinical validation through intraoperative CT, intraoperative MR, or intraoperative ultrasound can be prohibitively burdensome, expensive, or challenging. Although validation strategies using intraoperative imaging have been explored by groups including Heizmann *et al.* [123] and Clements *et al.* [5], other *in vivo* validation approaches mostly rely on surface residual error [2,121] or manual selection of surface-based landmarks [110]. However, surface accuracy may not be indicative of subsurface registration accuracy. Due to these limitations, efforts to quantify IGLS registration accuracy often employ well-documented tissue-mimicking liver phantoms to supplement the more restricted capabilities of *in vivo* validation [2, 110]. While somewhat intuitive, challenges remain; namely, in order to appropriately validate registration and navigation techniques in a phantom environment, an accurate representation of the intraoperative surgical scene must be established. The phantom setup used by Rucker *et al.* [2] incorporated surgical packing material to simulate intraoperative deformation caused by placement of laparotomy pads beneath the liver during open procedures. Banovac *et al.* [206] developed a liver phantom that reproduced respiratory motion for validation of liver biopsy guidance. Replicating the relevant dynamics of the surgical environment is an important concern towards providing value to the phantom

system. However, the ability to simulate the intricacies of the laparoscopic environment has not been adequately developed. In previous work, a silicone liver phantom was placed in a laparoscopic trainer box in an attempt to evaluate a deformation correction strategy in the laparoscopic setting [207]. However, this study failed to account for the fundamental anatomical changes that distinguish laparoscopic from open procedures.

In laparoscopic liver resection, deformation between the preoperative and intraoperative positions of the organ primarily arises from three sources. First, the abdominal cavity is insufflated with carbon dioxide during the procedure. This process displaces the abdominal wall, the diaphragm, and the tissues surrounding the liver. With the falciform ligament attaching the anterior side of the liver to the ventral wall and the left and right triangular ligaments attaching the superior side of the liver to the diaphragm (Figure A.1a), insufflation can cause significant motion of the organ. Zijlmans *et al.* [128] found that abdominal insufflation caused the liver to shift up 35 mm in a porcine study. In humans, we have observed that insufflation during laparoscopy causes suspension of the liver from the anterosuperior ligaments, including the falciform and triangular ligaments (Figure A.1b). In this work, we propose that suspension of the liver from these ligament attachments plays a central role in liver deformation during laparoscopic procedures.

In addition to insufflation, a second source of deformation arises from changes in patient positioning between preoperative imaging and the intraoperative presentation. While preoperative images are acquired with the patient completely supine, intraoperative forward inclines of 10–30° in the reverse Trendelenburg position are common. The forward incline changes the orientation of the liver with respect to gravity and contributes to deformation between intraoperative and preoperative states. More specifically, the forward incline may cause a partial shift in mechanical support from the falciform ligament, located anterior to the liver, onto the left and right triangular ligaments, located superior to the liver.

Finally, substantial soft tissue deformation can result from organ mobilization, where the supporting ligaments are dissected to improve the manipulability of the organ. In la-

paroscopic liver resections, the liver is usually incompletely mobilized from its ligamenture. In left lobe mobilization, the falciform and left triangular ligaments are typically divided whereas in right lobe mobilization, the falciform and right triangular ligaments are divided instead. As shown in Figure A.1c, the dissection of these ligaments can produce considerable deformation as the structures suspending the organ are cut away. In a phantom system, these conformational changes cannot be reproduced easily without placing the phantom under explicit control by the supporting ligaments

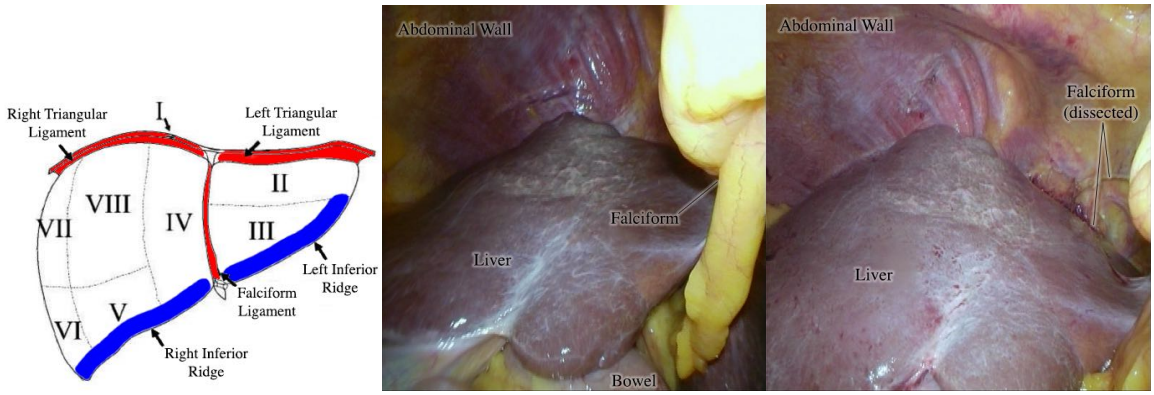

(a) (b) (c)

Figure A.1: (a) Diagram of the anatomical positions of the falciform and triangular ligaments on the liver (red) and the left and right inferior ridges (blue), adapted from Kingham *et al.* [23]. (b) Anterior surface of the right lobe of the liver during a laparoscopic procedure. After insufflation, the liver suspends from its ligaments and rests on the bowel. Note the tension where the liver attaches to the falciform ligament. (c) Anterior surface of the liver after dissection of the falciform and right triangular ligaments. The tension held by the ligaments relaxes and the shape of the liver changes, indicating intraoperative deformation. The phantom system aims to reproduce the distinct sources of deformation unique to laparoscopic procedures.

A.3.1 Objective

The purpose of this work is (1) to create a mock surgical system that reflects the dynamics of the intraoperative laparoscopic environment and (2) to demonstrate a system that can quantitatively assess registration accuracy in the setting of laparoscopic image-guided liver resection. Registration accuracy is assessed using the phantom and two laparoscopic meth-

ods of sparse intraoperative surface data collection. Rigid registration remains the standard registration method in clinically approved IGLS systems for open surgery, although no standard yet exists for laparoscopic IGLS. This preliminary study will establish a foundation for validating further developments in laparoscopic image guidance.

A.4 Methods

A phantom system was designed to reproduce the intraoperative conditions of laparoscopic liver procedures. The setup consists of an abdominal frame that mimics the insufflated abdomen, inside of which a soft tissue liver phantom is suspended. We use this mock laparoscopic setup to perform a preliminary analysis of rigid registration accuracy in the laparoscopic setting with regard to data acquired through various ports and with two different methods of intraoperative data acquisition. A qualitative comparison is also performed between the deformation produced by the phantom and the deformation observed in vivo during laparoscopic liver resection.

A.4.1 Laparoscopic Phantom System

To match the dimensions of the insufflated abdominal wall reported by Song *et al.* [126], the abdominal frame was constructed from a half-pipe of an 18-inch diameter PVC sleeve. Nine ports were placed in the mock abdominal wall to mimic laparoscopic access ports to the abdominal cavity. The mock ports were placed in accordance with commonly used port positions for laparoscopic right and left lobe liver resection as reported by Cho *et al.* [208] and Cherqui *et al.* [209]. The mock abdomen was mounted on four extensible legs to permit inclines between -30° and +30° as a patient may experience intraoperatively. Furthermore, the legs carry a platform that can be raised or lowered to apply or remove support from the bowel on the posterior of the liver. To provide locations for ligament attachment, supporting bars were attached to the interior of the abdominal cavity. A silicone liver phantom was suspended from these supporting bars at the falciform ligament, left triangular ligament, and right triangular ligament by Velcro® loop fabric strips. Any combination of the Vel-

cro® attachments can be removed to simulate dissection of ligaments. Figure A.2 shows the abdominal frame suspending the phantom before and after right lobe mobilization. Note that the primary structures providing mechanical support to the phantom are the ligament connections and a mock bowel placed beneath the liver, as is the case *in vivo* (Figure A.1). Finally, a rigid body fiducial was attached to the exterior of the abdominal frame to provide a reference for the optical tracking system in the registration study.

(a) (b)

Figure A.2: Inferior view of the soft-tissue liver phantom in the laparoscopic abdominal frame (a) with support, and (b) without support from the falciform and right triangular ligaments, simulating right lobe mobilization. Note the deformation that has occurred following removal of the ligament attachments to the liver.

A soft-tissue liver phantom was made from Ecoflex® 00-10 platinum-cure silicone (Smooth-On Inc., PA) mixed with Silicone Thinner® (31% mass) to decrease silicone stiffness and Slacker® Tactile Mutator (23% mass) to provide viscosity (Smooth-On Inc., PA). A mold for the liver phantom was created from a preoperative human CT scan. The mold was recast in plaster and modified to include 1.5 cm protrusions along the falciform, left triangular, and right triangular ligaments. After the phantom was removed from the mold, Velcro® hook strips were adhered to the protrusions using Sil-Poxy® Silicone Epoxy (Smooth-On Inc., PA) to complete the suspension mechanism from the abdominal frame. A total of 147 radiopaque plastic beads and 1-mm stainless steel ball bearings were

embedded in the phantom to serve as targets in CT images for quantitative validation of registration accuracy. The distribution of targets is shown in Figure A.3.

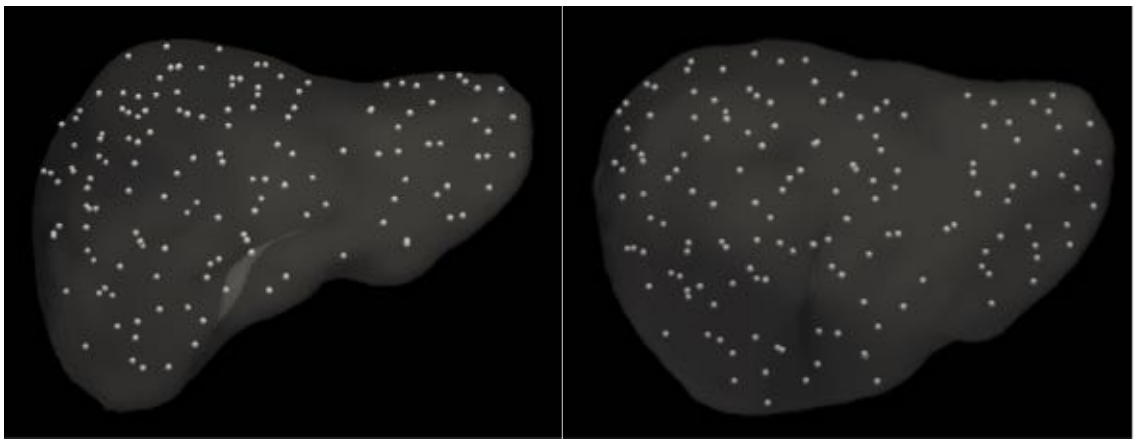

(a) (b)

Figure A.3: Target positions within the soft tissue phantom from the (a) anterior view, and (b) anterosuperior view. The 147 targets are dispersed consistently throughout the volume of the phantom.

A.4.2 Laparoscopic Registration Study

The described phantom system was used to perform and evaluate the accuracy of laparoscopic liver registrations. This process consisted of: (1) acquiring and processing preoperative and intraoperative CT scans of the phantom, (2) collecting intraoperative surface data, and (3) registering the intraoperative data and evaluating registration accuracy. To compare phantom and in vivo deformation, registrations using intraoperative surface data from the phantom were qualitatively compared to those using clinical intraoperative surface data from a previous study on laparoscopic IGLS.

A.4.2.1 CT Imaging and Segmentation

A preoperative CT of the liver phantom with embedded targets was acquired with the phantom inside a mold constructed from a clinical tomogram of a human liver. The phantom was removed from the mold and suspended in the abdominal frame, set at an incline of

16.7°. Left- and right-lobe mobilization were simulated by removing the falciform and the left or right triangular Velcro® ligaments, respectively. Intraoperative tomograms of the liver phantom and embedded targets were acquired with $0.62 \times 0.62 \times 3$ mm voxel spacing for both conditions of mobilization. Manual segmentation was performed to remove the ligament protrusions added to the phantom and to correctly establish correspondence between targets in the preoperative and intraoperative scans.

A.4.2.2 Collection of Intraoperative Sparse Surface Data

Intraoperative data consisted of sparse point clouds of the anterior surface of the liver, collected for left and right mobilization conditions through each of the nine ports. Following the procedure of the salient feature weighted iterative closest point (wICP) method in Clements *et al.* [121], sparse collections along three features (the falciform ligament, the left inferior ridge, and the right inferior ridge, see Figure A.1a) and the rest of the anterior surface were obtained. Two methods were used to acquire these sparse surfaces through the laparoscopic access ports. First, a trocar-compatible optically tracked stylus was used to manually swab the surface of the organ. Second, a trocar-compatible optically tracked handheld conoprobe MK3 [102, 103] (Optimet Inc., Jerusalem, Israel) was used to obtain similar data in a non-contact manner. Optical tracking was accomplished with an NDI Polaris Spectra camera (Northern Digital Inc., Waterloo, Canada). The experimental setup of the conoprobe and the port locations on the abdominal frame are shown in Figure A.4.

A.4.2.3 Registration to Intraoperative Data

The salient feature wICP method described by Clements *et al.* [121] was used to rigidly register the intraoperative sparse surface data and the intraoperative target positions to the preoperative anatomy. It should be noted that some features could not be accessed through several ports due to limited range of motion or line of sight with the optical tracking system, leading to some registrations being performed with fewer than three features. To measure the accuracy of the registration, target registration error (TRE) was computed as

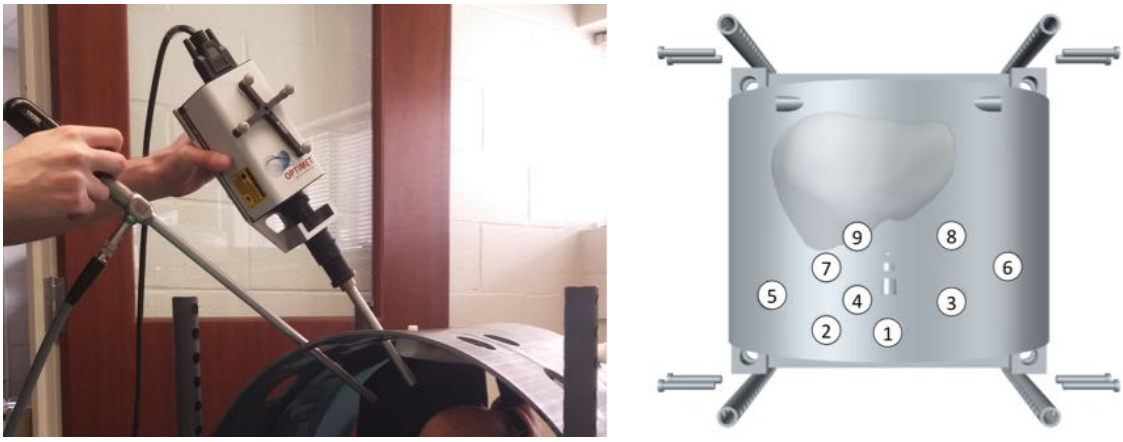

(a) (b)

Figure A.4: (a) Experimental setup of intraoperative data collection using the conoprobe. The conoprobe laser beam can be guided by a laparoscope. (b) Placement of the nine access ports in the abdominal frame. Port 1 is located at the umbilicus.

the Euclidean distance between the preoperative and registered intraoperative targets. A registration to the entire segmented surface of the intraoperative CT was also performed to represent the ideal rigid alignment.

A.4.2.4 Comparison to Clinical Deformation

Clinical laparoscopic image guidance data were obtained from a previous study by Kingham *et al.* [23] at Memorial Sloan-Kettering Cancer Center. Following rigid registration, the non-rigid misalignment resulting from *in vivo* deformation and the phantom deformation were qualitatively compared to estimate the suitability of the phantom system for reproducing laparoscopic deformation.

A.5 Results

A summary in Table A.1 shows the registration outcomes for left and right mobilization conditions using stylus and conoprobe acquisition through the umbilicus port, compared with a registration with ideal data using the full intraoperative surface from CT. In both states of deformation, the registration using data from the conoprobe achieves lower av-

Acquisition Method	Left Mobilization	Right Mobilization
Stylus	14.8 ± 5.6 mm	16.9 ± 7.0 mm
Conoprobe	13.0 ± 2.6 mm	11.4 ± 5.5 mm
Intraoperative CT	12.4 ± 2.5 mm	12.3 ± 4.8 mm

Table A.1: Target registration error (mean ± std) for simulated right and left lobe mobilization using stylus and conoprobe sparse surface acquisitions through the umbilicus port and the ideal registration using the intraoperative organ configuration from CT.

erage TRE and smaller standard deviations of target error than registrations to stylus-collected data. Additionally, the TRE for data acquired through each of the nine ports are shown in Figure A.5. Data acquired through the periumbilical ports tended to produce the best registrations, and lateral and superior ports could not access some salient features. These tendencies suggest that the region of data accessible through various ports is important to the process of registration. Across all ports, registrations using the conoprobe improved the average TRE by 2.0 mm, although the difference was not statistically significant ($p = 0.18$, paired sample t-test, $N = 18$).

A comparison between rigid registrations (Figure A.6) using clinical data from a previous laparoscopic image guidance study and phantom data from our laparoscopic system shows similar shift between the shape of the preoperative liver and the intraoperative surface. The similarity indicates that the phantom system is capable of producing organ deformation in agreement with the deformation seen *in vivo*.

A.6 Discussion

On average, sparse intraoperative surface data collected with the conoprobe resulted in rigid registrations with mean TRE of 2.0 mm less than those of registrations using surface data collected with the laparoscopic stylus. The tracked conoprobe may yield better registration outcomes due to its non-contact nature, whereas the tracked stylus may be prone to error due to the need for direct contact with the organ surface and difficulty coordinating the tip of the stylus in laparoscopic applications, where a fulcrum at the port mirrors motion and a long lever arm accentuates it. While the reduction in TRE between stylus and conoprobe

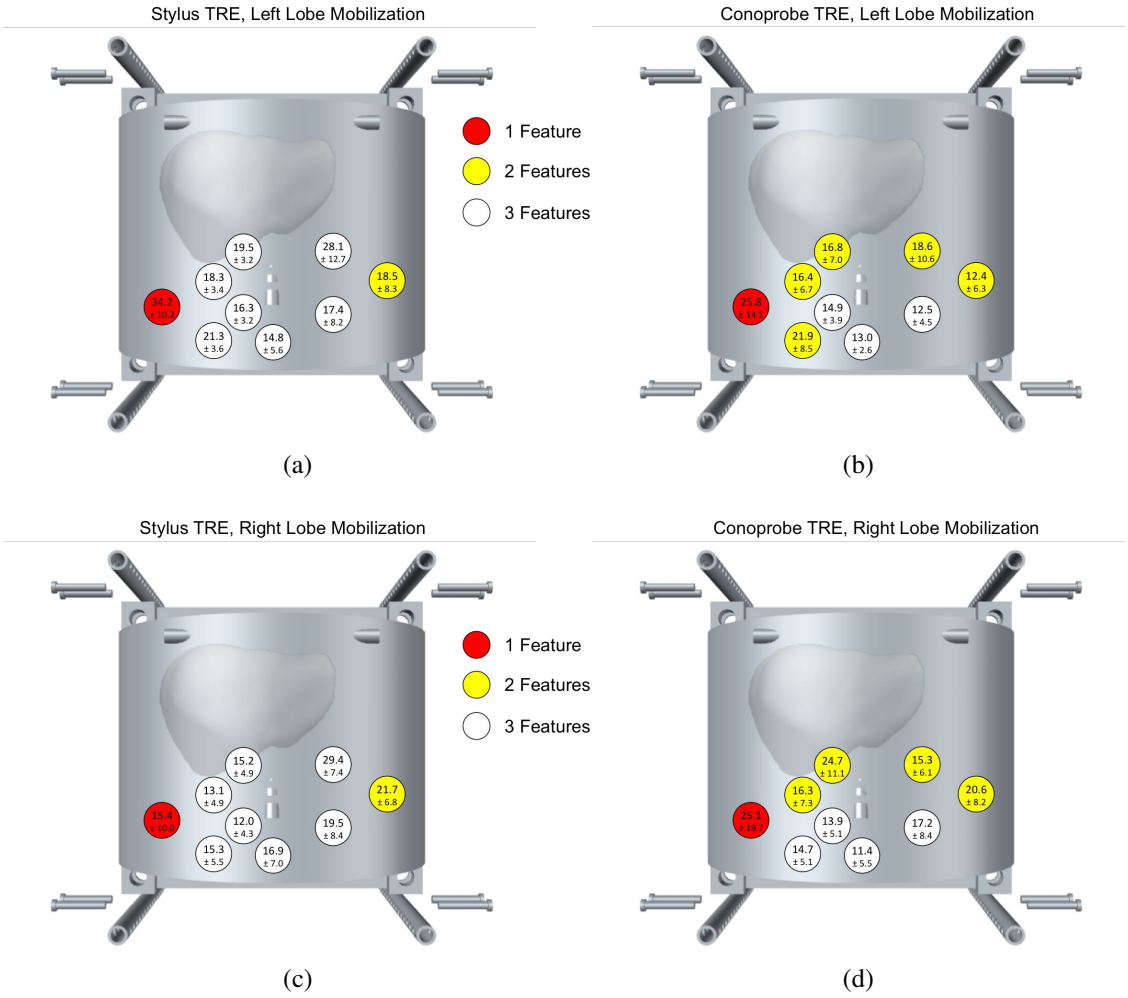

Figure A.5: Target registration error in mm (mean ± std) for simulated left lobe (a,b) and right lobe (c,d) mobilization using stylus (a,c) and conoprobe (b,d) acquisition from each port. Ports near the umbilicus have the best access to the features used in the wICP rigid registration method. Ports colored red, yellow, and white could access only one, two, or all three of the features, respectively. The extent of data accessible through the lateral and superior ports tended to limit feature acquisition with the conoprobe.

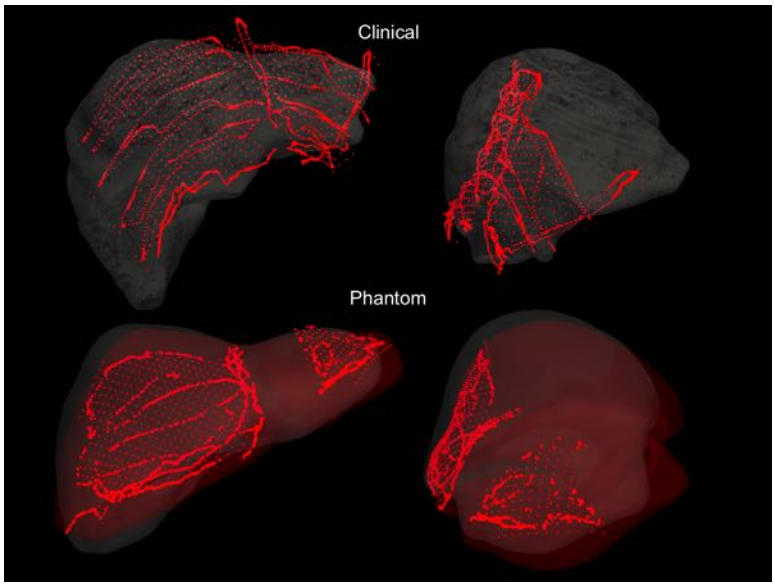

Figure A.6: Anterior view (left) and lateral view (right) of the observed deformation in a clinical laparoscopic case (top) compared to a phantom case (bottom). The white surface indicates the shape of the segmented preoperative liver and the red points indicate the rigidly registered intraoperative sparse surface data. To ease visual comparison, a spatial interpolation method was applied to produce an evenly spaced sampling of the best-fit intraoperative surface described by the sparse data collection. The red surface in the phantom case is the registered intraoperative configuration segmented from CT. In both scenarios, the registered intraoperative surface on the right lobe resides beneath the preoperative surface. The intraoperative CT of the phantom suggests the apparent flattening of the right lobe could result from shifting tension on the ligaments after insufflation distends the abdominal wall and diaphragm.

acquisitions was not found to be statistically significant, there are a number of confounding factors that impair direct comparison. First, the extents of data accessible with the conoprobe and stylus differ. While the conoprobe is capable of accurate measurement at angles of incidence up to 85º, in practice the tracked conoprobe has smaller coverage on the organ surface. The smaller surface coverage stems from difficulty measuring along the boundary of the liver due to handheld tremble potentially causing the conoprobe laser beam to leave the liver surface. Second, the absence of accessible salient features from several of the ports may impair the robustness of the registration algorithm. However, it is interesting to note that among ports which have all three features available in both the conoprobe and stylus acquisitions, the mean TRE of registrations using conoprobe surface data are still on average 2.1 mm smaller than the TRE of corresponding registrations with stylus surface data ($p = 0.07$, paired sample t-test, $N = 7$). Despite the lack of demonstrated statistical significance, the sample sizes in this preliminary study are too small to provide adequate statistical power. While registration accuracies between the two intraoperative surface acquisition methods remain comparable, further data from additional phantoms under varying states of mobilization are required to better understand the tradeoffs between the conoprobe and stylus.

The smallest magnitude of mean TRE we observed among all registrations was 11.4 ± 5.5 mm. Rigid registrations using complete organ surface data from the intraoperative CT produced TRE exceeding 12 mm in both left and right mobilization conditions. From these large magnitudes, we note that substantial non-rigid deformation may exist. This assertion is corroborated by the deformation observed in Figure A.6, where the shapes of the preoperative and the registered intraoperative livers evidently differ. These findings suggest that rigid registration alone is not completely suitable for laparoscopic registration. Future work will include development of non-rigid registration algorithms for the liver in the laparoscopic environment to better account for this deformation.

A.7 Conclusions

In this work, we have developed a laparoscopic liver phantom system that reproduces the intraoperative sources of deformation existing in laparoscopic procedures. Furthermore, we demonstrate that this phantom system can be used to quantitatively assess registration accuracy through computation of target registration error between preoperative and intraoperative post-deformation CT scans of the phantom. This contribution is valuable because it permits direct and quantitative validation of laparoscopic IGLS registration methodologies without introducing significant clinical burden. Our preliminary work indicates that this mock system produces deformation similar to that observed during in vivo procedures. An initial study of rigid registration accuracy suggests that registration accuracy may depend on the port through which data is collected, and hence the region of the organ accessed. Moreover, the presence of substantial soft tissue deformation may require development of non-rigid registration methodologies for laparoscopic IGLS.

Acknowledgements

This work was supported by the NIH grant R01-CA162477 and the NIH-NIBIB training grant T32-EB021937. We would like to thank the Vanderbilt Machine Shop for assistance in constructing the abdominal frame of the phantom.

Appendix B

The Image-to-Physical Liver Registration Sparse Data Challenge: Characterizing Inverse Biomechanical Model Resolution

B.1 Summary and Contributions

The image-to-physical liver registration sparse data challenge began in 2019 as an effort from our research group to provide a common benchmark dataset to the liver registration community. As part of the original submission [210], a silicone liver phantom was constructed with embedded validation targets and a challenge site was hosted using Amazon Web Services to automatically process submitted results. The challenge consisted of attempting to find the most accurate set of registrations based off a series of 112 sparse patterns of surface data that describe underlying liver deformations designed to reproduce intraoperative organ changes that occur during open liver surgery. As part of the challenge announcement, the deformation correction methods developed in Chapter IV were reported using this dataset.

In this chapter, this dataset is revisited following the algorithmic inverse modeling developments of Chapter V. Inside, an argument is presented for the importance of inverse modeling approaches to reconstruct deformation sources, and the inverse modeling approach is characterized to determine the optimal reconstructive resolution for open liver registration relative to data extent and conditioning. Furthermore, as curators of the challenge, a small update to resources provided to challenge participants is presented with the goal of improving offline testing capabilities.

The Image-to-Physical Liver Registration Sparse Data Challenge: Characterizing Inverse Biomechanical Model Resolution

The work presented in this chapter appears in and is reprinted with permission from,

[211]: J. S. Heiselman and M. I. Miga, "The Image-to-Physical Liver Registration Sparse Data Challenge: Characterizing Inverse Biomechanical Model Resolution," in *Proceedings of SPIE Medical Imaging*, vol. 11315, pp. 1–7, 2020. (© 2020 SPIE)

B.2 Abstract

Image-guided liver surgery relies on intraoperatively acquired data to create an accurate alignment between image space and the physical patient anatomy. Often, sparse data of the anterior liver surface can be collected for these registrations. However, achieving accurate registration to sparse surface data when soft tissue deformation is present remains a challenging open problem. While many approaches have been developed, a common standard for comparing algorithm performance has yet to be adopted. The image-to-physical liver registration sparse data challenge offers a publicly available dataset of realistic sparse data patterns collected on a deforming liver phantom for the purpose of evaluating and comparing potential registration approaches. Additionally, the challenge is designed to allow testing and characterization of these methods as a general utility for the registration community. Using this challenge environment, an inverse biomechanical method for deformable registration to sparse data was investigated with respect to how whole-organ target registration error (TRE) is impacted by a model parameter that controls the spatial reconstructive resolution of mechanical loads applied to the organ. For this analysis, this resolution parameter was varied across a wide range of values and TRE was calculated from the challenge dataset. An optimal parameter value for model resolution was found and average TRE across the 112 sparse data challenge cases was reduced to 3.08 ± 0.85 mm,

an approximate 32% improvement over previously reported results. The value of the data offered by the sparse data challenge is evident. This work was performed entirely using information automatically generated by the challenge submission and processing site.

B.3 Purpose

The image-to-physical liver registration sparse data challenge, announced last year at SPIE 2019 (www.sparsedatachallenge.org, [111, 210]), aims to provide the registration community with a common dataset that allows quantitative assessment of registration accuracy given an expansive set of sparse data patterns collected on the surface of a deformable liver phantom. Furthermore, the challenge is designed to create an online testing environment where algorithmic approaches can be explored with a public dataset and methods can be validated according to a common standard. The goal of this work is to characterize the performance of a deformable registration algorithm based on a reconstructive inverse biomechanical modeling approach adapted from [9] and [20] using this public dataset. Specifically, in this work we aim to optimize a critical parameter of the inverse model that controls the resolution with which intraoperative deformations can be reconstructed. This investigation harnesses the full power of the challenge dataset to advance understanding of the registration method. Also, to assist wider participation of the image guidance community with developing alternative methods for the sparse data challenge, this year additional data has been added to the challenge site to allow users the option to quantitatively examine their approaches offline before submitting results to the publicly displayed dashboard.

B.4 Methods

B.4.1 Overview of the Sparse Data Challenge

The challenge data consists of 112 sparse data patterns collected on the liver surface representative of realistic intraoperative data acquisition in the operating room environment. Given an initial image mask and a tetrahedral mesh of the liver, the objective of the challenge is to determine a deformable registration to each sparse data pattern that most ac-

curately predicts the whole-organ deformation based on the limited information provided. To permit quantitative validation of registration accuracy, these data were derived from a deformable silicone liver phantom with 159 embedded targets. To reproduce deformations similar to open liver surgery, surgical packing was placed under the posterior surface of the liver phantom. The sparse data patterns were obtained after these deformations were applied and the ground truth positions of the embedded targets were imaged for validation.

While the full validation data is hidden to participants, the challenge is hosted on an Amazon Web Services platform that is designed to allow rapid feedback about algorithm performance on a partial or full set of submitted results. For each of the 112 data patterns, participants submit a predicted displacement field sampled at each vertex of the tetrahedral grid that aims to most closely match the true deformation of the liver phantom. These submissions are automatically processed and output performance metrics are hosted on a public dashboard. These metrics include average target registration error (TRE) across all data sets, as well as TRE stratified over low, medium, and high levels of surface data coverage.

B.4.2 Additional Offline Testing Data for Participants

To promote further participation in the challenge, additional data has been offered for participants to more closely validate potential algorithms offline. Positions for a partial set of 35 of the 159 targets have been provided in the same space as the undeformed tetrahedral grid. Furthermore, the ground truth positions of these targets have been provided for four of the sparse data patterns: Sets 044, 057, 067, and 084. These additional data, shown in Figure B.1, are intended for users to be able to more closely analyze the behavior of their methods as they are being developed.

B.4.3 Overview of In-House Nonrigid Registration Algorithm

As sparse intraoperative data does not necessarily provide complete constraints to the unique solution, in general the sparse data registration problem is ill-posed. It is imper-

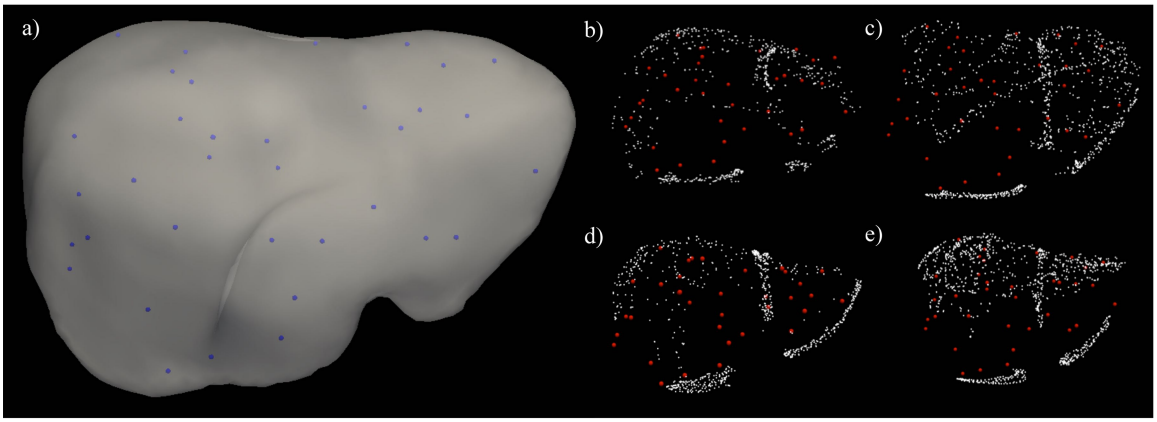

Figure B.1: Additional offline testing data for challenge participants. (a) Initial positions of the 35 provided targets (blue) from the total 159 targets inside the liver. (b–d) Deformed positions of the 35 provided targets (red) for the four selected sparse data patterns (white).

ative to note that ill-posed problems are still solvable. However, regularization methods and attention to the conditioning of the problem are important because it can become difficult to define how well determined a configuration of sparse data makes the underlying numerical problem. Often, algorithms can be parameterized to control performance in these situations. In this work, we show that the sparse data challenge can be used to characterize such performance-tuning parameters for registration algorithms, including our own, with a realistic dataset.

Our registration approach utilizes a linear elastic biomechanical model of the liver to minimize error between the observed sparse surface data and a deformable model of the organ described by a series of simulated superimposed deformations. This algorithm is represented by the nonrigid registration method described in [20], wherein deformations mirroring the mechanical loading configurations present during surgery are simulated by perturbing control points placed across the surface of the liver. Perturbing each control point creates a local mode of deformation that can be used to iteratively reconstruct an unknown distributed load placed on the boundary of the liver. This reconstruction minimizes the model-data error regularized by a strain energy penalty function. In this work, the algorithm is modified to match the mechanical loading configuration of open liver surgery

represented by the sparse data challenge by limiting control point placement to the posterior surface only, where surgical packing imparts mechanical excitation to the system.

Although it may be algorithmically tempting to apply boundary conditions directly on the anterior surface of the liver where data can be collected, this practice may give rise to substantial error compared to the underlying deformation of the organ. As demonstrated in Figure B.2, the internal displacements of simulations driven off the anterior surface can differ by approximately 50% of the RMS magnitude of the actual excitatory displacements applied to the posterior. Therefore, we contend that a reconstructive approach that attempts to solve for the unknown distributed loads applied to the liver is a preferable approach that can allow for better predictions of the internal and far-field displacements.

An important parameter in the reconstructive registration approach is the number of control points, which regulates the resolution with which the mechanical load applied to the organ can be represented. While a compromise between registration accuracy and computation time is to be expected, the nature of sparse data registration gives rise to an additional layer of complexity. Notably, a tradeoff exists between the number of control points and how well the control point motions can be resolved by sparse data. The objective of this paper is to characterize the performance of the algorithm across a wide range of control point densities to determine what level of numerical complexity is sufficiently constrained by typical extents of sparse surface data coverage.

B.4.4 Characterization of Control Point Density

Full submissions were made to the image-to-physical liver registration sparse data challenge for varying numbers of control points in the reconstructive algorithm. Control points were sampled using k-means clustering on the posterior surface of the liver mesh at the following values of k: 2, 3, 5, 7, 10, 15, 20, 30, 50, 70, 100, and 150. These values were selected to explore performance of control point density on a logarithmic scale. Figure B.2 shows several control point distributions on the challenge liver mesh. Challenge submis-

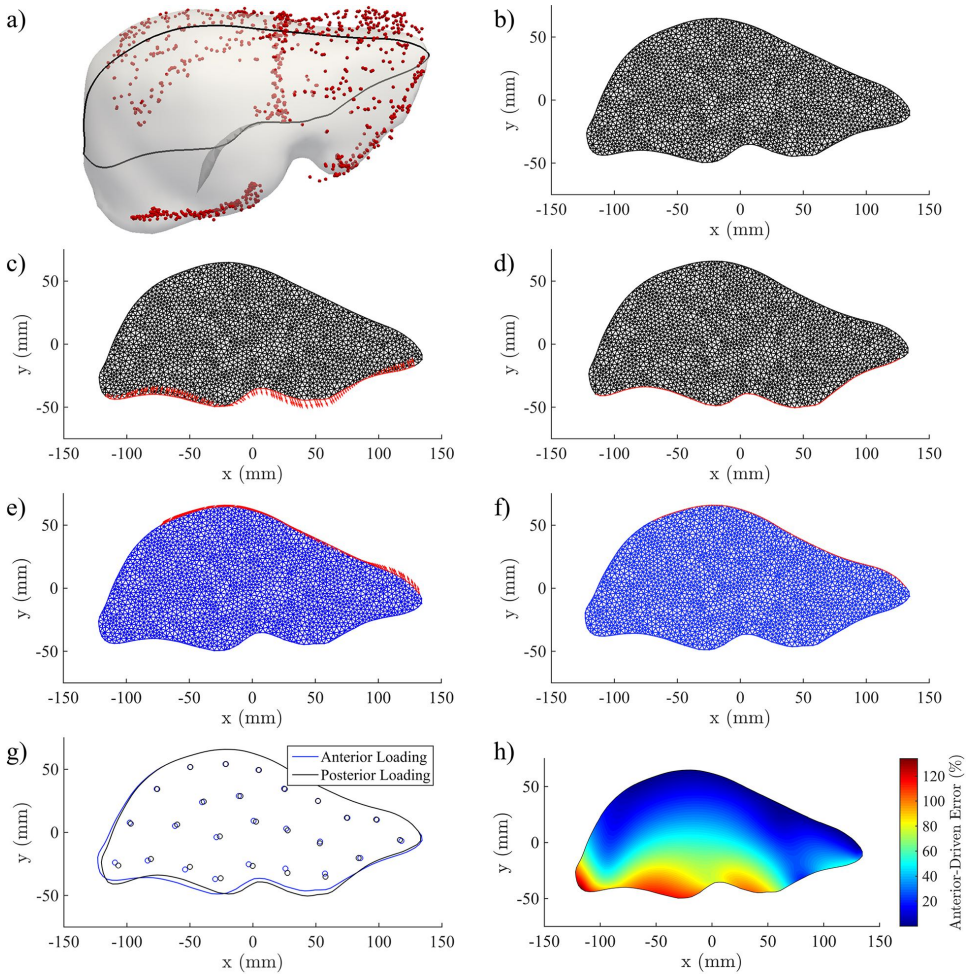

Figure B.2: Comparison of plane-strain linear elastic responses to loading conditions placed on the posterior and anterior surfaces of the liver. (a) A 2D slice (black contour) is taken from the sparse data challenge liver mesh. Rigidly registered anterior surface data from Set 057 (red points) shows approximate data coverage on the slice. (b) The 2D slice is triangulated into a finite element mesh with edge lengths under 4 mm. (c) A sinusoidal displacement profile with 6 mm amplitude is applied to the posterior aspect of the liver as boundary conditions to simulate an unknown mechanical load from surgical packing applied to the liver. All other boundary nodes are stress free. (d) The finite element response to the posterior displacement boundary conditions. (e) Exact displacements from the posteriorly-driven solution in (d) are applied to the original mesh from (b) as boundary conditions on the anterior surface where data coverage exists. All remaining boundary nodes are stress free. (f) The finite element response to the anterior displacement boundary conditions. (g) A comparison of the liver boundary between the posteriorly-driven deformation from (d) and the anteriorly-driven deformation from (f), with the positions of 25 internal nodes shown as mock targets. (h) The error in displacement solutions between the anteriorly- and posteriorly-driven deformations relative to the RMS of posterior displacements.

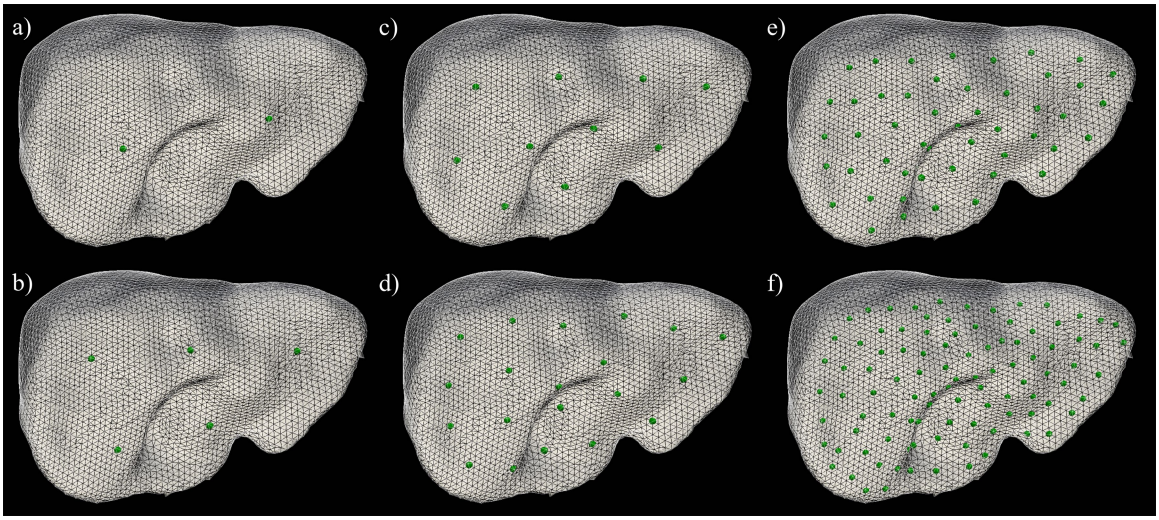

Figure B.3: Distribution of control points across the liver: (a) 2, (b) 5, (c) 10, (d) 20, (e) 50, (f) 100.

sions were made for each value of k, and the resulting TRE values were downloaded from the sparse data challenge website.

B.5 Results

In Figure B.4, average target registration error is plotted for each value of k. The shape of the semilogarithmic curve suggests an optimal value of k exists that minimizes TRE. Table B.1 shows the automatically generated results from the sparse data challenge for the optimal number of control points, $k = 20$, that produces the minimum average TRE on the challenge dataset. With this value of k, the overall TRE across the whole organ averaged over all 112 challenge cases was 3.08 ± 0.85 mm, showing that highly accurate registrations to sparse surface data can be made using a modest number of control points. This TRE represents a 32% improvement over the value reported in [210]. It is interesting to note that the algorithm performance degrades when the number of control points is too small or too large. In the former case, an insufficient number of control points likely prevents sufficiently detailed reconstruction of the mechanical loads applied to the organ. In the latter case, it is possible that the amount of data provided becomes insufficient to be able to resolve the behavior of each control point, leading to an underdetermined system that is more

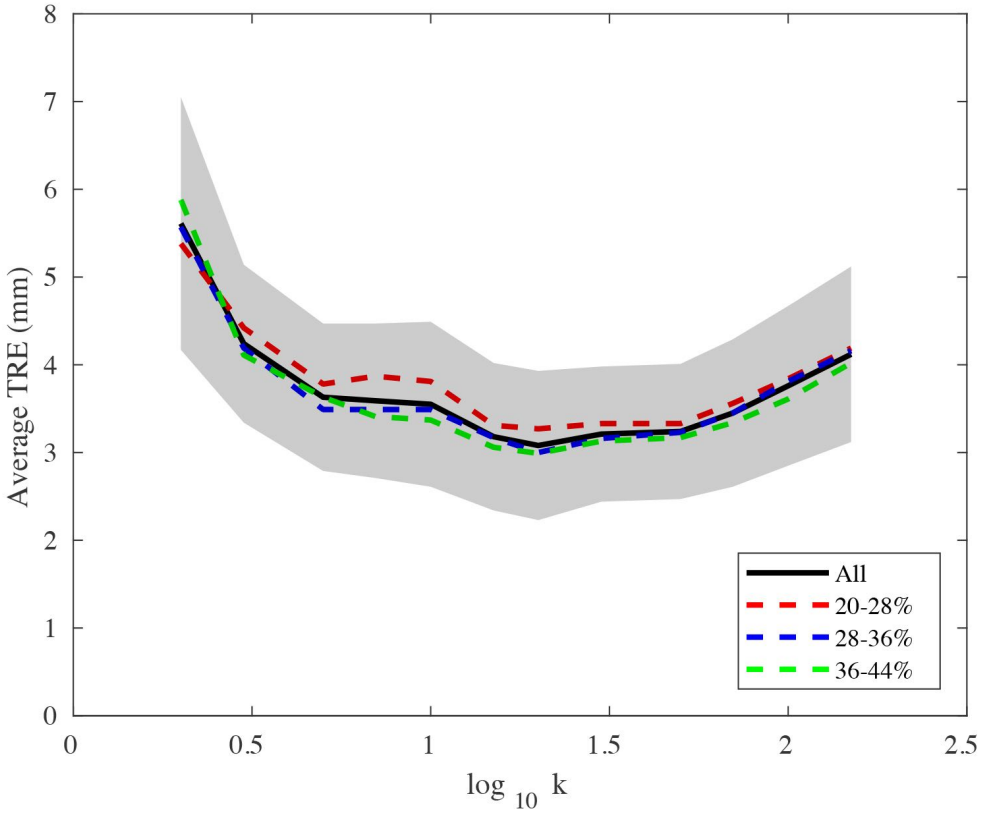

Figure B.4: TRE vs. number of control points plotted on logarithmic scale. The black line represents the mean value of TRE across all 112 challenge cases surrounded by one standard deviation in the gray region. The red, blue, and green dashed lines represent the mean TRE across the subset of cases in the low, medium, and high extent brackets, respectively.

susceptible to local minima. It is important to note that the most suitable number of control points may change depending on the amount of available intraoperative data. Information from additional subsurface, posterior surface, or more complete anterior surface data may shift the optimal value of k by improving the ability to resolve a greater number of control points.

B.6 Contributions

In addition to serving as a common benchmark for sparse data registration methods, the dataset made available with the image-to-physical liver registration sparse data challenge is

Surface Coverage	Average TRE (mm)	Median TRE (mm)
20–28%	3.27 ± 1.07	2.89
28–36%	3.00 ± 0.67	2.97
36–44%	2.99 ± 0.78	2.73
All Data Sets	3.08 ± 0.85	2.89

Table B.1: Sparse data challenge target registration error for the best control point sampling, found to be $k = 20$.

a powerful tool for identifying useful information about potential algorithmic approaches. In this work, our algorithm for nonrigid sparse data liver registration was analyzed for its ability to reconstruct mechanical deformations at varying levels of control point resolution. These findings were used to characterize and tune performance of the algorithm within the expected range of intraoperative surface data available in the clinical setting. The presented results represent an effort towards understanding the influence of how the nature of data sparsity influences registration methodology.

B.7 Conclusions

Registration to sparse data becomes a difficult problem if accurate and robust results are desired. In general, sparse data registration requires solution methods that simultaneously consider interpolative and extrapolative model effects in relation to the data made available, in addition to intraoperative considerations such as computation time. These methods can sometimes require careful characterization to understand how model parameters interact with sparse data and influence registration results. The image-to-physical liver registration sparse data challenge is designed to facilitate this characterization for developing new methods and to offer a public comparator of algorithm fidelity. In this work, the challenge data was used to characterize an essential parameter of the registration algorithm used by our group. This parameter, which controls the spatial resolution with which deformations applied to the organ can be reconstructed, was found to have an optimal value for registration to realistic patterns and extents of intraoperative sparse surface data collected during open liver surgery.

Appendix C

Deformable Registration of the Liver Using Sparse Intraoperative Data: Incorporating Hepatic Feature Constraints from Tracked Intraoperative Ultrasound

C.1 Summary and Contributions

In Chapter V, the preoperative liver model was registered using a novel deformable registration algorithm to data from multiple tracked iUS planes. In that work, registration accuracy was characterized across varying quantities of iUS planes made available for registration. In this chapter, registration accuracy is evaluated based on a separation of features visible within individual iUS liver images and the relative changes in TRE when these features are added or subtracted from the registration. This study attempts to address (a) whether informational redundancy might exist between vessel and posterior surface features when they are derived from the same image plane, (b) the potential need for manually defining correspondence of iUS vessel features to the correct branch of the 3D vessel model to reduce the potential for misregistration, and (c) the tradeoffs between centerline and contour representations of vessel features. The contributions of this work establish and summarize best practices for the utilization of iUS imaging feature content for deformable registration.

Deformable Registration of the Liver Using Sparse Intraoperative Data: Incorporating Hepatic Feature Constraints from Tracked Intraoperative Ultrasound

The work presented in this chapter appears in and is reprinted with permission from,

[212]: J. S. Heiselman, W. R. Jarnagin, and M. I. Miga, "Deformable registration of the liver using sparse intraoperative data: Incorporating hepatic feature constraints from tracked intraoperative ultrasound," in CARS 2020—Computer Assisted Radiology and Surgery Proceedings of the 34th International Congress and Exhibition, *International Journal of Computer Assisted Radiology and Surgery*, vol. 15, no. S1, pp. S146–S147, 2020.

C.2 Purpose

During liver surgery, successful delivery of treatment depends on a comprehensive understanding of the spatial relationships between interventional targets, hepatic vessels, and surgical instruments. Image guidance aims to localize these components by registering information from preoperative imaging with the intraoperative anatomy of the patient. However, accurate registration of subsurface structures remains challenging due to organ deformation that compromises the fidelity of image-to-physical registration. To compensate, many liver registration techniques rely on the shape of the organ surface to predict the underlying state of deformation. However, the visible extent of surface coverage is often limited and can be insufficient for achieving accurate registrations throughout the depth of the liver. Tracked intraoperative ultrasound (iUS) can extend the coverage of intraoperative data available for registration; however, limitations in lesion detection, interpretability, and workflow encumber iUS as the principal means of intraoperative guidance. In this work, we evaluate how information from very sparse iUS data can be applied to best improve the performance of

deformable liver registration by examining and comparing iUS feature constraints visible within individual iUS planes.

C.3 Methods

A simulation study was performed to compare registrations to subsurface features from 16 orientations of 2D tracked iUS imaging data. Models of the liver parenchyma and portal and hepatic veins were created from a contrast-enhanced preoperative CT of a deidentified human patient. A linear elastic finite element model was then used to deform the liver to a known intraoperative organ presentation using the data generative method from [20]. Intraoperative features from tracked iUS were simulated by intersecting 16 potential image plane orientations with the ground truth deformed model. In each iUS image plane, these features described the posterior surface of the liver typically visible in iUS and intrahepatic vessel contours with associated centerline positions approximated by feature centroids. Additionally, sparse anterior surface data were derived from a clinical pattern of digitization on the ground truth model for registration purposes. Figure C.1 shows one of the 16 configurations of data.

The linearized iterative boundary reconstruction method [20] was used for deformable registration of the original model to simulated data. While [20] aimed to understand how data from multiple iUS planes could be combined to improve registration accuracy, the focus of this work is to characterize how incorporating distinct feature constraints from a single iUS plane can impact registration accuracy. For each of the 16 iUS views, target registration error (TRE) was evaluated to determine: (I) whether informational redundancy might exist between vessel and posterior surface features when they are derived from the same image plane, (II) the potential need for manually defining correspondence of iUS vessel features to the correct branch of the 3D vessel model, and (III) the tradeoffs between centerline and contour representations of vessel features. TRE was computed as the average nodal distance between the ground truth and registered mesh, and differences in average

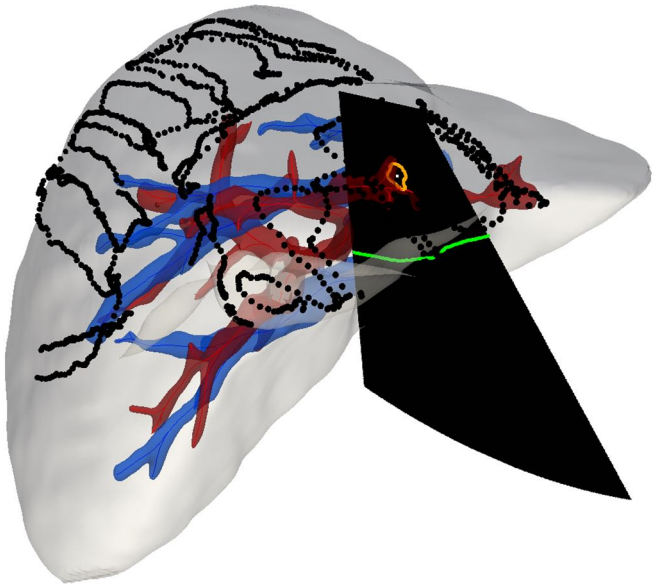

Figure C.1: Intraoperative ultrasound features. Preoperative liver model (gray), portal vein (red) and hepatic vein (blue) with rigidly registered data consisting of sparse anterior surface points (black) and iUS features including the posterior surface (green), vessel contour (orange), and vessel centerline point (white).

TRE were statistically tested against zero mean using a two-tailed, one-sample t-test at significance $\alpha = 0.05$.

C.4 Results

(I): Close spatial proximity of features within an iUS image plane may suggest that registering to only a subset of these features might be necessary for accurate alignment. To test this possibility, average TRE was computed for the 16 iUS registration scenarios in three conditions: using only vessel contour features (8.6 ± 1.8 mm), using only posterior surface contours (8.9 ± 1.7 mm), and using both posterior and vessel contours (7.6 ± 1.9 mm). Significant improvements in average TRE were observed when using both features, with average improvement of 1.0 ± 1.4 mm ($p = 0.01$) compared to using only vessels and 1.3 ± 1.5 mm ($p = 0.005$) compared to using only posterior, suggesting that vessel and posterior surface features visible in iUS offer partially independent constraints best leveraged together to improve registration accuracy. Overall distributions of the differences in

TRE are shown in the first two columns of Fig. 2. The largest improvement in average TRE across the mesh was 5.0 mm when using both features instead of a single feature in one of the 16 configurations of data, decreasing TRE from 11.4 ± 7.1 mm to 6.4 ± 4.5 mm. Reciprocally, it is possible that posterior surface data may help direct vessel features towards the correct branch of the vessel model, and vessel data may assist with regularizing the posterior constraint that can traverse across the rear surface of the liver.

(II): During registration, correspondence between iUS vessel features and the full 3D vessel model can be estimated by closest point distance. However, these correspondences can become incorrect when features are located near bifurcations or in regions with large deformation compared to the inter-branch distances of the vessel tree. In these cases, directing a skilled sonographer to manually label the vessel branch of correspondence during data collection can ensure correct alignment between the iUS feature and the model. With manual designation of centerline branches, average TRE improved by 0.4 ± 1.2 mm over unconstrained closest point correspondences (Figure C.2, third column), from 8.0 ± 2.2 mm to 7.6 ± 1.9 mm. While this difference was not statistically significant ($p = 0.17$), in one case the manual constraint improved TRE from 12.5 ± 6.1 mm to 7.8 ± 4.4 mm when a vessel feature had initially been misregistered to an incorrect branch. Steps to address vascular feature correspondence between 2D iUS planes and 3D models therefore may improve robustness of registration algorithms.

(III): Whereas vessel centerline representations have reduced dimensionality that may smooth the optimization landscape and obscure physiological changes to vasculature during registration, centerline approximations from iUS image planes may not be accurate when vessels are imaged obliquely or near bifurcations. Additionally, information encoding the orientation of the vessel is lost. Although registration using vessel contours may avoid these shortcomings, the apparent diameter of the intrahepatic blood vessels may change based on segmentation, pulsatility, and vasoregulation. To compare, differences in average TRE were computed for registrations to vessel contour and centerline approx-

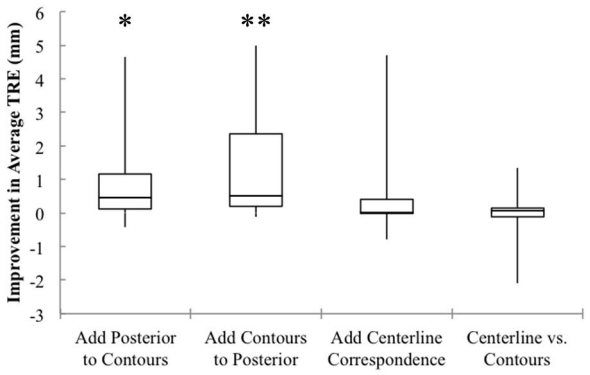

Figure C.2: Quartile distributions of the change in average TRE comparing iUS feature constraints across 16 registrations to simulated data ($*p = 0.01$; $**p = 0.005$).

imations of the portal and hepatic vein features in the simulated iUS planes. No significant difference in average TRE was found between using the unlabeled contour or the correspondence-labeled centerline representations of vessels ($p = 0.99$), with an average difference of 0.0 ± 0.7 mm (Fig. 2 fourth column). While this comparison was performed using simulated data free from noise, it is possible that combining contour and centerline feature constraints in more realistic registration scenarios may complement the shortcomings of each and improve overall registration robustness.

C.5 Conclusion

Feature constraints from tracked iUS were investigated for application in image-to-physical liver registration. Significant improvement in average TRE was found when registering to a combination of hepatic vessel features and posterior surface features detectable within single iUS images. Non-significant improvement was found when model-data correspondences of vessel features were manually constrained, and no difference in average TRE was found between registrations to unconstrained contour and manually constrained centerline representations of vessel features.

C.6 Appendix: Ultrasound Plane Location and TRE

This section includes renderings of the ultrasound plane locations used and registrations performed in this study that were not included in the conference proceedings due to space constraints. Figure C.3 shows the positions of the 16 simulated iUS planes, and Figure C.4 shows the TRE of registrations to each plane using all feature content from the iUS image planes (posterior surface, vessel contours, and branch-labeled vessel centerlines). Overall, TRE was found to be lowest when the posterior surface, vessel contour, and labeled centerline features from tracked iUS were all registered in conjunction with the anterior surface. With an initial TRE of 10.9 ± 8.5 mm after rigid registration, it should be noted that the distribution of surface data coverage did not cover areas of substantial organ deformation. Consequently, the deformable surface registration only marginally improved the average TRE across the mesh to 10.4 ± 8.2 mm. However, when features from one iUS plane were added, the average TRE decreased to a mean of 7.6 ± 1.9 mm across all 16 registrations to tracked iUS features. However, four of the 16 iUS registrations had average TRE below 6 mm, with the best registrations having average TRE of 5.4 ± 2.8 mm (U8) and 5.4 ± 3.0 mm (U15). A general trend should be noted in registration performance, where registrations that incorporate additional data from distant regions of the liver lead to more extensive spatial coverage and tended to be associated with more accurate results. This behavior suggests that deliberate collection of impactful iUS data may make it achievable to consistently obtain TREs in the lower range of variability between 5–6 mm throughout the organ, with the addition of data from just one iUS plane. The variability in TRE depending on the position of the iUS plane indicates that subsurface information from different regions provides different amounts of information to the registration.

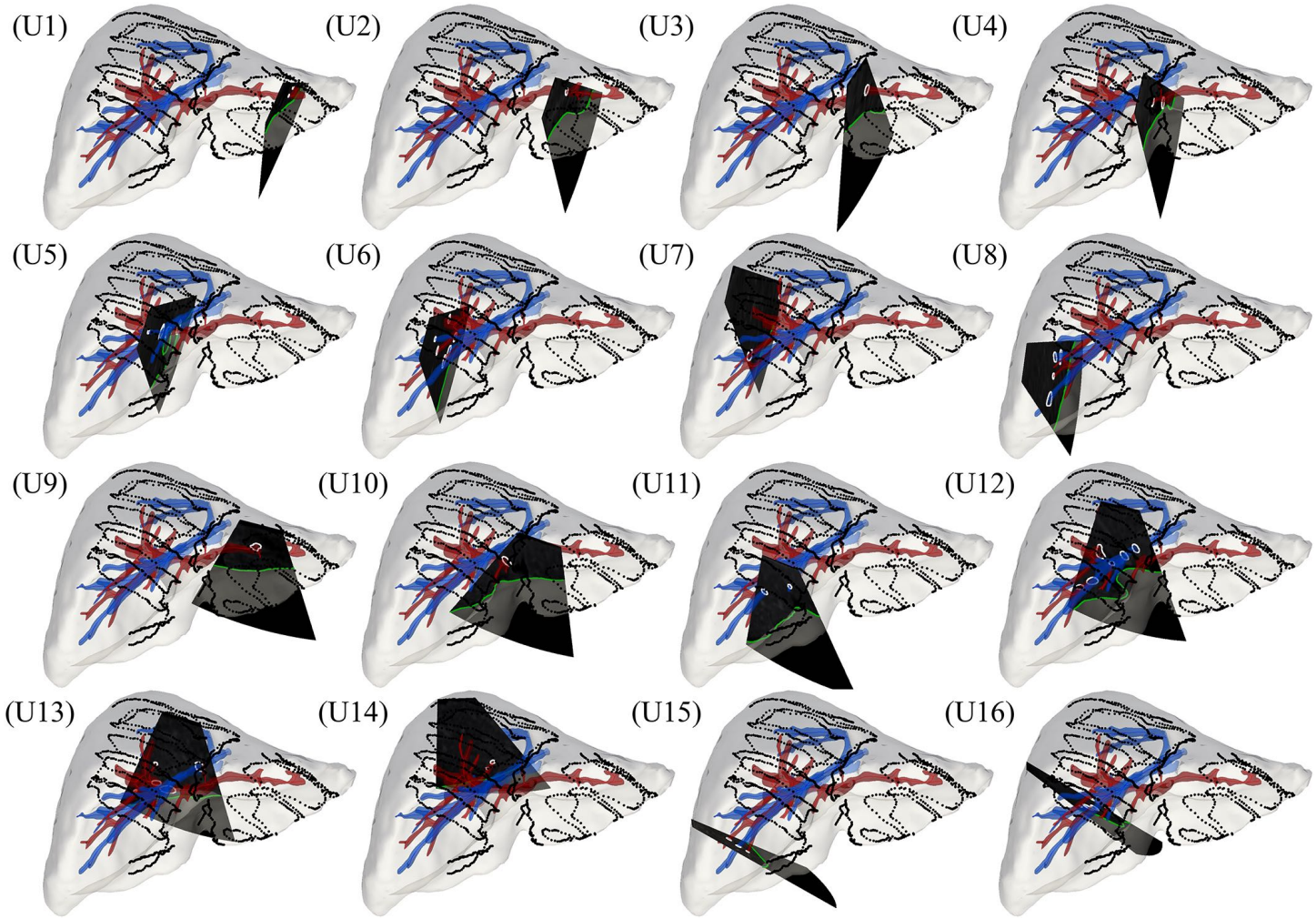

Figure C.3: Spatial positions of simulated ultrasound planes (U1–U16) for registration. The clinical pattern of anterior surface points and the ultrasound plane orientations are shown black. Vessel features visible in iUS are outlined in white, and the posterior surface features in green.

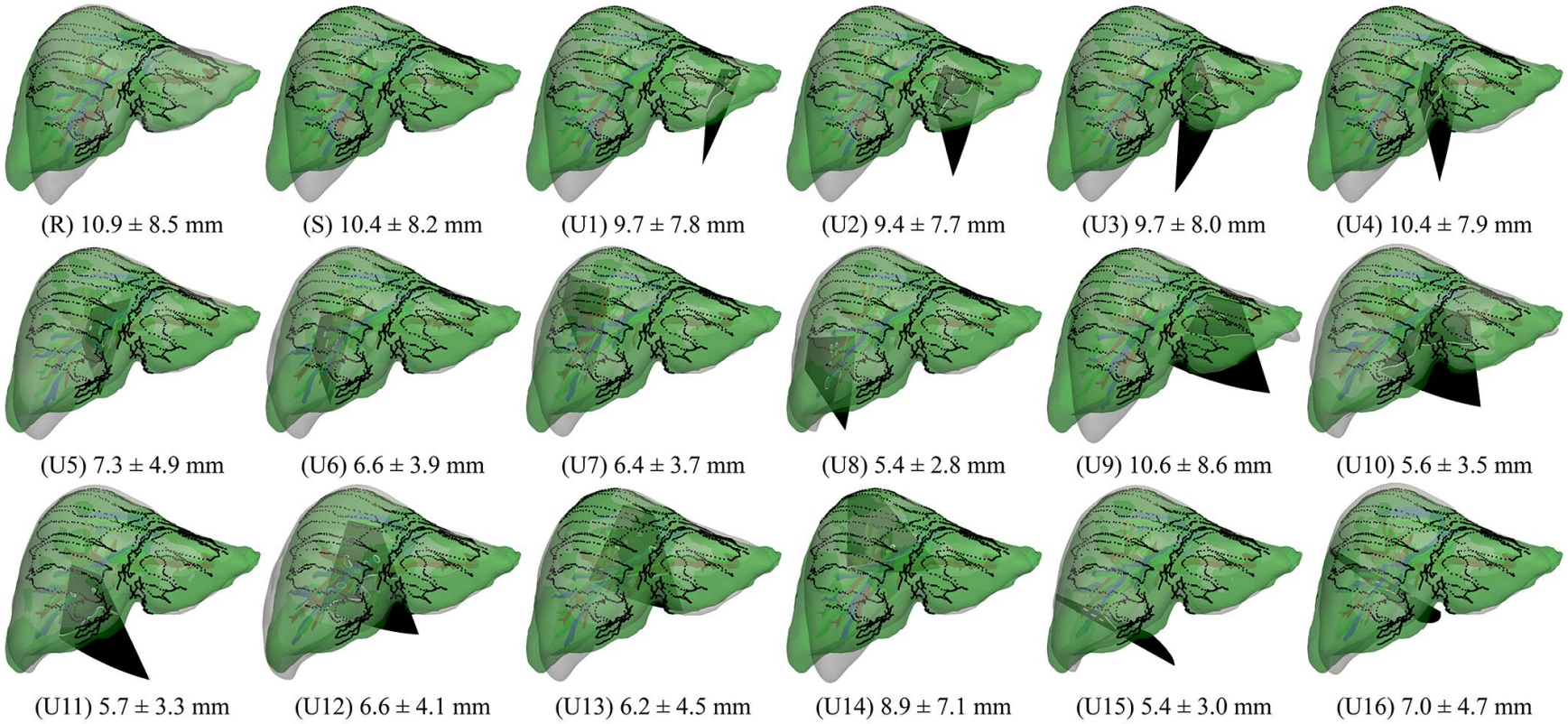

Figure C.4: Registration results. (R) Rigid registration to surface data; (S) Deformable registration to surface data; (U1–U16) Deformable registration to surface data plus features from one tracked iUS plane. The registered model is shown in white, the intraoperative data in black, and the ground truth mesh in green.

Appendix D

Additional Characterization Studies

This chapter includes additional characterization studies that were performed throughout the progress of this dissertation but were not included in the previous chapters due to space constraints when preparing publication manuscripts.

D.1 Comparison of TRE with Corotational Model Reconstruction

In Chapter IV, the potential for incorporating a corotational correction into the model reconstruction was described. Briefly, the corotational finite element approach attempts to remove excess strain energy introduced to a deformed system by pure rotational components of finite element displacements. This excess strain energy arises due to the fact that the linearized strain and stress tensors are not rotation invariant, and causes conventional linear elastic models to behave more stiffly than expected. The corotational correction is achieved by rotating local element equation sets to a rotation-free coordinate frame during the solution process by iteratively updating local element rotations when solving for displacement. This process expands the conventional finite element assembly and solution from $Ku = f$ to $RKR^T u = f + RK(x - R^T x)$, where RKR^T is a rotated stiffness matrix and $RK(x - R^T x)$ is a force correction vector to account for element rotations [164]. A total of 63 registration scenarios were derived from different mobilizations and extents of organ surface data collected on the laparoscopic phantom described in Chapter IV and Appendix A. Registrations were performed using the method reported in Chapter IV and using an analogous approach except replacing all instances of conventional linear elastic model solutions (modes and model relaxation) with corotational linear elastic model solutions instead. TRE was measured in both cases from the validation targets embedded in the phantom. The histogram of paired differences in TRE between co-rotational and conventional finite element model solutions is shown in Figure D.1 (difference defined as co-rotational TRE minus conven-

tional TRE). The average difference was -0.08 ± 0.72 (range -2.55–2.15), which was not found to differ significantly from zero (paired t-test, $p = 0.40$). While corotational models tend to provide more accurate forward simulations of deformation, it is likely that the incorporation of geometric nonlinearities works against the property of superposition upon which the reconstructive algorithm depends.

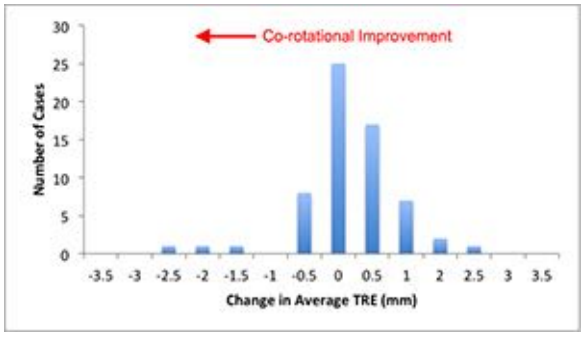

Figure D.1: Change in average TRE between conventional and co-rotational model solutions for reconstructive registration algorithm.

D.2 Characterization of Surface, Vessel, and Posterior Feature Weights

This section includes results from a characterization experiment on relative weights of surface and iUS features applied in the reconstruction algorithm presented in Chapter V. Sixteen iUS plane locations were simulated on a liver mesh subjected to a known ground truth deformation. Registrations were performed between the preoperative mesh and the following combinations of intraoperative data: (i) surface data plus vessel and posterior features from one iUS plane (n = 16), (ii) surface data plus vessel and posterior features from two iUS planes (n = 120), (iii) surface data plus vessel and posterior features from all 16 iUS planes (n = 1), and (iv) ground truth deformed surface meshes of liver and vessel branches (n = 1). With initial values of weights for intraoperative surface points w_s, subsurface vessel feature points w_{ss}, and posterior surface points w_p set to 1.0, each weight was independently varied in the range $w \in [0,2]$ and resulting target registration errors were measured. Figure D.2 shows the shift in distribution of TRE as the subsurface vessel weight w_{ss} is characterized while keeping w_s and w_p constant. Similarly, Figure D.3 shows

the shift in distribution of TRE as posterior feature weight w_p is varied, and Figure D.4 shows TRE when the weight of surface data w_s is varied. These characterizations suggest that the best results are achieved in this simulation environment when all weights are left equal at $w_s = w_{ss} = w_p = 1.0$. In clinical scenarios, optimal values for feature weights may differ depending on potential sources of measurement noise and the resulting variance of the measurement.

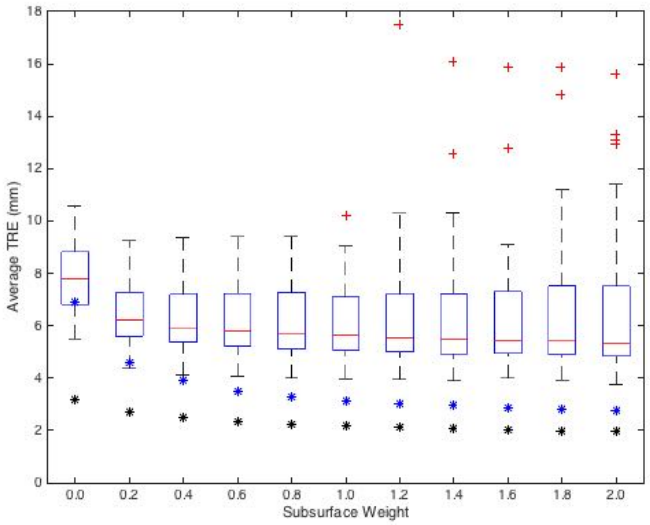

Figure D.2: TRE vs. Subsurface data weight. Quartiles represent distribution of average TRE from registrations to 136 total combinations of registration data from one or two iUS planes. Blue asterisks indicate registration to data from 16 different iUS planes, and black asterisks indicate registration to ground truth data.

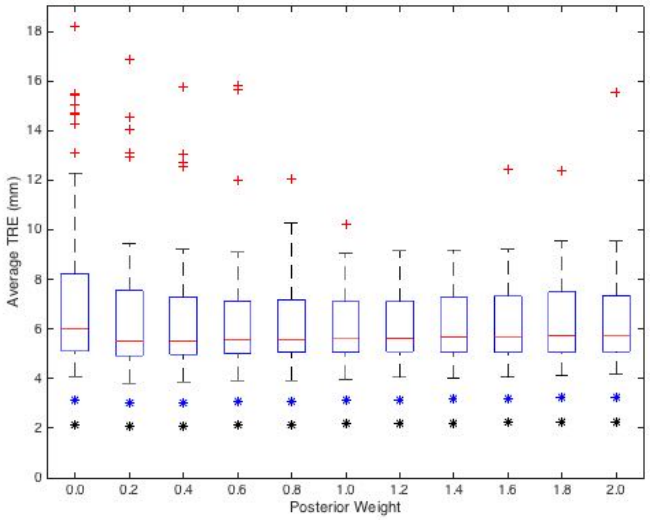

Figure D.3: TRE vs. Posterior data weight. Quartiles represent distribution of average TRE from registrations to 136 total combinations of registration data from one or two iUS planes. Blue asterisks indicate registration to data from 16 different iUS planes, and black asterisks indicate registration to ground truth data.

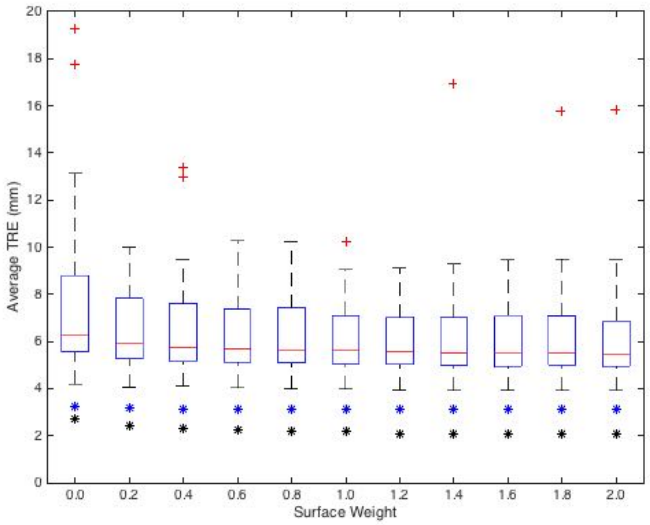

Figure D.4: TRE vs. Surface data weight. Quartiles represent distribution of average TRE from registrations to 136 total combinations of registration data from one or two iUS planes. Blue asterisks indicate registration to data from 16 different iUS planes, and black asterisks indicate registration to ground truth data.

D.3 Comparison of Bivariate Gamma and Lognormal Distribution Fits

This section includes plots for statistical regressions between residual TRE (E) and registration uncertainty (S_r and S_p) defined in Chapter VI. This section expands and further qualifies the bivariate gamma distribution fits from Section VI.8 through visualization of marginal distributions, in addition to a comparison with a bivariate lognormal distribution with location parameters as a potential alternative. Both distributions were fit using method of moments estimators followed by optimization of the Hellinger distance between empirical and regressed distributions. This section shows that the bivariate gamma distributions provide substantially better fit to data.

D.3.1 Bivariate Gamma Plots

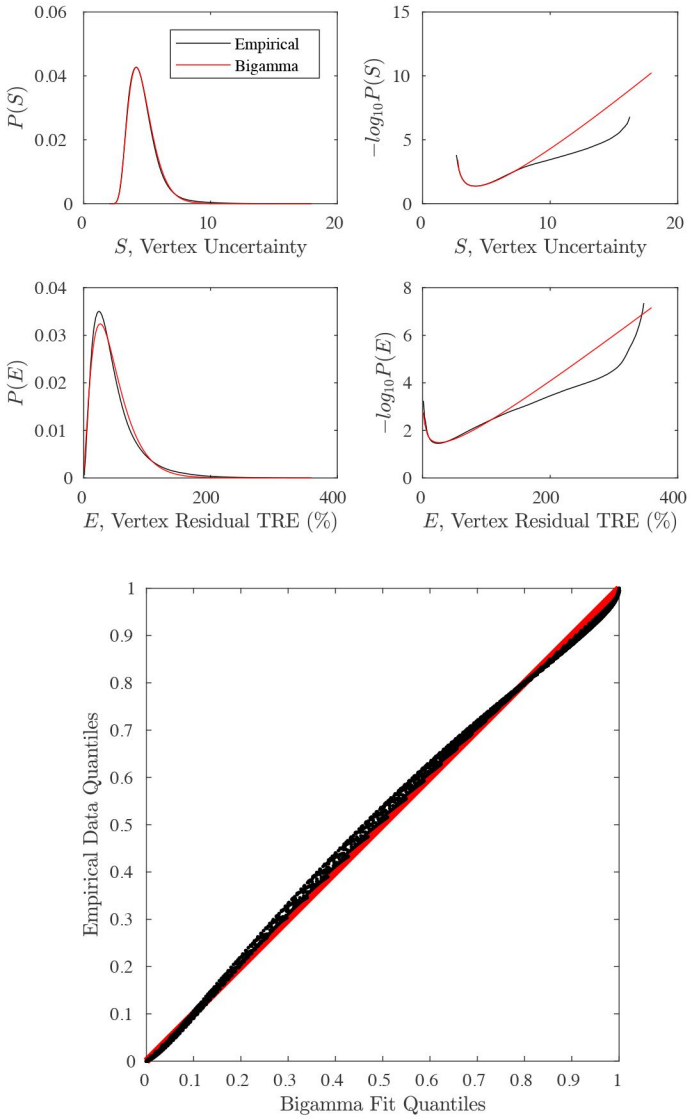

Figure D.5: Comparison of marginal distributions (top) and Q-Q plot (bottom) from empirical data with best-fit bivariate gamma distribution of residual TRE (E) and retrospective registration uncertainty (S_r).

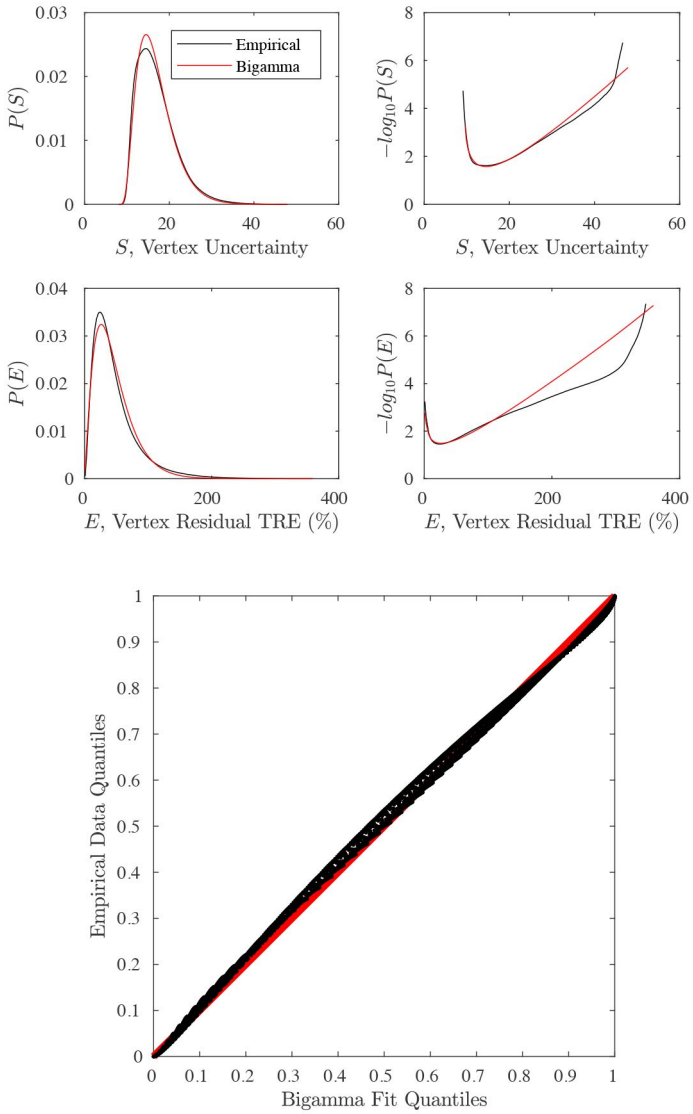

Figure D.6: Comparison of marginal distributions (top) and Q-Q plot (bottom) from empirical data with best-fit bivariate gamma distribution of residual TRE (E) and prospective registration uncertainty (S_p).

D.3.2 Bivariate Lognormal Plots

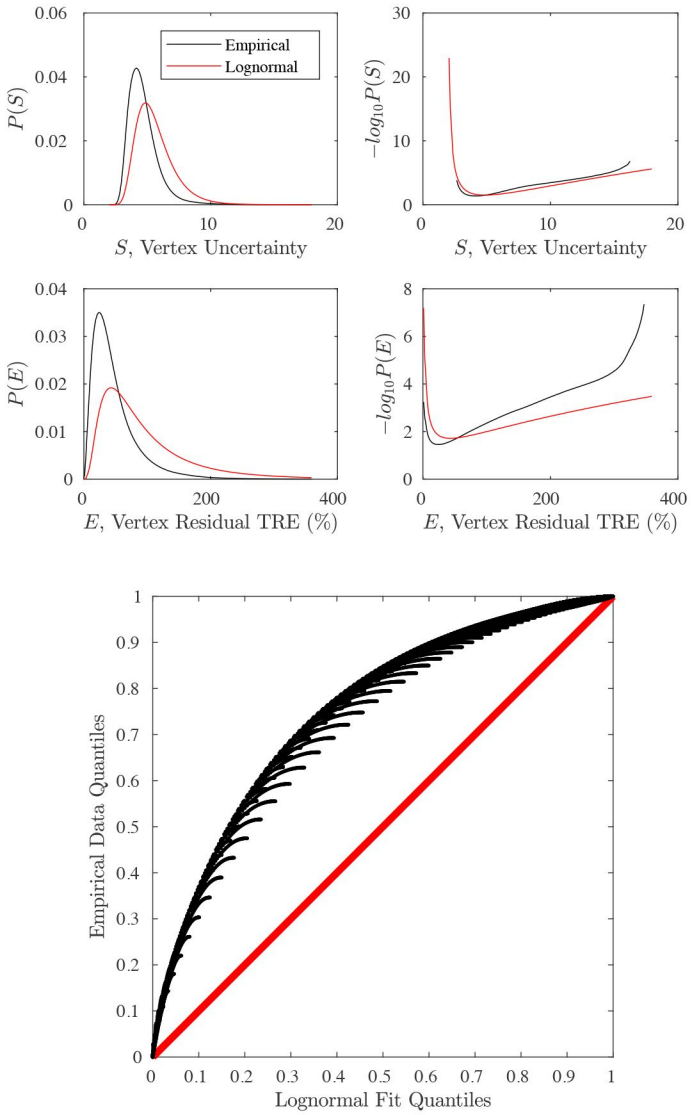

Figure D.7: Comparison of marginal distributions (top) and Q-Q plot (bottom) from empirical data with best-fit bivariate lognormal distribution of residual TRE (E) and retrospective registration uncertainty (S_r).

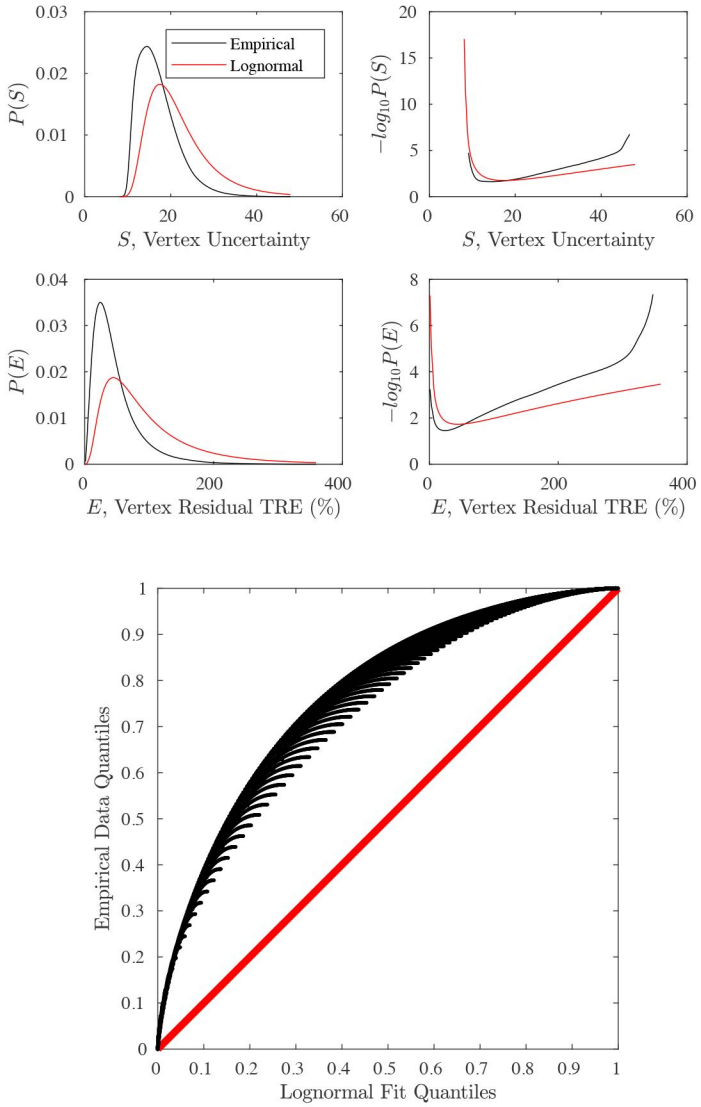

Figure D.8: Comparison of marginal distributions (top) and Q-Q plot (bottom) from empirical data with best-fit bivariate lognormal distribution of residual TRE (E) and prospective registration uncertainty (S_p).

BIBLIOGRAPHY

[1] S. Suwelack, S. Röhl, S. Bodenstedt, D. Reichard, R. Dillmann, T. dos Santos, L. Maier-Hein, M. Wagner, J. Wünscher, H. Kenngott, B. P. Müller, and S. Speidel, "Physics-based shape matching for intraoperative image guidance," *Medical Physics*, vol. 41, pp. 1–12, 2014.

[2] D. C. Rucker, Y. Wu, L. Clements, J. Ondrake, T. Pheiffer, A. Simpson, W. Jarnagin, and M. Miga, "A Mechanics-Based Nonrigid Registration Method for Liver Surgery using Sparse Intraoperative Data." *IEEE Transactions on Medical Imaging*, vol. 33, no. 1, pp. 147–158, 2014.

[3] M. Allan, A. Kapoor, P. Mewes, and P. Mountney, "Non Rigid Registration of 3D Images to Laparoscopic Video for Image Guided Surgery," *Computer-Assisted and Robotic Endoscopy*, vol. 9515, pp. 109–116, 2015.

[4] R. Plantefève, I. Peterlik, N. Haouchine, and S. Cotin, "Patient-Specific Biomechanical Modeling for Guidance During Minimally-Invasive Hepatic Surgery," *Annals of Biomedical Engineering*, vol. 44, no. 1, pp. 139–153, 2016.

[5] L. W. Clements, J. A. Collins, A. L. Simpson, L. B. Adams, W. R. Jarnagin, and M. I. Miga, "Evaluation of model-based deformation correction in image-guided liver surgery via tracked intraoperative ultrasound," *Journal of Medical Imaging*, vol. 3, no. 1, pp. 1–10, 2016.

[6] D. Reichard, D. Häntsch, S. Bodenstedt, S. Suwelack, M. Wagner, H. Kenngott, B. Müller-Stich, L. Maier-Hein, R. Dillmann, and S. Spiedel, "Projective biomechanical depth matching for soft tissue registration in laparoscopic surgery," *International Journal of Computer Assisted Radiology and Surgery*, vol. 12, no. 7, pp. 1101–1110, 2017.

[7] E. Özgür, B. Koo, B. Le Roy, E. Buc, and A. Bartoli, "Preoperative liver registration for augmented monocular laparoscopy using backward–forward biomechanical simulation," *International Journal of Computer Assisted Radiology and Surgery*, vol. 13, no. 10, pp. 1629–1640, 2018.

[8] I. Peterlík, H. Courtecuisse, R. Rohling, P. Abolmaesumi, C. Nguan, S. Cotin, and S. Salcudean, "Fast elastic registration of soft tissues under large deformations," *Medical Image Analysis*, vol. 45, pp. 24–40, 2018.

[9] J. S. Heiselman, L. W. Clements, J. A. Collins, J. A. Weis, A. L. Simpson, S. K. Geevarghese, T. P. Kingham, W. R. Jarnagin, and M. I. Miga, "Characterization and correction of soft tissue deformation in laparoscopic image-guided liver surgery," *Journal of Medical Imaging*, vol. 5, no. 2, p. 021203, 2018.

[10] R. Modrzejewski, T. Collins, B. Seeliger, A. Bartoli, A. Hostettler, and J. Marescaux, "An in vivo porcine dataset and evaluation methodology to measure soft-body laparoscopic liver registration accuracy with an extended algorithm that handles collisions," *International Journal of Computer Assisted Radiology and Surgery*, vol. 14, no. 7, pp. 1237–1245, 2019.

[11] J. M. Blackall, G. P. Penney, A. P. King, A. N. Adam, and D. J. Hawkes, "Tracking alignment of sparse ultrasound with preoperative images of the liver and an interventional plan using models of respiratory motion and deformation," *IEEE Transactions on Medical Imaging*, vol. 24, no. 11, pp. 1405–1416, 2005.

[12] M. Nakamoto, H. Hirayama, Y. Sato, K. Konishi, Y. Kakeji, M. Hashizume, and S. Tamura, "Recovery of respiratory motion and deformation of the liver using laparoscopic freehand 3D ultrasound system," *Medical Image Analysis*, vol. 11, no. 5, pp. 429–442, 2007.

[13] W. Wein, S. Brunke, A. Khamene, M. R. Callstrom, and N. Navab, "Automatic CT-ultrasound registration for diagnostic imaging and image-guided intervention," *Medical Image Analysis*, vol. 12, no. 5, pp. 577–585, 2008.

[14] T. Lange, N. Papenberg, S. Heldmann, J. Modersitzki, B. Fischer, H. Lamecker, and P. M. Schlag, "3D ultrasound-CT registration of the liver using combined landmark-intensity information," *International Journal of Computer Assisted Radiology and Surgery*, vol. 4, no. 1, pp. 79–88, 2009.

[15] D. Lee, W. H. Nam, J. Y. Lee, and J. B. Ra, "Non-rigid registration between 3D ultrasound and CT images of the liver based on intensity and gradient information," *Physics in Medicine and Biology*, vol. 56, no. 1, pp. 117–137, 2011.

[16] F. Nazem, A. Ahmadian, N. D. Seraj, and M. Giti, "Two-stage point-based registration method between ultrasound and CT imaging of the liver based on ICP and unscented Kalman filter: A phantom study," *International Journal of Computer Assisted Radiology and Surgery*, vol. 9, no. 1, pp. 39–48, 2014.

[17] Y. Song, J. Totz, S. Thompson, S. Johnsen, D. Barratt, C. Schneider, K. Gurusamy, B. Davidson, S. Ourselin, D. Hawkes, and M. J. Clarkson, "Locally rigid, vessel-based registration for laparoscopic liver surgery," *International Journal of Computer Assisted Radiology and Surgery*, vol. 10, no. 12, pp. 1951–1961, 2015.

[18] M. Yang, H. Ding, J. Kang, L. Cong, L. Zhu, and G. Wang, "Local structure orientation descriptor based on intra-image similarity for multimodal registration of liver ultrasound and MR images," *Computers in Biology and Medicine*, vol. 76, pp. 69–79, 2016.

[19] J. Ramalhinho, M. Robu, S. Thompson, P. Edwards, C. Schneider, K. Gurusamy, D. Hawkes, B. Davidson, D. Barratt, and M. J. Clarkson, "Breathing motion compensated registration of laparoscopic liver ultrasound to CT," *Proc. SPIE Medical Imaging*, vol. 101352V, pp. 1–9, 2017.

[20] J. S. Heiselman, W. R. Jarnagin, and M. I. Miga, "Intraoperative Correction of Liver Deformation Using Sparse Surface and Vascular Features via Linearized Iterative Boundary Reconstruction," *IEEE Transactions on Medical Imaging*, vol. 39, no. 6, pp. 2223–2234, 2020.

[21] A. L. Simpson, D. A. Geller, A. W. Hemming, W. R. Jarnagin, L. W. Clements, M. I. D'Angelica, P. Dumpuri, M. Gönen, I. Zendejas, M. I. Miga, and J. D. Stefansic, "Liver planning software accurately predicts postoperative liver volume and measures early regeneration," *Journal of the American College of Surgeons*, vol. 219, no. 2, pp. 199–207, 2014.

[22] L. W. Clements, J. A. Collins, J. A. Weis, and A. L. Simpson, "Deformation correction for image guided liver surgery: An intraoperative fidelity assessment," *Surgery*, vol. 162, no. 3, pp. 537–547, 2017.

[23] T. P. Kingham, S. Jayaraman, L. W. Clements, M. A. Scherer, J. D. Stefansic, and W. R. Jarnagin, "Evolution of Image-Guided Liver Surgery: Transition from Open to Laparoscopic Procedures," *J Gastrointest Surg*, vol. 17, pp. 1274–1282, 2013.

[24] T. P. Kingham, M. A. Scherer, B. W. Neese, L. W. Clements, J. D. Stefansic, and W. R. Jarnagin, "Image-guided liver surgery: Intraoperative projection of computed tomography images utilizing tracked ultrasound," *HPB*, vol. 14, no. 9, pp. 594–603, 2012.

[25] X. Liu, S. Kang, W. Plishker, G. Zaki, T. D. Kane, and R. Shekhar, "Laparoscopic stereoscopic augmented reality: toward a clinically viable electromagnetic tracking solution," *Journal of Medical Imaging*, vol. 3, no. 4, p. 045001, 2016.

[26] B. Menahem, J. Lubrano, C. Duvoux, A. Mulliri, A. Alves, C. Costentin, A. Mallat, G. Launoy, and A. Laurent, "Liver transplantation versus liver resection for hepatocellular carcinoma in intention to treat: An attempt to perform an ideal meta-analysis," *Liver Transplantation*, vol. 23, no. 6, pp. 836–844, 2017.

[27] L. R. Zarour, S. Anand, K. G. Billingsley, W. H. Bisson, A. Cercek, M. F. Clarke, L. M. Coussens, C. E. Gast, C. B. Geltzeiler, L. Hansen, K. A. Kelley, C. D. Lopez, S. R. Rana, R. Ruhl, V. L. Tsikitis, G. M. Vaccaro, M. H. Wong, and S. C. Mayo, "Colorectal Cancer Liver Metastasis: Evolving Paradigms and Future Directions," *Cellular and Molecular Gastroenterology and Hepatology*, vol. 3, no. 2, pp. 163–173, 2017.

[28] A. Dupré, R. P. Jones, R. Diaz-Nieto, S. W. Fenwick, G. J. Poston, and H. Z. Malik, "Curative-intent treatment of recurrent colorectal liver metastases: A comparison between ablation and resection," *European Journal of Surgical Oncology*, vol. 43, no. 10, pp. 1901–1907, 2017.

[29] R. Ciria, D. Cherqui, D. A. Geller, J. Briceno, and G. Wakabayashi, "Comparative Short-term Benefits of Laparoscopic Liver Resection: 9000 Cases and Climbing," *Annals of Surgery*, vol. 263, no. 4, pp. 761–777, 2016.

[30] A. A. Fretland, V. J. Dagenborg, G. M. Bjørnelv, A. M. Kazaryan, R. Kristiansen, M. W. Fagerland, J. Hausken, T. I. Tønnessen, A. Abildgaard, L. Barkhatov, S. Yaqub, B. I. Røsok, B. A. Bjørnbeth, M. H. Andersen, K. Flatmark, E. Aas, and B. Edwin, "Laparoscopic Versus Open Resection for Colorectal Liver Metastases: The OSLO-COMET Randomized Controlled Trial," *Annals of Surgery*, vol. 267, no. 2, pp. 199–207, 2018.

[31] L. Vigano, A. Laurent, C. Tayar, M. Tomatis, A. Ponti, and D. Cherqui, "The Learning Curve in Laparoscopic Liver Resection: Improved Feasibility and Reproducability," *Ann Surg*, vol. 250, no. 5, pp. 772–782, 2009.

[32] X. Cai, Z. Li, Y. Zhang, H. Yu, X. Liang, R. Jin, and F. Luo, "Laparoscopic liver resection and the learning curve: a 14-year, single-center experience," *Surg Endosc*, vol. 28, pp. 1334–1341, 2014.

[33] K. M. Brown and D. A. Geller, "What is the Learning Curve for Laparoscopic Major Hepatectomy?" *Journal of Gastrointestinal Surgery*, vol. 20, pp. 1065–1071, 2016.

[34] L. Viganò, A. Ferrero, M. Amisano, N. Russolillo, and L. Capussotti, "Comparison of laparoscopic and open intraoperative ultrasonography for staging liver tumours," *British Journal of Surgery*, vol. 100, no. 4, pp. 535–542, 2013.

[35] A. Ferrero, R. Lo Tesoriere, N. Russolillo, L. Vigano, F. Forchino, and L. Capussotti, "Ultrasound-guided laparoscopic liver resections," *Surg Endosc*, vol. 29, pp. 1002–1005, 2015.

[36] M. G. Van Vledder, T. M. Pawlik, S. Munireddy, U. Hamper, M. C. De Jong, and M. A. Choti, "Factors Determining the Sensitivity of Intraoperative Ultrasonography in Detecting Colorectal Liver Metastases in the Modern Era," *Annals of Surgical Oncology*, vol. 17, pp. 2756–2763, 2010.

[37] S. Benoist, A. Brouquet, C. Penna, C. Julie, M. E. Hajjam, S. Chagnon, E. Mitry, P. Rougier, and B. Nordlinger, "Complete Response of Colorectal Liver Metastases After Chemotherapy: Does It Mean Cure?" *Journal of Clinical Oncology*, vol. 24, no. 24, pp. 3939–3945, 2006.

[38] R. L. Siegel and K. D. Miller, "Cancer Statistics, 2020," *CA Cancer Journal for Clinicians*, vol. 70, no. 1, pp. 7–30, 2020.

[39] M. C. S. Wong, J. Y. Jiang, W. B. Goggins, M. Liang, Y. Fang, F. D. H. Fung, C. Leung, H. H. X. Wang, G. L. H. Wong, V. W. Wong, and H. L. Y. Chan, "International incidence and mortality trends of liver cancer: a global profile," *Nature Scientific Reports*, vol. 7, no. 45846, pp. 1–9, 2017.

[40] T. S. Helling and M. Martin, "Cause of Death from Liver Metastases in Colorectal Cancer," *Annals of Surgical Oncology*, vol. 21, no. 2, pp. 501–506, 2014.

[41] S. Tabaries and P. M. Siegel, "Liver Metastasis: Biology and Clinical Management," in *Cancer Metastasis - Biology and Treatment*, 1st ed., P. Brodt, Ed. New York: Springer Science and Business Media, Inc., 2011, vol. 16, ch. 10, p. 280.

[42] K. R. Hess, G. R. Varadhachary, S. H. Taylor, W. Wei, M. N. Raber, R. Lenzi, and J. L. Abbruzzese, "Metastatic Patterns in Adenocarcinoma," *Cancer*, vol. 106, no. 7, pp. 1624–1633, 2006.

[43] S. Lin, K. Hoffmann, and P. Schemmer, "Treatment of Hepatocellular Carcinoma: A Systematic Review," *Liver Cancer*, vol. 1, pp. 144–158, 2012.

[44] G. K. Glantzounis, A. Paliouras, M. Stylianidi, H. Milionis, P. Tzimas, D. Roukos, G. Pentheroudakis, and E. Felekouras, "The role of liver resection in the management of intermediate and advanced stage hepatocellular carcinoma: A systematic review," *European Journal of Surgical Oncology*, vol. 44, no. 2, pp. 195–208, 2018.

[45] G. P. Kanas, A. Taylor, J. N. Primrise, W. J. Langeberg, M. A. Kelsh, F. S. Mowat, D. D. Alexander, M. A. Choti, and G. Poston, "Survival after liver resection in metastatic colorectal cancer: review and meta-analysis of prognostic factors," *Clinical Epidemiology*, vol. 4, pp. 283–301, 2012.

[46] S. Kopetz, G. J. Chang, M. J. Overman, C. Eng, D. J. Sargent, D. W. Larson, A. Grothey, J. N. Vauthey, D. M. Nagorney, and R. R. McWilliams, "Improved survival in metastatic colorectal cancer is associated with adoption of hepatic resection and improved chemotherapy," *Journal of Clinical Oncology*, vol. 27, no. 22, pp. 3677–3683, 2009.

[47] S. G. Delis and C. Dervenis, "Selection criteria for liver resection in patients with hepatocellular carcinoma and chronic liver disease," *World Journal of Gastroenterology*, vol. 14, no. 22, pp. 3452–3460, 2008.

[48] D. Li, J. Kang, B. J. Golas, V. W. Yeung, and D. C. Madoff, "Minimally invasive local therapies for liver cancer," *Cancer Biology & Medicine*, vol. 11, no. 4, pp. 217–36, 2014.

[49] C. P. Raut, F. Izzo, P. Marra, L. M. Ellis, J.-N. Vauthey, F. Cremona, P. Vallone, A. Mastro, B. D. Fornage, and S. A. Curley, "Significant Long-Term Survival After Radiofrequency Ablation of Unresectable Hepatocellular Carcinoma in Patients with Cirrhosis," *Annals of Surgical Oncology*, vol. 12, no. 8, pp. 616–628, 2005.

[50] I. R. Andersen, F. V. Mortensen, J. Kirkegaard, F. Rasmussen, D. T. Nielsen, and D. W. Kjaer, "Long-Term Survival Following Ablation of Colorectal Liver Metastases," *Journal of Surgery*, vol. 6, no. 1, pp. 13–18, 2018.

[51] R. M. Eisele, U. Neumann, P. Neuhaus, and G. Schumacher, "Open Surgical is Superior to Percutaneous Access for Radiofrequency Ablation of Hepatic Metastases," *World Journal of Surgery*, vol. 33, pp. 804–811, 2009.

[52] T. Masuda, G. A. Margonis, N. Andreatos, J. Wang, S. Warner, M. B. Mirza, A. Angelou, C. Damaskos, N. Garmpis, K. Sasaki, J. He, K. Imai, Y.-i. Yamashita, C. L. Wolfgang, H. Baba, and M. J. Weiss, "Combined Hepatic Resection and Radiofrequency Ablation for Patients with Colorectal Cancer Liver Metastasis : A Viable Option for Patients with a Large Number of Tumors," *Anticancer Research*, vol. 38, no. 11, pp. 6353–6360, 2018.

[53] K. Tanaka, H. Shimada, Y. Nagano, and I. Endo, "Outcome after hepatic resection versus combined resection and microwave ablation for multiple bilobar colorectal metastases to the liver," *Surgery*, vol. 139, no. 2, pp. 263–273, 2005.

[54] E. K. Abdalla, J. N. Vauthey, L. M. Ellis, V. Ellis, R. Pollock, K. R. Broglio, K. Hess, and S. A. Curley, "Recurrence and Outcomes Following Hepatic Resection, Radiofrequency Ablation, and Combined Resection/Ablation for Colorectal Liver Metastases," *Annals of Surgery*, vol. 239, no. 6, pp. 818–827, 2004.

[55] A. Ferrero, L. Vigano, R. Polastri, A. Muratore, H. Eminefendic, D. Regge, and L. Capusotti, "Postoperative Liver Dysfunction and Future Remnant Liver: Where Is the Limit? Results of a Prospective Study," *World Journal of Surgery*, vol. 31, no. 8, pp. 1643–1651, 2007.

[56] T. M. Pawlik, R. D. Schulick, and M. A. Choti, "Expanding Criteria for Resectability of Colorectal Liver Metastases," *The Oncologist*, vol. 13, no. 1, pp. 51–64, 2008.

[57] Y. Wang, Y. Zhang, H. O. Peitgen, A. Schenk, L. Yuan, G. Wei, and Y. Sun, "Precise local resection for hepatocellular carcinoma based on tumor-surrounding vascular anatomy revealed by 3D analysis," *Digestive Surgery*, vol. 29, no. 2, pp. 99–106, 2012.

[58] A. Zendel, E. Lahat, Y. Dreznik, B. B. Zakai, R. Eshkenazy, and A. Ariche, ""Vanishing liver metastases"— A real challenge for liver surgeons," *Hepatobiliary Surgery and Nutrition*, vol. 3, no. 5, pp. 295–302, 2014.

[59] D. A. Bischof, B. M. Clary, S. K. Maithel, and T. M. Pawlik, "Surgical management of disappearing colorectal liver metastases," *British Journal of Surgery*, vol. 100, no. 11, pp. 1414–1420, 2013.

[60] D. I. Tsilimigras, I. Ntanasis-Stathopoulos, A. Z. Paredes, D. Moris, M. Gavriatopoulou, J. M. Cloyd, and T. M. Pawlik, "Disappearing liver metastases: A systematic review of the current evidence," *Surgical Oncology*, vol. 29, pp. 7–13, 2019.

[61] K. Kuhlmann, J. van Hilst, S. Fisher, and G. Poston, "Management of disappearing colorectal liver metastases," *European Journal of Surgical Oncology*, vol. 42, no. 12, pp. 1798–1805, 2016.

[62] K. T. Nguyen, T. C. Gamblin, and D. A. Geller, "World Review of Laparoscopic Liver Resection—2,804 Patients," *Ann Surg*, vol. 250, no. 5, pp. 831–841, 2009.

[63] S. M. Xie, J. J. Xiong, X. T. Liu, H. Y. Chen, D. Iglesia-García, K. Altaf, S. Bharucha, W. Huang, Q. M. Nunes, P. Szatmary, and X. B. Liu, "Laparoscopic Versus Open Liver Resection for Colorectal Liver Metastases : A Comprehensive Systematic Review and Meta-analysis," *Nature Scientific Reports*, vol. 7, p. 1012, 2017.

[64] G. A. Vilos, A. Ternamian, J. Dempster, and P. Y. Laberge, "Laparoscopic Entry: A Review of Techniques, Technologies, and Complications," *SOGC Clinical Practice Guideline*, no. 193, pp. 433–447, 2007.

[65] G. Wakabayashi, D. Cherqui, D. Geller, J. Buell, H. Kaneko, H. S. Han, H. Asbun, N. O'Rourke, M. Tanabe, A. J. Koffron, A. Tsung, and O. Soubrane, "Recommendations for Laparoscopic Liver Resection," *Ann Surg*, vol. 261, no. 4, pp. 619–629, 2015.

[66] I. Dagher, B. Gayet, D. Tzanis, H. Tranchart, D. Fuks, O. Soubrane, H.-s. H. K.-h. Kim, D. Cherqui, N. O. Rourke, R. I. Troisi, L. Aldrighetti, E. Bjorn, M. Abu, H. Giulio, B. Hironori, W. R. Jarnagin, C. Lin, J. Pekolj, J. F. Buell, and G. Wakabayashi, "International experience for laparoscopic major liver resection," *J Hepatobiliary Pancreat Sci*, vol. 21, pp. 732–736, 2014.

[67] J. S. Cardinal, S. K. Reddy, A. Tsung, J. W. Marsh, and D. A. Geller, "Laparoscopic major hepatectomy: pure laparoscopic approach versus hand-assisted technique," *Journal of Hepatobiliary and Pancreatic Sciences*, vol. 20, no. 2, pp. 114–119, 2013.

[68] B. Tamadazte, A. Agustinos, P. Cinquin, G. Fiard, and S. Voros, "Multi-view vision system for laparoscopy surgery," *International Journal of Computer Assisted Radiology and Surgery*, vol. 10, no. 2, pp. 195–203, 2015.

[69] R. I. Troisi, R. Montalti, J. G. M. Van Limmen, D. Cavaniglia, K. Reyntjens, X. Rogiers, and B. De Hemptinne, "Risk factors and management of conversions to an open approach in laparoscopic liver resection: analysis of 265 consecutive cases," *HPB*, vol. 16, no. 1, pp. 75–82, 2014.

[70] M. C. Halls, F. Cipriani, G. Berardi, L. Barkhatov, P. Lainas, M. Alzoubi, M. D'Hondt, F. Rotellar, I. Dagher, L. Aldrighetti, R. I. Troisi, B. Edwin, and M. A. Hilal, "Conversion for Unfavorable Intraoperative Events Results in Significantly Worse Outcomes During Laparoscopic Liver Resection: Lessons Learned From a Multicenter Review of 2861 Cases," *Annals of Surgery*, vol. 268, no. 6, pp. 1051–1057, 2018.

[71] R. Santambrogio, P. Bianchi, A. Pasta, A. Palmisano, and M. Montorsi, "Ultrasound-guided interventional procedures of the liver during laparoscopy: Technical considerations," *Surgical Endoscopy and Other Interventional Techniques*, vol. 16, no. 2, pp. 349–354, 2002.

[72] S. B. Ellebaek, C. W. Fristrup, and M. B. Mortensen, "Intraoperative ultrasound as a screening modality for the detection of liver metastases during resection of primary

colorectal cancer - A systematic review." *Ultrasound International Open*, vol. 3, no. 2, pp. 60–68, 2017.

[73] C. Vapenstad, A. Rethy, T. Lango, T. Selbekk, B. Ystgaard, T. Nagelhus Hernes, and R. Marvik, "Laparoscopic ultrasound: a survey of its current and future use, requirements, and integration with navigation technology," *Surg Endosc*, vol. 24, pp. 2944–2953, 2010.

[74] T. Langø, G. A. Tangen, R. Mårvik, B. Ystgaard, Y. Yavuz, J. H. Kaspersen, O. V. Solberg, and T. A. N. Hernes, "Navigation in laparoscopy – prototype research platform for improved image-guided surgery," *Minimally Invasive Therapy*, vol. 17, no. 1, pp. 17–33, 2008.

[75] U. Boggi, F. Caniglia, and G. Amorese, "Laparoscopic robot-assisted major hepatectomy," *J Hepatobiliary Pancreat Sci*, vol. 21, pp. 3–10, 2014.

[76] D. Daskalaki, R. Gonzalez-Heredia, M. Brown, F. M. Bianco, I. Tzvetanov, M. Davis, J. Kim, E. Benedetti, and P. C. Giulianotti, "Financial Impact of the Robotic Approach in Liver Surgery: A Comparative Study of Clinical Outcomes and Costs Between the Robotic anad Open Technique in a Single Institution," *Journal of Laparoendoscopic & Advanced Surgical Techniques*, vol. 27, no. 4, pp. 375–382, 2017.

[77] A. Tannapfel, H.-p. Dienes, and A. W. Lohse, "The Indications for Liver Biopsy," *Deutches Arzteblatt International*, vol. 109, no. 27-28, pp. 477–484, 2012.

[78] E. S. Bialecki, A. M. Ezenekwe, E. M. Brunt, B. T. Collins, T. B. Ponder, B. K. Bieneman, and A. M. Di Bisceglie, "Comparison of Liver Biopsy and Noninvasive Methods for," *Clinical Gastroenterology and Hepatology*, vol. 4, no. 3, pp. 361–368, 2006.

[79] S. K. Venkatesh, V. Chandan, and L. R. Roberts, "Liver Masses: A Clinical, Radiological and Pathological Perspective For: Perspectives in Clinical Gastroenterology and Hepatology," *Clinical Gastroenterology and Hepatology*, vol. 12, no. 9, pp. 1414–1429, 2015.

[80] A. M. Lucchese, A. N. Kalil, A. Schwengber, E. Suwa, and G. G. Rolim de Moura, "Usefulness of intraoperative ultrasonography in liver resections due to colon cancer metastasis," *International Journal of Surgery*, vol. 20, pp. 140–144, 2015.

[81] P. T. Pepple and D. A. Gerber, "Laparoscopic-assisted ablation of hepatic tumors: A review," *Seminars in Interventional Radiology*, vol. 31, no. 2, pp. 125–128, 2014.

[82] R. C. Martin, P. Philips, S. Ellis, D. Hayes, and S. Bagla, "Irreversible electroporation of unresectable soft tissue tumors with vascular invasion: effective palliation," *BMC Cancer*, vol. 14, no. 1, p. 540, 2014.

[83] D. J. Kilburn, A. K. H. Chiow, J. Lewin, N. Kienzle, D. J. Cavallucci, R. Bryant, and N. O'Rourke, "Laparoscopic approach to a planned two-stage hepatectomy for bilobar colorectal liver metastases," *ANZ Journal of Surgery*, vol. 86, no. 10, pp. 811–815, 2016.

[84] L. R. Jiao, D. N. Hakim, T. M. H. Gall, A. Fajardo, T. D. Pencavel, R. Fan, and M. H. Sodergren, "A totally laparoscopic associating liver partition and portal vein ligation for staged hepatectomy assisted with radiofrequency (radiofrequency assisted liver partition with portal vein ligation) for staged liver resection," *Hepatobiliary Surgery and Nutrition*, vol. 5, no. 4, pp. 382–387, 2016.

[85] M. Patricia, S. Boeti, R. Grigorie, and I. Popescu, "Laparoscopic Radiofrequency Ablation of Liver Tumors," in *Hepatic Surgery*, H. Abdeldayem, Ed. InTech, 2013, ch. 20, pp. 489–516.

[86] O. Birsen, S. Aliyev, E. Aksoy, H. E. Taskin, M. Akyuz, K. Karabulut, A. Siperstein, and E. Berber, "A critical analysis of postoperative morbidity and mortality after laparoscopic radiofrequency ablation of liver tumors," *Annals of Surgical Oncology*, vol. 21, no. 6, pp. 1834–1840, 2014.

[87] M. C. Giglio, B. Logghe, E. Garofalo, F. Tomassini, A. Vanlander, G. Berardi, R. Montalti, and R. I. Troisi, "Laparoscopic Versus Open Thermal Ablation of Colorectal Liver Metastases : A Propensity Score-Based Analysis of Local Control of the Ablated Tumors," *Annals of Surgical Oncology*, vol. 27, no. 7, pp. 2370–2380, 2020.

[88] R. Santambrogio, E. Opocher, M. Costa, A. Cappellani, and M. Montorsi, "Survival and intra-hepatic recurrences after laparoscopic radiofrequency of hepatocellular carcinoma in patients with liver cirrhosis," *Journal of Surgical Oncology*, vol. 89, no. 4, pp. 218–225, 2005.

[89] R. Z. Swan, D. Sindram, J. B. Martinie, and D. A. Iannitti, "Operative Microwave Ablation for Hepatocellular Carcinoma: Complications, Recurrence, and Long-Term Outcomes," *Journal of Gastrointestinal Surgery*, vol. 17, no. 4, pp. 719–729, 2013.

[90] P. Tinguely, M. Fusaglia, J. Freedman, V. Banz, S. Weber, D. Candinas, and H. Nilsson, "Laparoscopic image-based navigation for microwave ablation of liver tumors—A multi-center study," *Surgical Endoscopy and Other Interventional Techniques*, vol. 31, no. 10, pp. 4315–4324, 2017.

[91] T. Lange, M. Hünerbein, S. Eulenstein, S. Beller, and P. M. Schlag, "Development of Navigation Systems for Image-Guided Laparoscopic Tumor Resections in Liver Surgery," *Recent Results in Cancer Research*, vol. 167, pp. 13–36, 2006.

[92] T. P. Kingham, L. M. Pak, A. L. Simpson, U. Leung, A. Doussot, M. I. D'Angelica, R. P. DeMatteo, P. J. Allen, and W. R. Jarnagin, "3D image guidance assisted identification of colorectal cancer liver metastases not seen on intraoperative ultrasound: results from a prospective trial," *HPB*, vol. 20, no. 3, pp. 260–267, 2018.

[93] L. M. Pak, J. Gagnière, P. J. Allen, V. P. Balachandran, M. I. D'Angelica, R. P. DeMatteo, W. R. Jarnagin, M. I. Miga, A. L. Simpson, and T. P. Kingham, "Utility of Image Guidance in the Localization of Disappearing Colorectal Liver Metastases," *Journal of Gastrointestinal Surgery*, vol. 23, no. 4, pp. 760–767, 2019.

[94] A. L. Simpson and T. P. Kingham, "Current Evidence in Image-Guided Liver Surgery," *Journal of Gastrointestinal Surgery*, pp. 1265–1269, 2016.

[95] C. Fang, J. An, A. Bruno, X. Cai, J. Fan, J. Fujimoto, R. Golfieri, X. Hao, H. Jiang, L. R. Jiao, A. V. Kulkarni, H. Lang, C. R. A. Lesmana, Q. Li, L. Liu, Y. Liu, W. Lau, Q. Lu, H. Maruyama, C. Mosconi, N. Örmeci, M. Pavlides, G. Rezende, J. H. Sohn, S. Treeprasertsuk, V. Vilgrain, H. Wen, S. Wen, X. Quan, R. Ximenes, Y. Yang, B. Zhang, W. Zhang, P. Zhang, S. Zhang, and X. Qi, "Consensus recommendations of three - dimensional visualization for diagnosis and management of liver diseases," *Hepatology International*, 2020.

[96] M. Peterhans, A. vom Berg, B. Dagon, D. Inderbitzin, C. Baur, D. Candinas, and S. Weber, "A navigation system for open liver surgery: design, workflow and first clinical applications," *The International Journal of Medical Robotics and Computer Assisted Surgery*, vol. 7, no. 1, pp. 7–16, 2011.

[97] R. Elfring, M. de la Fuente, and K. Radermacher, "Assessment of optical localizer accuracy for computer aided surgery systems," *Computer Aided Surgery*, vol. 15, no. 1-3, pp. 1–12, 2010.

[98] H. Zhang, F. Banovac, R. Lin, N. Glossop, B. J. Wood, D. Lindisch, E. Levy, and K. Cleary, "Electromagnetic tracking for abdominal interventions in computer aided surgery aided surgery," *Computer Aided Surgery*, vol. 11, no. 3, pp. 127–136, 2010.

[99] D. Bouget, M. Allan, D. Stoyanov, and P. Jannin, "Vision-based and marker-less surgical tool detection and tracking: a review of the literature," *Medical Image Analysis*, vol. 35, pp. 633–654, 2017.

[100] D. M. Cash, M. I. Miga, S. C. Glasgow, B. M. Dawant, L. W. Clements, Z. Cao, R. L. Galloway, and W. C. Chapman, "Concepts and preliminary data toward the realization of image-guided liver surgery," *Journal of Gastrointestinal Surgery*, vol. 11, no. 7, pp. 844–859, 2007.

[101] C. W. Hammill, L. W. Clements, J. D. Stafansic, R. F. Wolf, P. D. Hansen, and D. A. Gerber, "Evaluation of a Minimally Invasive Image-Guided Surgery System for Hepatic Ablation Procedures," *Surg Innov*, vol. 21, no. 4, pp. 419–426, 2015.

[102] J. Burgner, A. L. Simpson, J. M. Fitzpatrick, R. A. Lathrop, S. D. Herrell, M. I. Miga, and R. J. Webster, "A study on the theoretical and practical accuracy of conoscopic holography-based surface measurements: Toward image registration in minimally invasive surgery," *International Journal of Medical Robotics and Computer Assisted Surgery*, vol. 9, no. 2, pp. 190–203, 2013.

[103] R. A. Lathrop, D. M. Hackworth, and R. J. Webster, "Minimally Invasive Holographic Surface Scanning for Soft-Tissue Image Registration," *IEEE Transactions on Biomedical Engineering*, vol. 57, no. 6, pp. 1497–1506, 2010.

[104] D. M. Cash, T. K. Sinha, W. C. Chapman, H. Terawaki, B. M. Dawant, R. L. Galloway, and M. I. Miga, "Incorporation of a laser range scanner into image-guided liver surgery: surface acquisition, registration, and tracking." *Medical physics*, vol. 30, no. 7, pp. 1671–1682, 2003.

[105] M. Fusaglia, H. Hess, M. Schwalbe, M. Peterhans, P. Tinguely, S. Weber, and H. Lu, "A clinically applicable laser-based image-guided system for laparoscopic liver procedures," *Int J CARS*, vol. 11, pp. 1499–1513, 2016.

[106] A. L. Simpson, J. Burgner, C. L. Glisson, S. D. Herrell, B. Ma, T. S. Pheiffer, R. J. Webster, and M. I. Miga, "Comparison study of intraoperative surface acquisition methods for surgical navigation," *IEEE Transactions on Biomedical Engineering*, vol. 60, no. 4, pp. 1090–1099, 2013.

[107] D. Stoyanov, M. V. Scarzanella, P. Pratt, and G.-Z. Yang, "Real-Time Stereo Reconstruction in Robotically Assisted Minimally Invasive Surgery," *Medical Image Computing and Computer-Assisted Intervention 2010*, vol. 6131, pp. 275–282, 2010.

[108] D. Reichard, S. Bodenstedt, S. Suwelack, B. Mayer, A. Preukschas, M. Wagner, H. Kenngott, B. Müller-Stich, R. Dillmann, and S. Speidel, "Intraoperative on-the-fly organ-mosaicking for laparoscopic surgery," *Journal of Medical Imaging*, vol. 2, no. 4, p. 045001, 2015.

[109] L. Maier-Hein, A. Groch, A. Bartoli, S. Bodenstedt, G. Boissonnat, P. L. Chang, N. T. Clancy, D. S. Elson, S. Haase, E. Heim, J. Hornegger, P. Jannin, H. Kenngott, T. Kilgus, B. Muller-Stich, D. Oladokun, S. Röhl, T. R. Dos Santos, H. P. Schlemmer, A. Seitel, S. Speidel, M. Wagner, and D. Stoyanov, "Comparative Validation of Single-Shot Optical Techniques for Laparoscopic 3-D Surface Reconstruction," *IEEE Transactions on Medical Imaging*, vol. 33, no. 10, pp. 1913–1930, 2014.

[110] S. Thompson, J. Totz, Y. Song, S. Johnsen, D. Stoyanov, K. Gurusamy, C. Schneider, B. Davidson, D. Hawkes, and M. J. Clarkson, "Accuracy Validation of an Image Guided Laparoscopy System for Liver Resection," in *Proc. of SPIE*, vol. 9415, no. 941509, 2015, pp. 1–12.

[111] J. A. Collins, J. A. Weis, J. S. Heiselman, L. W. Clements, A. L. Simpson, W. R. Jarnagin, and M. I. Miga, "Improving Registration Robustness for Image-Guided Liver Surgery in a Novel Human-to-Phantom Data Framework," *IEEE Transactions on Medical Imaging*, vol. 36, no. 7, pp. 1502–1510, 2017.

[112] G. Xiao, E. Bonmati, S. Thompson, J. Evans, J. Hipwell, D. Nikitichev, K. Gurusamy, S. Ourselin, D. J. Hawkes, B. Davidson, and M. J. Clarkson, "Electromagnetic tracking in image-guided laparoscopic surgery: Comparison with optical tracking and feasibility study of a combined laparoscope and laparoscopic ultrasound system," *Medical Physics*, vol. 45, no. 11, pp. 5094–5104, 2018.

[113] C. Ewertsen, A. Saftious, L. G. Gruionu, S. Karstrup, and M. B. Nielsen, "Real-Time Image Fusion Involving Diagnostic Ultrasound," *AJR Am J Roentgenol.*, vol. 200, pp. 249–255, 2013.

[114] G. Mauri, L. Cova, S. De Beni, T. Ierace, T. Tondolo, A. Cerri, S. N. Goldberg, and L. Solbiati, "Real-Time US-CT/MRI Image Fusion for Guidance of Thermal Ablation of Liver Tumors Undetectable with US: Results in 295 Cases," *Cardiovascular and Interventional Radiology*, vol. 38, no. 1, pp. 143–151, 2014.

[115] O. V. Solberg, T. Langø, G. A. Tangen, R. Mårvik, B. Ystgaard, A. Rethy, and T. A. Hernes, "Navigated ultrasound in laparoscopic surgery," *Minimally Invasive Therapy and Allied Technologies*, vol. 18, no. 1, pp. 36–53, 2009.

[116] H. G. Kenngott, M. Wagner, M. Gondan, and F. Nickel, "Real-time image guidance in laparoscopic liver surgery: first clinical experience with a guidance system based on intraoperative CT imaging," *Surg Endosc*, vol. 28, pp. 933–940, 2013.

[117] T. S. Pheiffer, R. C. Thompson, D. C. Rucker, A. L. Simpson, and M. I. Miga, "Model-based correction of tissue compression for tracked ultrasound in soft tissue image-guided surgery," *Ultrasound in Medicine and Biology*, vol. 40, no. 4, pp. 788–803, 2014.

[118] T. S. Pheiffer and M. I. Miga, "Toward a generic real-time compression correction framework for tracked ultrasound," *International Journal of Computer Assisted Radiology and Surgery*, vol. 10, no. 11, pp. 1777–1792, 2015.

[119] J. M. Fitzpatrick, D. L. G. Hill, and C. R. Maurer, "Image Registration," in *Handbook of Medical Imaging Volume 2: Medical Image Processing and Analysis*, 1st ed., J. M. Fitzpatrick and M. Sonka, Eds. SPIE Publications, 2000, ch. 8, pp. 447–514.

[120] P. J. Besl and N. D. McKay, "A Method for Registration of 3-D Shapes," *IEEE Transactions on Pattern Analysis and Machine Intelligence*, vol. 14, no. 2, pp. 239–256, 1992.

[121] L. W. Clements, W. C. Chapman, B. M. Dawant, R. L. Galloway, and M. I. Miga, "Robust surface registration using salient anatomical features for image-guided liver surgery: algorithm and validation." *Medical physics*, vol. 35, no. 6, pp. 2528–2540, 2008.

[122] L. W. Clements, P. Dumpuri, W. C. Chapman, B. M. Dawant, R. L. Galloway, and M. I. Miga, "Organ surface deformation measurement and analysis in open hepatic surgery: Method and preliminary results from 12 clinical cases," *IEEE Transactions on Biomedical Engineering*, vol. 58, no. 8, pp. 2280–2289, 2011.

[123] O. Heizmann, S. Zidowitz, H. Bourquain, S. Potthast, H. O. Peitgen, D. Oertli, and C. Kettelhack, "Assessment of intraoperative liver deformation during hepatic resection: Prospective clinical study," *World Journal of Surgery*, vol. 34, no. 8, pp. 1887–1893, 2010.

[124] J. Y. Cho, H.-s. Han, Y.-s. Yoon, and S.-H. Shin, "Feasibility of laparoscopic liver resection for tumors located in the posterosuperior segments of the liver, with a special reference to overcoming current limitations on tumor location," *Surgery*, vol. 144, pp. 32–38, 2008.

[125] M. Kleemann, S. Deichmann, H. Esnaashari, A. Besirevic, O. Shahin, H.-p. Bruch, and T. Laubert, "Laparoscopic Navigated Liver Resection: Technical Aspects and Clinical Practice in Benign Liver Tumors," *Case Reports in Surgery*, vol. 2012, pp. 1–8, 2012.

[126] C. Song, A. Alijani, T. Frank, G. B. Hanna, and A. Cuschieri, "Mechanical properties of the human abdominal wall measured in vivo during insufflation for laparoscopic surgery," *Surgical Endoscopy*, vol. 20, no. 6, pp. 987–990, 2006.

[127] M. L. N. G. Malbrain, Y. Peeters, and R. Wise, "The neglected role of abdominal compliance in organ-organ interactions," *Critical Care*, vol. 20, no. 67, pp. 1–10, 2016.

[128] M. Zijlmans, T. Langø, E. F. Hofstad, F. P. Van Swol, Christiaan, and A. Rethy, "Navigated laparoscopy – liver shift and deformation due to pneumoperitoneum in an animal model," *Minimally Invasive Therapy*, vol. 21, pp. 241–248, 2012.

[129] S. Vijayan, I. Reinertsen, E. F. Hofstad, A. Rethy, T. A. N. Hernes, and T. Langø, "Liver deformation in an animal model due to pneumoperitoneum assessed by a vessel-based deformable registration," *Minimally Invasive Therapy*, vol. 23, pp. 279–286, 2014.

[130] S. F. Johnsen, S. Thompson, M. J. Clarkson, M. Modat, Y. Song, J. Totz, K. Gurusamy, B. Davidson, Z. A. Taylor, D. J. Hawkes, and S. Ourselin, "Database-Based Estimation of Liver Deformation under Pneumoperitoneum for Surgical Image-Guidance," *MICCAI 2015*, pp. 450–458, 2015.

[131] Y. Masutani and F. Kimura, "A new modal representation of liver deformation for non-rigid registration in image-guided surgery," *International Congress Series*, vol. 1230, pp. 20–26, 2001.

[132] D. M. Cash, M. I. Miga, T. K. Sinha, R. L. Galloway, and W. C. Chapman, "Compensating for intraoperative soft-tissue deformations using incomplete surface data and finite elements," *IEEE Transactions on Medical Imaging*, vol. 24, no. 11, pp. 1479–1491, 2005.

[133] P. Dumpuri, L. W. Clements, B. M. Dawant, and M. I. Miga, "Model-updated image-guided liver surgery: Preliminary results using surface characterization," *Progress in Biophysics and Molecular Biology*, vol. 103, no. 2-3, pp. 197–207, 2010.

[134] A. Myronenko and X. Song, "Point Set Registration: Coherent Point Drift," *IEEE Transactions on Pattern Analysis and Machine Intelligence*, vol. 32, no. 12, pp. 2262–2275, 2010.

[135] M. Pfeiffer, C. Riediger, J. Weitz, and S. Speidel, "Learning soft tissue behavior of organs for surgical navigation with convolutional neural networks," *International Journal of Computer Assisted Radiology and Surgery*, vol. 14, no. 7, pp. 1147–1155, 2019.

[136] J. Ramalhinho, M. R. Robu, S. Thompson, K. Gurusamy, B. Davidson, D. Hawkes, D. Barratt, and M. J. Clarkson, "A pre-operative planning framework for global registration of laparoscopic ultrasound to CT images," *International Journal of Computer Assisted Radiology and Surgery*, vol. 13, no. 8, pp. 1177–1186, 2018.

[137] T. Wakai, Y. Shirai, J. Sakata, V. A. Valera, P. V. Korita, K. Akazawa, Y. Ajioka, and K. Hatakeyama, "Appraisal of 1 cm hepatectomy margins for intrahepatic micrometastases in patients with colorectal carcinoma liver metastasis." *Annals of Surgical Oncology*, vol. 15, no. 9, pp. 2472–81, 2008.

[138] J. M. Fitzpatrick, "Fiducial registration error and target registration error are uncorrelated," in *Proceedings of SPIE Medical Imaging 2009: Visualization, Image-Guided Procedures, and Modeling Conference*, vol. 726102, 2009, pp. 1–12.

[139] C. T. McKee, J. A. Last, P. Russell, and C. J. Murphy, "Indentation versus tensile measurements of Young's modulus for soft biological tissues," *Tissue Engineering - Part B*, vol. 17, no. 3, pp. 155–164, 2011.

[140] E. J. Chen, J. Novakofski, W. K. Jenkins, and W. D. O'Brien, "Young's Modulus Measurements of Soft Tissues with Application to Elasticity Imaging," *IEEE Transactions on Ultrasonics, Ferroelectrics, and Frequency Control*, vol. 43, no. 1, pp. 191–194, 1996.

[141] M. I. Miga, K. D. Paulsen, F. E. Kennedy, P. J. Hoopes, A. Hartov, and D. W. Roberts, "Modeling Surgical Loads to Account for Subsurface Tissue Deformation During Stereotactic Neurosurgery," *SPIE Proceedings of Laser-Tissue Interaction IX, Part B: Soft-Tissue Modeling*, vol. 3254, pp. 501–511, 1998.

[142] R. Plantefève, I. Peterlik, and S. Cotin, "Intraoperative Biomechanical Registration of the Liver: Does the Heterogeneity of the Liver Matter?" *Innovation and Research in Biomedical Engineering*, vol. 39, pp. 18–25, 2018.

[143] N. Haouchine, S. Cotin, I. Peterlik, J. Dequidt, M. Sanz-Lopez, E. Kerrien, and M.-O. Berger, "Impact of Soft Tissue Heterogeneity on Augmented Reality for Liver Surgery," *IEEE Transactions on Visualization and Computer Graphics*, vol. 21, no. 5, pp. 584–597, 2015.

[144] C. Chui, E. Kobayashi, X. Chen, T. Hisada, and I. Sakuma, "Combined compression and elongation experiments and non-linear modelling of liver tissue for surgical simulation," *Medical and Biological Engineering and Computing*, vol. 42, no. 6, pp. 787–798, 2004.

[145] A. R. Kemper, A. C. Santago, J. D. Stitzel, J. L. Sparks, and S. M. Duma, "Biomechanical response of human liver in tensile loading," *Annals of Advances in Automotive Medicine*, vol. 54, pp. 15–26, 2010.

[146] J. M. Sullivan, G. Charron, and K. D. Paulsen, "A three-dimensional mesh generator for arbitrary multiple material domains," *Finite Elements in Analysis and Design*, vol. 25, pp. 219–241, 1997.

[147] R. Von Mises, "On Saint Venant's principle," *Bulletin of the Americal Mathematical Society*, vol. 51, pp. 555–562, 1945.

[148] E. Sternberg, "On Saint-Venant's principle*," *Quarterly of Applied Mathematics*, vol. 11, pp. 393–402, 1953.

[149] R. A. Toupin, "Saint-Venant's Principle," *Archive for Rational Mechanics and Analysis*, vol. 18, no. 2, pp. 83–96, 1965.

[150] M. E. Gurtin, *Mechanics of Solids II: Linear Theories of Elasticity and Thermoelasticity & Linear and Nonlinear Theories of Rods, Plates, and Shells*, 1st ed., C. Truesdell, Ed. New York: Springer-Verlag, 1984.

[151] M. Capurro and F. Barberis, "Evaluating the mechanical properties of biomaterials," in *Biomaterials for Bone Regeneration: Novel Techniques and Applications*, 2014, ch. 9, pp. 270–323.

[152] J. S. Heiselman, J. A. Collins, L. W. Clements, J. A. Weis, A. L. Simpson, S. K. Geevarghese, T. P. Kingham, W. R. Jarnagin, and M. I. Miga, "Technical note: Non-rigid registration for laparoscopic liver surgery using sparse intraoperative data," in *SPIE Medical Imaging*, vol. 10576, 2018, pp. 1–12.

[153] M. D. Kluger, L. Vigano, R. Barroso, and D. Cherqui, "The learning curve in laparoscopic major liver resection," *J Hepatobiliary Pancreat Sci*, vol. 20, no. 10, pp. 131–136, 2013.

[154] T. Nomi, D. Fuks, Y. Kawaguchi, F. Mal, Y. Nakajima, and B. Gayet, "Learning curve for laparoscopic major hepatectomy," *BJS*, vol. 102, no. 7, pp. 796–804, 2015.

[155] N. C. Buchs, F. Volonte, C. Toso, M. Fusaglia, K. Gavaghan, P. E. Majno, M. Peterhans, S. Weber, and P. Morel, "Augmented environments for the targeting of hepatic lesions during image-guided robotic liver surgery," *Journal of Surgical Research*, vol. 184, no. 2, pp. 825–831, 2013.

[156] J. S. Heiselman, J. A. Collins, L. W. Clements, J. A. Weis, A. L. Simpson, S. K. Geevarghese, W. R. Jarnagin, and M. I. Miga, "Emulation of the laparoscopic environment for image-guided liver surgery via an abdominal phantom system with anatomical ligamenture," in *Proc. of SPIE Medical Imaging*, vol. 10135, 2017, pp. 1–9.

[157] J. D'Errico, "Surface fitting using gridfit," 2005. [Online]. Available: https://www.mathworks.com/matlabcentral/fileexchange/8998-surface-fitting-using-gridfit

[158] H. Edelsbrunner and D. G. Kirkpatrick, "On the Shape of a Set of Points in the Plane," *IEEE Transactions on Information Theory*, vol. 29, no. 4, pp. 551–559, 1983.

[159] H. Edelsbrunner and E. P. Mücke, "Three-Dimensional Alpha Shapes," *ACM Transactions on Graphics*, vol. 13, no. 1, pp. 43–72, 1994.

[160] M.-p. Dubuisson, A. K. Jain, E. Lansing, and A. B. B, "A Modified Hausdorff Distance for Object Matching," in *Proc. International Conference on Pattern Recognition*, 1994, pp. 566–568.

[161] H. S. Kim, S. B. Park, S. S. Lo, J. I. Monroe, and J. W. Sohn, "Bidirectional local distance measure for comparing segmentations," *Medical Physics*, vol. 39, no. 11, pp. 6779–6790, 2012.

[162] C. O. Horgan and L. E. Payne, "Saint-Venant's Principle in Linear Isotropic Elasticity for Incompressible or Nearly Incompressible Materials," *Journal of Elasticity*, vol. 46, pp. 43–52, 1997.

[163] F. Devernay, "CMinpack," 2007. [Online]. Available: https://github.com/devernay/cminpack

[164] J. Georgii and R. Westermann, "Corotated Finite Elements Made Fast and Stable," in *Workshop in Virtual Reality Interactions and Physical Simulation VRIPHYS*, 2008, pp. 11–19.

[165] S. Marschesseau, S. Chatelin, and H. Delingette, "Non linear Biomechanical Model of the Liver: Hyperelastic Constitutive Laws for Finite Element Modeling," in *Biomechanics of Living Organs*, Y. Payan and J. Ohayon, Eds. Elsevier, 2017, pp. 602–623.

[166] N. Archip, S. Tatli, P. R. Morrison, F. Jolesz, S. K. Warfield, and S. G. Silverman, "Non-rigid registration of pre-procedural MR images with intra-procedural unenhanced CT images for improved targeting of tumors during liver radiofrequency ablations," *Medical Image Computing and Computer-Assisted Intervention*, vol. 10, no. 2, pp. 969–977, 2007.

[167] L. Antiga, M. Piccinelli, L. Botti, B. Ene-Iordache, A. Remuzzi, and D. A. Steinman, "An image-based modeling framework for patient-specific computational hemodynamics," *Medical and Biological Engineering and Computing*, vol. 46, no. 11, pp. 1097–1112, 2008.

[168] T. K. Chen, A. D. Thurston, R. E. Ellis, and P. Abolmaesumi, "A real-time freehand ultrasound calibration system with automatic accuracy feedback and control," *Ultrasound in Medicine and Biology*, vol. 35, no. 1, pp. 79–93, 2009.

[169] J. E. Bresenham, "Algorithm for computer control of a digital plotter," *IBM Systems Journal*, vol. 4, no. 1, pp. 25–30, 1965.

[170] B. Vallet and B. Lévy, "Spectral Geometry Processing with Manifold Harmonics," *Eurographics*, vol. 27, no. 2, 2008.

[171] T. Möller, "A fast triangle-triangle intersection test," *Journal of Graphics Tools*, vol. 2, no. 2, pp. 1–5, 1997.

[172] J. M. Fitzpatrick, J. B. West, and C. R. Maurer, "Predicting Error in Rigid-Body Point-Based Registration," *IEEE Transactions on Medical Imaging*, vol. 17, no. 5, pp. 694–702, 1998.

[173] J. M. Fitzpatrick and J. B. West, "The distribution of target registration error in rigid-body point-based registration," *IEEE Transactions on Medical Imaging*, vol. 20, no. 9, pp. 917–927, 2001.

[174] A. D. Wiles, A. Likholyot, D. D. Frantz, and T. M. Peters, "A Statistical Model for Point-Based Target Registration Error With Anisotropic Fiducial Localizer Error," *IEEE Transactions on Medical Imaging*, vol. 27, no. 3, pp. 378–390, 2008.

[175] M. H. Moghari and P. Abolmaesumi, "Distribution of target registration error for anisotropic and inhomogeneous fiducial localization er," *IEEE Transactions on Medical Imaging*, vol. 28, no. 6, pp. 799–813, 2009.

[176] A. Danilchenko and J. M. Fitzpatrick, "General Approach to First-Order Error Prediction in Rigid Point Registration," *IEEE Transactions on Medical Imaging*, vol. 30, no. 3, pp. 679–693, 2011.

[177] A. Sotiras, C. Davatzikos, and N. Paragios, "Deformable Medical Image Registration : A Survey," *IEEE Transactions on Medical Imaging*, vol. 32, no. 7, pp. 1153–1190, 2013.

[178] K. K. Brock, M. B. Sharpe, L. A. Dawson, S. M. Kim, and D. A. Jaffray, "Accuracy of finite element model-based multi-organ deformable image registration," *Medical Physics*, vol. 32, no. 6, pp. 1647–1659, 2005.

[179] S. Frisken, M. Luo, P. Juvekar, A. Bunevicius, I. Machado, P. Unadkat, M. M. Mertotti, M. Toews, W. M. Wells, M. I. Miga, and A. J. Golby, "A comparison of thin-plate spline deformation and finite element modeling to compensate for brain shift during tumor resection," *International Journal of Computer Assisted Radiology and Surgery*, vol. 15, no. 1, pp. 75–85, 2020.

[180] M. Bro-Nielsen, "Surgery Simulation using Fast Finite Elements," in *Visualization in Biomedical Computing*, K. H. Höhne and R. Kikinis, Eds. Berlin, Heidelberg: Springer Berlin Heidelberg, 1996, pp. 529–534.

[181] S. P. Timoshenko and J. N. Goodier, *Theory of Elasticity*, 3rd ed. New York: McGraw-Hill, 1970.

[182] J. K. Knowles and C. O. Horgan, "On the exponential decay of stresses in circular elastic cylinders subject to axisymmetric self-equilibrated end loads," *International Journal of Solids and Structures*, vol. 5, no. 1, pp. 33–50, 1969.

[183] G. F. Miller and H. Pursey, "On the partition of energy between elastic waves in a semi-infinite solid," *Proceedings of the Royal Society of London, Series A, Mathematical and Physical Sciences*, vol. 233, no. 1192, pp. 55–69, 1955.

[184] T. Piboongungon, V. A. Aalo, C. D. Iskander, and G. P. Efthymoglou, "Bivariate generalised gamma distribution with arbitrary fading parameters," *IEEE Electronics Letters*, vol. 41, no. 12, pp. 709–710, 2005.

[185] R. T. Clarke, "Bivariate gamma distributions for extending annual streamflow records from precipitation: Some large-sample results," *Water Resources Research*, vol. 16, no. 5, pp. 863–870, 1980.

[186] G. C. Ghirtis, "Some problems of statistical inference relating to the double-gamma distribution," *Trabajos de Estadistica*, vol. 18, pp. 67–87, 1967.

[187] R. R. Shamir, L. Joskowicz, and S. Spektor, "Localization and registration accuracy in image guided neurosurgery : a clinical study," *International Journal of Computer Assisted Radiology and Surgery*, vol. 4, pp. 45–52, 2009.

[188] R. R. Shamir, L. Joskowicz, and Y. Shoshan, "Fiducial Optimization for Minimal Target Registration Error in Image-Guided Neurosurgery," *IEEE Transactions on Medical Imaging*, vol. 31, no. 3, pp. 725–737, 2012.

[189] J. Shindoh, J.-N. Vauthey, G. Zimmitti, S. A. Curley, S. Y. Huang, A. Mahvash, S. Gupta, M. J. Wallace, and T. A. Aloia, "Analysis of the efficacy of portal vein embolization for patients with extensive liver malignancy and very low future liver remnant volume including a comparison to the associating liver partition with portal vein ligation for staged hepatectomy approach," *Journal of the American College of Surgeons*, vol. 217, no. 1, pp. 1–14, 2013.

[190] K. P. Van Lienden, V. D. E. J. W, W. De Graaf, S. Bipat, J. S. Lameris, T. M. Van Gulik, and O. M. Van Delden, "Portal Vein Embolization Before Liver Resection: A Systematic Review," *Cardiovascular and Interventional Radiology*, vol. 36, pp. 25–34, 2013.

[191] A. Chan, W. Y. Zhang, K. Chok, J. Dai, R. Ji, C. Kwan, N. Man, R. Poon, and C. M. Lo, "ALPPS Versus Portal Vein Embolization for Hepatitis-related Hepatocellular Carcinoma: A Changing Paradigm in Modulation of Future Liver Remnant Before Major Hepatectomy," *Annals of Surgery*, 2019 (pre-print).

[192] S. Yamashita, J. Shindoh, T. Mizuno, Y. S. Chun, C. Conrad, T. A. Aloia, and J.-n. Vauthey, "Hepatic atrophy following preoperative chemotherapy predicts hepatic insufficiency after resection of colorectal liver metastases," *Journal of Hepatology*, vol. 67, no. 1, pp. 56–64, 2017.

[193] N. W. Y. Leung, P. Farrant, and T. J. Peters, "Liver Volume Measurement by Ultrasonography in Normal Subjects and Alcoholic Patients," *Journal of Hepatology*, vol. 2, pp. 157–164, 1986.

[194] T. Liem, H. Applebaum, and B. Herzberger, "Hemodynamic and ventilatory effects of abdominal CO2 insufflation at various pressures in the young swine," *Journal of Pediatric Surgery*, vol. 29, no. 8, pp. 966–969, 1994.

[195] E. A. Antoniou, E. V. I. Kairi, G. A. Margonis, N. Andreatos, K. Sasaki, C. Damaskos, N. Garmpis, M. Samaha, E. Argyra, G. Polymeneas, M. J. Weiss, T. M. Pawlik, D. Voros, and G. Kouraklis, "Effect of Increased Intra-abdominal Pressure on Liver Histology and Hemodynamics: An Experimental Study," *In Vivo*, vol. 32, no. 1, pp. 85–91, 2018.

[196] S. Takagi, "Hepatic and portal vein blood flow during carbon dioxide pneumoperitoneum for laparoscopic hepatectomy." *Surgical endoscopy*, vol. 12, no. 5, pp. 427–431, 1998.

[197] Y. Liu, W. Cao, Y. Liu, Y. Wang, R. Lang, Y. Yue, and A. S. Wu, "Changes in duration of action of rocuronium following decrease in hepatic blood flow during pneumoperitoneum for laparoscopic gynaecological surgery," *BMC Anesthesiology*, vol. 17, no. 1, pp. 1–9, 2017.

[198] K. D. Paulsen, M. I. Miga, F. E. Kennedy, P. Jack Hoopes, A. Hartov, and D. W. Roberts, "A computational model for tracking subsurface tissue deformation during stereotactic neurosurgery," *IEEE Transactions on Biomedical Engineering*, vol. 46, no. 2, pp. 213–225, 1999.

[199] A. Sen, B. M. Anderson, G. Cazoulat, M. M. Mcculloch, D. Elganainy, B. A. Mcdonald, and Y. He, "Accuracy of deformable image registration techniques for alignment of longitudinal cholangiocarcinoma CT images," *Medical Physics*, vol. 47, no. 4, pp. 1670–1679, 2020.

[200] M. Yarahmadian, Y. Zhong, C. Gu, and J. Shin, "Soft tissue deformation estimation by spatio-temporal Kalman filter finite element method," *Technology and Health Care*, vol. 26, no. S1, pp. 317–325, 2018.

[201] I. Peterlik, N. Haouchine, L. Ručka, and S. Cotin, "Image-driven Stochastic Identification of Boundary Conditions for Predictive Simulation," in *MICCAI 2017: Medical Image Computing and Computer-Assisted Intervention*, 2017.

[202] S. Nikolaev and S. Cotin, "Estimation of boundary conditions for patient-specific liver simulation during augmented surgery," *International Journal of Computer Assisted Radiology and Surgery*, vol. 15, pp. 1107–1115, 2020.

[203] A. D. Speers, B. Ma, W. R. Jarnagin, S. Himidan, A. L. Simpson, and R. P. Wildes, "Fast and accurate vision-based stereo reconstruction and motion estimation for image-guided liver surgery," *Healthcare Technology Letters*, vol. 5, no. 5, pp. 208–214, 2018.

[204] J. A. Collins, J. S. Heiselman, L. W. Clements, D. B. Brown, M. I. Miga, J. A. Collins, J. S. Heiselman, L. W. Clements, D. B. Brown, and M. I. Miga, "Multi-physics modeling toward enhanced guidance in hepatic microwave ablation: a preliminary framework," *Journal of Medical Imaging*, vol. 6, no. 2, p. 025007, 2019.

[205] I. Paolucci, M. Schwalbe, G. A. Prevost, A. Lachenmayer, D. Candinas, S. Weber, and P. Tinguely, "Design and implementation of an electromagnetic ultrasound-based navigation technique for laparoscopic ablation of liver tumors," *Surgical Endoscopy and Other Interventional Techniques*, vol. 32, no. 7, pp. 3410–3419, 2018.

[206] F. Banovac, J. Tang, S. Xu, D. Lindisch, H. Y. Chung, E. B. Levy, T. Chang, M. F. McCullough, Z. Yaniv, B. J. Wood, and K. Cleary, "Precision targeting of liver lesions using a novel electromagnetic navigation device in physiologic phantom and swine." *Medical Physics*, vol. 32, no. 8, pp. 2698–2705, 2005.

[207] Y. Wu, D. C. Rucker, R. H. Conley, T. S. Pheiffer, A. L. Simpson, S. K. Geevarghese, and M. I. Miga, "Registration of liver images to minimally invasive intraoperative surface and subsurface data," in *Proc. SPIE Medical Imaging*, vol. 9036, 2014, pp. 1–8.

[208] J. Y. Cho, H.-S. Han, Y.-S. Yoon, and S.-H. Shin, "Outcomes of Laparoscopic Liver Resection for Lesions Located in the Right Side of the Liver," *Arch Surg*, vol. 144, no. 1, pp. 25–29, 2009.

[209] D. Cherqui, E. Husson, R. Hammoud, and B. Malassagne, "Laparoscopic Liver Resections : A Feasibility Study in 30 Patients," *Annals of surgery*, vol. 232, no. 6, pp. 753–762, 2000.

[210] E. L. Brewer, L. W. Clements, J. A. Collins, D. J. Doss, J. S. Heiselman, M. I. Miga, C. D. Pavas, and E. H. Wisdom, "The image-to-physical liver registration sparse data challenge," in *Proceedings of SPIE Medical Imaging 2019: Image-Guided Procedures, Robotic Interventions, and Modeling Conference*, vol. 10951, 2019, pp. 1–7.

[211] J. S. Heiselman and M. I. Miga, "The image-to-physical liver registration sparse data challenge: characterizing inverse biomechanical model resolution," in *Proc. of SPIE Medical Imaging*, no. 11315, 2020, p. 113151F.

[212] J. S. Heiselman, W. R. Jarnagin, and M. I. Miga, "Deformable registration of the liver using sparse intraoperative data: Incorporating hepatic feature constraints from tracked intraoperative ultrasound," *International Journal of Computer Assisted Radiology and Surgery*, vol. 15, no. S1, pp. S146–S147, 2020.